Technische Universität München

Lehrstuhl für Experimentelle
Astroteilchenphysik

Setup of a Neutron Scattering Facility for the Measurement of Scintillation Light Quenching Factors of Low-Temperature Detectors Used in the Direct Dark Matter Search Experiments CRESST and EURECA

Christian Ciemniak

Vollständiger Abdruck der von der Fakultät für Physik der Technischen Universität München zur Erlangung des akademischen Grades eines

Doktors der Naturwissenschaften (Dr. rer. nat.)

genehmigten Dissertation.

Vorsitzender:		Univ.-Prof. Dr. A. Ibarra
Prüfer der Dissertation:	1.	Univ.-Prof. Dr. F. von Feilitzsch
	2.	Priv.-Doz. Dr. A. Ulrich

Die Dissertation wurde am 31.05.2011 bei der Technischen Universität München eingereicht und durch die Fakultät für Physik am 05.07.2011 angenommen.

Abstract

Technological advances, in particular during the last decade, have made it possible to perform precision tests of cosmological models. These only conform with general relativity if large amounts of non-baryonic Dark Matter are present in the Universe. The nature of Dark Matter still remains unknown. Well-motivated candidates are Weakly Interacting Massive Particles (WIMPs), i.e. neutral, massive and non-relativistic particles that interact with baryonic matter only on a scale no stronger than the weak interaction.

A promising approach to direct WIMP detection is the search for nuclear recoils of a few keV induced by WIMP-nucleon scattering. The CRESST (Cryogenic Rare Event Search with Superconducting Thermometers) experiment, located at the Gran Sasso underground laboratory LNGS (Laboratori Nazionali del Gran Sasso), features a multiple-target approach by employing scintillating $CaWO_4$ crystals as bulk detector material. Each crystal is equipped with a transition edge sensor (TES), which allows to measure the energy transfer into the phononic system of the crystal due to a particle interaction. In good approximation, this phonon signal determines the total energy deposition of the interaction. The scintillation light emitted simultaneously is measured by a light detector, where the energy deposition is also detected by a TES. The ratio of the produced scintillation light and phonons depends on the interacting particles: For an electron recoil, induced by background radiation of gammas and betas, the ratio is higher by an order of magnitude compared to nuclear recoils. The reduced light output for nuclear recoils is called quenching, and allows - with high significance - to suppress the bulk of events caused by background radiation inducing electron recoils. The quenching factors, which quantify the expected light output dependent on the recoil type, vary for the different constituents of $CaWO_4$, and allow us, within the resolution of the light detector, to discriminate between the various types of nuclear recoil. Nuclear recoils induced by background neutrons, for example, will scatter for kinematic reasons most prominently off oxygen. For WIMP scattering, the nuclear recoil rates for the different target nuclei are expected to be proportional to A^2, where A is the number of nucleons in a nucleus. Due to the finite energy threshold of a detector, light WIMPs (few GeV) can only produce a signal above the detection threshold if scattering off the lighter nuclei (O, Ca), while heavy WIMPs ($> 20GeV$) will show up mainly as W-recoils. The ability of CRESST to check in situ the rate-consistency for different target nuclei and to probe for light and heavy-WIMP scenarios is a unique feature of this experiment. The planned future large-scale multi-material experiment EURECA (European Underground Rare Event Calorimeter Array) will extend the multi-target approach by combining the technology of CRESST and EDELWEISS (Expérience pour DEtecter Les Wimps En Site Souterrain), which, similar to CDMS (Cold Dark Matter Search), uses germanium as target material.

To measure the bulk quenching factors in $CaWO_4$ and other detector materials (e.g. $ZnWO_4$ or NaI), a unique neutron scattering facility has been set up at the Maier-Leibnitz-Laboratorium in Garching. In this facility, nuclear

recoils are induced by neutrons of known energy (typically $\sim$ 11 MeV) in a bulk target crystal operated as a CRESST-like detector at mK temperatures. The combined triple coincidence measurement of the neutrons' time-of-flight, the scattering angle and the energy deposition in the target crystal allows us to identify the recoiling nucleus and to measure the quenching factors directly.

In the scope of the present work, a detector module together with a SQUID-based readout system was installed in a low-temperature cryostat (^{3}He/^{4}He dilution refrigerator). To meet the requirements imposed by the combination of a slow cryogenic detector ($\sim ms$) with an array of fast ($\sim ns$) neutron detectors, a new VME-based data acquisition (DAQ) was designed and a customized DAQ software was developed. The complex data analysis is performed offline. For this purpose, a complete software pipeline for the coincidence analysis was developed, including a suite for the substantial treatment of the data of the cryogenic detector module. All these efforts have been successfully finalized and thoroughly tested in several beam times.

An in-depth analysis of a complete beam time campaign is presented in detail: From this measurement, 20 events fulfilling the coincidence condition were extracted with a signal to background ratio of 10:1, and the underlying scattering mechanisms were identified for all events. The statistical yield of a beam time is limited by the slow cryogenic detector (that can only cope with rates of $\sim 10 - 15Hz$) and the solid angle covered by the neutron detectors. While the slow pulses are an intrinsic feature of cryogenic detectors, the covered solid angle has been doubled by adding large-area neutron detectors for future beam times. However, the most promising approach to reduce the measurement time required to determine high quenching factors is an increase of the energy resolution of the scintillation light detector. The achieved resolution in the analyzed beam time is $4.7keV$ (at 1σ level) for a nuclear recoil energy of $100keV$ and a scintillation light output of $\sim 10keV$ electron equivalent. At this energy, quenching factors of up to 50 can be determined in $\sim$4 weeks of measurement time if the resolution of the light detector is increased by a factor of two. Significant efforts in this direction have also been undertaken by upgrading the scintillation light detector with Neganov-Luke (NL) capability, which is a technique to amplify the scintillation light signal and greatly improve the signal to noise ratio. The low-temperature detector module was equipped with NL-light amplification and the threshold to discriminate between electron and nuclear recoils was improved with the employed light detector by a factor of ~ 3. The gained understanding of this technique will be useful for future phases of the CRESST experiment as well as for EURECA.

An exact measurement of the bulk quenching factors is important for the interpretation of the CRESST data and will allow the comparison of observed nuclear recoil events with predictions for WIMP-nucleon scattering rates, and thus significantly increase the WIMP-discovery potential of the CRESST and EURECA experiments.

Zusammenfassung

Sowohl terrestrische als auch satellitengestützte Experimente ermöglichten im Laufe des letzten Jahrzehnts präzise Messungen wichtiger kosmologischer Grössen. Deren Ergebnisse sind nur dann mit der allgemeinen Relativitätstheorie in Einklang zu bringen, wenn in unserem Universum große Mengen kalter, dunkler, nicht-baryonischer Materie existieren. Bisher unentdeckte, von der Theorie jedoch gut motivierte Kandidaten für die dunkle Materie sind sogenannte WIMPs (Weakly Interacting Massive Particles). Unter diesem Begriff versteht man neutrale und massereiche Teilchen, deren Kopplungsstärke an baryonischer Materie die der schwachen Wechselwirkung nicht übersteigt.

Eine vielversprechende Methode zur direkten Messung von WIMPs in erdbasierten Experimenten ist die Suche nach den durch sie induzierten Kernrückstößen, welche bei kleinen Energien (einige keV) erwartet werden. Das CRESST (Cryogenic Rare Event Search with Superconducting Thermometers) Experiment am LNGS (Laboratori Nazionali del Gran Sasso) in Italien beruht auf dieser Methode. Als Detektormaterial werden hier szintillierende $CaWO_4$ Einkristalle bei tiefen Temperaturen (einige mK) betrieben. Jeder Kristall ist mit einem Phasenübergangsthermometer (transition edge sensor, TES) ausgestattet. Ein TES erlaubt die direkte Bestimmung der in einer Teilchenwechselwirkung produzierten Phononen (Wärme), was in guter Näherung einer Messung der gesamten Energiedeposition entspricht. Das gleichzeitig emittierte Szintillationslicht wird von einem separaten Lichtdetektor absorbiert; die deponierte Energie wird dabei ebenfalls durch ein TES erfasst. Das Verhältnis zwischen produziertem Szintillationslicht und Phononen hängt von der Art der Teilchenwechselwirkung ab: Kernrückstöße produzieren im Vergleich zu Elektronenrückstößen, die von Gamma- und Beta-Strahlung herrühren, etwa eine Größenordnung weniger Licht. Dieser als Quenching bezeichnete Effekt wird genutzt, um auf die Art der Wechselwirkung zu schließen. Bei CRESST kann dadurch der größte Teil des Untergrunds, nämlich Elektronenrückstöße, mit hoher Signifikanz ausgeschlossen werden. Die Quenchingfaktoren, welche die Reduktion der produzierten Lichtmenge bei Kernrückstößen quantifizieren, sind für jeden Atomkern in $CaWO_4$ anders und ermöglichen es (im Rahmen der Auflösung des Lichtdetektors) auf den rückgestreuten Atomkern zu schließen. So werden durch Untergrundneutronen induzierte Kernrückstöße aus kinematischen Gründen hauptsächlich an Sauerstoff nachgewiesen. Für WIMPs hingegen skaliert die erwartete Rate aufgrund der vorhergesagten Kohärenz der WIMP-Nukleon-Streuung mit A^2, wobei A die Anzahl der Nukleonen im Streuzentrum ist. Schwere WIMPs ($> 20\,GeV$) führen deshalb vornehmlich zu W-Rückstößen. Aufgrund der endlichen Energieschwelle der eingesetzten Detektoren können leichte WIMPs (einige GeV) eine nachweisbare Wechselwirkung jedoch nur an den leichten Kernen (O, Ca) hervorrufen. Der Einsatz unterschiedlicher Materialien in einem Experiment ist ein einzigartiges Merkmal von CRESST. Dadurch wird es möglich, sowohl die erwartete A^2-Ratenabhängigkeit direkt zu beobachten als auch gleichzeitig nach leichten wie auch schweren WIMPs zu

suchen.

Um die Quenchingfaktoren von $CaWO_4$ und anderen Detektormaterialien (z.B. $ZnWO_4$ und NaI) zu messen, wurde am Maier-Leibnitz-Laboratorium (MLL) in Garching ein weltweit einzigartiges Neutronen-Streuexperiment bei tiefen Temperaturen aufgebaut. Die zu charakterisierenden Kernrückstöße werden dort durch Neutronen bekannter Energie ($\sim$ 11 MeV) im gesamten Detektorvolumen bei einer Betriebstemperatur von einigen mK erzeugt. Die koinzidente Flugzeitmessung der Neutronen und ihres Streuwinkels sowie der im Tieftemperaturdetektor deponierten Energie erlaubt es, den Rückstoßkern zu identifizieren und somit die Quenchingfaktoren direkt zu bestimmen.

Im Rahmen der vorliegenden Arbeit wurden ein dem CRESST-Design nachempfundener Detektor sowie ein SQUID-basierendes Auslesesystem in einem ^{3}He/^{4}He Entmischungskryostaten installiert. Die Kombination eines langsamen ($\sim$ ms) Tieftemperaturdetektors mit den zur Flugzeitmessung benötigten schnellen ($\sim$ ns) Flüssigszintillatordetektoren wurde realisiert, indem eine speziell an das Experiment angepasste Datenaufnahme entworfen und eine dazugehörige Software entwickelt wurde. Die komplexe Datenanalyse wird offline durchgeführt. Um diese Aufgabe zu bewältigen, wurden die benötigten Schritte zur Extraktion der Koinzidenzereignisse erfolgreich automatisiert und eine umfangreiche Auswertungssoftware für die Ereignisse im Tieftemperaturdetektor entwickelt. Alle Maßnahmen wurden abgeschlossen und ihre Funktionalität vollumfänglich in mehreren Strahlzeiten gezeigt.

Die Leistungsfähigkeit des experimentellen Aufbaus und der Datenanalyse wird in der vorliegenden Arbeit anhand einer detaillierten Auswertung einer kompletten Strahlzeit gezeigt. Bei dieser Messung wurden 20 koinzidente Ereignisse mit einem Signal- zu Untergrundverhältnis von 10:1 aus insgesamt drei Millionen Ereignissen im Tieftemperaturdetektor extrahiert. Alle 20 Ereignisse konnten dem jeweiligen zugrundeliegenden Streumechanismus zugeordnet werden. Die statistische Ausbeute einer Strahlzeit ist limitiert durch den verhältnismäßig langsamen Tieftemperaturdetektor, der maximal Raten von $\sim$ 15 Hz erlaubt, sowie den durch die Neutronendetektoren abgedeckten Raumwinkel. Die langsamen Pulse des Tieftemperaturdetektors sind eine intrinsische Eigenschaft und können als solche nicht geändert werden. Der sensitive Raumwinkel hingegen wurde durch den Einsatz von großflächigen Neutronendetektoren verdoppelt. Der aussichtsreichste Ansatz, um die benötigte Messzeit zur Bestimmung von hohen Quenchingfaktoren zu reduzieren, ist jedoch eine Verbesserung der Auflösung des Lichtdetektors. Die erreichte Auflösung der präsentierten Strahlzeit liegt bei $\sim$ 4.7 keV (1σ C.L.) für Kernrückstöße von $\sim$ 100 keV, welche Szintillationslicht von $\sim$ 10 keV Elektronen-Äquivalent produzieren. Wenn die Auflösung des Lichtdetektors um einen Faktor zwei verbessert würde, könnten bei dieser Energie Quenchingfaktoren von bis zu 50 innerhalb von $\sim$ 4 Wochen gemessen werden. Zu einer Auflösungsverbesserung können Neganov-Luke (NL) Lichtdetektoren beitragen, deren Einsatz am MLL im Rahmen dieser Arbeit ermöglicht wurde. Die NL-Technik ermöglicht es, ein gemessenes Lichtsignal zu verstärken und so das Signal-zu-Rausch Verhältnis stark zu verbessern.

Mit dem eingesetzten Detektor wurde so eine Verbesserung der Trennschwelle zwischen Elektronen- und Kernrückstößen um einen Faktor von $\sim$ 3 erreicht. Die mit dieser Technologie gewonnene Erfahrung ist von großer Bedeutung für die zukünftigen Mess-Perioden von CRESST und für das geplante EURECA (European Underground Rare Event Calorimeter Array) Experiment.

Die exakte Messung der Quenchingfaktoren ist von äußerster Wichtigkeit für die Interpretation der CRESST-Daten und wird es ermöglichen, die gemessenen Kernrückstoßraten mit den Vorhersagen für die WIMP-Nukleon-Streuung zu vergleichen. Dadurch wird das Potential von CRESST und EURECA signifikant erhöht, WIMPs in unserem Universum direkt nachzuweisen und verschiedene WIMP-Massen-Hypothesen zu testen.

Contents

1 Introduction **1**
1.1 Dark Matter . . . 1
1.1.1 Evidence for Dark Matter . . . 1
1.1.1.1 Dark Matter in Galaxy Clusters . . . 1
1.1.1.2 Dark Matter in Galaxies . . . 3
1.1.1.3 Cosmic Microwave Background . . . 3
1.1.1.4 Structure Formation . . . 5
1.1.1.5 The Bullet Cluster . . . 5
1.1.2 Dark Matter Candidates . . . 6
1.1.2.1 WIMPs . . . 7
1.1.2.2 Axions . . . 7
1.1.2.3 Neutrinos . . . 8
1.1.2.4 Sterile Neutrinos . . . 8
1.1.2.5 Other Candidates . . . 9
1.1.2.6 Alternative Theories . . . 9
1.2 Detection of WIMPs . . . 10
1.2.1 Indirect Dark Matter Search . . . 10
1.2.2 Fundamentals of Direct WIMP Search Experiments . . . 11
1.2.2.1 WIMP-Nucleon Interaction . . . 11
1.2.2.2 Annual Modulation of WIMP Recoil Rate . . . 12
1.2.3 Direct Dark Matter Search . . . 13
1.2.3.1 DAMA . . . 14
1.2.3.2 CoGeNT . . . 15
1.2.3.3 Liquid Noble Gas Detectors . . . 15
1.2.3.4 Low-Temperature Detectors . . . 16

2 The CRESST II Experiment **17**
2.1 Experimental Conception of the CRESST Experiment . . . 17
2.1.1 Transition Edge Sensors and Readout . . . 17
2.1.2 Detector Design . . . 19
2.1.3 Cryostat and Shielding . . . 20
2.1.4 Calibration and Stabilization . . . 22
2.2 CRESST Data Analysis and Results . . . 23
2.2.1 Quenching Factor and Light Yield . . . 23
2.2.2 Background Discrimination and Signal Identification . . . 24
2.2.2.1 Identification of Nuclear Recoils . . . 24

2.2.2.2 Expected WIMP Signal in CRESST 26
2.2.2.3 Expected Background in CRESST 28
2.2.3 Latest CRESST Results 30
2.2.3.1 Results of the Data Analysis 31
2.2.3.2 Additional Background Considerations 32
2.2.3.3 Interpretation and Planned Upgrades 33
2.2.3.4 Exclusion Limits for Inelastic Dark Matter . . . 34
2.3 Relevance of Quenching Factors 34

3 Experimental Setup for Quenching Factor Measurements 37
3.1 Overview 38
3.2 Neutron Production 40
3.2.1 The Accelerator 40
3.2.1.1 Tandem Accelerator 40
3.2.1.2 Generation of a Pulsed Beam 41
3.2.2 Nuclear Reaction and Target Cell 43
3.2.3 Neutron Source Performance 45
3.3 Neutron Detector Arrays 48
3.3.1 Liquid Scintillators and Pulse Shape Discrimination . . . 48
3.3.2 Employed Neutron Detectors 49
3.3.3 Neutron Detector Timing Performance 50
3.4 The Low-Temperature Detector Module 51
3.4.1 Phonon Detector 51
3.4.2 Scintillation Light Detector 52
3.4.3 Detector Operation 53
3.4.3.1 Temperature Stabilization 53
3.4.3.2 Electrothermal Feedback 54
3.5 The Cryostat 54
3.5.1 SQUID Installation 55
3.5.2 Detector Installation I: First Generation Detector Holder 58
3.5.3 Detector Installation II: Light-Weight Holder 58
3.5.4 General Cryostat Performance 58
3.6 Implementation of Neganov-Luke Light Amplification 61
3.7 SQUID Readout 62
3.8 Data Acquisition 62
3.8.1 Data Acquisition Hardware 63
3.8.1.1 Wiring of the VME modules 63
3.8.1.2 v2718 VME Controller 64
3.8.1.3 v812 Constant Fraction Discriminators 65
3.8.1.4 v1190 Time to Digital Converter (TDC) 65
3.8.1.5 Sis3320 Flash Analog to Digital Converters for PMT Readout 67
3.8.1.6 Sis3302 Flash Analog to Digital Converter for the Cryodetector Readout 67
3.8.2 Data Acquisition Software 68
3.8.2.1 Back-End 68
3.8.2.2 Front-End 69

4 Data Analysis 73
4.1 Data Organization . . . 73
4.2 Data Analysis Overview . . . 73
4.3 Synchronizing the Module Clocks . . . 75
4.4 Double Coincidence Analysis . . . 76
4.4.1 Liquid Scintillator Pulse Shape Analysis . . . 76
4.4.2 Time of Flight Analysis . . . 77
4.4.3 Precise Determination of the Incident Neutron Energy . . 80
4.5 Analysis of the Low-Temperature Detector Data . . . 82
4.5.1 Calculation of all Pulse Parameters . . . 83
4.5.2 Determination of the Pulse Onset . . . 85
4.5.3 Flux Quantum Loss Compensation . . . 87
4.5.4 Stability Cut . . . 89
4.5.5 Standard Event Fit . . . 90
4.5.5.1 Building a Standard Event . . . 92
4.5.5.2 Truncated Standard Event Fit . . . 93
4.5.5.3 Truncated Standard Event Fit for Pileup Pulses 96
4.5.6 Mandatory Cuts . . . 96
4.5.7 Working Point and Neganov-Luke Drift Correction . . . 97
4.5.8 Phonon Detector Calibration . . . 99
4.5.8.1 Single Measurement Calibration . . . 100
4.5.8.2 Applying a Known Calibration . . . 101
4.5.9 Linearization and Calibration of the Light Detector . . . 102

5 Beam Time Analysis I: Low-Temperature Detector Analysis 105
5.1 October 2010 Beam Time: Overview . . . 105
5.2 Performing the Calibration . . . 106
5.2.1 General Calibration Procedure . . . 106
5.2.2 Calibration Data . . . 108
5.2.3 Calibration of the Beam Time Data . . . 110
5.2.3.1 Overview: Combination of Different Working Points . . . 111
5.2.3.2 Comparability of the 18 Data Sets . . . 112
5.3 Cryodetector Data Discussion . . . 113
5.3.1 Observed Features and General Properties . . . 113
5.3.2 Uncertainties in the Calibration and Possible Corrections 116
5.3.3 Composition of the Nuclear Recoil Band and Resolution of the Scintillation Light Detector . . . 119

6 Beam Time Analysis II: Triple-Coincidences 123
6.1 Triple-Coincidence Timing and the Signal Region . . . 123
6.1.1 Testing the Triple-Coincidence Timing with Hadronic Showers . . . 124
6.1.2 Definition of a Suitable Data Set for the Quenching Factor Analysis . . . 125
6.1.3 Discussion of Neutron-Induced Electron Recoils and Low-Energetic Neutrons . . . 129

6.1.3.1 Neutron-Induced Electron Recoils 129
6.1.3.2 Incident Neutron Energies below 7 MeV 133
6.2 Evaluation of the Events Used for the Quenching Factor Measurement 134
6.2.1 Expected Triple-Coincidence Distribution Based on Measured Cross Sections and Simulations 134
6.2.2 Error Estimation 136
6.2.3 Observed Events for the Evaluation of the Quenching Factor 138
6.3 Beam Time Summary 140

7 Ongoing Upgrades and Future Improvements 143
7.1 Required Statistics 143
7.2 Increasing the Number of Observed Triple-Coincidences per Beam Time 145
7.2.1 Beam Time Optimization 145
7.2.2 Increasing the Number of Neutron Detectors 145
7.3 Improving the Resolution of the Light Detector 146
7.3.1 Higher Total Energy Deposition 147
7.3.2 Calibration and Working Point Stability 147
7.3.3 Detected Scintillation Light: Different Crystal Geometry and Increased Absorption 148
7.3.4 Produced Scintillation Light: Composite Detector Design 148
7.3.5 Intrinsic Resolution: Neganov-Luke-Light Amplification . 149
7.3.5.1 Neganov-Luke Technique 149
7.3.5.2 Achieved Amplification under Optimal Conditions 150
7.3.5.3 Preliminary Neganov-Luke Setup at the Neutron Scattering Facility 151
7.4 Concluding Remarks on Future Upgrades and Measurements . . 153

8 Conclusions 155

Appendices 161

A EJ-301 Data Sheet 161

B Expanding the Dynamic Range of the v1190 TDC 163

C Data Analysis Details 167
C.1 Details on Data Organization 167
C.1.1 Folder Structure 167
C.1.2 Measurements 167
C.1.3 Files and File Types 168
C.1.3.1 v1190 TDC files 168
C.1.3.2 Sis3302 ADC files 168
C.1.3.3 Sis3320 ADC files 169
C.2 Low Level Data Access 169
C.2.1 Sis3302 Data Access 169
C.2.2 Sis3320 Data Access 170

C.2.3 v1190 TDC Data Access 170
C.3 Module Clock Synchronization 170
C.3.1 About Clock Deviation 171
C.3.2 Clock Synchronization Technique 171

D Nuclear Recoil Band Composition **175**

Bibliography **179**

Danksagung **186**

Chapter 1

Introduction

Section 1.1 presents cosmological evidence for the existence of Dark Matter and discusses possible Dark Matter candidates. Section 1.2 focuses on techniques and experiments for the search of WIMPs (Weakly Interacting Massive Particles), which are Dark Matter candidates currently very well motivated by theory.

1.1 Dark Matter

The existence of hidden mass is derived from numerous observations, the most important of which are outlined in section 1.1.1. Several particles have been suggested to explain these observations, some well motivated candidates are presented in section 1.1.2.

1.1.1 Evidence for Dark Matter

The cosmological observations presented in this section strongly suggest the existence of additional non-luminous and non-baryonic matter in the universe, dominating the evolution and dynamics of stellar bodies on all length scales, from galaxies to clusters and superclusters.

1.1.1.1 Dark Matter in Galaxy Clusters

The Swiss astrophysicist Fritz Zwicky was the first to provide evidence for non-luminous matter dominating the dynamics of stellar bodies. In 1933 he applied the virial theorem to the Coma Cluster of Galaxies and inferred that the average density of matter exceeds the density of luminous matter by a factor of 400 [1,2]. He was the first to use the term 'Dark Matter'.

More recent projects also measure the mass-to-light ratio in galaxy clusters, as before done by Zwicky. The mass of a Galaxy Cluster can be determined by

gravitational lensing, which describes the distortion of a background image by the bending of space time by a massive foreground object. This effect was first observed by Dennis Walsh, Bob Carswell and Ray Weymann [3]. Based on gravitational lensing, newer observations show that the total mass in galaxy clusters exceeds the mass of luminous matter approximately by an order of magnitude (see [4] and [5]), showing that Dark Matter exists as a major component in these clusters.

A popular example of strong lensing (meaning that the background image is visible multiple times as a ring-like structure) is the observation of the galaxy cluster Abell 1689, where the image distortions are clearly visible [6], see figure 1.1.

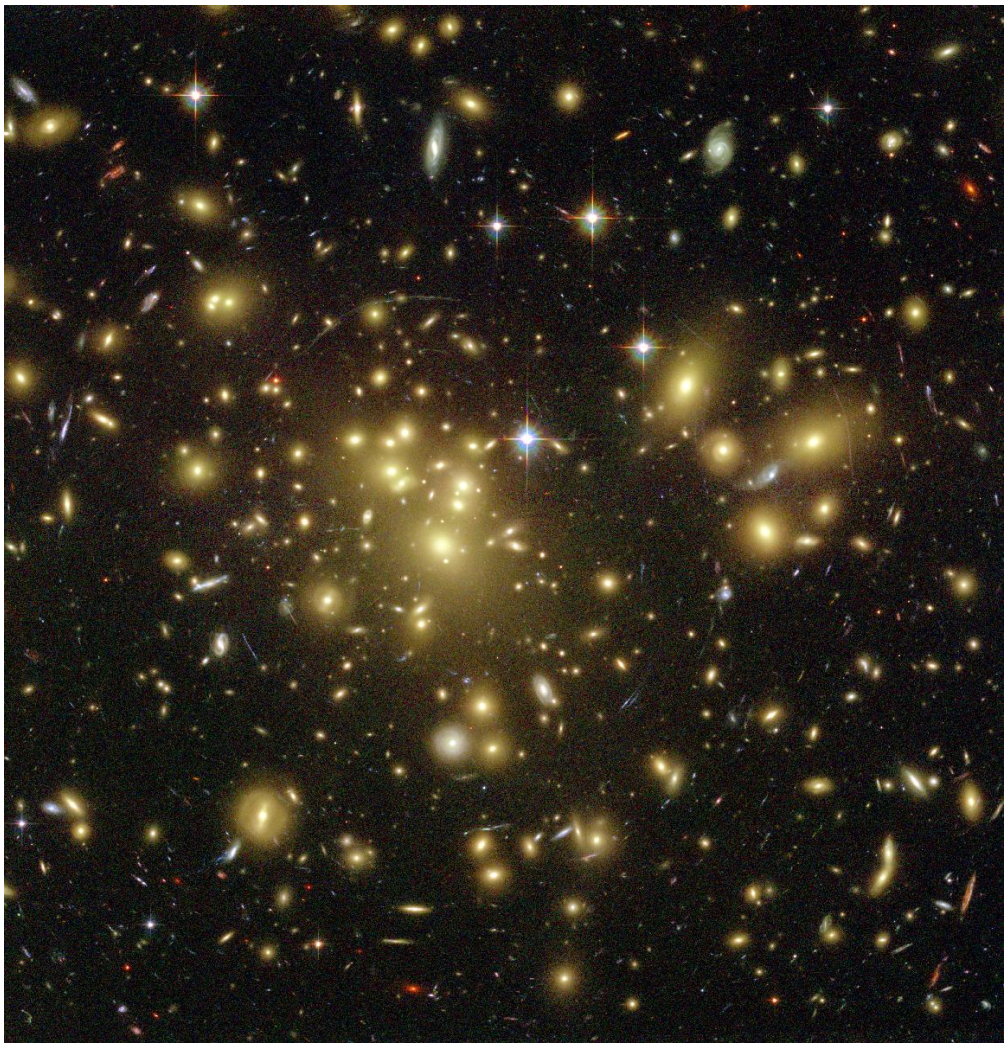

Figure 1.1: Abell 1689 as seen by the Hubble Space Telescope. The photograph is a prominent example for strong lensing, as multiple distortions are visible in the picture. Credits: NASA.

1.1.1.2 Dark Matter in Galaxies

In the 60s and 70s, the American astronomer Vera Cooper Rubin studied the rotation curves of spiral galaxies with unprecedented precision. The results, which are presented in [7] and [8], show that in spiral galaxies most stars orbit with approximately the same speed, even stars orbiting at the outer rim of the galaxy (see the left panel of figure 1.2). Since for halo stars nearly all visible

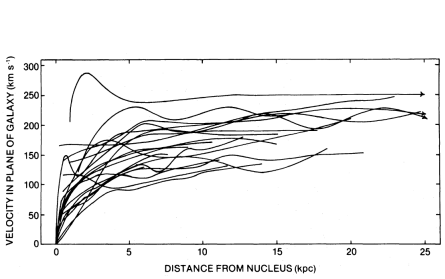

(a) measured velocity distribution in 21 spiral galaxies

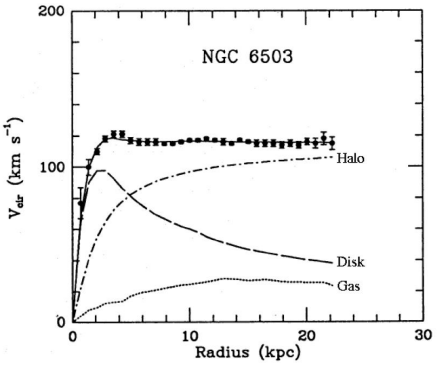

(b) observed velocity distribution in NGC 6503 and multi-component fit

Figure 1.2: Panel (a), taken from [8]: The velocity distribution for 21 spiral galaxies, as observed by V.C. Rubin. Panel (b): The observed rotation curve of the galaxy NGC 6503 (points) and a fitted model of contributions from the disk, gas and a dark matter halo (figure from [9]). See the main text for a discussion.

mass of the system is within their orbit, the expected velocity distribution from newtonian dynamics is a $1/\sqrt{r}$ dependence. The observed velocity distribution hints to the matter density in the halo of the galaxy being constant up to large radii, and thus differing substantially from the visible mass distribution. This is shown in the right panel of figure 1.2, where the observed rotation curve of the galaxy NGC 6503 is explained with a dark matter halo extending to large radii [9].

These observations do not allow to conclude on the nature of the Dark Matter other than it being non-luminous and interacting gravitationally.

1.1.1.3 Cosmic Microwave Background

In 1964, Penzias and Wilson measured an excess of antenna temperature that they estimated to be $\sim 3.5\ K$ [10]. The picked-up radiation was isotropic and free from seasonal variations. A remnant radiation originating from shortly after the big bang was predicted earlier by Gamow [11, 12], and the excess radiation measured by Penzias and Wilson was interpreted as such.

Since then, the Big Bang is the most accepted theory of the origin and ensuing evolution of the universe. The radiation originates from the early phase of the

universe, when the expansion had cooled it sufficiently to allow the recombination of charged particles at $\sim$ 300.000 years after the Big Bang. At this point radiation was no longer trapped: with free charged particles gone, the universe became transparent to radiation. This remnant radiation further cooled due to the expansion of the universe and is visible today as the Cosmic Microwave Background (CMB) at a temperature of $2.725K$ [13].

Already shortly after the discovery of the CMB, Sachs and Wolfe predicted anisotropies in the CMB due to gravitational potential fluctuations produced by density perturbations [14]. While they overestimated the effect of these perturbations, the anisotropies were detected 1992 as a $\Delta T/T \approx 10^{-5}$ effect via analysis of RELIKT-1 data and by the team behind the COBE mission [13, 15]. Figure 1.3 shows the full sky map of the anisotropies after seven years of WMAP (Wilkinson Microwave Anisotropy Probe) data [16] and after subtraction of parasitic background radiation from the galactic plane.

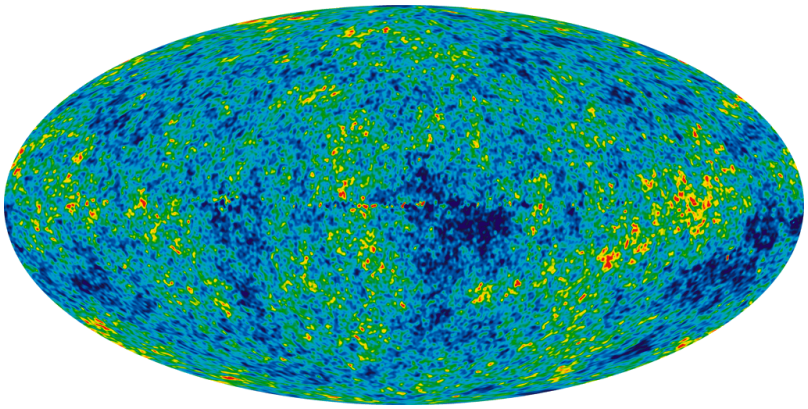

Figure 1.3: WMAP full sky map after seven years of data. The background of the milky way as well as the dipole moment originating from the earth's movement relative to the CMB has been subtracted. The image shows a temperature range of $\pm 200\mu K$ [17].

The data is interpreted in the context of the ΛCDM model[1], that allows to extract the cosmological parameters which are imprinted on the small-scale fluctuations of the CMB via analysis of the angular power spectrum of the CMB anisotropies. Among the parameters that can be extracted from the data is the matter composition of the universe, since the fluctuations are dependent on the density of the baryonic and non-baryonic matter. Current observations are all compatible with a geometrically flat universe [18], which requires that the total density of energy and matter in the universe is equal to the critical

[1] ΛCDM is short for Lambda Cold Dark Matter. The ΛCDM model is based on the Friedmann-Lemaitre-Robertson-Walker (FLRW) metric, the Friedmann equation and the cosmological equations of state to describe the universe (after the inflationary epoch). The FLRW metric is an exact solution of Einstein's field equations of general relativity, it assumes the cosmological principle, i.e. a spatially homogeneous and isotropic universe. A universe following the cosmological principle is described by the Friedmann equations.

density ρ_c of the Friedmann universe. This is indeed observed: Defining the parameter $\Omega = \frac{\rho}{\rho_c}$, where ρ is the average density, the various contributions to Ω (which are given in the table below) add to $\Omega_{total} = 1.080^{+0.093}_{-0.071}$. The individual contributions derived from the WMAP 7-year data [16] are:

Baryon Density/Critical Density	$\Omega_b = 0.0449 \pm 0.0028$
Cold Dark Matter Density/Critical Density	$\Omega_{DM} = 0.222 \pm 0.026$
Dark Energy/Critical Density	$\Omega_\Lambda = 0.734 \pm 0.029$
Total density of the Universe	$\Omega_{total} = 1.080^{+0.093}_{-0.071}$

The term 'Cold Dark Matter' describes non-baryonic matter that has a non-relativistic velocity distribution about $1y$ after the big bang [19]. These characteristics can be extracted from the small-scale fluctuations, which would be more washed out if the Dark Matter would be relativistic at this time. The nature of the Dark Energy is still not known.

1.1.1.4 Structure Formation

Large-scale structure formation describes the formation of galaxies, galaxy clusters and super clusters, as well as the voids in between. The cold Dark Matter model as well as the theory of inflation after the big bang make a clear prediction for the initial conditions to draw the current picture of the universe.

The driving force for structure formation is gravity. It can be shown that the gravitation of the visible components in the universe is not sufficient to arrive at todays universe after $\sim 13.75\ Gyr$ (which is the derived age of our universe [16]) of evolution and that in addition non-baryonic cold Dark Matter is required [20].

1.1.1.5 The Bullet Cluster

Of special interest are the results obtained from observations in the so-called 'bullet cluster'. The bullet cluster consists of two colliding clusters of galaxies, as shown in figure 1.4. In the collision process, the baryonic matter (mostly in the form of interstellar gas, which is detected in X-rays) interacting electromagnetically is slowed down. The potential wells formed by the mass of the two systems can be mapped by gravitational lensing. Their peaks show an offset of $\sim 8\sigma$ from their respective plasma clouds [21]. This can only be explained if most of the mass does not interact in the collision process, excluding most of the Dark Matter to be baryonic in nature.

The observations in the bullet cluster are of significant importance since they can't be fully explained by a modified theory of gravitation (e.g. MOND), see section 1.1.2.6 for details.

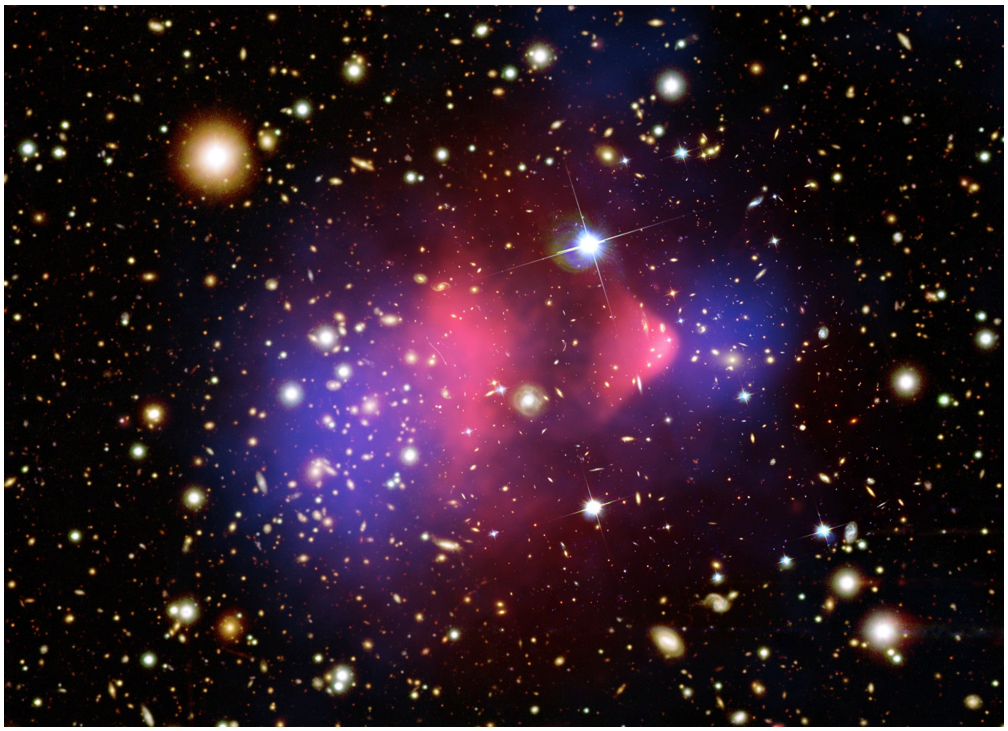

Figure 1.4: The bullet cluster, composed of several pictures (x-ray, visible light and gravitational lensing). The gas distribution shown in pink has been derived from an X-ray photo of the Chandra X-ray Observatory. The gas distribution forms the bulk of the visible mass of the colliding systems, it has been slowed down in the collision. In blue the gravitational potential is shown, as derived from lensing. The gravitational centers show a significant spatial offset to the center of the baryonic mass. (Credits for the figure: X-ray: NASA/CXC/CfA/M.Markevitch et al.; Optical: NASA/STScI; Magellan/U.Arizona/D.Clowe et al.; Lensing Map: NASA/STScI; ESO WFI; Magellan/U.Arizona/D.Clowe et al.)

1.1.2 Dark Matter Candidates

The combined astrophysical evidence for Dark Matter presented in section 1.1.1 does not put many constraints on the nature of Dark Matter apart from two facts:

- The Dark Matter content compared to the total matter content of the universe is roughly 20% and non-baryonic, while the baryonic mass is approximately 5%.

- Most of the Dark Matter must be non-relativistic, otherwise it would not clump under its own gravity and would lead to a different universe than we observe today, i.e. large scale structures would be different.

Within these constraints there are many possibilities of what Dark Matter might be. Some popular candidates are discussed in sections 1.1.2.1 to 1.1.2.6.

1.1.2.1 WIMPs

The 'Weakly Interacting Massive Particle' (WIMP) is a hypothetical particle introduced to solve the Dark Matter problem. Its properties are:

- The WIMP is stable and, in case the WIMP is its own anti-particle, the WIMP-WIMP annihilation cross section is sufficiently low to explain current observations.
- The WIMP only interacts via the weak nuclear force (or no other force stronger than that) and gravity.
- The WIMP has a large mass compared to standard particles (it is on the $\sim GeV/TeV$ scale).

The standard model of particle physics does not know a particle with these three characteristics combined, therefore the WIMP only exists in theories that extend beyond the standard model.

A popular expansion of the standard model of particle physics is the theory of supersymmetry. The MSSM (Minimal Supersymmetric Standard Model) predicts four neutralinos ($\widetilde{\chi}_1^0$, $\widetilde{\chi}_2^0$, $\widetilde{\chi}_3^0$, $\widetilde{\chi}_4^0$) that are all mixtures of the Bino ($\widetilde{B}$), Wino ($\widetilde{W}_3$) and the two Higgsinos ($\widetilde{H}_1^0$, $\widetilde{H}_2^0$), where the lightest neutralino would be stable [22]. The Bino, Wino and Higgsinos are the superpartners of the B, W_3 gauge bosons and the neutral Higgs Bosons (H_1^0 and H_1^0). The four neutralino states they mix into are Majorana mass eigenstates. As Majorana particles, each neutralino is its own anti-particle.

Without requiring fine-tuning, the characteristics of the lightest neutralino perfectly match the definition of the WIMP and would satisfy the observed properties of Dark Matter. Most of today's Dark Matter search experiments focus on the WIMP. Section 1.2 will present more on the framework of WIMP search as well as some experiments and results in detail.

1.1.2.2 Axions

The Lagrangian of quantum chromodynamics (QCD) includes the possibility of a CP violation, which is not observed by experiments; this is called the 'strong CP problem'. In 1977, Roberto Peccei and Helen Quinn proposed an additional quantum field to solve the strong CP problem [23, 24]. With the additional quantum field, a new particle is predicted, called the 'Axion', which is a candidate for particle Dark Matter that would have been produced in the early universe [25]. The mass of the axion m_α is inversely proportional to the Peccei-Quinn symmetry breaking f_α, the smaller the axion mass, the weaker axions couple to baryonic matter. Constraints on the axion mass come from astrophysical observations and are estimated by G. Raffelt et al. [26] to be smaller than 0.01 meV/c^2.

The axion can possibly be detected by its weak coupling to the electromagnetic

force, where, in the presence of a strong magnetic field, it can resonantly decay into two photons. This so-called 'Primakoff effect' [27] is utilized by the CAST collaboration [28] in an effort to experimentally prove the existence of axions. With no positive signal, the limit given by the CAST collaboration on the photon-axion coupling is $8.8 * 10^{-11} GeV^{-1}$ at 95% CL for an axion mass $m_\alpha \leq 0.02\ eV/c^2$ [29] and $2.2 * 10^{-10} GeV^{-1}$ for $m_\alpha \leq 0.4\ eV/c^2$ [30]. Also other experiments like ADMX [31] have as of now not seen a positive axion signal.

In 2009, the theorists Kathrine Mack and Paul Steinhardt stated that tuning the parameter space for axion existence being still compatible with current observations created a new fine tuning problem [32,33]. This fine tuning problem might be larger than the one that was supposed to be solved by the introduction of the Peccei-Quinn field.

1.1.2.3 Neutrinos

In the 1950s Bruno Pontecorvo [34] predicted the existence of neutrino-flavor oscillations if neutrinos had a non-zero rest mass. While there were strong hints to neutrino oscillations already in the 1960s by Davis' Homestake experiment [35], indisputable proof was delivered in 2001 by the Sudbury Neutrino Observatory (SNO), where the solar neutrino oscillations could be measured directly [36]. With neutrino oscillations observed, it became clear that neutrinos must have a rest mass and are thus a candidate for particle Dark Matter.

Today's best upper limits on the mass of neutrinos come from cosmology, where the combination of data from the WMAP three year result, the analysis of the baryon acoustic peak, the SN Ia data and the Lyman-α forest yield an upper limit for the sum of all neutrino masses of $\sum_\nu m_\nu \leq 0.4\ eV/c^2$ [37].

The most stringent constraint on the neutrino relic density comes from analysis of the CMB anisotropies combined with large-scale structure data, suggesting $\Omega_\nu \leq 0.0067$ (95% confidence limit) [22], meaning that neutrinos can only make up a small fraction of Dark Matter ($\Omega_{DM} = 0.214 \pm 0.072$, see 1.1.1.3).

Furthermore, neutrinos being nearly collisionless relativistic particles, erase density fluctuations in the early universe below a scale of 40 Mpc [38]. This would imply a top-down formation history in the universe, where big structures form first. The opposite case being observed is a further argument against the neutrino being a viable Dark Matter candidate (see [22] for further discussion).

1.1.2.4 Sterile Neutrinos

As shown by Chien-Shing Wu, the weak force violates parity conservation [39]. The weak force exclusively acts on left-handed particles and right-handed anti-particles. A right handed neutrino (or a left handed anti-neutrino) would be similar to a standard model neutrino but without the standard model weak

interaction (except for mixing), meaning it would only interact via the gravitational force.

This hypothetical particle is called the 'Sterile Neutrino', and it was proposed as a Dark Matter candidate for the first time in 1993 by Dodelson and Widrow [40]. Based on current observational data, the sterile neutrino can in most cases be excluded as cold Dark Matter, but remains a viable possibility for hot Dark Matter (see [22] and references therein).

1.1.2.5 Other Candidates

There is no shortage of Dark Matter candidates. In the selection of particles presented above, the neutrino is the only particle of which the existence is already proven, while the other candidates are popular and well motivated but remain hypothetical particles as of now.

The supersymmetric extension of the standard model allows further particles that could make up Dark Matter, such as the Sneutrinos (the supersymmetric partners of the standard model neutrino), the Gravitino (superpartner of the graviton) or the axino (the superpartner of the axion). Other theories spawn further Dark Matter candidates, like Kaluza-Klein particles which appear in models of extra dimensions or superheavy particles, sometimes referred to as *Wimpzillas*. Some of these are already excluded by experiments while some still remain viable. For an extensive discussion of candidates, see [22].

1.1.2.6 Alternative Theories

As of now, there is no direct-observational proof that Dark Matter exists, but Dark Matter is the most popular explanation for the astrophysical and cosmological observations discussed in section 1.1.1. To infer the existence of additional mass from these observations, a theory of gravitation is required. Developed by Einstein, general relativity is the only theory of gravitation that passed every test, and its appliance on the phenomena discussed above led to the conviction of the existence of Dark Matter.

Alternative theories used to explain the observed inconsistencies between visible and required matter in the universe rely on a different theory of gravitation, where gravity behaves differently on cosmological scales than predicted by general relativity or newtonian dynamics, while on small scales they behave in the same way as the traditional theories.

The first theory of modified newtonian dynamics as a possible alternative to the hidden mass hypothesis is *MOND* [41]. It enhanced the gravitational field on large scales to correctly predict rotational curves of elliptic galaxies without the need of non-luminous matter, but it fell short in describing the lensing effect, the bullet cluster (see section 1.1.1.5) and multi-body problems. Also, momentum conservation is violated, which is a big theoretical problem.

These shortcomings led to further alternative gravitational theories, of which the *Tensor-vector-scalar gravity* [42] developed by Bekenstein gained most popularity. It was partially disproved by the latest results of the *Sloan Digital Sky Survey* [43]. Observational evidence not yet allows to completely rule out all proposed alternative scenarios aiming to disprove the existence of Dark Matter.

1.2 Detection of WIMPs

As described in section 1.1.1, a large fraction of the mass of a galaxy is made up of Dark Matter, most of which must be in the form of non-baryonic particles. In section 1.1.2, different Dark Matter candidates were discussed. Most Dark Matter search experiments, including the CRESST experiment (which motivated the present work), focus on the detection of WIMPs. It is also one of the best theoretically motivated candidates, since the most promising extensions of the Standard Model (i.e. supersymmetry) provide the lightest neutralino as a WIMP and also have the virtue of producing the correct relic abundance in the early universe without the need for fine tuning [44]. For these reasons, the remainder of this chapter will focus on the discussion of WIMP detection.

WIMP search experiments can be divided into direct and indirect search experiments. They exploit different properties of WIMPs to identify a positive signal. The indirect search experiments (section 1.2.1) scan the galactic plane for an excess of gamma radiation, originating from the WIMP-WIMP annihilation. Most direct detection experiments search for nuclear recoils as a signature for a WIMP interaction, while other experiments exploit an expected annual modulation in WIMP-detector interaction rates. The general framework (see section 1.2.2) for direct Dark Matter search experiments as well as important experiments and their results (see section 1.2.3) will be discussed below.

1.2.1 Indirect Dark Matter Search

For a neutral spin 1/2 particle it is possible to be its own anti-particle. If this would apply to the WIMP, it would be a Majorana particle (see [45] for a review on that topic, also note section 1.1.2.1 for details). Indirect-detection experiments typically look at places where the annihilation signal would be prominent due to an accumulation of Dark Matter in that region, in particular the galactic center, halo clumps, the sun or the earth, since the annihilation rate would be proportional to the square of the Dark Matter density, $\Gamma \propto \sigma_{DM}^2$.

If the WIMP is the neutralino χ, the (for the detection) relevant final states of the annihilation process are neutrinos[2], photons[3] or e^+/e^--pairs[4]. For further details and branching ratios of neutralino annihilation see [46].

[2]Produced by direct production, decay of heavy quarks, hadronization followed by decay of charged pions.

[3]Produced by direct production, hadronization and decay of neutral pions.

[4]Produced by direct production or hadronization followed by decay of charged pions.

Ground- and satellite based γ-ray telescopes are suited to search for WIMP annihilation radiation. The experiments H.E.S.S and MAGIC search for an excess of γ-rays coming from the galactic plane, but as of now no positive detection can be reported [22, 47]. The *Compton Gamma Ray Observatory*, equipped with the gamma-ray telescope EGRET, reported in the late 90s the observation of a point-like γ-ray source at the galactic center [48]. A possible explanation is the annihilation radiation from supersymmetric Dark Matter [49]. The EGRET mission also observed the extragalactic gamma spectrum, and a large fraction of the gammas at energies between $1GeV$ and $20GeV$ might result from annihilating WIMPs [50]. However, the extragalactic spectrum could also be explained by the decay of the Gravitino [51].

Generally, observations of the galactic halo in search of an excess of gamma rays are not yet conclusive, as the background is not fully understood and the statistical basis is not yet sufficient (see [22] and also [52]).

1.2.2 Fundamentals of Direct WIMP Search Experiments

Models of our own galaxy that incorporate a Dark Matter halo with a local (at the earth) density of $\rho_{DM}(local) = 0.385 \pm 0.027\ GeVcm^{-3}c^{-2}$ match observational data very well, see [53] for details[5]. Direct search experiments use earth-based detectors to search for WIMP-nucleon interactions. Due to the velocity of the earth around the galactic center, a local detector is subjected to the WIMP wind and is likely to detect these particles passing the earth. Section 1.2.2.1 discusses the fundamentals of the WIMP-nucleon interaction and section 1.2.2.2 discusses the expected annual rate modulation caused by the periodic orbit of the earth around the sun.

1.2.2.1 WIMP-Nucleon Interaction

If WIMPs scatter elastically off nuclei, one can make predictions for expected event rates on different target materials.

The typical form of a differential energy recoil spectrum with the assumption of the scattering being isotropic, i.e. uniform in $cos\theta$, is

$$\frac{dR}{dE_r} = \frac{R_0}{E_0 r} e^{-E_r/E_0 r} \tag{1.1}$$

where R is the event rate per unit mass, E_r is the observed recoil energy in the detector, E_0 the most probable incident kinetic energy of the WIMP and r a kinematic factor given as

$$r = \frac{4M_{DM}M_T}{(M_{DM} + M_T)^2}$$

[5]Most publications still use a value of $\rho_{DM}(local) = 0.3\ GeVcm^{-3}c^{-2}$. To maintain compatibility with other publications, the following calculations will also use this value.

with M_{DM} the mass of the WIMP particle and M_T the mass of the target nucleus. R_0 in equation 1.1 is the event rate per unit mass and is dependent on the WIMP properties. With the additional assumption that the escape velocity for WIMP particles in the galaxy is infinite and the earth velocity relative to the rotating milky way is zero, it can be expressed as [54],

$$R_0 = \frac{2}{\pi^{1/2}} \frac{N_0}{A} \frac{\rho_{DM}}{M_{DM}} \sigma_0 v_0, \tag{1.2}$$

with N_0 being the Avogadro number, A the mass of the target nucleus. ρ_{DM} is the local Dark Matter density, for the following calculations assumed to be 0.3 GeV/cm^3c^2 [55, 56]. v_0 is the speed of the detector relative to the Dark Matter halo or the rotation speed of the milky way at the location of the earth: 230 km/s [53, 54]. σ_0 is the WIMP-nucleus cross section. If the wavelength of the interaction h/q, with q being the momentum transfer $q = \sqrt{2M_T E_R}$, is no longer large compared to the nuclear radius, the effective cross section decreases with increasing q. This behavior can be described by an additional 'form factor', which is a function of the dimensionless quantity $qR_N/\hbar$, with R_N being the nuclear radius. The distribution proposed by Helm [57] is of the form

$$F^2(qR_N/\hbar) = (3\frac{j_1(qR_N/\hbar)}{qR_N/\hbar} e^{-(qs)^2/2})^2 \tag{1.3}$$

with s being the shell thickness of the target nucleus ($\sim$ 1 fm) and j_1 the spherical bessel function of first order.

The WIMP-nucleus cross section σ_0 in equation 1.2 can be derived from a WIMP-nucleon cross section [54] in the form

$$\sigma_0 \propto \mu^2 I_c F^2(qR_N/\hbar)\sigma_{WN} \tag{1.4}$$

with σ_{WN} being the WIMP-nucleon cross section, F^2 the form factor discussed previously, μ the reduced mass and I_c an enhancement factor taking into account that the WIMP-nucleus interaction is coherent for a sufficiently low energy transfer. In the simplest case, $I_c \equiv A^2$.

Applying the equations discussed above on different target materials commonly used in direct Dark Matter search experiments gives the energy-dependent count rate shown in figure 1.5. For the calculation, a WIMP-nucleon cross section of $\sigma_{WN} = 10^{-44} cm^2$ (being compatible with the null-result of experiments) and a WIMP mass of 60 GeV/c^2 was assumed [58]. The deep drop predicted for W at a recoil energy of $\sim$ 50 keV is due to the Helm form factor.

If comparing different target materials and experiments, the relative event rates and the spectral shape in each material matching the predictions are strong evidence for a positive Dark Matter signal.

1.2.2.2 Annual Modulation of WIMP Recoil Rate

The general assumption is that the Dark-Matter halo in our galaxy is at rest while the baryonic mass is rotating. The local velocity of the sun is $\sim$ 230 km/s

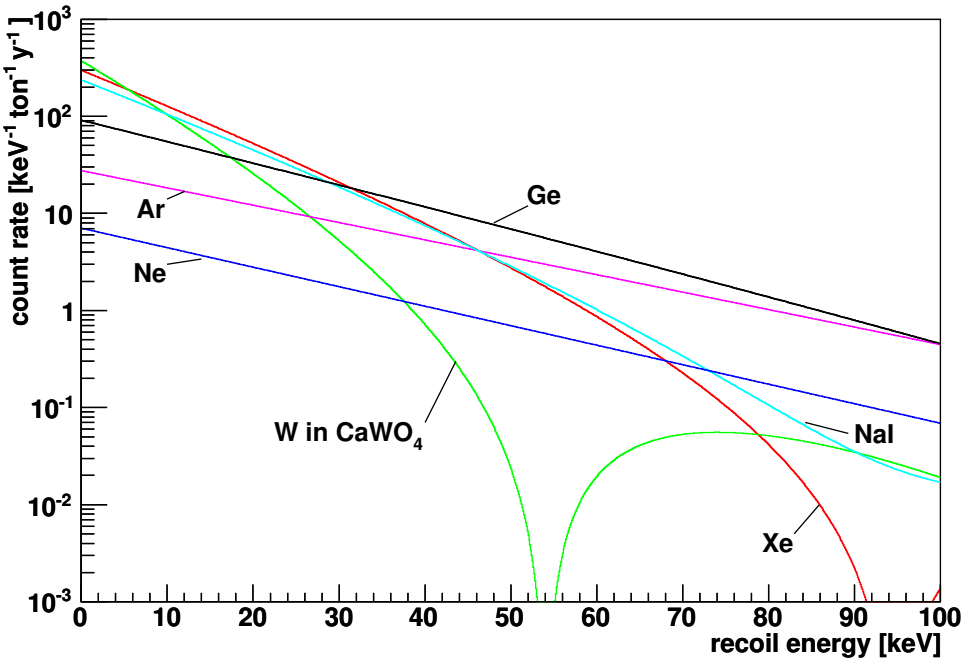

Figure 1.5: Expected event rates from WIMP interactions for different target materials under the assumption of a WIMP-mass of $M_{WIMP} = 60GeV$ and a WIMP-nucleon cross section of $\sigma_{WN} = 10^{-44}cm^2$. Figure from [58].

[53,54]. With the earth rotating around the sun at a velocity of $\sim 30\ km/s$, the event rates of WIMP-nucleus scattering would be modulated with a periodicity of $1y$ [59], see figure 1.6. While this annual modulation should be visible in any earth-based direct-detection experiment given sufficient statistics of the positive Dark-Matter signal, it can be used as the sole indication of WIMP detection, especially if no other means of background discrimination are available.

1.2.3 Direct Dark Matter Search

The expected low event rates from WIMPs scattering off a target material pose a significant challenge for direct-detection experiments. The suppression of background is of high importance, for this reason direct-detection experiments are typically located in underground sites to be shielded from cosmic rays. Experiments are hosted at the Soudan Mine, the SNOLAB at Sudbury, the Gran Sasso National Laboratory, the Boulby Underground Laboratory and other locations typically several hundreds of meters below ground - corresponding to an equivalent depth in water of few thousand meters.

Different approaches are used for direct-detection experiments. The techniques and some experiments are briefly discussed in the following sections.

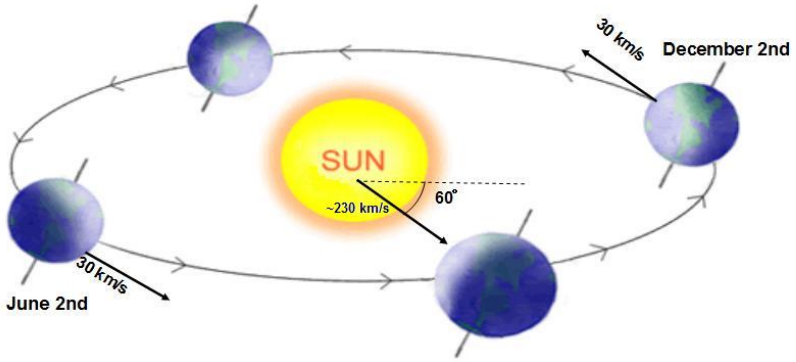

Figure 1.6: The movement of the sun around the galactic center ($v_{sol} \approx 230km\,s^{-1}$) combined with the movement of the earth ($v_{earth} \approx 30km\,s^{-1}$ around the sun) increases event rates of WIMPs in June compared to December. The velocity of the earth projected onto the velocity of the sun is maximal on June 2nd, giving the phase of the modulation. Figure from [60].

1.2.3.1 DAMA

The DAMA/LIBRA (DArk MAtter/Large sodium Iodide Bulk for RAre processes) experiment [61] relies on the annual modulation of the event rates discussed in section 1.2.2.2 to identify a positive Dark Matter signal. In its current state, it features a target mass of $250kg$ of NaI crystals, the scintillation light of each of the 25 detectors is read out by two photomultiplier tubes. The latest result of the experiment is shown in figure 1.7. DAMA/LIBRA report the de-

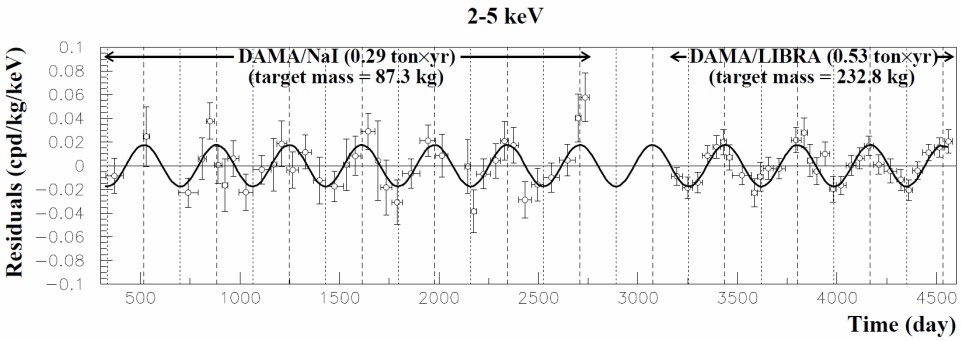

Figure 1.7: Latest results from the DAMA/LIBRA experiment. Over a timespan of $\sim$ 11 years, the residuals of the event rate compared to the mean are shown for the window of $2-5keV$ registered energy in the PMTs. The detection of the observed modulation has a significance of 8.9σ. The period of $1y$ and the phase giving a maximum in the event rate on June 2^{nd} match the expected phase and period of a positive Dark Matter signal [62].

tection of an annual modulation in the event rate with a significance of 8.9σ [62]. If the origin of this modulation is attributed to nuclear recoils from WIMPs, it contradicts the results of several other experiments (see below for details).

Different scenarios have been proposed to reconcile the DAMA/LIBRA results with the null-result from other experiments. The possibility of inelastic Dark Matter [63, 64], where the Dark Matter particle is left in an excited state after the scattering in the detector material, is no longer in agreement with new experimental data, see [65] and section 2.2.3.4 for details.

An effort has been made to reach compatibility with most other experiments by taking the *Channeling Effect* [66] into account. It leads to an increased light output for ions moving along a channel (i.e. a low-index crystal axis) in the NaI crystal if the ion energy is sufficiently low (few keV), by transferring more energy to the electronic system than to nuclei (ions).

1.2.3.2 CoGeNT

CoGeNT (*Coherent Germanium Neutrino Technology*) is a small experiment operated in the Soudan mine in a depth of 700 meters. In its current state, it features a 440g germanium crystal with a P-type point contact. The collaboration reports an excess of events below 1.5 keV which is attributed to WIMP recoils [67].

This result can be reconciled with the DAMA result [68], but presently there is doubt if all possible backgrounds have been fully taken into consideration [69].

1.2.3.3 Liquid Noble Gas Detectors

Another approach to Dark Matter detection is the use of liquid noble gases like argon, xenon, and neon as detector material. Particles interacting in the liquid phase produce scintillation light as well as ionization, which can be measured independently and allows to discriminate between different types of interaction and thus to reject background events.

Currently, the best limit for direct Dark Matter search experiments is coming from the XENON100 experiment. It features a target mass of 62 kg of liquid xenon with a fiducial volume containing 40 kg. With three events observed in the signal region and an expected background of 1.8 ± 0.6 events, they exclude spin-independent WIMP-nucleon elastic scattering above a cross section of $7.0 \times 10^{-45} cm^2$ for a WIMP mass of 50 GeV/c^2 at 90% confidence level [70, 71]. For light WIMPs of a mass of less than $20 GeV$ their result is not in agreement with the detection reported by DAMA and CoGeNT, but the claimed sensitivity of XENON100 in this region has been disputed [72].

Other experiments based on liquid noble gases include WARP[6] [73] and ArDM[7] [74], both of which use argon as detector material, and the CLEAN[8] experiment [75], which uses liquid neon.

[6] Wimp ARgon Program
[7] Argon Dark Matter
[8] Cryogenic Low Energy Astrophysics with Noble gases

1.2.3.4 Low-Temperature Detectors

Low-temperature detectors typically employ a target material that emits scintillation light upon energy deposition by an incident particle or that allows the collection of ionization charge. Additionally, since these detectors run at a few mK, the bulk of the energy of the interaction can be measured by detecting the phonons (heat) being produced by a particle scattering off the detector material, since nearly all energy dissipates in this channel [76]. By measuring both quantities, heat and either scintillation light or ionization yield, a discrimination between the type of interaction is possible, allowing to discriminate between background and a possible WIMP signal.

The CDMS II (Cryogenic Dark Matter Search) experiment [77] utilizes the heat/ionization technique, and is the low-temperature experiment currently giving the best exclusion limit for WIMPs. Using germanium detectors, the produced charge and phonons of a particle interaction can be measured independently. During the 2007/2008 measurement campaign, CDMS II took data using 30 low-temperature particle detectors at the Soudan-Underground Laboratory. With a raw exposure of 612 kg days, they reported that after the application of all cuts two events remained in their signal region. They estimate the probability of observing two or more background events to be 23%. All combined CDMS results yield an upper limit for the spin independent WIMP-nucleon cross section of $3.8 * 10^{-44} cm^2$ for a WIMP mass of 70 GeV/c^2 [78, 79].

Examples of other low-temperature experiments are EDELWEISS (Expérience pour DEtecter Les Wimps En Site Souterrain) [80], which also employs germanium detectors of a total mass of 4 kg, and the CRESST-II experiment using $CaWO_4$-crystals, which will be presented in more detail in the next chapter.

Chapter 2

The CRESST II Experiment

'Cryogenic Rare Event Search with Superconducting Thermometers' (CRESST) is an experiment for the direct detection of Dark Matter. The current phase of the experiment, which is called CRESST II, is located in Hall A of the Gran Sasso Underground Laboratory (*Laboratori Nazionali del Gran Sasso*, LNGS).

A CRESST detector module, consisting of the target crystal, a phonon detector, and a scintillation light detector, allows the simultaneous measurement of scintillation light and phonons (heat) produced by the same event in the target crystal. $CaWO_4$ crystals are mainly employed as target material but the modular design [81, 82] allows also the use of other materials, e.g. $ZnWO_4$, which is also incorporated in the current setup.

Section 2.1 gives an overview of the experiment and section 2.2 presents a brief summary of current results. The relevance of the quenching factors, which motivated the present work, is discussed in section 2.3.

2.1 Experimental Conception of the CRESST Experiment

Up to 33 detector modules (equaling 66 channels) at a working temperature of $5-10\ mK$ can currently be housed in the cryostat of the CRESST experiment, corresponding to a total mass of $\sim 10\ kg$. An energy deposition in a CRESST detector is read out by employing transition edge sensors and SQUIDs, as is discussed in section 2.1.1. The detector design is detailed in section 2.1.2, the cryostat and the shielding are briefly presented in section 2.1.3. Procedures for calibration and temperature stabilization are described in section 2.1.4.

2.1.1 Transition Edge Sensors and Readout

Signal detection in a CRESST-detector module is accomplished via a so-called transition edge sensor (TES). It can detect very small energy depositions with

very high precision. It consists of a thin metal layer (tungsten in the case of CRESST) of $\sim 100 - 500nm$ thickness. The employed metal layer must have a transition to the superconducting phase, typically employed besides tungsten is for example iridium (often in combination with gold to lower the transition temperature). The metal layer is stabilized in its transition temperature from the normal to the superconducting phase. Thus a small change in temperature leads to a large change in resistance, as shown in figure 2.1. The temperature

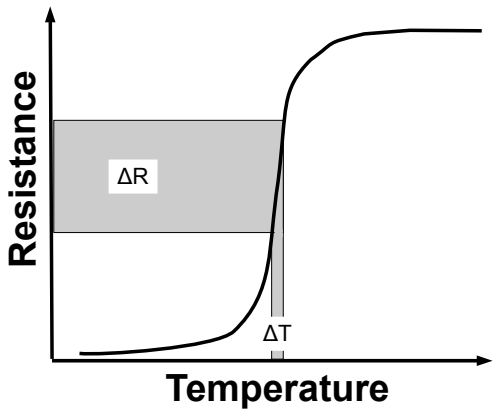

Figure 2.1: Working principle of a TES: A thin metal layer is stabilized in its transition from the normal to the superconducting phase. A small change in temperature ΔT leads to a large change in resistance ΔR.

change ΔT depends on the energy deposition E and the heat capacity C of the sensor: $\Delta T = \frac{E}{C}$. To achieve maximum sensitivity, a low heat capacity C is desirable, hence transition temperatures as low as possible are chosen. In the CRESST experiment, a total detector mass of several kg is employed; for a mass of this order temperatures of few mK can be achieved by employing commercially available ^{3}He/^{4}He dilution refrigerators. Tungsten-thin films typically have their phase transition in this temperature range. They can be evaporated directly onto the absorber material (either a $CaWO_4$ crystal or a sapphire substrate) or on an additional substrate which is then glued on the absorbing material, allowing a so-called composite detector design [83].

The TESs are read out via SQUIDs (Superconducting Quantum Interference Devices). A SQUID is a very sensitive magnetometer, the readout scheme is depicted in figure 2.2. It consists of a superconducting loop containing two Josephson Junctions. A constant current flows through the TES, a parallel reference resistor (2R), and an input coil producing a magnetic field. The magnetic field is dependent on the branching of the current through the parallel resistors. A magnetic flux Φ generated by the input coil through the SQUID leads to a compensating current over the Josephson Junctions. When the critical current of the Junctions is exceeded, a voltage V_{SQUID} appears over them. The voltage is periodic with the flux Φ, which is why the external flux is compensated by an additional feedback coil to determine the magnetic flux produced by the input

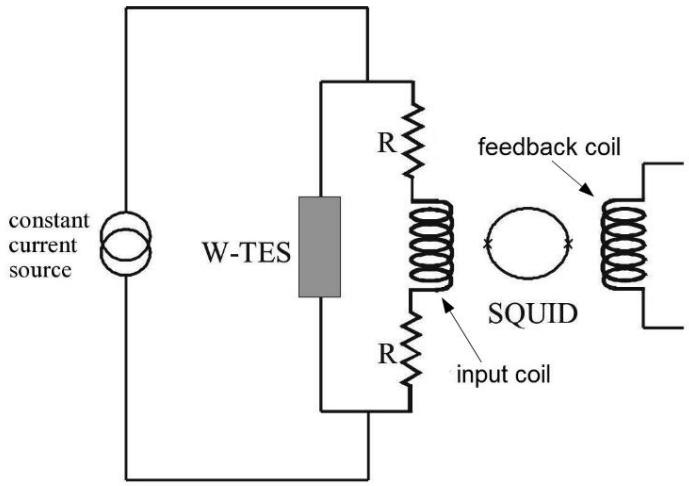

Figure 2.2: TES readout via a SQUID. The detector bias produced by a constant current source flows over the resistance of the TES and a parallel resistor of $2R$ and the input coil. A change in resistance of the W-TES leads to a different current flow in the input coil and to a change of magnetic flux. The magnetic flux is picked up by the SQUID, which consists of two Josephson Junctions. The flux produced by the input coil is compensated by the feedback coil, to keep the absolute flux through the SQUID constant. See the main text for further details.

coil unambiguously. This compensating current running through the feedback coil is the actual recorded signal. Thus for external flux changes sufficiently slow the effective flux through the SQUID remains constant. For CRESST, this is realized with a 66 channel SQUID readout system [84].

While a TES is a very sensitive sensor, the response upon an energy deposition depends on the position in the transition curve, since the slope is not constant and homogeneous over the whole transition. To obtain an unambiguous signal, special care has to be taken to stabilize the detector at a specific temperature (see section 2.1.4).

2.1.2 Detector Design

A scintillating crystal and a light detector, both encapsulated in a reflective housing, form a CRESST detector module. A schematic view is shown in figure 2.3. The scintillating crystal (cylindrical in shape, $\varnothing = 40mm$, $h = 40mm$, weight is $\sim 300\ g$, in most cases made of $CaWO_4$) is equipped with a tungsten TES (see section 2.1.1) to detect the energy deposition in the crystal. The simultaneously produced scintillation light ($\sim 440nm$ [85]) is detected by the light detector, which is a sapphire substrate with a thin silicon layer to absorb the light, also equipped with a tungsten TES.

Upon a particle interaction in the target crystal, part or all of the energy of the incident particle is transferred onto an electron or a nucleus, depending on

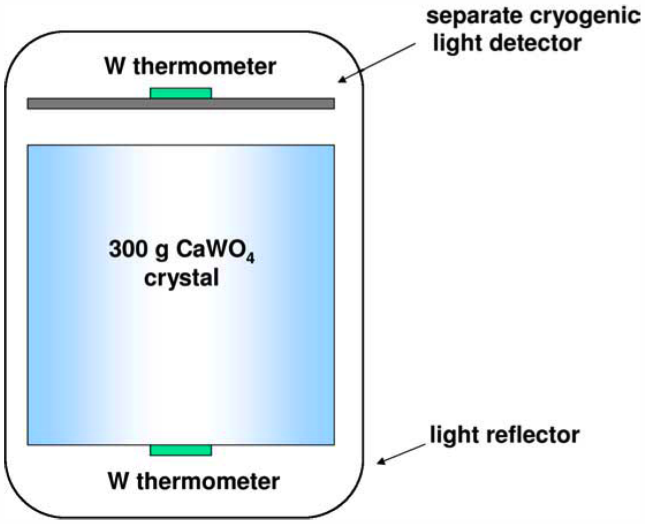

Figure 2.3: Schematic view of a CRESST detector module. The bulk detector material is a scintillating $CaWO_4$ crystal equipped with a W-TES (in the figure referred to as a 'W thermometer') to detect phonons caused by an event in the crystal. A separate light detector detects the simultaneously emitted scintillation light, the energy deposition is also read out with a TES. To maximize the light collection, the phonon and light detector are encapsulated within a reflective and scintillating foil.

the nature of the incident particle. Carrying kinetic energy, the electron or the nucleus will then move through the crystal lattice, transferring most of its energy into phonons [76]. The phonons partly thermalise in the TES leading to a measurable change in resistance.

Only a small fraction of the energy is transformed into scintillation light [86], which is partly absorbed by the light detector. To maximize the light collection, the target crystal and the light detector are encapsulated by a reflective foil, which is also scintillating. The scintillation light produced by the foil is of importance for the rejection of background events, see section 2.2.2.3 for details on this topic. A photograph of a disassembled detector module is shown in figure 2.4.

2.1.3 Cryostat and Shielding

To reduce the background caused by secondaries of cosmic rays, the CRESST II experiment is situated in hall A of the Gran Sasso Underground Laboratory, (Laboratori Nazionali del Gran Sasso, LNGS, Italy), where the shielding of the rock amounts to $\sim$ 3500 meter water equivalent. Figure 2.5a shows the cryostat, the shielding, and the position of the detectors in the experiment. To moderate neutrons produced in the rock by natural radioactivity or muons, approximately 10 t of polyethylene are used. A lead shielding ($\sim$ 24t) and an innermost

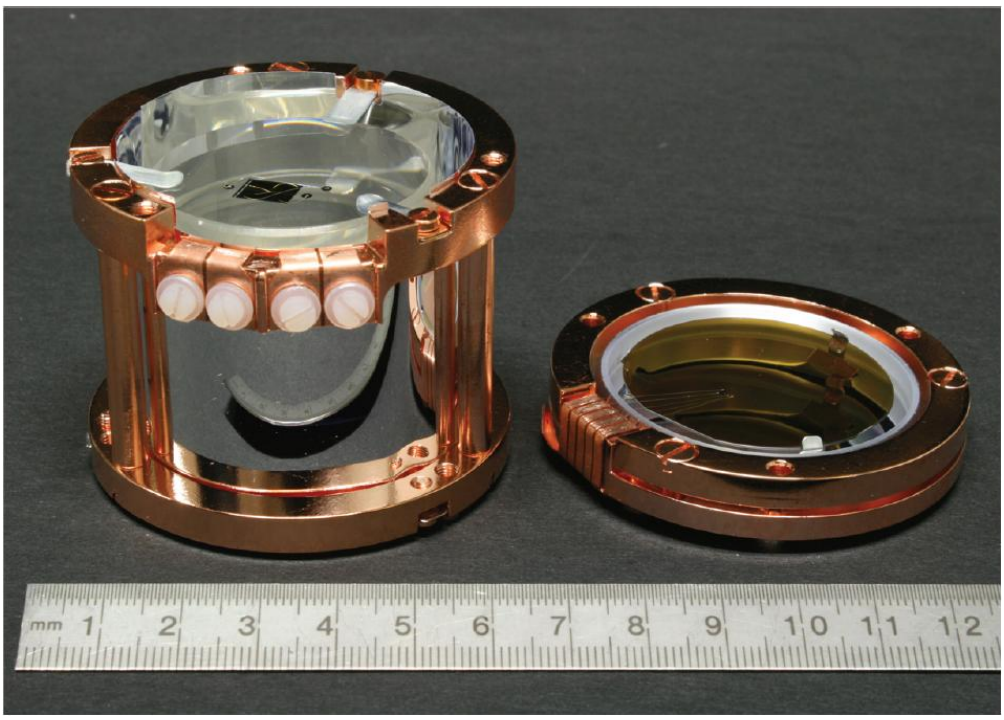

Figure 2.4: A disassembled detector module: On the left is the $CaWO_4$ target crystal held by clamps and surrounded by the reflective and scintillating foil. The tungsten TES is visible on the crystal. On the right is the light detector, made of a silicon layer evaporated on a sapphire substrate. The TES and the bonding wires can be seen.

shielding of copper ($\sim 10t$) are used to reduce the gamma background. To reject neutron events produced inside the shielding by muons, the setup is surrounded by plastic scintillator panels read out by photomultiplier tubes (PMTs), acting as an active muon veto.

The detector modules are mounted in a support structure called the carousel, shown in figure 2.5b. Since low background rates are crucial, the carousel is not mounted in the direct vicinity of the cryostat which contains some components not sufficiently radiopure, but is in a separate coldbox connected via a coldfinger of 1.5 m length to the mixing chamber of the cryostat. To be shielded from this radioactivity, an internal lead shielding is mounted between the mixing chamber and the coldbox.

The inner shielding of pure copper, lead and polyethylene surrounding the cold box with the detectors is encapsulated in an air-tight box (called the radon box). It is constantly flushed with clean nitrogen (evaporated from liquid nitrogen) to prevent radioactive radon produced in the surrounding rocks (that leads to a ^{210}Pb contamination in the surroundings of the detectors) from reaching the inner part of the shielding.

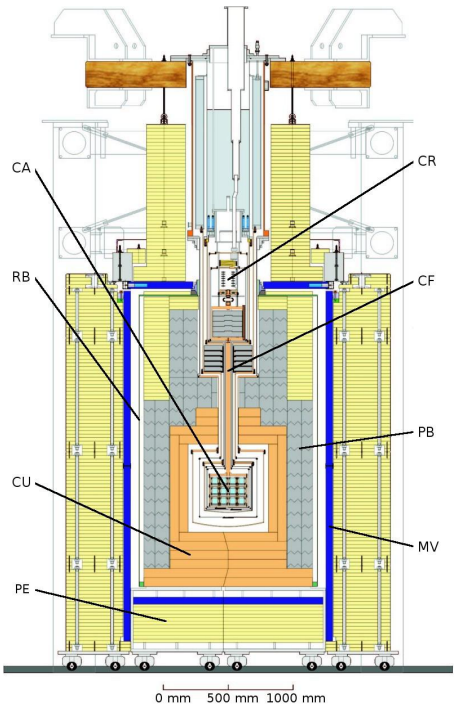

(a) The cryostat, shielding and the position of the detectors.

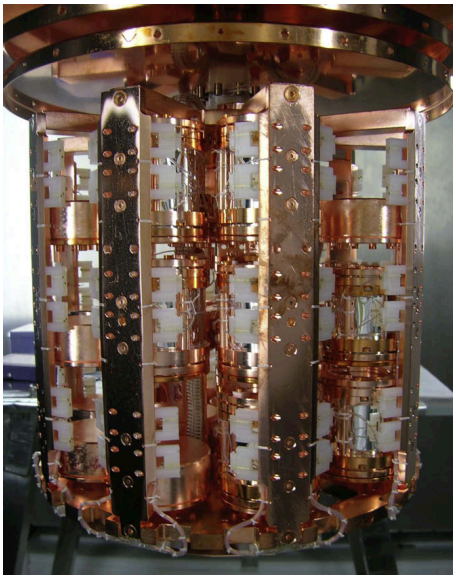

(b) The carousel serves as the support structure for currently up to 33 CRESST detector modules.

Figure 2.5: Panel (a): The CRESST setup at the Gran Sasso Underground Laboratory. Depicted in the figure are the polyethylene shielding (PE) to moderate neutrons, the muon veto (MV) consisting of plastic scintillator panels (read out by PMTs) surrounding the cryostat, the radon box (RB), the lead (PB) and copper (CU) shielding, the cryostat (CR) connected via a coldfinger (CF) to the carousel (CA) holding the detectors. A photograph of the copper carousel is shown in (b).

2.1.4 Calibration and Stabilization

The detector response of a CRESST detector module to an energy deposition is dependent on the working temperature of the TES, as has been discussed in section 2.1.1. Comparability at all times and between all detectors and ensuring validity of the calibration over the whole runtime ($\sim$ 1 year) are achieved in the following way:
Each TES is equipped with a resistive heater (a small gold structure evaporated onto the TES), with which heater pulses can be injected directly into the TES [81]. The absolute energy deposition of such a pulse is not known a priori. To relate the pulse height to an absolute energy deposition, a ^{57}Co source is used for calibration purposes. The pulse height of the injected heater pulse is tuned until it matches the pulse height of the 122 keV line of the ^{57}Co source.

The output power of the module generating the heater pulses is linearized, thus all other energies can be calibrated with one known calibration point by

injecting a set of heater pulses with different amplitudes. The heater pulses are injected continuously over the whole runtime of the experiment at a rate of $\sim 0.3Hz$ to monitor the stability of each detector and (by correcting the temperature of each TES based on the observed response to the injected heater pulses) stabilize it at a defined point in the transition curve.

This procedure is carried out for the phonon detector and the light detector. The produced scintillation light in the $CaWO_4$ crystal by the 122 keV gamma is used as a reference point for the light detector. The energy scales obtained for both detectors are referred to as *'keV electron equivalent'* or keV_{ee}, since they relate the observed pulse heights to a pulse height produced by a gamma of known energy leading to an electron recoil in the target crystal. At the end of the measurement campaign, the calibration can be cross-checked with the spectral features produced by the background during the Dark-Matter run [87].

2.2 CRESST Data Analysis and Results

The CRESST experiment searches for WIMP recoils in its detector material $CaWO_4$. As discussed in section 1.2.2.1, the expected signature of such an event is a nuclear recoil. With the help of the quenching factor (defined in section 2.2.1) a possible signal can be discriminated against background events (discussed in section 2.2.2). The latest CRESST results are presented in section 2.2.3.

2.2.1 Quenching Factor and Light Yield

Quenching factor and light yield are defined as follows:

Quenching Factor
The light output of the scintillating crystal is dependent on the amount of deposited energy and the type of interaction. For nuclear recoils, induced for example by neutrons or WIMPs, the light output is lower in comparison to an electron recoil (typically induced by gammas and betas) of the same energy. This is quantitatively expressed by the quenching factor, QF. It is defined energy dependent for each particle as

$$QF := \frac{\overline{E_R}}{\overline{E_{ee}}} \tag{2.1}$$

$\overline{E_R}$ is the mean detected energy deposition (averaged over many events where the same total energy is deposited) in keV_{ee} in the phonon channel and $\overline{E_{ee}}$ the mean visible amount of scintillation light in the light channel, also in keV_{ee}, where the subscript 'ee' stands for 'electron equivalent'.

Since more than 95% of the energy of an interaction go into the production of phonons, the detected energy in the phonon channel can be considered in good

approximation to be equal to the total energy deposition in the crystal. This effectively means, that phonon quenching can be neglected [88,89]. Since in the present work every energy deposition of a particle interaction is compared to the electron equivalent scale (since no other means of calibration were employed), keV is used throughout this work for the keV_{ee} scale for simplicity. Only for special emphasis the term electron equivalent will be used.

For the calibration method described in section 2.1.4 follows immediately that the quenching factor is 1 for electron recoils of 122 keV. As will be seen below, for almost all cases the quenching factor can be considered 1 for all electron recoils at all energies. The quenching factor for other energies and particles is discussed in section 2.2.2.1.

Light Yield
The light yield LY for a single event is defined as the energy in keV_{ee} detected in the light channel divided by the energy in keV in the phonon channel,

$$LY := \frac{E_{ee}}{E_R}. \tag{2.2}$$

For a hypothetical detector with perfect resolution and no line broadening by statistical effects, the LY of an event is equal to the reciprocal of the quenching factor for this interaction, $1/QF$.

2.2.2 Background Discrimination and Signal Identification

Expected event rates in direct Dark Matter search experiments are of the order of few tens of events per kg detector mass and year observational time, or less. Background suppression and discrimination is very important to identify these few events. The passive shielding and the active muon veto of the experiment have been discussed in section 2.1.3. This section focuses on CRESST's capability to distinguish the type of interaction (section 2.2.2.1) and how this feature allows to discriminate a possible signal (section 2.2.2.2) from the background (section 2.2.2.3).

2.2.2.1 Identification of Nuclear Recoils

Two measurements with a CRESST detector are shown in figure 2.6. The scatter plots show a measurement with a ^{57}Co gamma and a ^{90}Sr beta source on the left and with an additional AmBe-neutron source on the right [90]. With the neutron source present, an additional recoil band becomes visible. It is attributed to nuclear recoils. With the whole energy deposition basically visible in the phonon channel, the effect of a heavily reduced light output in comparison to electron recoils for the same total energy deposition is visible for nuclear recoils. Figure 2.7 shows the energy deposition in the light and phonon

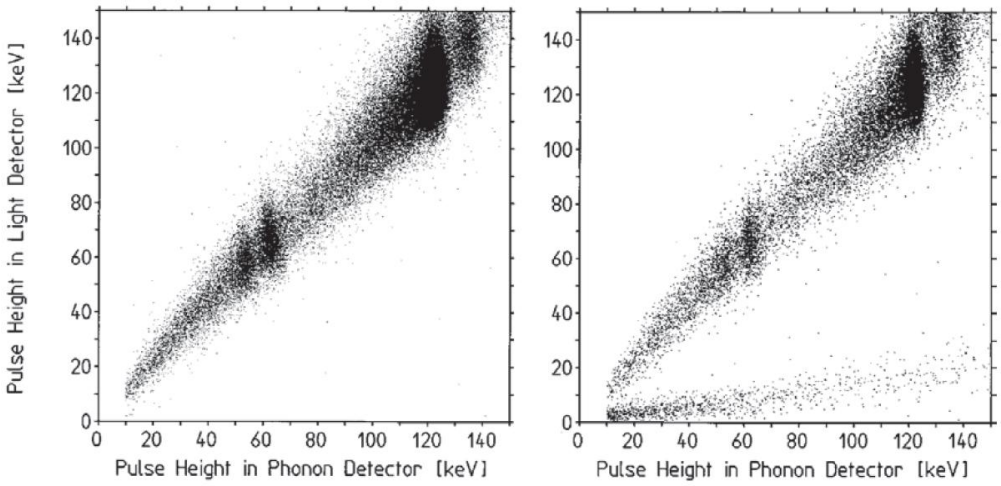

Figure 2.6: Two measurements (scatter plots) with a CRESST detector module consisting of a phonon and a light detector are shown with their energy depositions in both channels. For the measurement shown at left, a ^{57}Co and a ^{90}Sr source have been used, inducing only electron recoils. While performing the measurement shown at right, also an $AmBe$ neutron source inducing nuclear recoils was present [90].

channels for an exposure of $\sim$ 12 $kg\,days$ in the high energy region. Here, nuclear recoils are induced not by neutrons but by internal alpha-decays in the crystal coming from very small contaminations with radioactive isotopes.

The light output for nuclear recoils coming from alphas is less reduced than the light output from neutrons scattering off oxygen, calcium or tungsten. The nuclear recoil bands coming from scattering off these three elements are described by their quenching factors. Measurements from ion irradiation allow to calculate the quenching factors [92]:

Oxygen	9 ± 0.7
Calcium	15.7 ± 1.5
Tungsten	25.6 ± 3

For this measurement, oxygen, calcium and tungsten ions are used as projectiles with energies of few tens of keV to induce nuclear recoils in the crystal. These measurements are only sensitive to the surface of the crystal and can not be performed at the working temperatures of the CRESST detectors (few mK).

Due to the finite resolution of the light detector and photon statistics, the three nuclear recoil bands are broadened and overlap in the energy region relevant for WIMP detection ($\leq 40keV$). For nuclear recoils with a sufficiently high energy deposition, the three bands would disentangle. Due to kinematic reasons, the maximum energy transferable by neutrons onto a heavy nucleus like tungsten via elastic scattering is $\sim$ 2% of their energy under 180°-scattering, making the

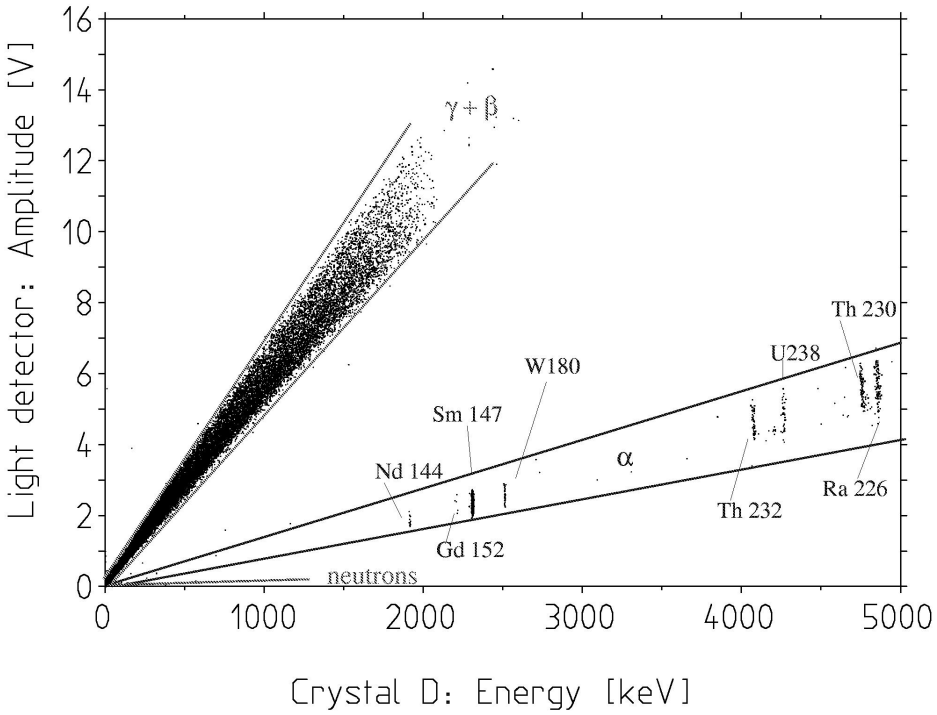

Figure 2.7: The high energy region in the CRESST module (D) for an exposure of $\sim 12\ kg\,days$. All the mono-energetic alpha decay lines originating from the decay of very low contamination of radioactive isotopes in the crystal are identified. The light output of alpha particles is less quenched than for nuclear recoils originating from neutrons scattering off oxygen, calcium or tungsten. Figure from [91].

region where the nuclear recoil bands no longer overlap difficult to access for typical neutron sources with an energy of few MeV.

Figure 2.8 shows the neutron calibration data recorded during the commissioning run of 2007 for the detector module Verena/SOS21 [82]. In this presentation of the data, the light yield as defined by equation 2.2 is plotted versus the energy in the phonon channel, showing the electron recoils with a light yield of 1 and the nuclear recoils with a LY of ~ 0.1 for high energies. Due to the finite resolution of the light detector, the bands broaden at low energies. 90% of all oxygen recoils are expected below the (red) line, which is calculated assuming a quenching factor for oxygen recoils of $QF_{Oxygen} = 9$ and taking into account the resolution of the light detector [82].

2.2.2.2 Expected WIMP Signal in CRESST

Applying the equations from section 1.2.2.1 to oxygen, calcium and tungsten for a 60 GeV-WIMP weighted with their mass fractions in a $CaWO_4$ crystal yield the relative expected event rates shown in figure 2.9. In this scenario, WIMP

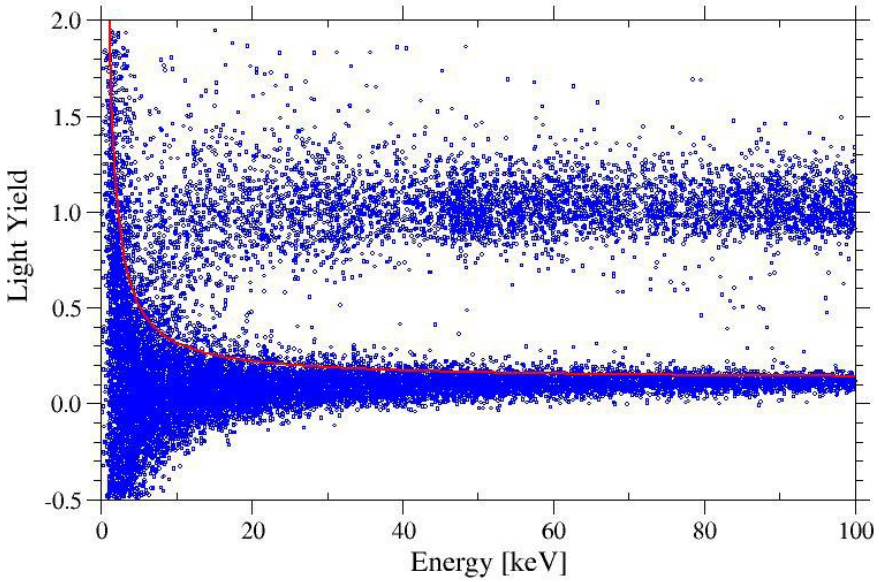

Figure 2.8: The light yield scatter plot during the neutron calibration for the detector module Verena/SOS21 from the 2007 commissioning run of CRESST [82]. On the x-axis is the energy detected in the phonon detector, on the y-axis the light yield as defined by equation 2.2. The (red) line indicates the region below which 90% of all oxygen recoils are expected when assuming a quenching factor of 9 for oxygen recoils and taking into account the resolution of the light detector.

recoils are expected on tungsten up to an energy of $\sim 40\,keV$. While the cross section for coherent scattering is always amplified by a factor of A^2 (with A being the mass of the target nucleus), WIMPs much lighter than 60 GeV will for kinematic reasons only transfer a small fraction of their incident energy on a tungsten nucleus, which might be below current detector thresholds.
Assuming an analysis threshold of 10 keV, which is regularly achieved[1] for most CRESST detectors [65, 94], the expected relative recoil rates for $CaWO_4$ are shown in figure 2.10.

WIMPs are expected to scatter mainly off oxygen for a WIMP mass of 10 GeV or less, and off tungsten for a WIMP mass of 20 GeV or more, and off calcium in between. With background difficult to handle at the low energy region and taking into account the low event rates expected from WIMPs, the different target nuclei in a $CaWO_4$ crystal provide an excellent way to verify a positive WIMP signal, since the expected spectrum and rate of WIMP interactions depend in a known way on the target nucleus - assuming of course a coherent behavior of the interaction.

[1] For some detectors, analysis thresholds of $\sim 5keV$ are achieved [93].

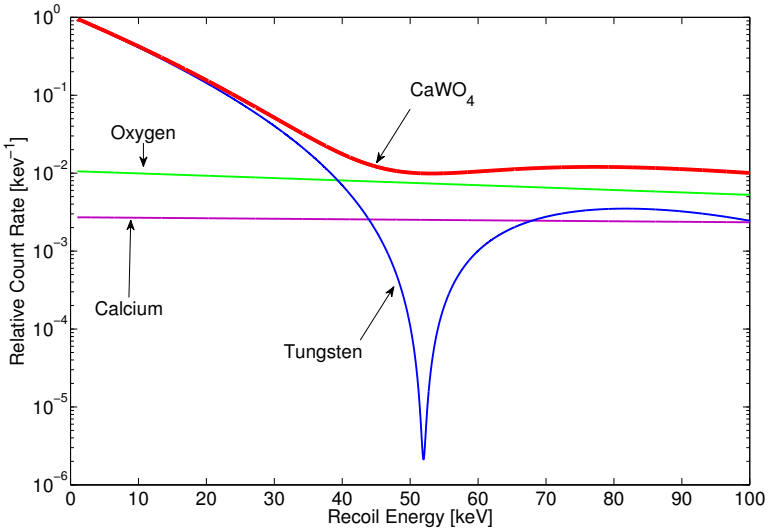

Figure 2.9: Expected relative rates for WIMPs with a mass of 60 GeV. In this scenario, the relevant WIMP signal are recoils off tungsten nuclei up to 40 keV. The dip in the W spectrum is due to the Helm form factor (see section 1.2.2.1).

2.2.2.3 Expected Background in CRESST

Background events in the signal region can have different causes. They are discussed in this section.

Gamma Leakage
In the low-energy region, gamma events can be misidentified as nuclear recoils if the overlap between the electron and nuclear recoil band is significant. For the latest data analysis, the lower end of the signal region has been defined so that a leakage of not more than 0.1 gamma events are expected into the oxygen recoil band [65].

Alpha Decays
Alpha decays in the direct surroundings of the detector crystal can lead to different background events, depending on the location of the radioactive isotope and the absorbing materials for the emitted alpha particle and recoiling nucleus.

- **Internal decay in a $CaWO_4$ crystal:** A contamination within the crystal leads to the deposition of all energy (several MeV) in the bulk detector material. This effect is visible in figure 2.7 and there is no risk of leakage into the signal region.
- **Surface decay:** Surface contamination of ^{210}Po coming from ^{222}Rn decay can lead to different kinds of events depending on the absorbing material for the alpha and the recoiling ^{206}Pb.

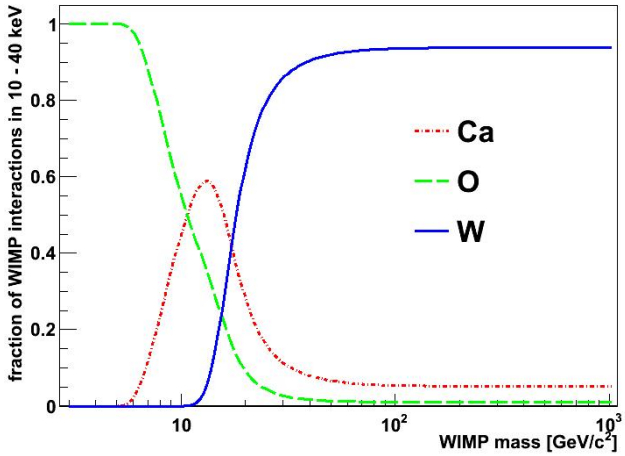

Figure 2.10: The expected total rates for the constituents of a $CaWO_4$-crystal calculated for different WIMP masses. An analysis threshold of 10 keV has been assumed for this calculation [65].

  - **Alpha absorbed by the reflecting foil:** The reflecting foil encapsulating the detector (see section 2.1.2) is also scintillating. If the alpha is absorbed in the foil, it will lead to a high light output lifting the recoil well above the signal region defined by the nuclear recoil band.
  - **Alpha completely absorbed in the crystal:** For kinematic reasons, the alpha carries most of the energy of the alpha decay. Depositing several MeV, such an event is well outside the signal region.
  - **Alpha absorbed by non-scintillating material:** A very small solid angle in the CRESST detector is covered with non-scintillating material, mainly the clamps holding the detector. If the recoiling heavy ^{206}Pb-nucleus is absorbed in the phonon detector crystal while the alpha is absorbed in the clamps, this event can lead to a nuclear recoil in the signal region, since the quenching factor of a heavy nucleus like lead is similar to that of tungsten [95].

- **Degraded alpha:** If the decaying nucleus is implanted several atomic layers in the non-scintillating material, the alpha can lose an arbitrary amount of energy undetected before depositing its remaining energy in the target crystal. Such an alpha can have any energy, potentially leaking into the signal region. This is called a degraded alpha.

Neutron Background

A neutron scattering elastically off a target nucleus can mimic a WIMP signal. Neutrons are the most dangerous background in the CRESST experiment. Some neutron events can be rejected when they deposit energy in more than one detector, since coincident events are not expected from WIMPs.

The following mechanisms can make a relevant contribution to neutron background in the CRESST experiment:

- **Neutron production by natural radioactivity:** Neutrons can be produced by natural radioactivity in an (α, n) reaction. The following scenarios can be distinguished:
  - **Neutron production outside the shielding:** Ambient neutrons from concrete and rock produced outside the shielding are heavily moderated. Their contribution to the signal region is estimated by simulations to be $\sim\ 1 * 10^{-4}\ cts/kgd$ [96].
  - **Neutron production inside the shielding:** Assumed impurities in the polyethylene, lead and copper shielding lead to a total expected event rate in the signal region of $\sim\ \ 1 * 10^{-3}\ cts/kgd$ in Monte Carlo simulations [96].
- **Muon induced neutrons:** Muons can produce secondary neutrons by deep inelastic scattering off a nucleus or in a directly produced electromagnetic or indirectly produced hadronic shower [97]. The following cases are possible:
  - **Muon interacts with muon veto:** If the muon interacts with the muon veto, all events in the low-temperature detectors are discarded for a period of few ms.
  - **Secondaries interact in the muon veto:** If the muon interacts just outside the muon veto, sufficient energy might still be deposited in the muon veto panels by particles produced in the shower. In this case, events in the cryodetector are also discarded.
  - **No detected energy in the muon veto:** A muon can produce neutrons with energies in the GeV range. These can be produced either outside the muon veto and can then enter the setup without registering energy above threshold in the veto, or the muon itself entered the setup undetected and produced the neutrons there. High energetic neutrons can multiply by inelastic scattering in the Pb/Cu shielding [97]. There is still a chance of these events being discarded if multiple interactions take place at the same time in more than one cryodetector, which is not expected for a WIMP. From simulations, expected rates of nuclear recoils from neutrons produced by muons in the signal region are $\sim\ 4 * 10^{-4}\ cts/kgd$ [96]. However, current data suggest a larger contribution, see the discussion on page 32.

2.2.3 Latest CRESST Results

Nine channels corresponding to a total target mass of $2.7kg$ were fully operational in the last run, which started in June 2009. Data taking stopped in April

2011. More than $1000kg$ of raw data were recorded in this time [93]. About 400 kgd of data from this run have been analyzed up to this date [65].

2.2.3.1 Results of the Data Analysis

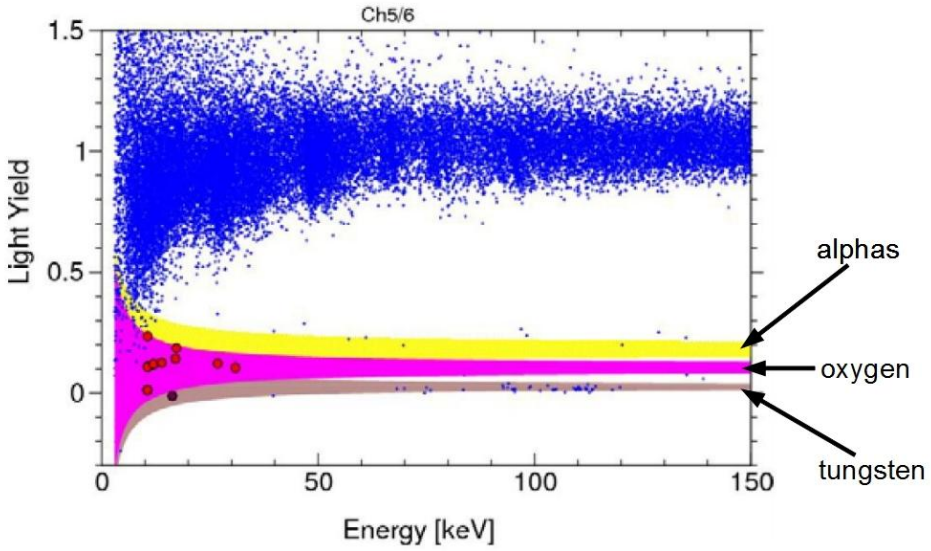

Figure 2.11: Data of detector module ch5/6. The magenta colored area is the oxygen band, where 80% of the oxygen recoils are expected (90% below the upper and 10% below the lower end). The region where no-light events are expected (which can be attributed to tungsten) are shown in brown. The yellow region marks where alpha recoils are expected. Events marked in red and brown are recoils in the signal region of expected oxygen and tungsten recoils, respectively. See text for further details, figure from [65].

As an example, the data recorded between September 2009 and May 2010 for Channel 5/6 is shown in figure 2.11. Under the assumption of a quenching factor of 9.6 for oxygen [65], a number of events in the signal region for oxygen recoils (marked in magenta) have been observed. With the recoil bands of oxygen and tungsten (marked in brown) overlapping in the low-energy region due to a finite resolution of the light detector and photon statistics, some events can be attributed to tungsten as well as to oxygen. The yellow area with a light yield of $LY = 0.25$ belongs to alpha recoils. Generally, the energy of alpha recoils is of the order of several MeV, but the *degraded alphas* discussed in section 2.2.2.3 can lead to alpha events in the low energy region.

All nine active channels exhibit a similar pattern to that shown in figure 2.11: An excess of low energetic oxygen recoils is observed. Discarding all events that can not be clearly attributed to oxygen but might be caused by recoils off tungsten, all remaining recorded events for all channels are summarized in table 2.1 [65]. Some events in the signal region are not only visible in one

Detector	not coincident	coincident
Ch05	5	0
Ch20	2	0
Ch29	4	1
Ch33	2	1
Ch43	4	1
Ch45	2	0
Ch47	4	0
Ch51	5	0
Ch55	3	0
total	**31**	**3**

Table 2.1: Number of oxygen recoil events observed in the signal energy range of each detector, with possible tungsten events discarded. Some recoils were observed in coincidence in more than one detector module. The total exposure is about 400 kg-days.

detector but have a coincident energy deposition in at least one other detector module. In the table, these are called coincident events. The three coincident recoils are in fact two events. One of these events leads to oxygen recoils in two detectors with an additional 1.8 MeV gamma event in a third detector. The second coincident event is an oxygen recoil in the signal energy range of one detector, a 33keV gamma in a second detector, together with an 1.16 MeV gamma in a third one. The origin of these events remain unclear, but the high energetic gammas suggest that it might be muon-induced with the muon remaining undetected. This is further strengthened by the fact that the neutron calibration carried out showed that less than 1 out of 1000 recoils is accompanied by an MeV gamma [65], statistically making it improbable that the observed coincident events originate from $\sim MeV$ neutrons.

2.2.3.2 Additional Background Considerations

Complex Monte Carlo simulations were carried out to estimate the different contributions to the background [96]. But these simulations do not take into account the efficiency of the muon veto, degraded alphas, and the detector resolution. The observed data from the Dark Matter run and calibration allow to estimate the following contributions:

Muon Induced Single Scatters in the Signal Region Considering the two observed coincident events as muon-induced with an undetected muon, there is also some probability that single scatters are caused by undetected muons. The number of these can be estimated as follows:
In total, 8 single oxygen scatters in the signal region are visible in only one detector module and 17 with energy deposition in at least one additional detector have been observed in coincidence with the muon veto (and were thus discarded

for the subsequent analysis).
The observed ratio of muon induced single scatters to muon induced multiple scatters is $8/17 = 0.47 \pm 0.14$ [65].
With two multi-site events possibly caused by undetected muons observed, the number of detected single scatters in the signal region caused by unobserved muons can be estimated to be $2 * 0.47 \approx 0.9 \pm 0.8$ counts [65].

Degraded Alphas Leaking into the Signal Region Alphas originating from α-emitters implanted in the surface of a non-scintillating material can be absorbed in the $CaWO_4$ crystal while previously having lost an arbitrary amount of energy undetected. This leads to the existence of alpha events down to the energy window of interest (10-40 keV).
To estimate the number of degraded alphas leaking into the signal region, the energy E_{cross} defined by the intersection of the center of the alpha band with the upper 90% confidence line of the oxygen band is used. Then the alphas between E_{cross} and $E_{cross} + 100\,keV$ are summed up, allowing to estimate the number of events below E_{cross} by assuming a constant spectral energy density. As a result, in total, 6.9 ± 2.1 alpha events in the signal region are expected [65].

Total Estimated Background In total, the expected background is:

muon induced neutron background	0.9 ± 0.8
degraded alphas	6.9 ± 2.1
gamma leakage[2]	0.9
total	8.7 ± 1.4

In total 31 single oxygen scatters have been observed, with an estimated background of 8.7 ± 1.4 events. This amounts to an observed rate of $0.8 - 1.0 \times 10^{-1} cts\,kg^{-1}\,d^{-1}$.

Part of the background was simulated, the numbers given in section 2.2.2.3 add up to a background rate of $5.15 * 10^{-3} cts/kgd$, which is less than the background estimated from the actual data. The reason is that the components coming from gamma leakage and degraded alphas were not included, since these have not been within the scope of the simulation.

2.2.3.3 Interpretation and Planned Upgrades

In the analyzed $400 kg\,days$ of data, 31 events that can be attributed to oxygen recoils have been detected. The estimated background is 8.7 ± 1.4 events.

Interpreting the observed recoils as a WIMP Dark Matter signal, the events would have to originate from light WIMPs in the range of $M_{WIMP} \leq 15 GeV$

[2]The lower end of the signal region is defined in such a way that not more than 0.1 gamma events are expected to leak into the oxygen recoil band per detector, see section 2.2.2.3.

with an elastic spin independent WIMP-nucleon cross section of $\sigma_{WN} \sim 10^{-5} pb$ [65].

The collection of further data and a complete understanding of the background is needed to substantiate this possibility. With current statistics, other WIMP signatures such as an annual rate modulation can not be detected.

The major contribution of the background comes from degraded alphas originating mainly from alpha emitters implanted in the surface of the clamps holding the detector, since the clamps are the only non-scintillating material in the direct vicinity of the target crystal.
In the next experimental run it is planned to implement scintillating clamps to get rid of this major contribution to the background. Also the effective target mass is planned to be roughly doubled.

2.2.3.4 Exclusion Limits for Inelastic Dark Matter

Inelastic Dark Matter was proposed to reconcile the reported positive Dark Matter detection claimed by the DAMA collaboration with the null-result of other experiments (see section 1.2.3.1). In this scenario, the WIMP is left in an excited state after the interaction in the detector. This suppresses the WIMP-nucleus scattering for light target nuclei. Due to the large mass of the tungsten nucleus ($A \sim 184$), CRESST is very sensitive to this type of Dark Matter. The mass (energy) splitting between the ground state and exited state is discussed to be in the order of $\delta \sim 100 keV$. Figure 2.12 shows the exclusion limits coming from the latest CRESST run for inelastic Dark Matter and the regions of compatibility for DAMA for mass splittings from 80 keV to 140 keV, ruling out this scenario [65].

2.3 Relevance of Quenching Factors

The discussion in section 2.2.3 showed the importance of quenching factors for the interpretation of the CRESST data:
The WIMP recoil rates and spectra differ between different target materials in a known way (see section 1.2.2.1). Different target materials will thus allow to extract the nature of the WIMP and to verify a positive signal. Characterizing the QF of the target materials in the bulk of the target crystal at working conditions (i.e. at mK temperatures) of the detector is of high importance. Other tungstates (e.g. $ZnWO_4$) or (especially to investigate light WIMP candidates) NaI-cryogenic detectors are of immediate interest for the CRESST and possible follow-up experiments.

The quenching factor measurements giving the results shown on page 25 were performed by irradiating the target crystal with ions, testing mainly the surface of the crystal at a temperature of 4.2 K or higher. To measure the bulk

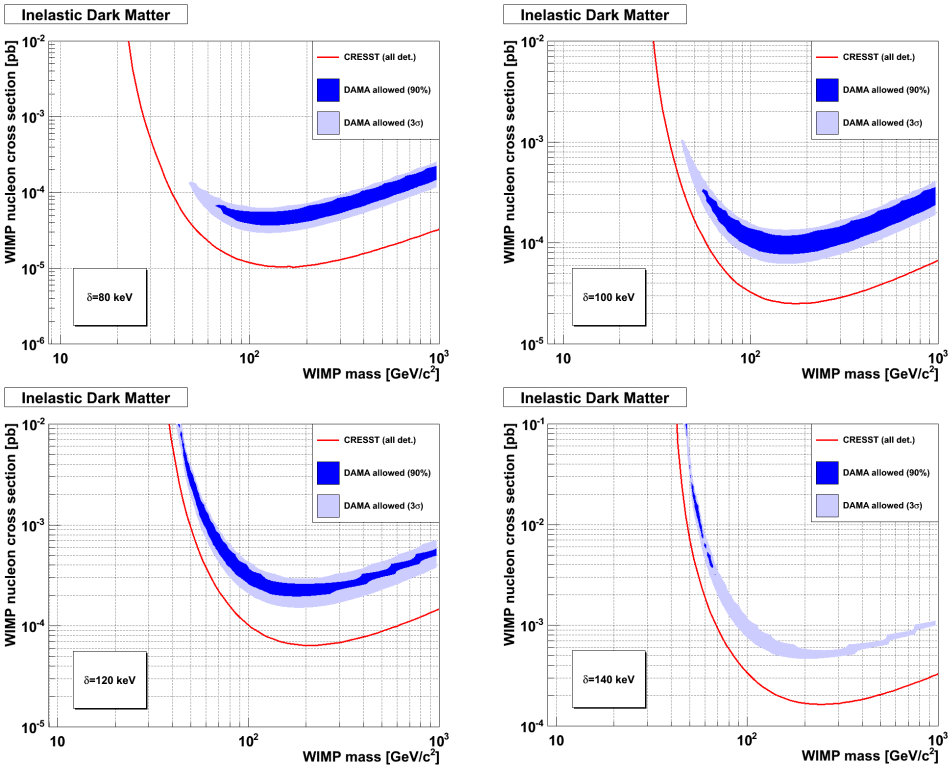

Figure 2.12: CRESST exclusion limits for inelastic Dark Matter and the positive detection of DAMA when interpreted as inelastic Dark Matter for mass splittings of 80, 100, 120 and 140 keV [65].

quenching factors in cryogenic detectors at mK temperatures, a neutron scattering facility has been set up, which will be described in the next chapter.

Chapter 3

Experimental Setup for Quenching Factor Measurements

The goal of the present work was to set up an experiment allowing to measure the scintillation light quenching (see section 2.2.1) of nuclear recoils in the bulk of the detector material of a low-temperature detector. To perform such a measurement, a way to produce nuclear recoils in the bulk of the target material is needed, as well as a technique allowing the measurement of the quenching factors (QFs) of all constituents in a given multi-target detector, e.g. $CaWO_4$ or any other target material that might be judged suitable in future direct Dark Matter searches. Due to the limited resolution of a real detector, the different types of recoils that account for the nuclear recoil band may overlap. As the neutron calibration data of a working CRESST detector show (see figure 2.6), this is the case for the $CaWO_4$ (having three nuclear recoils bands from the three constituents) detectors currently used. Thus a way to disentangle the nuclear recoil band independently of the resolution of the light detector is required. This is achieved by inducing nuclear recoils with neutrons of known energy and by measuring all kinematic parameters of the interaction in a triple coincidence measurement.

Section 3.1 gives an overview of the general setup, the following sections 3.2 to 3.8 give a detailed description of the individual components of the experiment: neutron production, the neutron detector arrays, the ^{3}He/^{4}He dilution refrigerator and the SQUID installation, the additional wiring required for Neganov-Luke light amplification, the SQUID read out and the data acquisition hardware and software.

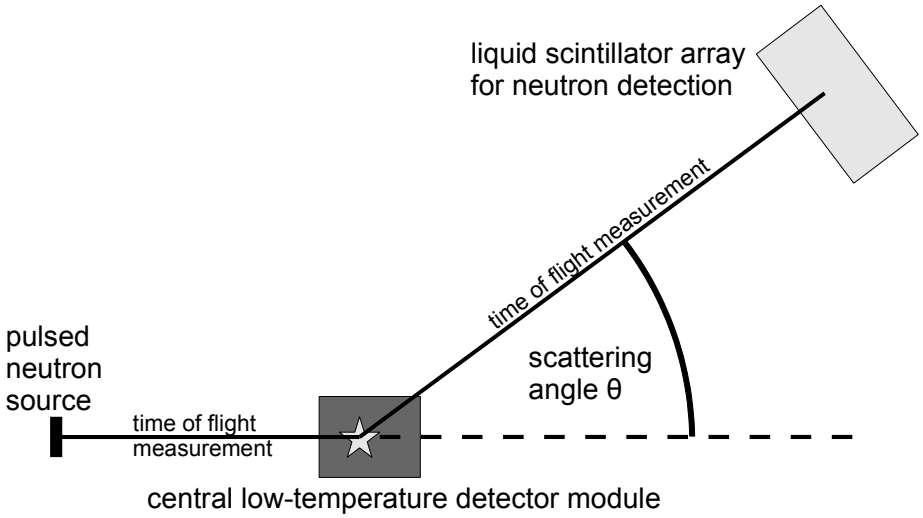

Figure 3.1: Concept of a facility for quenching factor measurements. The central detector, here referred to as the central low-temperature detector module, is irradiated by a pulsed neutron beam. By measuring the time of flight of a neutron, the deposited energy in the scattering process, and the scattering angle, the mass of the target nucleus on which the scattering occurred can be determined, allowing the measurement of the quenching factor for each nucleus independently.

3.1 Overview

Nuclear recoils can be induced by neutrons. The knowledge of all kinematic parameters of a neutron interaction in a given target material allows to measure the quenching factors directly. The kinematic parameters are:

- incident neutron energy
- deposited energy in the crystal of the central detector
- scattering angle

A schematic sketch of an experiment allowing to measure all these parameters independently is shown in figure 3.1. The scattering angle can be determined by detection of the neutrons after the interaction in a central detector. If a pulsed neutron source is used, the neutron energy is known by the measurement of the time of flight. Since typical flight-times for neutrons with energies of $\sim MeV$ are of the order of $10 - 50\ ns/m$, a pulsed neutron source needs a pulse width $\leq 5ns$. This can be achieved with a pulsed ion accelerator producing neutrons in a nuclear reaction.

The principle design of the quenching factor (QF) measurement is based on the setup already utilized by Thomas Jagemann, see [98] and [99].

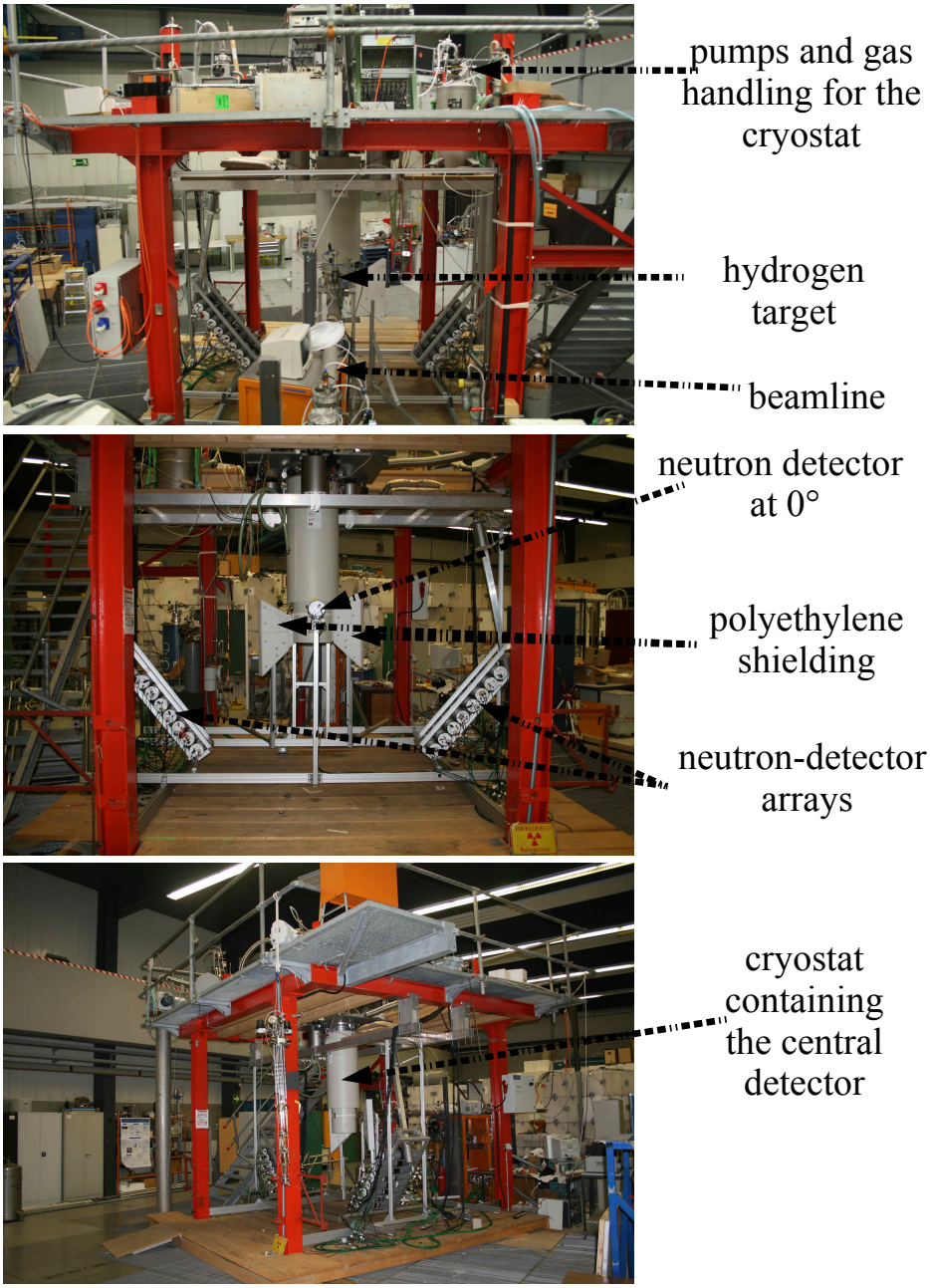

Figure 3.2: Scattering facility at the MLL. The neutrons are produced in a hydrogen target located at the end of the beamline. Neutrons scattered in the central detector housed in the cryostat can be detected in the neutron detector arrays (here at 80° scattering angle) which are shielded from direct neutrons via polyethylene plates.

Pictures of the experiment following the method outlined above are shown in figure 3.2. The neutrons are produced in a nuclear reaction (e.g. a ^{11}B beam on a hydrogen target) and scatter in a central low-temperature detector (cryodetector) operated at mK temperatures. The scattered neutrons can be detected by arrays of liquid scintillator cells coupled to photomultiplier tubes (PMTs). All components of importance are introduced in the following sections.

3.2 Neutron Production

Neutrons can be produced in different nuclear reactions [100]. Inverse kinematics allow the production of a directed neutron beam by employing a heavy ion beam, which is generated by a particle accelerator of which the different relevant components are introduced in section 3.2.1. Section 3.2.2 describes the nuclear reaction and section 3.2.3 shows the performance of the neutron source.

3.2.1 The Accelerator

The Tandem Accelerator (section 3.2.1.1) located at the Maier-Leibnitz Laboratorium in Garching allows the generation of a pulsed ion beam (section 3.2.1.2) with sufficient intensity and energy to produce a neutron beam suited for the measurement of quenching factors.

3.2.1.1 Tandem Accelerator

The neutrons for the quenching factor measurements are produced in a nuclear reaction with inverse kinematics (see section 3.2.2). To reach the required ion-energies, a tandem accelerator of the Van de Graaff type is used. Moving belts produce a very high and stable voltage of up to 15 MV. The positive terminal voltage is used twice for the acceleration of ions (hence the name 'tandem accelerator') by inverting the charge of the ion:
First, by passing through several atomic layers of Cs atoms, an electron is added to the projectile at the negative ion injector and the ion is accelerated using the full voltage. By directing the beam through a thin foil, electrons are stripped and a positive ion is produced and the full voltage is used again. Depending on the number of stripped electrons, ions with different energies exist at the end of the accelerator. A specific charge state is selected by an analyzing magnet located behind the accelerator tube, as seen in figure 3.3. By a magnetic field of $\sim 1\ T$ the ion beam is diverted by an angle of 90°. Similar to a mass spectrometer, only one mass, energy and charge state 'survives' the analyzing magnet, allowing to produce only mono-energetic ions after this point.

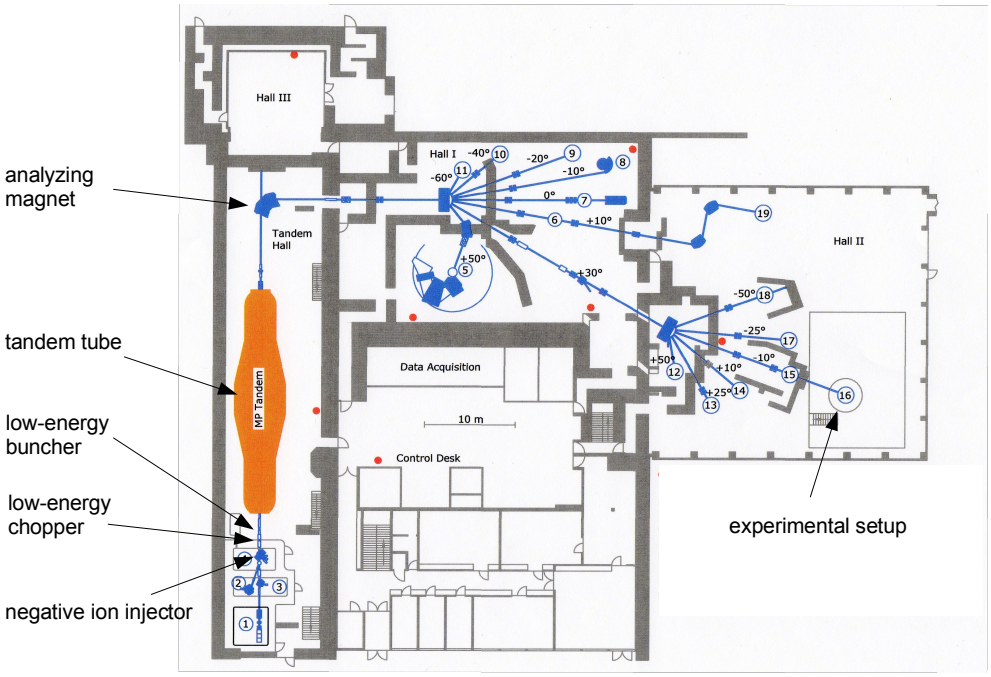

Figure 3.3: Overview of the Maier-Leibnitz Laboratorium in Garching. A neutron beam is produced at the experimental setup by a nuclear reaction induced by an ion beam coming from the tandem accelerator. The ion beam can be pulsed via a system of choppers and bunchers, see the main text for further details.

3.2.1.2 Generation of a Pulsed Beam

Since the measurement principle requires a time-of-flight (ToF) measurement, a pulsed ion beam is required. A three stage system consisting of a low-energy chopper, low-energy buncher and a high-energy chopper is used.

Working Principle of a Chopper

A chopper cuts part of the beam by periodically diverting the beam from the optical axis confined by an aperture. The working principle is shown in figure 3.4. By increasing the amplitude of the electrical field and by closing the aperture, the beam pulse can in principle be infinitely short in time at the cost of beam intensity.

The chopper is operated at a frequency of $f = 5\ MHz$. The possibility to accept only pulses being a multiple of 2^n with $n = 1, 2, 3, ...$ is also given. Typically, for the neutron scattering facility values of $n = 4$ or $n = 5$ are used, resulting in a chopper rate of $300\,kHz$ or $150\,kHz$.

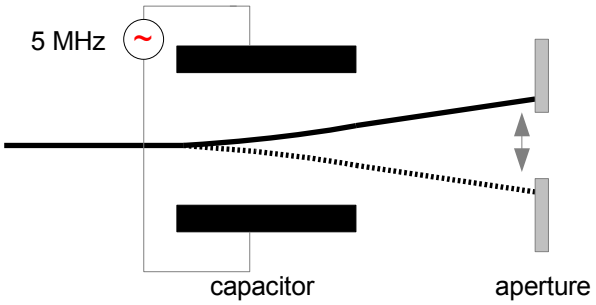

Figure 3.4: Working principle of a chopper: The ion beam is diverted periodically ($f = 5\ MHz$) by a capacitor producing an alternating electrical field. The beam sweeps over an aperture with an adjustable width, which cuts away parts of the beam. Figure from [101].

Working Principle of a Buncher

The working principle of a buncher is shown in figure 3.5. The buncher is

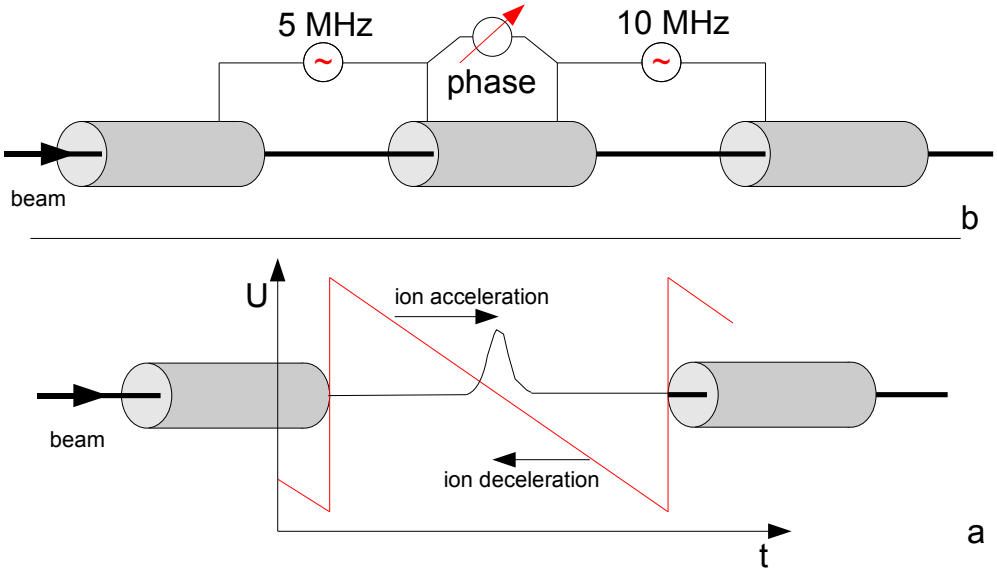

Figure 3.5: The working principle of a buncher is shown. (a) A saw-tooth shaped voltage accelerates and decelerates different parts of the pulse. The point of convergence has to be at the experimental setup (see figure 3.3), so that the beam pulse is sharpest in time at this point. (b) In reality, the saw tooth is not ideal but a superposition of a 5 MHz and a 10 MHz sine. Figure from [101].

used to concentrate the ions in time at a specific location, preferably at the experimental setup where a sharp ion pulse is required for a time-of-flight measurement. A saw-tooth voltage is applied to the ions before entering the tandem tube, producing an electrical field in direction of the beam. Depending on the timing, some ions are accelerated and some are decelerated by this field. This leads to a converging effect that has its maximum depending on the amplitude of the saw tooth and the ion energy. The width of the ion pulse can be checked

directly at the experimental setup by positioning a neutron detector in the ion beam (see the neutron detector at 0° in figure 3.2 and section 3.2.3). This allows to optimize the buncher parameters. Contrary to chopping, bunching does not affect beam intensity. But generally a DC offset remains, which is discussed in the next paragraph.

The saw tooth is approximated by a superposition of two sines of 5 MHz and 10 MHz as seen in figure 3.5.

Chopper and Buncher Timing
A sharply pulsed beam with sufficient intensity can only be produced by using both the buncher and the chopper. The buncher produces a sharp pulse with no loss of intensity, but it leaves a DC offset (as seen in the schematic view in figure 3.6). The offset must be discarded by the chopper. To get a sharp,

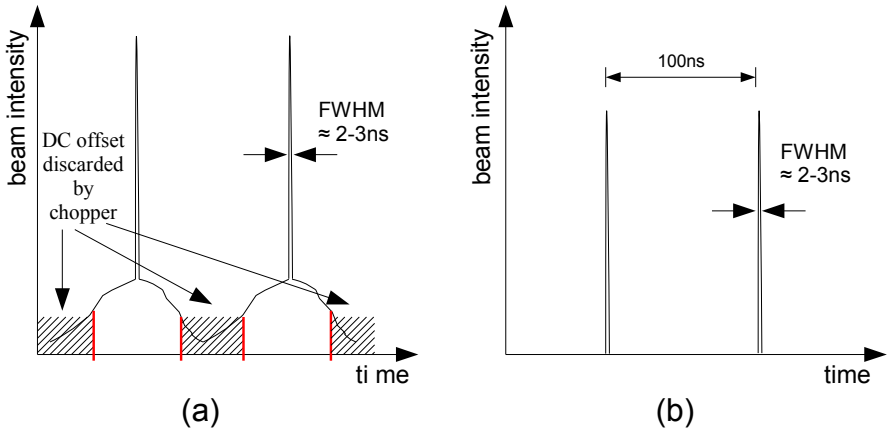

Figure 3.6: a) The buncher leads to a converging effect for the ion pulse. Between two pulses a DC offset (hatched areas) appears, which has to be removed by the chopper. The obtained result is a sharp, periodic signal at the experimental setup (b).

symmetric beam pulse with maximum intensity, the timing between the chopper and the buncher is important. The data acquisition (see section 3.8.2.2) allows the real time monitoring of the beam pulse properties by reading out a neutron detector positioned in the optical axis of the produced neutron beam. This allows to conveniently monitor and optimize the buncher and chopper parameters.

3.2.2 Nuclear Reaction and Target Cell

The neutron beam is produced in a nuclear reaction with inverse kinematics. Two reactions can be used to produce monoenergetic neutrons (after inverting projectile and target), which are of specific interest for the scattering facility: $^{1}\mathrm{H}(^{11}\mathrm{B}, n)^{11}\mathrm{C}$ and $^{1}\mathrm{H}(^{15}\mathrm{N}, n)^{15}\mathrm{O}$ [100]. All beam times with the scattering

facility were based on the first reaction, utilizing a ^{11}B beam on a hydrogen target.

The energy of the produced neutrons depends on the incident energy of the particle and the nuclear excitation levels that can be populated in the produced ^{11}C nucleus. This is depicted in figure 3.7. An ion energy of $\sim 55MeV$ allows

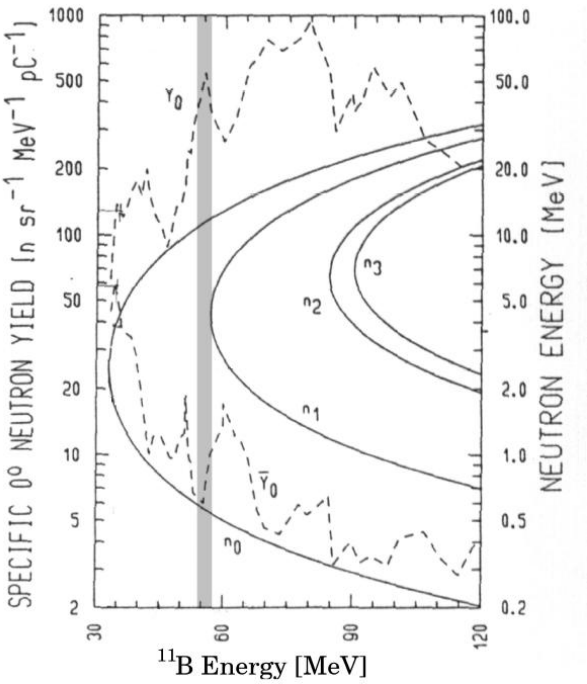

Figure 3.7: The dependence of the neutron energies (solid curves) of the ^{1}H(^{11}B, n)^{11}C reaction populating the four lowest levels in ^{11}C. The dashed lines give the specific °0 neutron yield of the high energetic (Y_0) and the low energetic ($\overline{Y_0}$) branch of the n_o neutron group. The gray vertical line indicates the ^{11}B energy used in the experiment. Figure from [100].

the production of monoenergetic neutrons n_0 in the center of mass frame. Increasing the energy above $\sim 55MeV$ allows the population of the second excited state in ^{11}C, producing the neutron group n_1. In the center of mass frame, the neutrons are produced at all solid angles. In the laboratory system, this leads to two neutron groups produced for °0 (one for the neutrons produced in direction of the beam and one for the opposite direction) with energies of $\sim 11MeV$ and $\sim 0.5MeV$ (see figure 3.7), respectively.

A schematic view of the hydrogen cell is shown in figure 3.8. Pressurized hydrogen (3 bar) is separated against the vacuum in the beam line by a molybdenum foil (5 μm thickness). To match the nominal energy of 55 MeV required for the nuclear reaction, the effect of energy loss by passing through the molybdenum foil as well as an energy loss in the hydrogen cell have to be taken into account. They are estimated in [99] to be 4.8 MeV (in the Mo-window) and 1.3 MeV (in

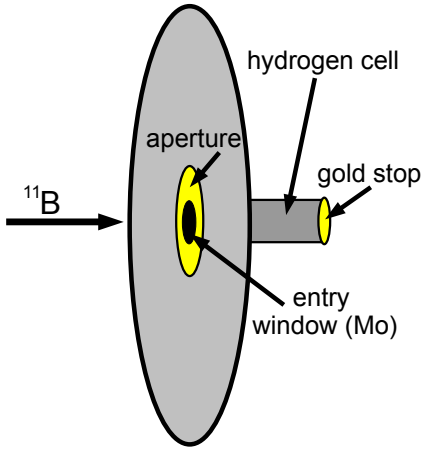

Figure 3.8: Schematic view of the hydrogen cell. The ^{11}B beam enters the cell through an entry window made of molybdenum (thickness: 5 μm) separating the hydrogen from the vacuum in the beam line. The golden beamstop and aperture are insulated against the beamline to allow a measurement of the beam current.

the hydrogen cell), leading to a required beam energy of $\sim$ 61.5 MeV. This was also verified experimentally by varying the beam energy in 0.5 MeV steps from 60MeV to 63MeV.

Parasitic neutrons are produced by spallation in all surrounding materials. To reduce this background, the cross section of the beam has to be sufficiently small to hit the hydrogen cell only. The golden beamstop and aperture depicted in figure 3.8 are electrically insulated against their surroundings (to read out the beam current). Cross section and position of the beam can thus be optimized.

3.2.3 Neutron Source Performance

All measurements at the neutron scattering facility to date have been performed with the neutron production reaction ^{1}H(^{11}B, n)^{11}C described in section 3.2.2. A typical time of flight spectrum obtained with a liquid scintillator detector (see section 3.3.2) positioned 2.05m behind the hydrogen cell in the optical axis defined by the ^{11}B beam is shown in figure 3.9. The kinetic energy of the ^{11}B beam is partly converted into the production of gammas. Based on the measured distance and the speed of light, these gammas reach the neutron detector after an expected time of 6.84ns. The gamma peak is used as a calibration point to define the zero-time for the time of flight measurement: the zero-time is given by the time when the ^{11}B beam interacts with the hydrogen cell. For this procedure, the gamma peak is fitted with a Gaussian to obtain the current position. By adding a constant offset to all measured time of flights, the resulting position of the gamma peak is shifted to a time of 6.84ns. Accordingly, the

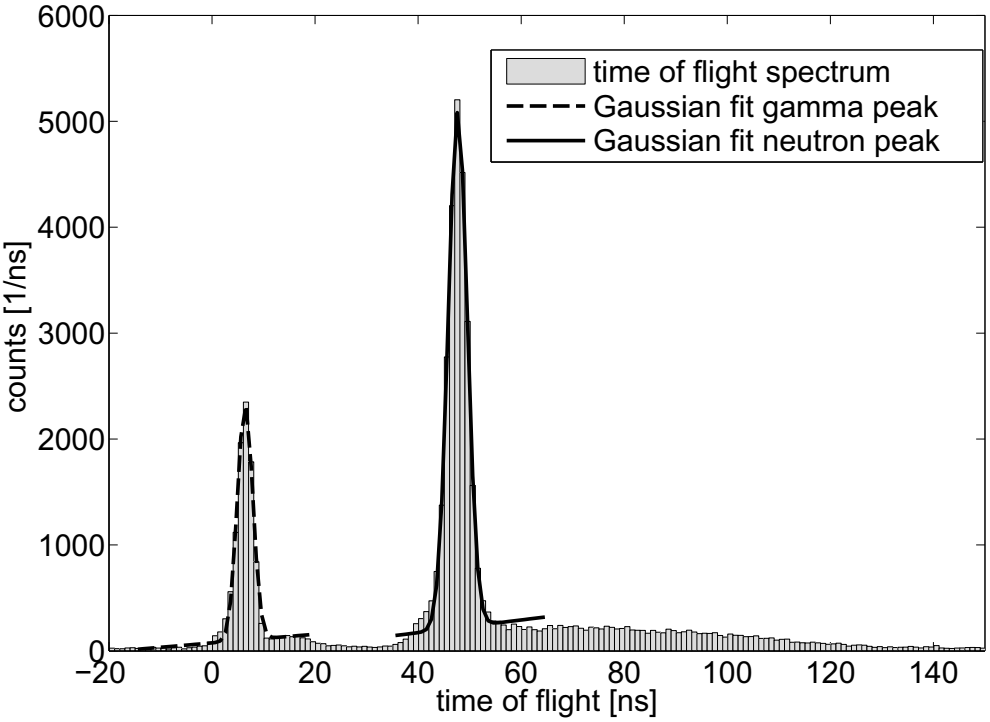

Figure 3.9: Measured time of flight spectrum for the gammas and the neutrons produced in the reaction of 61.5 MeV ^{11}B on a hydrogen cell. The neutron detector (a liquid scintillator cell of $5cm$ depth) is $2.05m$ behind the hydrogen cell on the optical axis defined by the ^{11}B-beam (see the neutron detector at 0° in figure 3.2). The first peak in the figure is produced by gammas, traveling at the speed of light. The second peak belongs to the $\sim 11MeV$ neutrons, which reach the detector after a time of flight of $\sim 48ns$. Both peaks have been fitted locally with a Gaussian plus a linear term, see the main text for details.

fitted[1] position shown in figure 3.9 is $6.84 \pm 0.07\ ns$. The width σ obtained by the fit is $1.49 \pm 0.07\ ns$. The shape of the gamma peak is not perfectly Gaussian but exhibits increased intensity to lower and higher time of flights. There are two main causes: Primarily, increased intensity at larger times is caused by Compton scattering of gammas off the cryostat, the dewar or other surrounding materials. This can cause gammas not produced parallel to the optical axis defined by the beam to reach the neutron detector, and thus having a larger time of flight. Secondarily, the ^{11}B beam bunch is not perfectly symmetric in time, which is mainly the reason for the increased intensity at lower times. The asymmetry can be reduced by cutting part of the beam with the chopper, but this reduces the intensity of the beam.

Applying the same fit model to the second peak (see figure 3.9), which is caused by neutrons, gives a peak position of $47.69 \pm 0.06\ ns$ and a width σ of $1.85 \pm 0.06\ ns$. Neutrons are also observed at flight-times larger than $100ns$. These low-energetic neutrons are produced by the ^{11}B-beam in other processes than the desired $^{1}\mathrm{H}(^{11}\mathrm{B}, n)^{11}\mathrm{C}$ reaction. These neutrons are also visible if the target cell is evacuated and not filled with hydrogen. The width of the observed peaks is not only dependent on the time spread of the ^{11}B-ion bunch and the timing resolution of the detector, but is also dependent on the geometry of the hydrogen target (the target cell has a length of $4cm$) and the depth of the liquid scintillator cell of the neutron detector.

Calculated relativistically, a time of flight of $47.69ns$ for $2.05m$ results in a kinetic energy of the neutron of $9.81MeV$. Calculating the spectral distribution of neutron energies for all times of the measurement shown in figure 3.9 (after applying an additional cut on the pulse shape, using only neutrons for the calculation) results in the neutron-energy spectrum shown in figure 3.10. The neutron energy peaks at $10.61 \pm 0.02\ MeV$, the peak position is derived by fitting with a Gaussian and a linear term. The σ-width of the peak is $0.78 \pm 0.03\ MeV$ (FWHM: $1.83 \pm 0.07 MeV$). Since the neutron energy is proportional to $1/\sqrt{1-(t/s)^2}$, with t being the time of flight and s the distance, a Gaussian is not a perfect representation of the data especially for short time of flights (leading to high neutron energies), as can also be seen in figure 3.10: The neutron spectrum shows neutron energies of $15MeV$, which exceeds the theoretically expected neutron energy. These are caused by the uncertainty in the time of flight measurement and the imperfections of the ^{11}B-bunch. A small deviation to shorter time of flights increases the calculated neutron energy drastically. As was mentioned previously, the observed increase of intensity (compared to the Gaussian fit) at lower time of flights is a result of a ^{11}B beam bunch not perfectly concentrated in time. For few neutrons, the time of flight analysis leads to wrong results, causing an overestimation of the neutron energy by several MeV. The errors are discussed in detail in section 6.2.2.

[1] The fitted model is $F = Ae^{-\frac{(x-b)^2}{2\sigma^2}} + mx + c$, with the linear term and the constant used to describe the local background. The fit is only applied locally around the peak, all data further than $20ns$ away from the peak position is discarded for the fit.

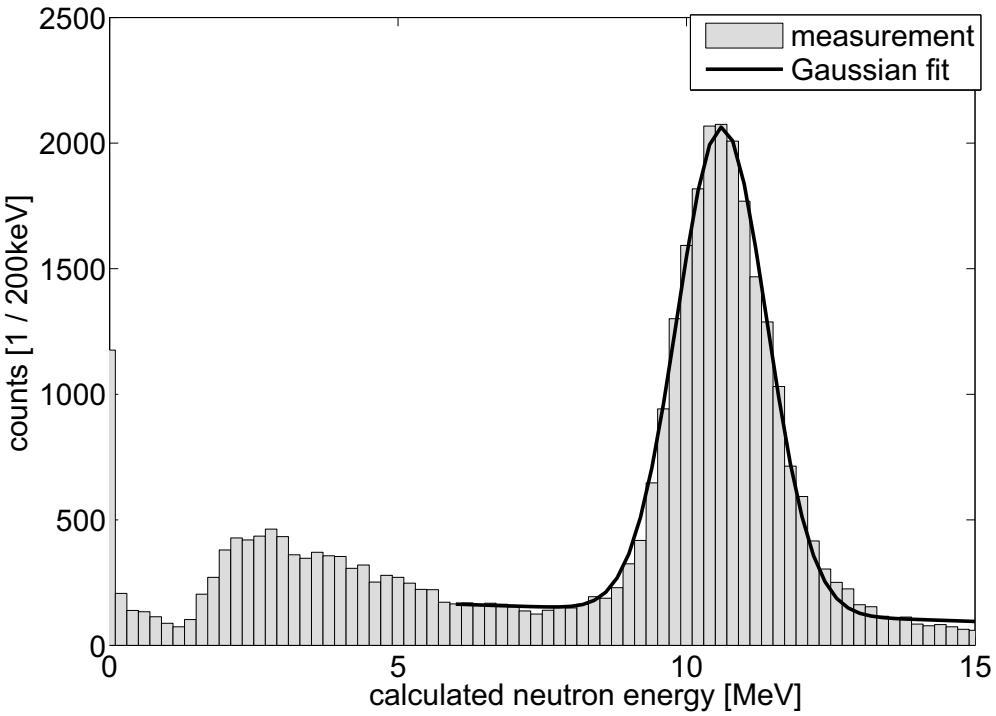

Figure 3.10: Neutron energy spectrum for the ^{11}B+^{1}H reaction with a ^{11}B energy of 61.5 MeV. The energy is calculated from the measured time of flight shown in figure 3.9 and the distance (2.05 m) of the neutron detector to the hydrogen cell. Fitting the high energetic peak with a Gaussian plus a linear term gives a position of 10.61 ± 0.02 MeV and a σ-width of 0.78 ± 0.03 MeV. At lower ($\leq 3MeV$) incident energies, the neutrons no longer produce sufficient scintillation light and are no longer detected. The spectral distribution below $\sim 3MeV$ is thus not measured reliably.

3.3 Neutron Detector Arrays

For the neutron detection, particle discrimination is as important as the extraction of the timing information (for the time-of-flight measurement). Liquid scintillators are very fast (rise times of ~ 1 ns are common) and provide means of particle identification via pulse shape discrimination (see section 3.3.1). Photomultiplier tubes (see section 3.3.2) are very sensitive light detectors that are also sufficiently fast to read out the scintillation light. The achieved timing resolution is discussed in section 3.3.3.

3.3.1 Liquid Scintillators and Pulse Shape Discrimination

Liquid scintillators typically have a fast and a slow decay component for their scintillation light. The slower component originates from triplet states (excited by an energy deposition) of which the transition to the ground state is forbidden, while the fast component originates from excited singlet states relaxing to

the ground state. Triplet states can only be populated if two ionized molecules recombine, thus the intensity of excited triplet states depends on the ionization density (see [102] and references therein). The ionization density is dependent on the energy deposition per unit length dE/dx which is higher for protons than for electrons. This leads to an amplified slow component for nuclear recoils induced by neutrons compared to electron recoils induced by gammas, as qualitatively shown in figure 3.11. This effect can be exploited for particle

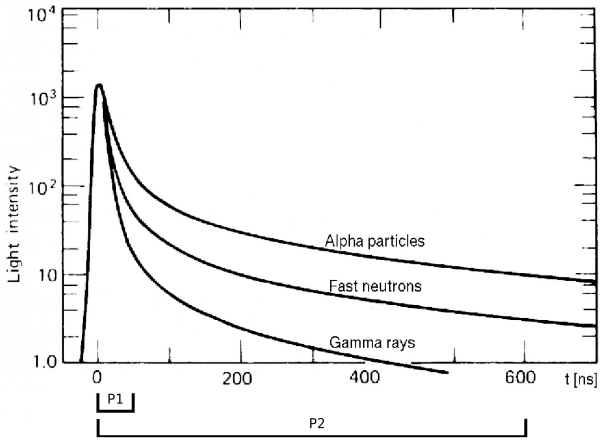

Figure 3.11: Scintillation-light pulse shapes in liquid scintillators shown qualitatively for different ionizing particles. By integrating over the fast and the slow components (integration gates denoted as P1 and P2) the type of particle interaction can be discriminated. Figure from [103].

identification, for example by integrating over the slow component and the fast component. The ratio between the two integrals is dependent on the kind of interaction.

NE-213 is a liquid scintillator widely used for pulse-shape discrimination since it has an enhanced slow component. It was formerly produced by 'Nuclear Enterprises Limited', today an identical replacement from 'Eljen Technology' [104] called EJ-301 is available. The mean decay times for the first three components are 3.16 ns, 32.3 ns and 270 ns [105]. The data sheet of EJ-301 is appended on page 161.

3.3.2 Employed Neutron Detectors

34 neutron detectors that were formerly used by the SICANE ('SIte de CAlibration NEutron') team for nuclear recoil calibration tests [106] are currently employed at the neutron scattering facility. A schematic view of a detector and its arrangement in an array is shown in figure 3.12. A Philips XP-3461-B photomultiplier is optically coupled with silicone oil to a perspex window of the hexagonal cell (inner diameter: ~ 9.1 cm, height: ~ 5 cm) containing the liquid scintillator. The PMTs are operated with a negative voltage of $-1900\,V$.

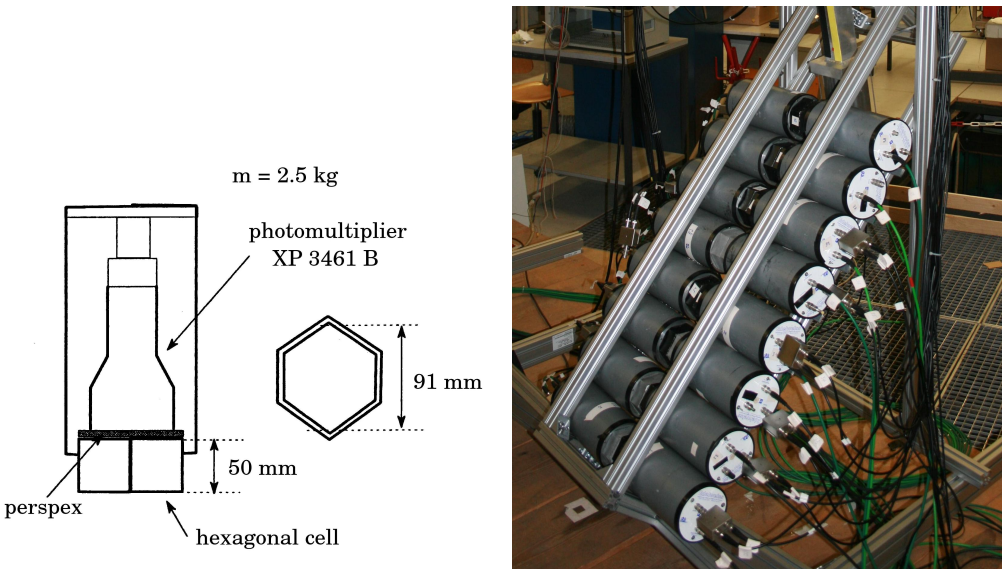

(a) Schematic view of a neutron detector. **(b)** 16 neutron detectors in an array.

Figure 3.12: The left figure (a) shows the schematic view of a neutron detector. The hexagonal cell contains the liquid scintillator EJ-301. On the right (b), an array of neutron detectors is shown. Each detector is connected to a high voltage power supply, each anode output is connected to a constant fraction discriminator and an ADC.

The liquid scintillator contained in the cells was degraded since it was partially exposed to oxygen. All scintillator cells have been refilled with new scintillator and were resealed [101]. The neutron detector arrays are shielded from direct neutrons by polyethylene plates positioned in the direct line of sight between the hydrogen cell and the detector arrays (see figure 3.2).

3.3.3 Neutron Detector Timing Performance

The timing resolution can be tested by detecting the two annihilation gammas of a ^{22}Na-source in coincidence with two neutron detectors. For this measurement, two neutron detectors are placed on an optical axis with the ^{22}Na source in between. The gammas are emitted simultaneously, the absolute time difference between the detection of the two gammas in the different detectors is shown in figure 3.13. The offset of $-29.85(3)ns$ is an intrinsic property of the different PMTs. This is corrected for in the data analysis software, where the *zero time* of each detector is defined. The σ-width of the peak, as derived by a fit with a Gaussian, is $1.10(2)ns$ (FWHM: $2.59(4)ns$). This is below the σ-width of $1.49(7)ns$ (FWHM: $3.51(16)ns$) of the gamma peak caused by the ^{11}B-beam as measured in section 3.2.3. This shows that the limiting factor of the time of flight measurement is not the intrinsic resolution of the detector but the width of the ^{11}B-bunch.

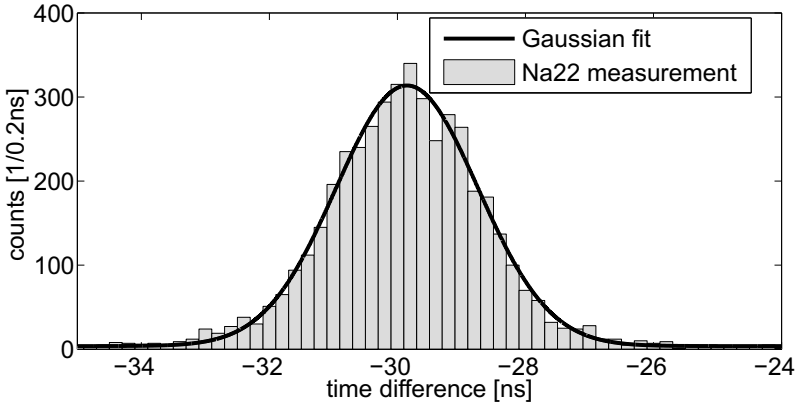

Figure 3.13: A ^{22}Na-source is used for a timing test by employing two neutron detectors placed with the source in between them on the optical axis. The two $511keV$ annihilation gammas of the source are emitted in opposite directions. The time difference between the hits in the two PMTs are shown in the histogram. The σ-width given by a Gaussian fit is $1.10(2)ns$ (FWHM: $2.59(4)ns$). The position of the peak ($-29.85(3)ns$) is dependent on the individual PMT and the cable length. It is corrected for in the analysis software.

3.4 The Low-Temperature Detector Module

The low-temperature detector module employed at the neutron scattering facility generally follows the design of the CRESST detectors described in section 2.1.2. The phonon detector is discussed in section 3.4.1 and the scintillation light detector in section 3.4.2. The detector operation is discussed in section 3.4.3. The detector was designed, manufactured and tested in [86], where a detailed discussion on all properties of the detector is given.

3.4.1 Phonon Detector

The low-temperature phonon detector used for all beam times is shown in the left panel of figure 3.14. It was developed specifically to meet the requirements of the neutron scattering facility, which are:

- Sufficiently small to reduce multiple scattering of neutrons in the crystal
- High dynamic range of the detector
- Fast phonon collection to cope with the high count rates[2]

The target crystal is cylindrical in shape with a diameter of $2cm$ and a height of $0.5cm$, it weighs $9.4g$. The number of multiple scatters of neutrons with $10MeV$

[2]CRESST, shielded by massive amounts of rock, is subjected to event rates $< 1Hz$. The low-temperature detector employed at the neutron scattering facility is situated above ground and irradiated by a neutron beam. Rates of $10-20Hz$ are expected here. Typical event rates without the ion beam are $\sim 5Hz$ for the employed detector, which is ~ 30 times smaller than a CRESST detector.

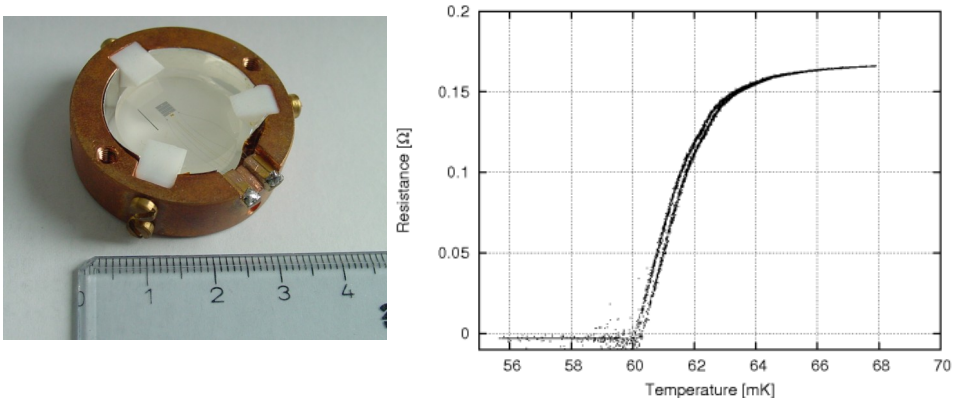

Figure 3.14: The left panel shows a photograph of the phonon detector. The cylindrical $CaWO_4$ crystal has a diameter of $2cm$ and a height of $0.5cm$. An $IrAu$-TES is evaporated directly onto the crystal to measure the energy deposition. For electrical and thermal contact, thin wires are bonded on bond pads evaporated on the crystal. The transition curve is shown on the right. Newer measurements indicate that the thermometer used for this measurement has an offset of $\sim 15mK$ to higher temperatures, placing the transition to the superconducting state at a temperature of $\sim 45mK$. Measurement, figures and detector from [86].

is estimated to be 7% [86]. The TES is a structure of 28 individual iridium-gold TES operated in parallel, each connected to 10 aluminum phonon collector fins that allow for fast phonon collection [86]. The total area for phonon collection is $3.5mm^2$. Thermal contact between the target crystal and the detector holder is realized via thin gold wires bonded on the crystal and the copper holder. The TES is contacted by using aluminum bonds. The transition curve shown on the right panel in figure 3.14 exhibits a transition width of less than $3mK$. While the shown measurement places the transition temperature at $\sim 60mK$, a new measurement indicates a transition temperature of $\sim 45mK$ for this detector. The discrepancy is caused by the incorrect calibration of the employed thermometer of the first measurement.
The high linearity of the transition curve to low temperatures provide the detector with a high dynamic range. The full width at half maximum of the $5.9keV$ line (produced by a ^{55}Fe)-source) is $340eV$, that of the $356keV$ (isotope[133]Ba) is $3.1keV$ [86]. The detector was developed and tested in the scope of [86].

3.4.2 Scintillation Light Detector

The light detector is a rectangular silicon absorber of $525\mu m$ thickness of dimensions $20 \times 20mm^2$. The design and contacting of the transition edge sensor is similar to that of the phonon detector described in section 3.4.1. The detector is shown in the left panel of figure 3.15, the right panel displays the transition curve from the normal to the super-conducting phase. The transition temperature is at $\sim 37mK$ with a width of $\sim 2mK$. The detector was developed and

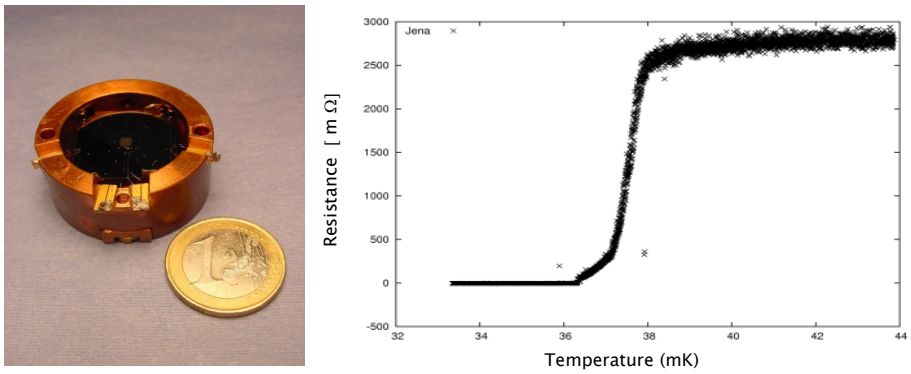

Figure 3.15: Left panel: Photograph of the scintillation light detector. It is made of silicon, the energy readout is realized with a $IrAu$-TES. Right panel: Transition curve of the TES. The phase transition is observed at $37mK$ and has a width of $\sim 2mK$. Measurement, figures and detector from [86].

tested in the scope of [86].

3.4.3 Detector Operation

While the CRESST detectors are stabilized by injecting pulses of known energy directly into the TES and correcting the working point according to the observed response to this energy deposition (see section 2.1.4), a different approach is followed for the low-temperature detector employed at the neutron scattering facility. Here each detector holder is stabilized at a preset temperature (as described in section 3.4.3.1) and the position in the transition curve of the TES is stabilized by using the effect of electrothermal feedback (section 3.4.3.2).

3.4.3.1 Temperature Stabilization

The phonon and the scintillation light detector are each mounted in separate holders, which are thermally decoupled from each other. Each detector holder is equipped with a strongly temperature-dependent resistor R_{Th} for example made of ruthenium oxide (RuO_2), which is used as a thermometer, and a heater with a resistance of $\sim 120\Omega$. The resistance of the thermometer is read out continuously by an AVS47 resistance bridge manufactured by Picowatt [107]. With a heater current through the 120Ω-heater, the temperature of the holder can be adjusted. A proportional-integral-derivative (PID) controller is used to control this heater current. The stabilization at a specific resistance is very reliable, but it has been observed that the resistance readout itself is very susceptible to external noise. The wiring scheme is shown in figure 3.16. For further details see [86].

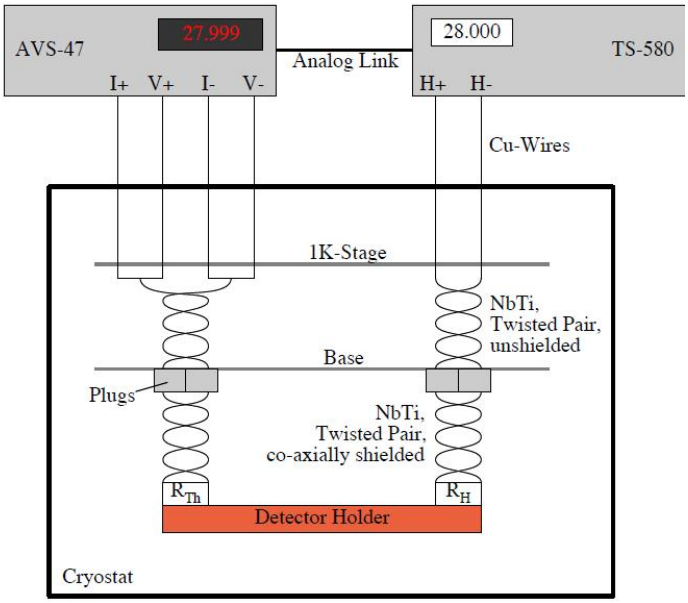

Figure 3.16: Wiring scheme of the temperature stabilization for a detector: Each detector holder is equipped with a thermometer, which is a strongly temperature dependent resistor R_{Th}. R_{Th} is read out by an AVS-47 resistance bridge manufactured by Picowatt by employing a 4-point probe. The measured resistance is transmitted via an analog signal to a Picowatt TS-580A temperature controller, which is a PID controller regulating the current through the heater $R_H \approx 120\Omega$ minimizing the difference between the measured resistance R_{Th} and the target resistance. The different temperature stages, here referred to as $1K$-stage and base (which is $\sim 10mK$), are explained in detail in section 3.5. Figure from [86].

3.4.3.2 Electrothermal Feedback

The SQUID based readout, for which the wiring will be discussed further in sections 3.5.1 and 3.7, requires a detector bias current which produces a magnetic field in the input coil which is then picked up by the SQUID. This is shown schematically in the upper part of figure 3.17. It becomes apparent that the employed wiring scheme has a self-stabilizing effect: If the TES drifts to higher temperatures, the current flow is reduced leading to less heat production in the TES (which results in a net-cooling effect). In the opposite case, the lower resistance leads to a higher current and heats the sensor back to the desired working point. This is illustrated in the lower part of figure 3.17.

3.5 The Cryostat

The detectors are used under similar conditions as in the CRESST experiment, meaning that they are operated at a working temperature of few mK. This temperature can be achieved by commercially available ^{3}He/^{4}He-dilution re-

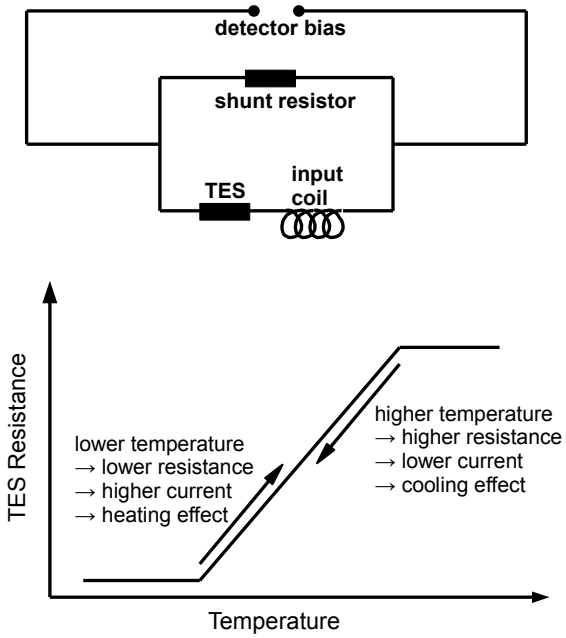

Figure 3.17: Working principle of electrothermal feedback: A constant current (detector bias) flows through a constant shunt resistor, the transition-edge sensor (TES) and the (superconducting) input coil. If an energy deposition changes the resistance of the TES, the resulting increase or decrease of the current over the TES has a stabilizing effect. This also leads to faster pulses, since an energy deposition due to a particle interaction reduces the heating effect of the detector bias since the current flowing through the TES is decreased.

frigerators. The working principle and a detailed description are given in [108]. A *Kelvinox 400* by *Oxford Instruments* [109] is used for this purpose. It has a cooling power of 400 μW at a temperature of $100mK$ and is specified to reach a base temperature of $\sim 10\ mK$ which has been demonstrated in a commissioning run. It has been wired and equipped with two SQUIDs (see section 3.5.1) to read out an installed detector module consisting of a light and a phonon detector. For the cryodetector, different mounting systems were tested (discussed in sections 3.5.2 and 3.5.3). The system was lately updated with the possibility of operating light detectors based on the Neganov-Luke light amplification, which is discussed separately in section 3.6. The cryostat performance after installation of all components is discussed in section 3.5.4.

3.5.1 SQUID Installation

The TES is read out, as in the CRESST setup, with a SQUID (see section 2.1.1). The employed DC SQUIDs of type 'cs blue' manufactured by Supracon AG [110] work at a temperature of $\leq 5\ K$. Since the SQUIDs are operated in a vacuum

and are not equipped with any kind of heat exchanger, the only means of reaching this temperature is by cooling via the wiring. Several modifications that were each tested in separate cooldowns were made to achieve this goal. The general wiring scheme is depicted in figure 3.18, the final wiring and the cryostat are shown in figure 3.19.

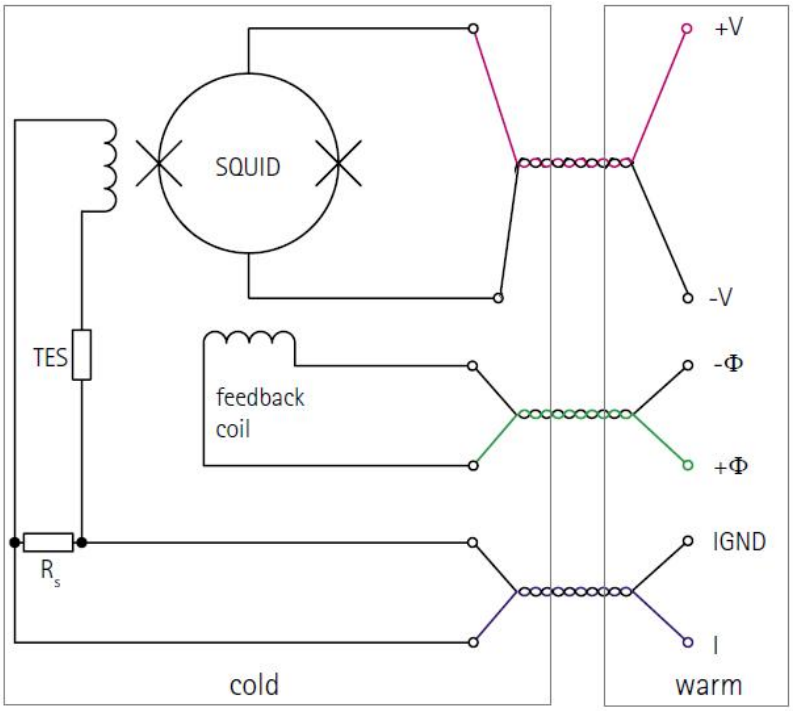

Figure 3.18: General wiring scheme: Wires for the SQUID voltage ($\pm V$), flux ($\pm\Phi$) and the detector bias (I and Gnd) as well as the SQUID heater (not shown in the figure) go down to low temperatures. The SQUID itself is located at the 1K stage, the shunt resistor R_S and the TES are at mK temperatures. Figure from [111].

Twisted-pair $NbTi$ wires with an internal diameter of 0.1 mm in a Cu-Ni matrix with additional shielding are used for the detector bias, the flux, and the SQUID heater. Since these cables have a high resistance at $T \geq 9K$ (they become superconducting at $\sim 9\ K$), the SQUID voltage and current connections consist of twisted-pair copper cables (0.1 mm diameter) to achieve maximum sensitivity.

Since parts of the SQUID remain normal conducting, heat can be produced in them. This proved to be a problem resulting in a warm-up of the SQUID within few hours after the exchange gas was absorbed (see section 3.5.4). To maintain stable working conditions for the SQUIDs, all $NbTi$ wires which in their superconducting state have a very low heat conductance were replaced by copper cables on the last few cm to couple the SQUID more effectively to the 1K-stage of the dilution refrigerator. See the caption of figure 3.19 for further details on the wiring.

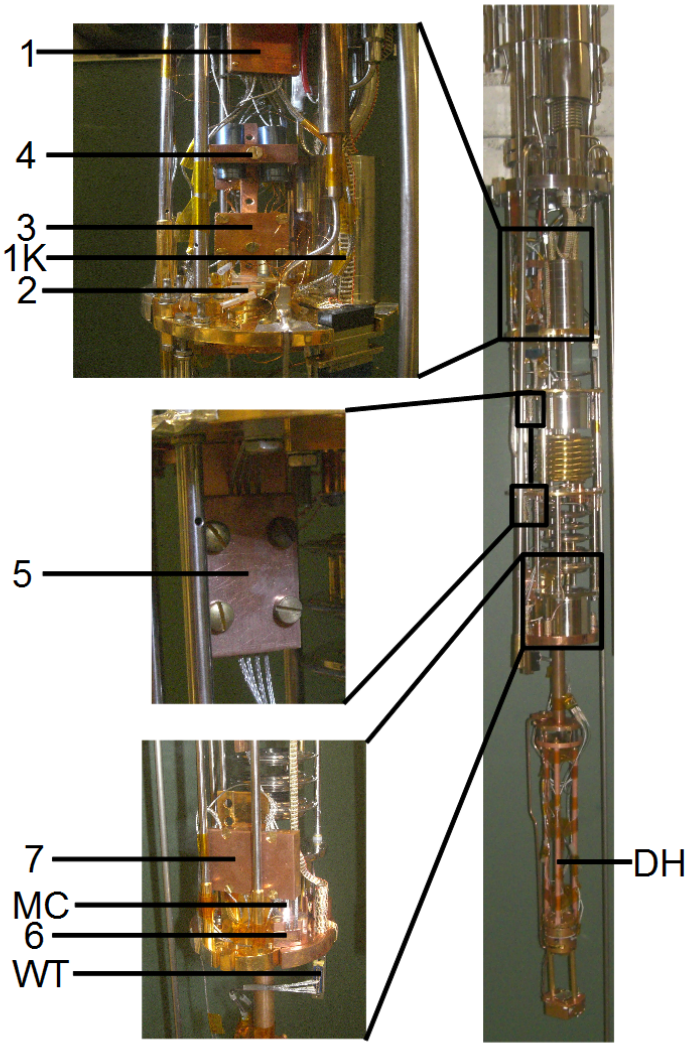

Figure 3.19: Wiring of the cryostat: Twisted-pair NbTi wires (for the SQUID heater, flux and the detector bias, in a Cu-Ni matrix, diameter: 0.1 mm) and twisted pair copper cables (0.1 mm, for the SQUID voltage connection), both with coax shielding, coming from room temperature are coupled to the helium bath at **1**. To cool the SQUIDs, the NbTi wires are exchanged by Cu wires (**2**) and thermally connected via copper clamps and low-temperature varnish at **3** to the 1K-pot (**1K**). The two SQUIDs (**4**) are encapsulated in Nb tubes to be shielded from magnetic fields. Going through two copper clamps (**5**) located at the $\sim$ 700 mK and the $\sim$ 100 mK stages, the cables for the detector bias and from the input coils continue to the mixing chamber (**MC**). They are coupled to the MC by an additional copper clamp (**6**) before they enter the shunt box (**7**) where the shunt resistors (100 $m\Omega$) are located. Together with additional wires for the thermometry (**WT**) they continue to the detector holder (**DH**).

3.5.2 Detector Installation I: First Generation Detector Holder

The design of the cryodetector installation is shown in figure 3.20. The cryodetector has to be positioned in the optical axis of the neutron beam. This is achieved by extending the cryostat with a tripod made of annealed copper. The whole support structure is decoupled from the mixing chamber using sintimid, which has a low thermal conductivity. Each detector is then thermally weakly coupled via copper wires to the mixing chamber and equipped with a ruthenium oxide thermometer and a resistive heater to stabilize the detectors independently (see section 3.4.3.1). The thermal coupling to the mixing chamber is weak enough so that a temperature gradient of $\sim 20\ mK$ does not affect the temperature of the mixing chamber notably. See the caption of figure 3.20 for further details.

3.5.3 Detector Installation II: Light-Weight Holder

Since neutrons scattering in the surroundings of the cryodetector will produce undesired background by inelastic processes (see section 6.1.3.1 for an extensive discussion), the detector installation was exchanged by a new design with reduced mass as seen in figure 3.21 [112]. Here the copper tripod seen in the old setup (figure 3.20) is exchanged by a carbon tube, which has the property of offering high stability together with very little mass. The detector holder itself (seen assembled in the two right panels in figure 3.21) was changed from the massive copper holder to two thermally decoupled copper rings. Each of the rings, which are thermally coupled via thin gold wires bonded on either the phonon or the light detector, is equipped with a thermometer and a heater (as discussed in section 3.4.3.1). The target crystal is held by small clamps connected to the rings. In total, the mass of the detector holder was reduced by a factor of ~ 10.

3.5.4 General Cryostat Performance

The cooldown procedure can be performed completely within 24 hours. The general steps are as follows:

1. pump the internal vacuum chamber (IVC). The IVC contains all parts being cooled below 4.2 K.
2. insert 2-3 cm^3 of gaseous helium into the IVC as exchange gas to ensure cooling of all inner parts.
3. lower the insert into the main bath and fill the main bath with liquid nitrogen. The insert temperature drops to $\sim 80\ K$ within 5-10 hours depending on the quantity of the exchange gas.

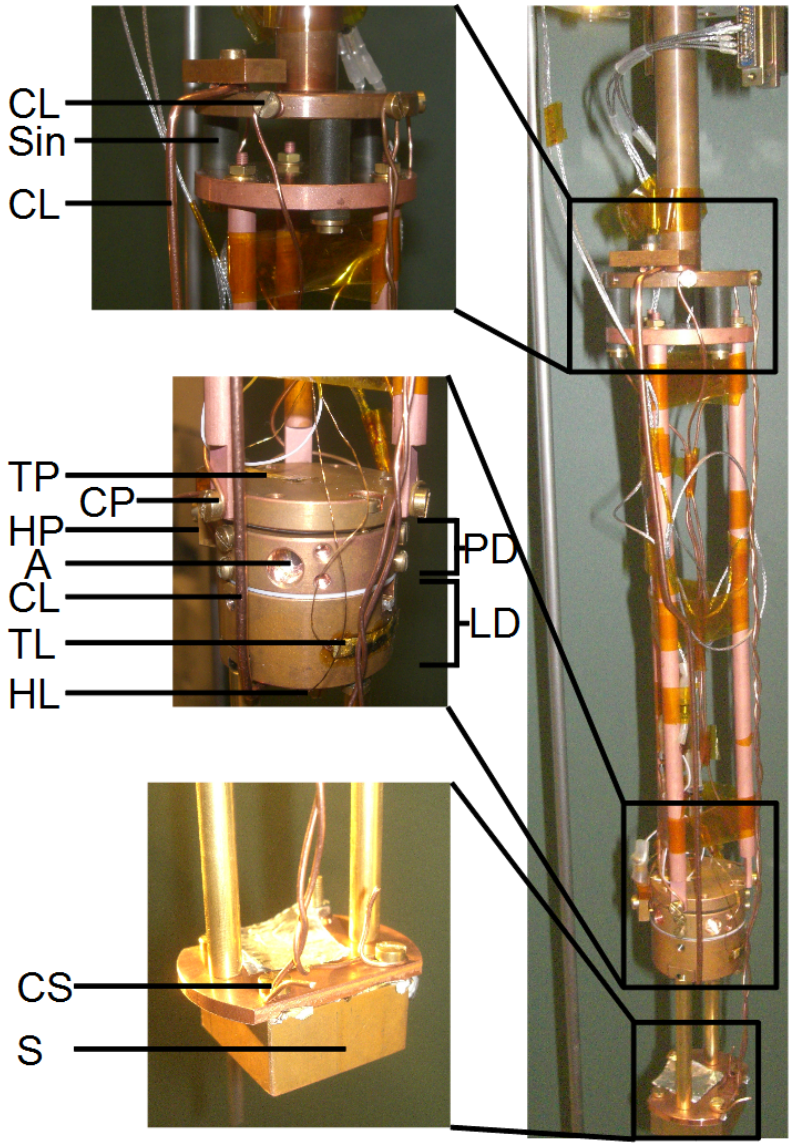

Figure 3.20: Detector holder design I: The phonon detector (**PD**) and the light detector (**LD**) are installed at the end of a tripod. The whole structure is thermally decoupled from the mixing chamber via sintimid (**Sin**). The light detector is coupled weakly to the mixing chamber with a copper wire of 2 mm diameter (**CL**), the phonon detector with three wires each of 0.5 mm diameter (**CP**). Each detector is equipped with a ruthenium oxide thermometer (**TL** for the light channel and **TP** for the phonon channel) and a separate heater (**HL** and **HP**). For calibration purposes, a ^{55}Fe source (**S**) is attached to the detector, thermally coupled to the mixing chamber (**CS**). Additionally, an aperture (**A**) in the crystal holder can be used to calibrate with external low-energetic sources.

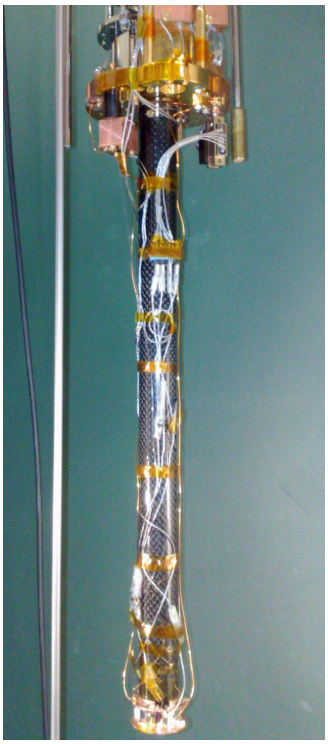

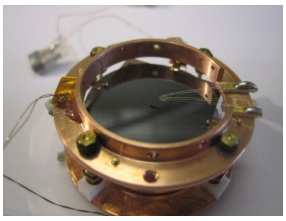

Detector module (top view)

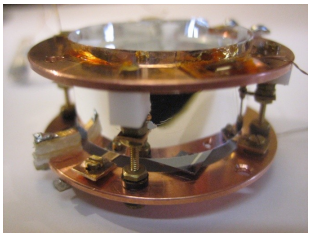

Detector module (side view)

Figure 3.21: Light-weight support structure: The copper tripod seen in figure 3.20 was exchanged by a hollow carbon tube. The detector holder, which was a hollow cylinder of $5mm$ wall thickness previously, was exchanged by two copper rings held with four $1mm$ screws. The top view of the assembled detector module (right panels) shows the light detector and the bond wires used for electrical and thermal contact. The mass of the detector holder was reduced by a factor of ~ 10 to reduce parasitic scattering of neutrons in the direct surroundings of the detector.

4. blow out the liquid nitrogen and fill liquid helium. To keep the exchange gas from being trapped in the sorb (an absorbing material with a large surface), heat the sorb to 30 K for $\sim 5\ h$

5. shut down all heaters and insert the mixture in the cryostat. The mixture condenses in the mixing chamber within $\sim$ 2 hours.

6. start circulating the mixture. A temperature of 20 mK is reached within 2 additional hours.

Figure 3.22 shows the temperature of the mixing chamber in Kelvin versus the time of a cooldown procedure beginning with the circulation process. 20 mK are reached within less than two hours after starting the circulation. The mixing chamber is equipped with an additional heater and can be stabilized at a specified temperature. This is also seen in the figure. An overshoot in temperature can occur if the PI-parameters of the stabilization algorithm are

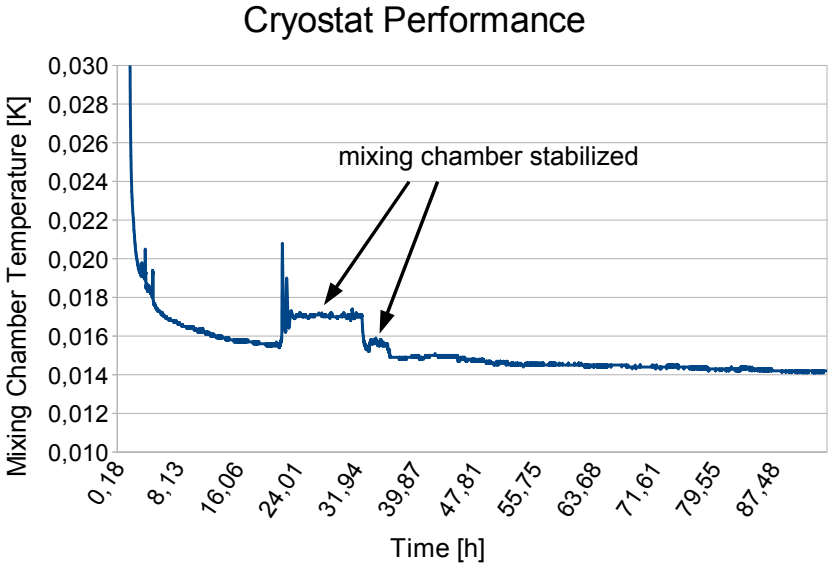

Figure 3.22: Cooldown procedure with all wiring, SQUIDs, and detectors installed: The temperature is shown over time. At the time $t = 0\ h$ circulation of the ^{3}He/^{4}He mixture is started. Within two hours, a temperature of T = 20 mK is reached (where the detectors can be operated). A cooling effect is still visible after ~ 3 days. Comparing the calibration of the mixing chamber thermometer (shown in the figure) against a ^{60}Co nuclear orientation calibration [113] shows that the actual temperature is $\sim 2\ mK$ lower than indicated in the very low-temperature range.

badly tuned. Even after three days the cryostat cools down further. This effect is not of importance for the detectors, since these can be stabilized separately.

3.6 Implementation of Neganov-Luke Light Amplification

Neganov-Luke-light amplification is a technique to greatly increase the signal to noise ratio of an energy deposition registered in the light detector. This technique is discussed extensively in [114] and section 7.3.5. In the scope of [112, 114] and the present work, the cryostat was equipped with the necessary wiring to operate a Neganov-Luke-amplified light detector. Electrical lines for applying a high voltage (up to $200V$) to the detector operated at mK temperatures are required. To sustain the high signal amplification that can be achieved with Neganov-Luke amplification, the detector has to be regenerated regularly to neutralize space charges weakening the external electric field. For this purpose, a LED was installed at the mK stage of the cryostat. The LED is controlled

with a programmable pulser from Rohde and Schwarz [115] ('Am300 Arbitrary Function Generator'). The light produced by the LED is guided via an optical fiber to the detector.

3.7 SQUID Readout

The wiring and installation of the SQUID in the low temperature environment was described in section 3.5.1. At room temperature, the flux locked loop (FLL) stage of the SQUID electronics is installed directly at the cryostat, to avoid additional wiring susceptible to pick-up of electromagnetic noise. In the FLL stage, the signal is amplified. To optimize the trigger threshold, each FLL unit has been equipped with an additional amplifier with adjustable gain. The FLL stages are connected to 'Je-SEF SQUIDcontrol L1' SQUID electronics manufactured by Jena (now Supracon, [110]). Due to the way the SQUIDs are operated, the DC position of the baseline is not constant. This is caused by flux quantum losses, which are discussed in section 4.5.3. They occur when the *slew rate* of the SQUID is exceeded by a fast signal and the compensation of the external magnetic flux by the field produced in the feedback coil fails (see also section 2.1.1). In this setup, pulses which have a significant portion of their signal in the $\sim MHz$ range cause flux quantum losses. This is the case for energy depositions of $\sim 600keV$ and higher. Each flux quantum loss shifts the baseline by $\sim -0.5V$. For this reason, the SQUID electronics are modified and equipped with an adjustable auto reset, which resets the SQUID as soon as the output voltage is outside the range of $\pm 0.5V$, $\pm 1V$, $\pm 2V$, $\pm 5V$ or $\pm 10V$. After a SQUID reset, the DC output is returned to zero. Since the response of the low-temperature detector to an energy deposition of $1MeV$ results in a signal height of several Volts, the highest auto-reset value of $\pm 10V$ is selected.

The analog output signal of the SQUID is of high impedance, while the flash analog to digital converter used to sample the signal (see section 3.8.1.6) has an input stage of $10k\Omega$. For this reason an impedance converter is used. Each SQUID-output signal is divided into two signals, one is connected directly to the Flash-Analog-to-Digital Converter (FADC, see section 3.8.1.6) and the other is AC filtered (filtering time is $\sim 5ms$) to shift the baseline to $0V$ as is required for the triggering process.

3.8 Data Acquisition

A complete data acquisition (DAQ) has been designed in the scope of the present work. The experimental requirements are as follows:

- The time of flight (ToF) for a neutron has to be measured for ~ 40 liquid scintillator cells coupled to PMTs

- Particle identification via pulse shape discrimination in the neutron detector arrays is required
- Pulses in the cryodetector must be sampled with high precision
- Possibility to identify triple coincidences (neutron production, neutron scatter in the central detector, neutron detection in the neutron detector array) is needed
- All parameters (neutron production, timing, pulse shape discrimination) must be monitored constantly in real time

DAQ hardware based on the VME standard has been selected with these requirements in mind. A DAQ software has been written to configure and read out the different modules.

3.8.1 Data Acquisition Hardware

The following modules were selected:

- **VME controller:**
  - v2718 optical link controller from Caen [116]
- **PMT readout (and ToF measurement):**
  - Sis3320 analog digital converter (ADC) from Struck [117]
  - v812 constant fraction discriminator (CFD) from Caen [116]
  - v1190 time to digital converter (TDC) from Caen [116]
- **Cryodetector readout:**
  - Sis3302 ADC from Struck [117]

The wiring is discussed in section 3.8.1.1, the different modules are detailed in sections 3.8.1.2 to 3.8.1.6.

3.8.1.1 Wiring of the VME modules

The wiring scheme is shown in figure 3.23. The anode signals of the up to 40 PMTs is connected to the CFDs and to the Sis3320 ADCs. The CFDs produce logic ECL (Emitter-Coupled Logic) signals, which are fed to the v1190 TDC. The Sis3302 ADC samples the pulses coming from the cryodetector. If a trigger occurs, the trigger is also registered by the TDC. For simplicity, a direct connection between the Sis3302 and the v1190 is shown. This connection is realized via a CFD, to convert the NIM signal to ECL 110 Ω standard. The Sis3302 is triggered internally if the signal exceeds a certain threshold. Since the position of the baseline (the DC output from the SQUID electronic) is not

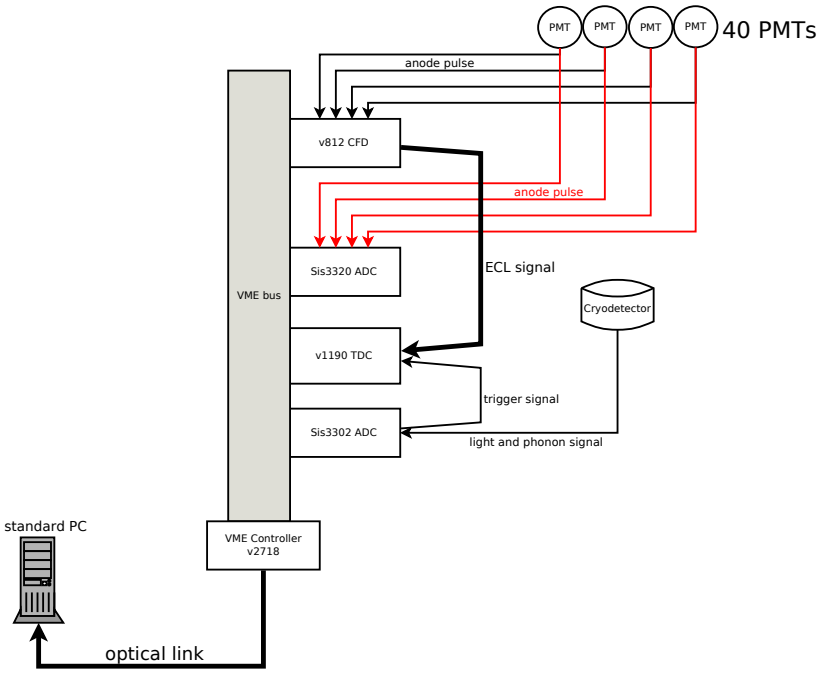

Figure 3.23: Wiring of the different modules. The signal of each PMT is split and supplied to a CFD and a Sis3320 flash ADC. The timing signal given by the CFD is then recorded by the TDC. The cryodetector pulses are recorded by the Sis3302 which is triggered internally. The trigger information is passed on to the TDC to compare it with all other times. The VME modules are configured and read out via the VME bus.

constant (see section 3.7), an AC filter is applied to the pulse before feeding it into the trigger channel. The pulses themselves are recorded without any filter.

3.8.1.2 v2718 VME Controller

A v2718 VME controller manufactured by Caen is used as a VME bus master and to access the VME bus. The v2718 also houses two configurable pulsers and a scaler. It can be controlled by a standard PC equipped with the PCI controller card a2818. The connection between the v2718 and the a2818 is realized through an optical fiber cable. The sustained data transfer rate is up to 70 MByte/s. The two pulsers can be used for time-stamp synchronization between all modules and is of importance to upgrade the TDC to an infinite range, as described in section 3.8.1.4.

The main function of the v2718 is to access all modules connected to the VME

bus for configuration and readout. When a module has accumulated enough[3] data it places an interrupt on the VME bus. The v2718 recognizes the interrupt signal and handles the module accordingly. This is explained in more details at the sections where the specific modules are described.

3.8.1.3 v812 Constant Fraction Discriminators

Constant fraction discriminators (CFDs) are used to determine the exact time of a pulse coming from one of the photomultiplier tubes (PMTs) coupled to the liquid scintillator cells. The CFDs used are of the type v812 and are manufactured by Caen. Each v812 hosts 16 channels with an input impedance of 50 Ω. Output signals are of type ECL, 110 Ω impedance. The output signals are directly inserted in the v1190 TDC. Trigger thresholds and active channels can be configured via the VME bus. Each pair of two channels has the constant fraction time configurable with an on-board jumper[4]. It allows time constants from 1-20 ns.

The v812 modules are also used to convert other logic signals to ECL levels and to feed them to the v1190 TDC.

3.8.1.4 v1190 Time to Digital Converter (TDC)

The typical dynamic range of a time to digital converter (TDC), as used for time of flight (ToF) measurements, is in the range of microseconds. Since the ToF of a particle traveling at more than 5% of the speed of light (which applies to $\sim MeV$ neutrons) is in the range of tens of nanoseconds per meter (or less), the dynamic range of a TDC already exceeds the requirement of a typical ToF measurement by more than two orders of magnitude. For this experiment, this is still not sufficient: Since a cryodetector is a very slow detector with a signal-rise time of several 10 to 100 microseconds, the uncertainty of the trigger alone exceeds the dynamic range of all commercially available TDCs. This enforces two key differences to typical ToF measurements:

1. The dynamic range of the TDC has to be expanded.
2. For data reduction purposes, a TDC is typically operated in a triggered mode. A trigger (for example given by the arrival of a neutron pulse) starts the TDC search logic looking for hits in a user defined search window, selected to meet the time of flight requirements. Due to the long

[3] All modules used have a buffer size allowing to store several thousands of events. Each module is configured to signal the need for data readout when $\sim$ 5 % of its total buffer is filled.

[4] The constant-fraction times can be set in a range of 5-20 ns (in 5 ns steps) and 1-5 ns (in 1 ns steps) depending on the configuration delivered by the manufacturer. Currently, most CFDs are configured for the higher range, lowering the instrumental resolution of the time of flight measurement (the PMTs have a rise time of $\sim 2\ ns$, this means that the CFD is more similar to a rising edge detector in its current configuration).

rise times of the low-temperature detectors, the TDC has to run continuously[5]. This is challenging since the TDC buffer is limited and is quickly filled (within milliseconds) if working in untriggered mode.

The HPTDC (high performance time to digital converter), developed at CERN and in use in particle detectors in LHC experiments (see [118]) is currently the most powerful TDC chip available. It is featured with a VME interface in the Caen v1190. The interface allows to readout and program the HPTDC. The resolution can be set to 100ps, 200ps or 800ps. The dynamic range is $96\mu s$, meaning that every $96\mu s$ its clock rolls over to zero. To avoid ambiguous timestamps (due to the rollover), the rollovers are counted by the DAQ software. For this purpose, it has to be ensured that at least one hit is registered every $96\mu s$. This is achieved by using a pulser housed in the VME controller. See appendix B for details about expanding the full dynamic range.

The data is stored in an unaccessible internal buffer that can hold up to $\sim$ 32000 events. From this buffer, up to 512 events are transferred into a readout buffer. If the events in the readout buffer are read via the VME bus, they are replaced with the next hits stored in the internal buffer, freeing up the memory. This means that new events can be stored while old events are read out, leading to no dead time as long as the maximum of 32000 internally stored events is not exceeded (buffer overflow). Since one channel is reserved for the chopper signal (see section 3.2.1.2) to determine the timing of each neutron bunch, the buffer is quickly filled by this signal[6]. For example, if operated at a chopper frequency of $\sim 300\ kHz$, the buffer is filled within 100 ms. This means that the v1190 has to be read out more than ten times per second *while still handling the readout of all other modules* in the time between. If this fails, not only a dead-time is introduced, but also the rollovers can no longer be counted. Depending on the chopper frequency f, this happens as often as several times per minute ($f \approx 1MHz$) or basically never ($f < 150kHz$). This fault is automatically recognized. The DAQ software forces all other modules to restart and reset their internal clocks to avoid ambiguous timestamps in case of such a buffer overflow (see section 3.8.2.1).

The v1190 only accepts input signals of type ECL/LVDS (Emitter-Coupled Logic/Low-Voltage Differential Signaling) on 110 Ω impedance.

[5]Typically, a neutron pulse is produced every few μs. For general ToF applications, an acceptance window of few tens of ns after the generation of the neutron pulse is sufficient. Since the uncertainty in the trigger of a low-temperature detector exceeds the neutron-pulse periodicity by far, no reasonable coincidence window can be defined.

[6]The chopper is typically operated at a frequency of $100kHz$ to $1MHz$. In comparison, each of the 40 PMTs has a trigger rate of $\sim 100Hz$, leading to a total rate of $4kHz$. Thus the time until the TDC buffer is filled is determined basically only by the chopper rate.

3.8.1.5 Sis3320 Flash Analog to Digital Converters for PMT Readout

Five flash analog to digital converters (FADCs) with eight channels each are used to sample the data of up to 40 PMTs. The FADCs are of the type Sis3320, manufactured by Struck. The sampling rate of the Sis3320 is adjustable from 50 to 250 MHz. The resolution is 12 bit with an input range from 3 to 5 V, the input impedance is 50 Ω. Each input stage is equipped with a 16-bit DAC (Digital to Analog Converter) to shift the input range by a constant offset.

To minimize the size of an event, the firmware of the Sis3320 is designed not to store the full pulse, but only the information needed for pulse-shape discrimination (PSD). In a similar way this is done for a QDC (charge to digital converter), where the charge is integrated over a given time. In the case of the Sis3320, 8 integration gates with length and timing relative to the trigger can be set in units of samples for each channel. Trigger settings can be set individually for all channels. The employed trigger is a finite impulse-response (FIR) trapezoidal trigger. It calculates a smoothed derivative of the pulse and fires when a certain slope is exceeded. Once a trigger fires, all 8 channels are stored in the onbard memory. The memory is 128 MB per channel, divided into two banks. One bank can be read out while data is stored in the other bank, allowing for practically deadtime-less data acquisition.

For all events, the time of the hit is stored. The timing is given in units of the sample clock of each module. They are later compared to the time of each pulse stored in the TDC to combine the PSD information acquired in the ADC with the ToF measured by the TDC.

3.8.1.6 Sis3302 Flash Analog to Digital Converter for the Cryodetector Readout

For cryodetector readout, a Sis3302 (manufactured by Struck) is used. The Sis3302 is an eight channel FADC with an adjustable sampling rate of up to 100 MHz and a resolution of 16 bit. The input range is ± 10 V[7] with an impedance of 10 $k\Omega$, matching the output signal of the SQUID electronics (see section 3.7). Trigger properties can be set individually for each channel, but once the trigger of one channel fires, the data is stored for all channels. The memory per channel is 128 MB. It can be divided in subpages to store several events before data is read out. To mimic slower ADCs, the on-board firmware can average over a adjustable subset of samples. This feature can also be used to reduce noise of the ADC or the signal. During data readout, no new samples can be stored. This means that the data acquisition is not deadtime free, but the large memory allows to store up to 30000 events before readout is pending.

[7] More precisely, the input range is $20V$ total but can be shifted by any offset by adding a constant voltage with the help of a 16-bit DAC (Digital to Analog Converter) that is installed for each ADC channel.

The trigger is a simple threshold trigger, that fires as soon as the signal exceeds a selectable ADC channel. Since the DC output of the SQUID is not constant, the signal is AC filtered for the triggering process as described in section 3.7. This filtered signal is *only* used for the trigger, an unfiltered signal is sampled and saved for the data analysis. For each trigger, the time in units of the sample clock is stored, giving a precise time stamp for every event. The module can be configured and read out via the VME bus.

3.8.2 Data Acquisition Software

The description of the data acquisition (DAQ) software is divided into the back-end (section 3.8.2.1) and the front-end (section 3.8.2.2).

3.8.2.1 Back-End

Previous data acquisition software employed at the neutron scattering facility (or generally at our institute) was based on LabVIEW [119]. It is neither suited for high trigger rates of several kHz (as produced by the chopper and the neutron detectors), nor for the large amounts of data produced by the low-temperature detector module. Consequently, the experimental requirements of the neutron scattering facility could only be met by a fast programming language. For the back-end[8] of the DAQ software, C++ was chosen as the programming language.

After the program call, the DAQ software reads all default values and programs the modules accordingly:

- trigger thresholds (Sis3302, Sis3320, v812)
- trigger modes (Sis3302, Sis3320, v1190)
- active channels (Sis3302, Sis3320, v1190, v812)
- pulser settings for 'TDC-keep-alive' (see appendix B) (v2718)
- DAC settings for offset correction (Sis3302, Sis3320)
- buffer settings (Sis3302, Sis3320, v1190)
- resolution and clock settings (Sis3302, Sis3320, v1190)
- integral gate properties for pulse-shape discrimination (Sis3320)

After that the DAQ software is ready for data-taking. A flow chart illustrating the acquisition cycle is shown in figure 3.24 with a short description given in the figure caption.

[8] The back-end is the part of the program that is not directly visible to the user, whereas the front-end allows the user a limited indirect access to the back-end features.

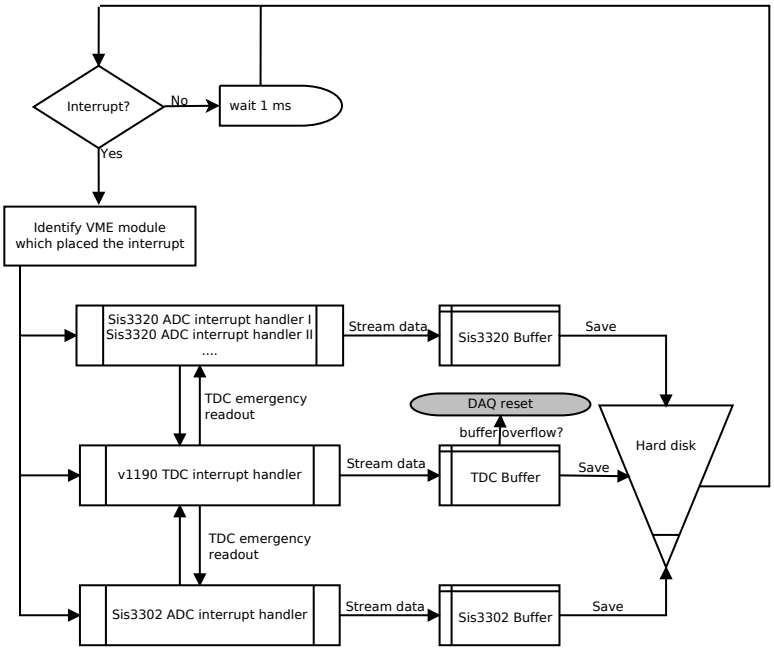

Figure 3.24: The DAQ software in the state of acquisition. It constantly polls for a VME interrupt. An interrupt is set if the internal event buffer of a VME module exceeds a programmable threshold. If the interrupt is registered, the corresponding VME module is read out and the data is streamed to a buffer in the RAM of the controlling PC. In the buffer, basic consistency checks are performed, after that the data is streamed to disk. Since the internal buffer size of the v1190 TDC holds no more than 32000 events (which lasts for $\sim 10 - 100\,ms$ of measurement time), the ADC readouts are segmented and between each segment the v1190 is polled for new data (TDC emergency readout). If, nevertheless, a v1190 buffer overflow is detected, the buffer resets the whole DAQ system to avoid ambiguity of the timestamps. After all data is streamed to disk, the VME bus is polled for the next pending interrupt.

3.8.2.2 Front-End

The graphical user interface, also called front-end, is written utilizing the C++ based Qt libraries developed by Trolltech (now owned by Nokia) [120]. It features:

- live display of all pulses (phonon, light, liquid scintillator)
- live displays of all trigger rates
- live display of all buffer settings
- live double-coincidence analysis and display
- live neutron/gamma discrimination plot
- all pulse shape discrimination parameters can be changed online with direct feedback

- programming of all trigger thresholds
- selection of active channels
- selection of all clock settings and averaging modes
- channel sweep to determine the correct DAC settings for the correct DC value[9]

Generally, all parameters can be changed online and become active immediately. They can even be changed during data taking: if conditions relevant for the analysis are changed, a new measurement is started automatically and the changes are flagged in the saved files. Exemplary screenshots of the DAQ software are shown in figures 3.25 and 3.26. A manual for both the front-end and the back-end is in preparation.

[9]Each of the Struck FADCs (Sis3302 and Sis3320) have their input stage fixed, i.e. it can not be altered after installation. The total range is thus fixed, for example $20V$ for the Sis3302. The relative range is selected by adding a DC voltage internally (before the actual sampling process) to the input signal. Each FADC channel has a 16-bit DAC (digital to analog converter) installed for this purpose on the VME board. All DAC values can be run through automatically to find the DAC value required for the desired relative range, e.g. $\pm 10V$ for the Sis3302.

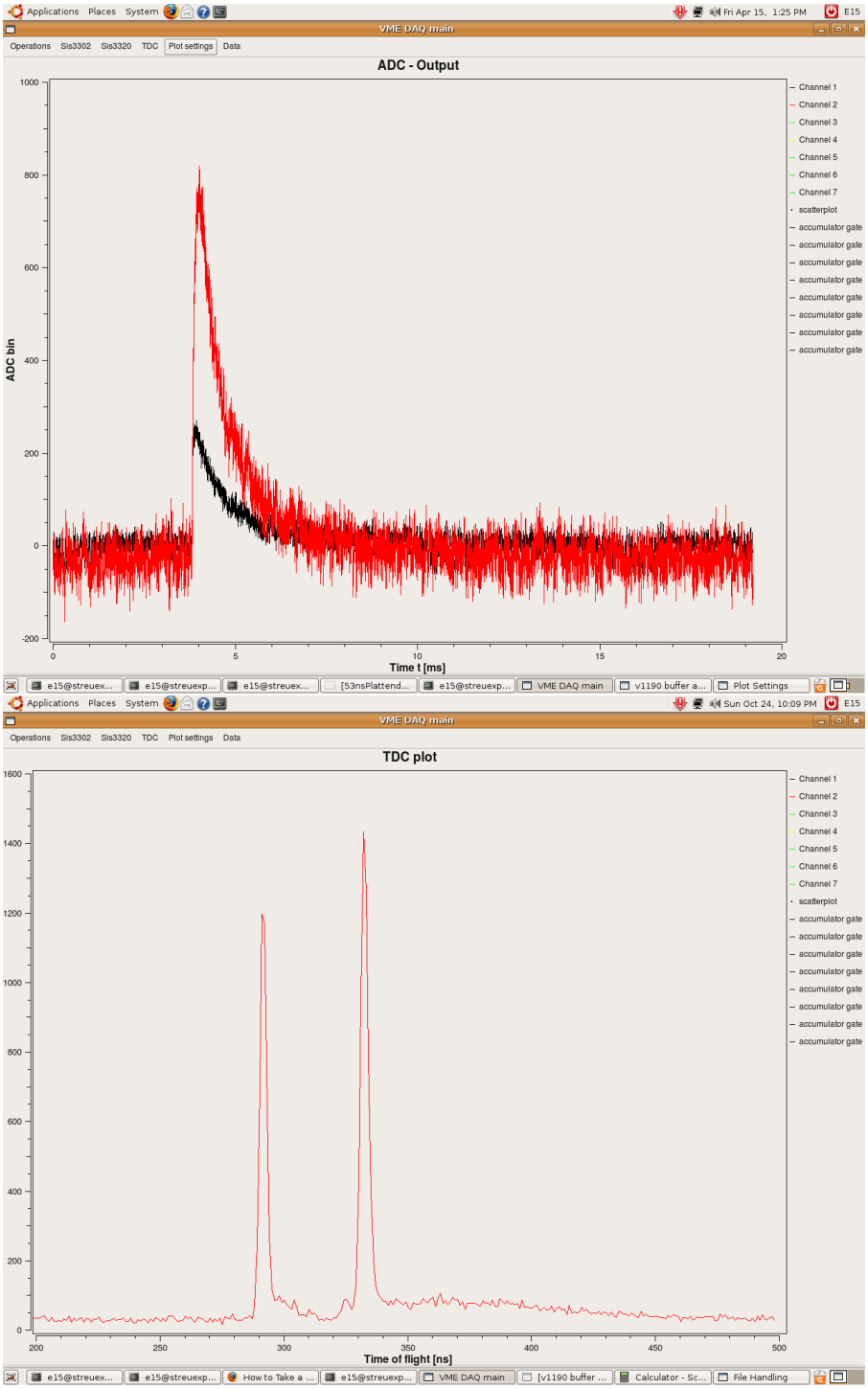

Figure 3.25: Exemplary screenshots of the data acquisition software: The first panel displays a live phonon and scintillation light pulse and the second a live time of flight measurement showing a gamma and a neutron peak.

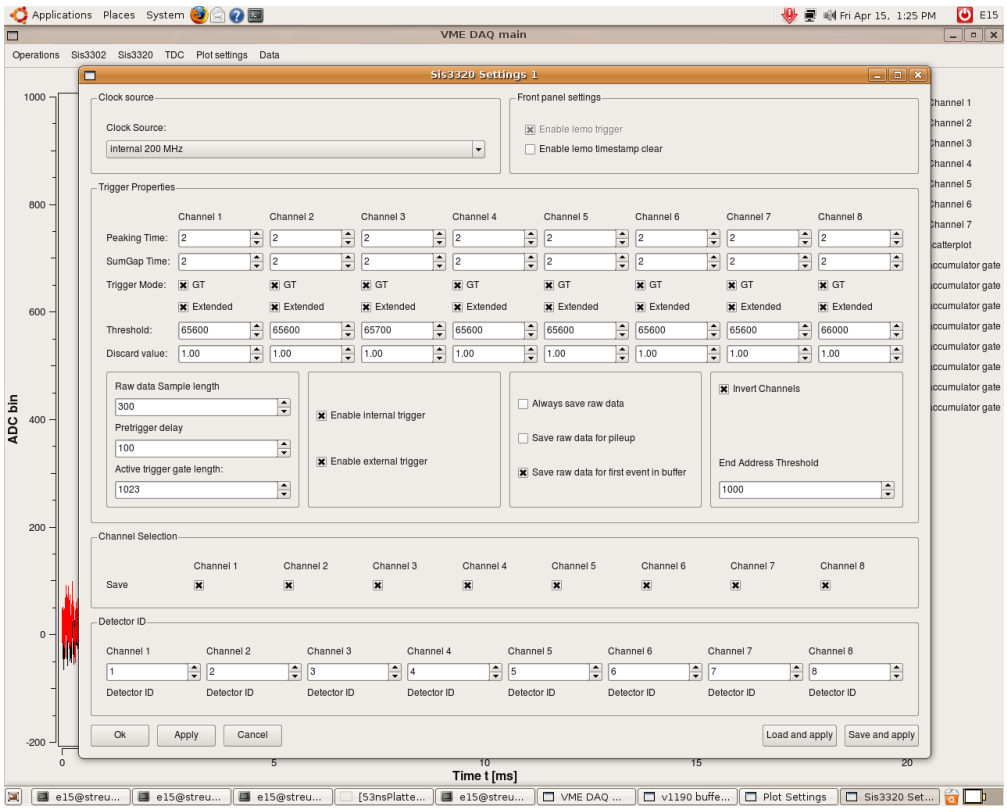

Figure 3.26: Graphical user interface to adjust the trigger and acquisition settings for one Sis3320 FADC.

Chapter 4

Data Analysis

After acquisition, all data (see section 4.1) is streamed to disk for the offline analysis. To handle the data analysis, a complete toolset was written in Matlab [121]. It can be broken down into three branches, as discussed in section 4.2. The three branches are combined by synchronizing the absolute times of the different modules, which is done offline (section 4.3). The analysis tools for the events recorded in the liquid scintillator array are presented in section 4.4, the vast branch for the treatment of the data recorded from the low-temperature detector module is detailed in section 4.5.

4.1 Data Organization

Due to the large amount of data from all modules and the complexity of the individual analysis steps, no online analysis is possible with the limited computational power available. Instead all data is streamed directly to disk where it is saved for offline analysis. Each type of module (the v1190 TDC, the Sis3320 FADCs and the Sis3302 FADC) streams data in its own file(s) with a given format. Details on data organization are found in appendix C.1.

4.2 Data Analysis Overview

The quenching factor is determined by events detected in a threefold coincidence, since for these events all kinematic parameters are determined and the recoiling nucleus is known independently of the resolution of the scintillation light detector. The three coincidence signals are:

1. Neutron production, given by the chopper signal
2. Energy deposition in the central cryogenic detector
3. Neutron detection in the neutron detector array

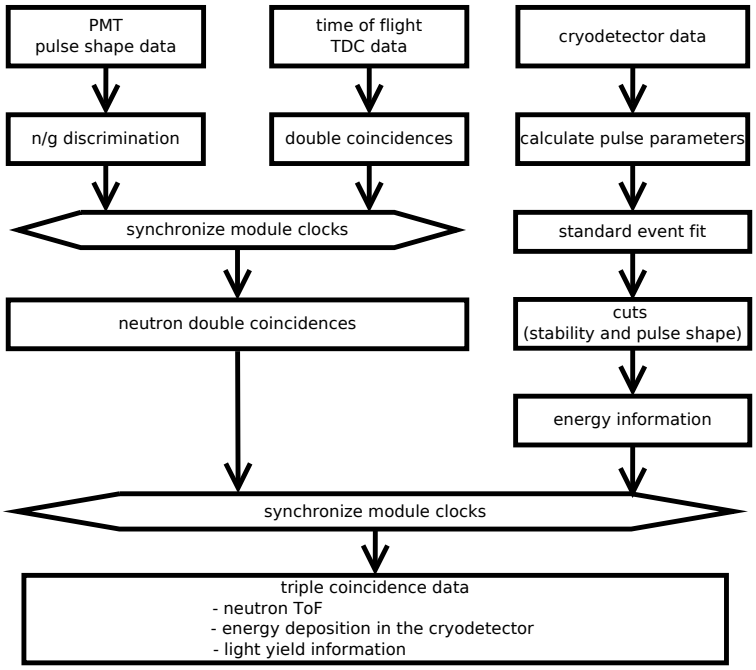

Figure 4.1: Data analysis overview. The different data analysis steps are explained in detail in the text.

This coincidence condition is checked offline. During the beam time, all data is streamed to disk, all parameters necessary for the offline analysis are saved. An overview over the analysis process is shown in figure 4.1. The data analysis can be broken down into three branches: the analysis of the pulse shape data extracted from the scintillation light pulses of the neutron detectors, the timing information giving the time of flight and coincidence data, and the data analysis of the scintillation light and heat (phonons) pulses from the cryogenic detector module.
First, the two branches dealing with the PMT data (i.e. pulse shape parameters and time of flight measurement) are combined to extract all double coincidences of neutron production and subsequent detection. Since the resolution of the timing information in the PMT is $\sim 3\,ns$ and the typical time of flight of a neutron in the setup is $\sim 30\,ns$ and the neutrons can be discriminated against gammas reliably by their pulse shape (see section 3.3.1), this process identifies scattered neutrons very well.
For the cryodetector data, consisting of the sampled data of the light and phonon channel, first the pulse parameters like amplitude, noise and pileup are extracted. The pulses are then fitted by a standard event, allowing to correct for pulse shape distortions caused by non-linearity of the transition edge sensor. Furthermore, a drift correction is applied, correcting small-scale working point drifts of the cryodetector caused by electromagnetic noise and temperature fluctuations in the cryogenic system. Stability and pulse shape cuts are applied before the energy information of each channel is obtained by comparing

the pulse heights with calibration data. The following sections will discuss all analysis steps in details.

4.3 Synchronizing the Module Clocks

For each event sampled by one of the FADCs, a timestamp is saved in the corresponding VME module. The timestamp is derived from the sampling clock of each module, this means that the clock is given in units of FADC cycles (i.e. in units of $10ns$ for the $100\,MHz$ Sis3302 FADC and in units of $5\,ns$ for the $200\,MHz$ Sis3320 FADC). The timestamp is the time of the trigger of the FADC. Neither the accuracy of the clock itself nor the precision of the trigger process[1] is suited to extract the time of flight data, which necessitates the use of a separate time to digital converter (TDC). The timing information of a pulse can be extracted with sufficient precision using the constant fraction technique and the v1190 TDC which handles the timing information supplied by the CFDs (constant fraction discriminators) and runs with a resolution of $200\,ps$. This means that the timing information is extracted and saved separately from the pulse shape information, which makes it necessary to make a non-ambiguous connection between a hit recorded in the TDC and a hit recorded in the ADC. The timestamps of each ADC hit is used to make this connection. Both this timestamp and a hit in the TDC is given in absolute units and not relative to the chopper signal (as would be common for traditional start-stop TDCs which measure the time difference between two signals).

The sampling clocks of the different VME modules run on different frequencies, be it because they are of different types or because of the typical deviation of a few percent that is to be expected even for clocks of the same type. The TDC runs on a 40 MHz clock with internal clock multiplication (resulting in a clock frequency of up to $10\,GHz$) while the Sis3320 and Sis3302 run at 200 MHz or a maximum of 100 MHz, respectively. In principle, there are two different ways to synchronize the clocks:

- The clocks can be synchronized by supplying an external clock signal to each VME module. To achieve this a clock with phase locked frequencies of 200 MHz (Sis3320) and 40 MHz (v1190 TDC) and the desired sample clock for the Sis3302 (maximum of 100 MHz) is needed. The advantage of this technique is that it is very easy to handle in the subsequent offline analysis. The disadvantage is the missing flexibility of the clock frequency supplied to the Sis3302 ADC.
- The clocks can also be synchronized later in offline analysis. This requires a more complex analysis algorithm but allows for maximum flexibility during data taking.

[1] The trigger of the Sis3320 FADC is based on a smoothed derivative of the pulse. If the trigger condition (i.e. exceeding a certain slope) is met, the data is saved. This trigger jitters by ± 1 sample, which equals $\pm 5\,ns$ in addition to the general resolution of $5ns$ given by the (for time-of-flight applications) slow sampling clock.

For the present work, the second option was chosen. All clocks run at their own speed, with the clock setting of the Sis3302 free to be set by the user. This makes it necessary to synchronize the clocks after data taking. All clocks will be synchronized relative to the v1190 TDC, since due to its number of channels it can supply timestamps to 64 detectors.

The clocks typically deviate on the level of 1%. This means that after a measurement time of 1 minute the typical offset between two clocks is of the order of $\sim 10 - 100\ ms$. Typical trigger rates of $\sim 100\,Hz$ place two hits closer in time than this deviation. Since the trigger rates are dominated not by the periodic neutron bunches but by pulses from natural radioactivity occurring in a random pattern, the synchronization can be achieved by a one-dimensional pattern-recognition algorithm developed in the scope of the present work and described in appendix C.3.

4.4 Double Coincidence Analysis

The double coincidence analysis is the combination of the analyzed pulse shape data (section 4.4.1) given by the Sis3320 ADC and the time-of-flight data (see section 4.4.2) given by the TDC. The double coincidence is between the neutron production that can be related to the chopper signal and the neutron detection in the neutron detector arrays. After the energy deposition in the cryogenic detector module is known (which requires the full triple-coincidence analysis to which chapter 6 is dedicated), the exact incident neutron energy can be calculated as shown in section 4.4.3.

4.4.1 Liquid Scintillator Pulse Shape Analysis

The type of interaction in the liquid scintillator can be identified by the analysis of the pulse shape, as described in section 3.3.1. In principal, the Sis3320 offers to configure up to eight integration gates; for n/γ-discrimination the use of three gates as depicted in figure 4.2 is sufficient. These three gates are:

- The baseline integration used to determine the DC offset, i.e. the zero value of the ADC
- A short gate of typically ~ 5 samples (equivalent to $\sim 25\,ns$ integration time) over the fast decay component of the scintillation light
- A long integration gate of ~ 60 samples, equaling to an integration time of $\sim 300\,ns$ over the whole pulse

Subtracting the DC offset as derived from the baseline gate and plotting the integrated ADC values in the short gate versus the long gate results in the distribution shown on the top panel of figure 4.3. This measurement was taken

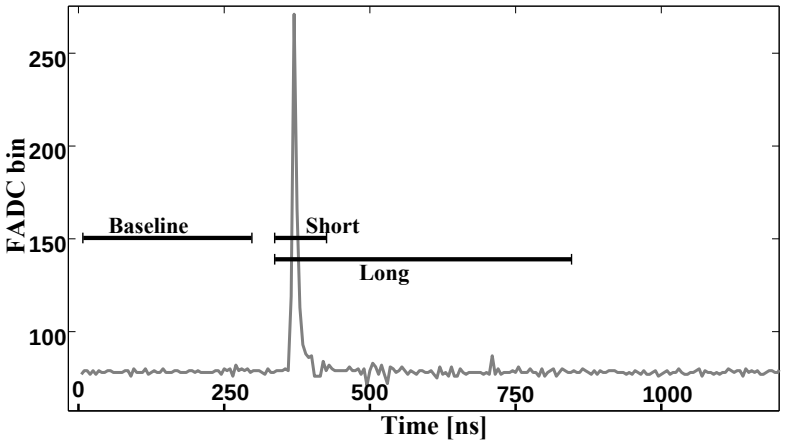

Figure 4.2: A scintillation light pulse of a neutron detector as sampled by the Sis3320 FADC. Usually not the whole pulse is saved, but the integrated sample values of three integration gates: a baseline gate to determine the DC offset and a long and a short gate over the pulse itself. The integration gates are defined relative to the trigger.

in the presence of the neutron beam. The longer time constant is amplified in the case of nuclear recoils, as induced by neutrons. The events with this enhanced delayed scintillation light emission show up in the lower branch, since the delayed emission is detected by the long integration gate. The ratio of the short/long integration gate compared to only the short gate, as seen in the lower panel of figure 4.3, allows to effectively select the nuclear recoils. The analysis software offers a set of tools to apply the n/γ cut graphically. A comparison with a gamma calibration to increase the cut efficiency is possible as well as a preselection of neutrons based on the time of flight parameters. The cut coordinates in the ratio vs the short-gate plane defining the neutron cut for each of the detectors is saved and applied automatically for all data sets.

4.4.2 Time of Flight Analysis

The 64 channel v1190 TDC records all hits in the liquid scintillator (referred to as PMT hits) as well as all chopper signals defining the time of the neutron production[2]. For this purpose, 40 TDC channels are reserved for the up to 40 PMTs used for the neutron detector arrays, an additional channel is connected to the chopper of the tandem accelerator. The typical trigger rate of a PMT in the experimental setup is $\sim 100\,Hz$ (dominated by dark noise and natural radioactivity), while the typical chopper rate is $> 50\,kHz$. Consequently, more than 90% of the TDC buffer is filled by chopper signals. The time of flight analysis is a two-step process:

[2]As will be seen below, there is an offset between the neutron production and the chopper signal.

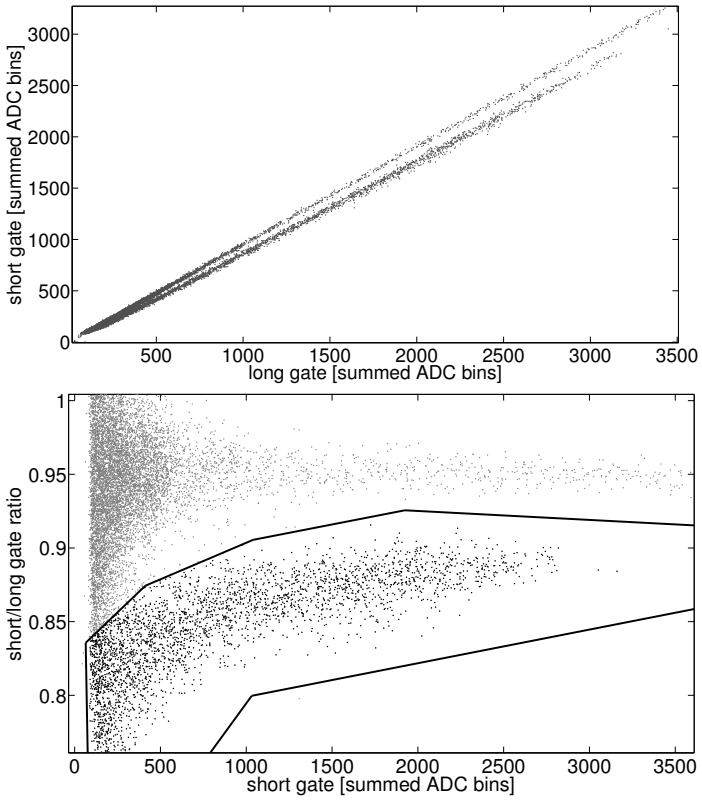

Figure 4.3: The top panel shows the short gate plotted versus the long gate (after baseline subtraction) in the presence of the neutron beam. The lower band comes from nuclear recoils in the liquid scintillator, having an enhanced delayed emission visible in the long gate. This is better visualized in the lower panel, where the ratio of the two gates has been plotted versus the short gate. The analysis software allows to apply the neutron cut graphically, as seen in the lower panel.

1. The TDC data for all 40 PMTs is selected. For each PMT datum the nearest chopper pulse in time is selected. Since the chopper rate is $> 50\,kHz$, two beam bunches are placed $20\mu s$ apart. Consequently, the time difference between a PMT datum and the nearest chopper pulse can not exceed $10\mu s$.

2. The connection between a recorded hit in the TDC and the corresponding hit in the ADC is made by comparing the module clocks as described in section 4.3.

Since the TDC only saves timestamps, it is only after step 2 that the time-of-flight is linked to an energy deposition. The combined TDC/FADC data is shown in figure 4.4. The energy deposition[3] is given in units of summed

[3]Figure 4.4 shows that the maximum visible scintillation light resulting from energy deposition of gammas produced by the ^{11}B beam is lower than the scintillation light output produced by neutrons. This seems to contradict the data shown in figure 4.3, where the output of scintillation light from gamma interactions is higher. The reason for this is that in figure 4.3 all electron recoil events are included, not only the ones caused by the ^{11}B beam. They are also visible in figure 4.4 but are equally distributed over the whole area.

ADC bins sampled in the short integration gate. The first distribution belongs

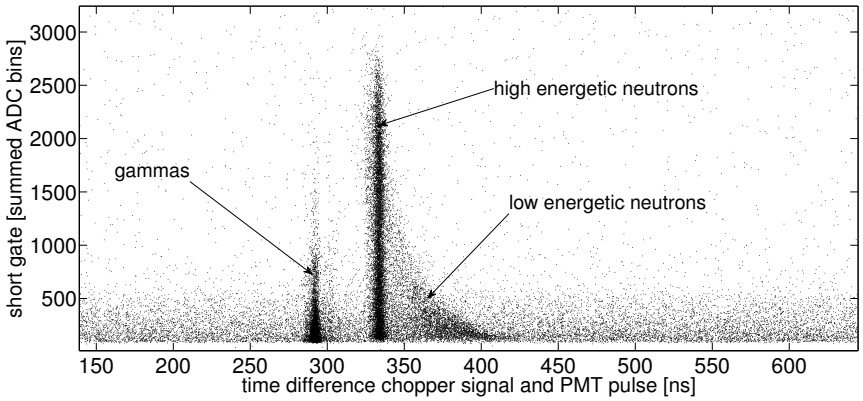

Figure 4.4: The amount of scintillation light (given by the short-gate integral) plotted against the time difference between the chopper signal and the time of the energy deposition. The position of the gammas allows to determine the zero-time for the ToF measurement. The zero time is strongly dependent on the buncher parameters and has to be treated accordingly for different measurements.

to the gammas, that travel at the speed of light and deposit their energy few ns after the ^{11}B-beam hits the hydrogen cell. The second distribution arriving $\sim 40\,ns$ later belongs to the fast neutrons that can be considered monoenergetic. Neutrons with lower energies are also produced, they arrive later and produce less scintillation light. As can be seen, the buncher signal has an offset of $\sim 280\,ns$ to the time of the neutron production. This offset is strongly dependent on the buncher and chopper timings and can be as high as several μs. It can be corrected for by fitting the position of the gamma peak and subtracting the ToF of the gammas, which is known since the distance of each neutron detector from the hydrogen cell is measured. After this ToF-calibration, the ToF of each event is known.

The maximal amount of scintillation light visible in the neutron peak (figure 4.4) is dependent on the neutron energy and is due to the maximal energy transfer of the neutron onto a proton in the liquid scintillator[4]. This allows to utilize the neutron scattering facility to characterize the response of liquid scintillators to nuclear recoils. By dedicating one FADC and one TDC channel to these measurements, they can be performed simultaneously to the quenching factor measurements of the low-temperature detector material during each scheduled beam time campaign. Employing the data acquisition and analysis tools developed in the scope of the present work, the proton quenching factor for the liquid scintillator used in the Double CHOOZ [122] has been obtained [123]. For the investigation of further liquid scintillators, for example used in the LENA

[4]In the center of mass frame of the incoming neutron and the interacting proton in the liquid scintillator the condition for the maximal energy transfer is backscattering. In the laboratory frame, the neutron can be considered to be at rest after the scattering process while the proton carries all kinetic energy.

(Low Energy Neutrino Astronomy [124]) experiment, further measurements are planned [125].

Binning the events dependent on their detection time and plotting the frequency in a histogram yields the plot shown in figure 4.5. Here the data is

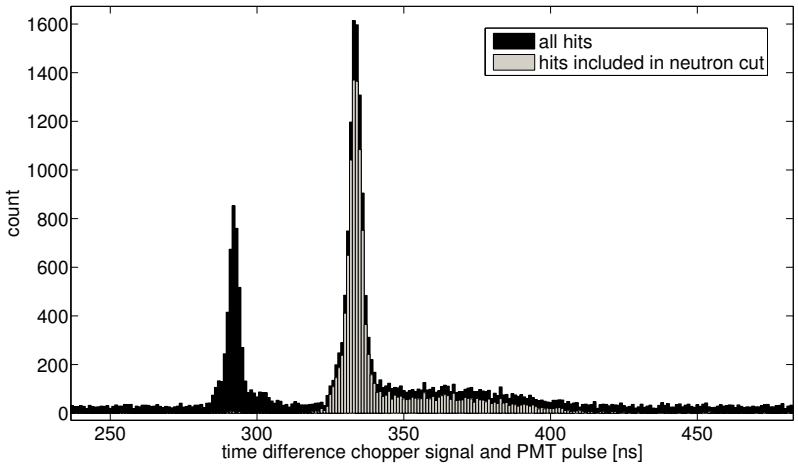

Figure 4.5: The data shown in figure 4.4 binned in a histogram with the neutron cut applied. The pulse shape discrimination identifies the neutrons in the second peak.

shown combined with the pulse shape discrimination discussed in the previous section, giving two distinct distributions: one from electron recoils (gammas), and one from nuclear recoils (neutrons). Gammas are expected mainly in the first peak, while neutrons are expected in the second. A contribution of gammas is expected to the neutron peak since some neutrons produce gammas in inelastic processes in direct vicinity to the neutron detectors. In the gamma peak, 0.27% of all events are misidentified as neutrons. The high efficiency of the neutron cut is important to reduce the number of wrongly identified events leading to accidental coincidences.

4.4.3 Precise Determination of the Incident Neutron Energy

The time of flight of a neutron with a kinetic energy of $10MeV$ is of the order of $\sim 50ns$ for the typical distance of $1.5m$ used in the scattering facility. The timing resolution of the cryogenic detector module is of the order of few μs, as will be shown in section 6.1.1 based on hadronic shower data. To identify the events forming a threefold coincidence, in a first step the neutrons detected in one of the neutron detector arrays are tagged based on their pulse shape.

They are then matched to the event nearest in time in the cryogenic detector module and accepted as a candidate for the threefold coincidence. After the time of flight calibration described in section 4.4.2, the real ToF of each neutron is known.

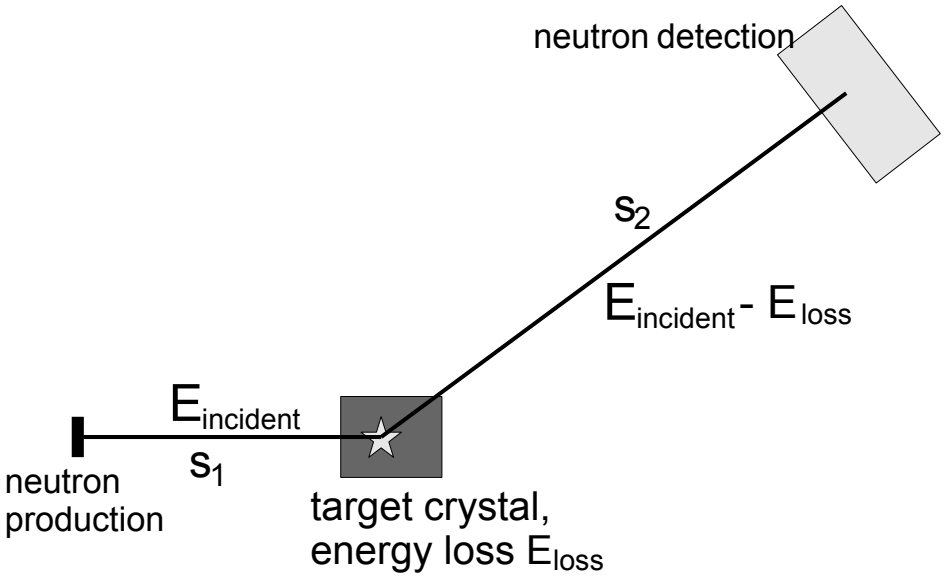

Figure 4.6: Calculation of the incident neutron energy $E_{incident}$: The measured quantities are the energy loss E_{loss} in the cryogenic detector and the time between the neutron production and the neutron detection, which is the time of flight for $s_1 + s_2$. The path length between the neutron production and the cryogenic detector module, s_1, and the distance between cryogenic detector and the neutron detector array, s_2, are known for each neutron detector. The incident neutron energy $E_{incident}$ is calculated to match the measured energy loss and the flight times corresponding to s_1 and s_2.

Figure 4.6 shows a diagram indicating the measured quantities that allow the calculation of the incident neutron energy $E_{incident}$. The measured time of flight is the time between the neutron production and detection. The total path length is given by $s_1 + s_2$. The neutron has the energy $E_{incident}$ for the path s_1. Assumung that the total energy loss is detected in the cryogenic detector module, the neutron energy for the path s_2 is $E_{incident} - E_{loss}$.

The total time of flight, measured as T_{total}, is thus given by

$$T_{total} = T_1 + T_2 \tag{4.1}$$

$$= \frac{s_1}{v_1} + \frac{s_2}{v_2} \tag{4.2}$$

Here T_1 and T_2 is the ToF for s_1 and s_2, respectively, and v_1 and v_2 are the corresponding velocities. From the formula for the kinetic energy,

$$E_{kin} = m_0 c^2 \left(\frac{1}{\sqrt{1 - (v/c)^2}} - 1 \right) \tag{4.3}$$

follows

$$v = c \sqrt{1 - \frac{m_0 c^2}{m_0 c^2 + E_{kin}}} \tag{4.4}$$

Using equations 4.4, 4.2 gives

$$T_{total} = \frac{s_1}{c\sqrt{1 - \frac{m_0c^2}{m_0c^2+E_{incident}}}} + \frac{s_2}{c\sqrt{1 - \frac{m_0c^2}{m_0c^2+E_{incident}-E_{loss}}}} \tag{4.5}$$

with m_0 being the rest mass of the neutron. Equation 4.5 now contains only the measured quantities T_{total}, s_1, s_2, and E_{loss}. The incident neutron energy $E_{incident}$ is determined by varying this quantity until it matches the measured total ToF, T_{total}. The calculation is only precise as long as the total energy deposited in the cryogenic detector E_{loss} is measured. But the influence of E_{loss} on the calculated neutron energy is generally low, since the energy loss in the scattering process is low compared to the total neutron energy.

The error of the energy determination is mainly dominated by uncertainties in the time of flight measurement (which is $\sim 2ns$) and the uncertainties in the scattering angle and the distances s_1 and s_2 due to the finite size of the hydrogen cell and a neutron detector in the detector array.

4.5 Analysis of the Low-Temperature Detector Data

The cryogenic detector consists of a phonon and a light detector in a modular design, see section 3.4 for details. If an energy deposition in one of the channels exceeds the trigger threshold, the full pulse is sampled for a duration of $\sim 20\,ms$ and written to disk for both the phonon and the light channels. An event with

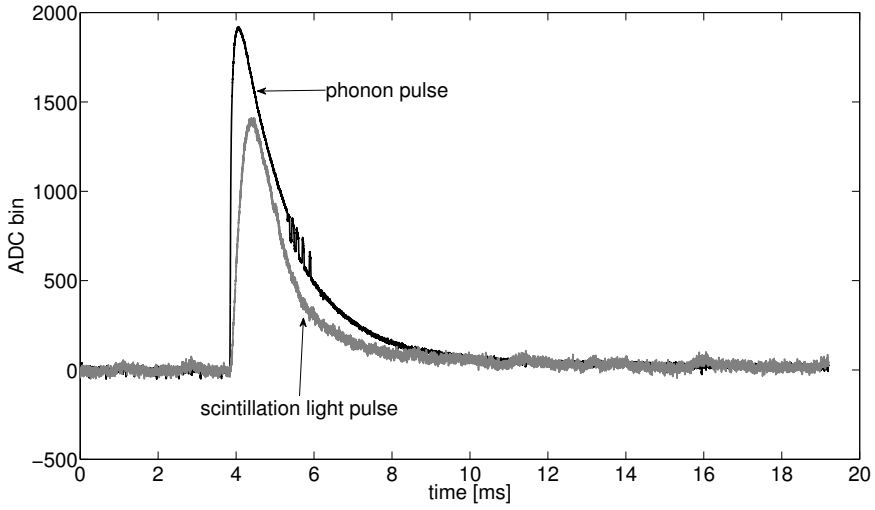

Figure 4.7: Scintillation light and phonon (heat) pulse in the cryogenic detector module. The ripples in the falling edge of the phonon pulse are an artifact of the TES.

an energy deposition of $\sim 150\,keV$ is shown in figure 4.7. About $4\,ms$ of data are read out before the trigger is registered. This pretrigger information allows

to calculate the noise and the DC offset of this pulse. For figure 4.7, the DC offset has been corrected using this pretrigger information. The DC output of the SQUID electronic is not constant but can be within the whole range of $\pm 10\,V$ (see section 3.7).

The pulse shown in figure 4.7 can be considered ideal in the sense that no distortion[5] is visible. This is true for $\sim 75\%$ of all cryogenic pulses recorded during a beam time, while the other $\sim 25\%$ suffer either from pileup or SQUID resets. All low-temperature-detector events recorded are treated in a vast data analysis pipeline that was developed in the scope of the present work. The individual steps are detailed in sections 4.5.1 to 4.5.9. Also featured in the data analysis pipeline are several algorithms allowing to reconstruct the energy deposition of distorted pulses with very high efficiency.

4.5.1 Calculation of all Pulse Parameters

For all subsequent analysis steps, a rough characterization of each cryogenic pulse is required. Also identified within this step are faults like missing ADC data and pileup. This is done independently for both the phonon and the light channel. A $\sim 20\,ms$ trace of a pulse is shown in figure 4.8, here with sample number on the x-axis since the annotated features are also identified in units of samples.

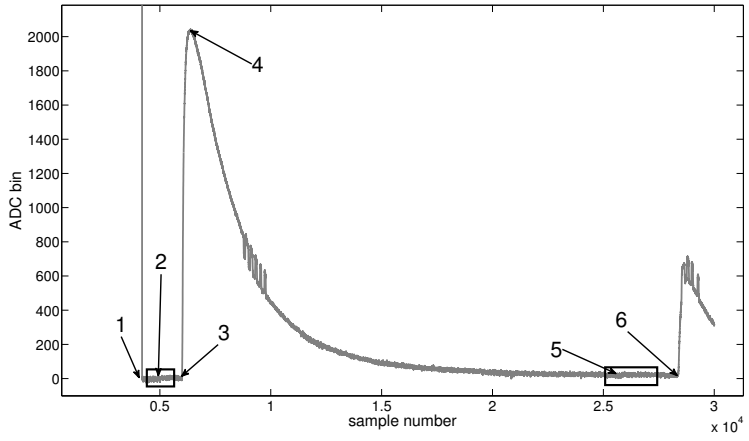

Figure 4.8: A pulse recorded in the phonon channel of the cryogenic detector module showing all features that are identified by the algorithm determining basic pulse shape properties. These are the begin of the pretrigger information **(1)**, which is only in rare cases (as the one shown) different from 0, the properties of the baseline **(2)**, the pulse onset **(3)**, the pulse height **(4)**, the properties of the right baseline **(5)** and the begin of a pileup pulse **(6)** if one occurred in the time recorded by the FADC after the triggering process. See the text for further details.

[5]Typical distortions include missing pretrigger data, pileup and flux quantum losses. All these cases are discussed in detail in the following sections.

The automated recognition of all important pulse features includes the calculation of the following parameters, as numbered in figure 4.8:

- **(1) begin of pretrigger information** The use of a flash ADC allows to acquire pretrigger information, i.e. data samples recorded by the FADC before a trigger condition was fulfilled. The amount of pretrigger samples are defined by the user and can exceed the actual amount of data sampled before the trigger fired. If for example 1000 data points were sampled since the last page flip[6] and a new trigger occurs but a total of 6000 data samples are read out prior to the trigger (as is the case in figure 4.8), the first $\sim$ 5000 samples will contain random numbers or data from a previous pulse already read out. This is recognized by the data analysis and flagged accordingly. In all subsequent analysis steps, only samples after the begin of the actual data are handled.

- **(2) left baseline properties** The left baseline is mainly used to determine the DC offset, which can vary between $-10V$ and $+10V$, and to characterize the noise. In figure 4.8 this DC offset is already subtracted so the baseline is shown at ADC bin $\sim$ 0. Calculated baseline parameters are the position and the standard deviation as well as the end of the baseline information (which is shortly before the rising edge of the pulse begins).

- **(3) onset** Since the hardware trigger is based on a filtered pulse exceeding a certain threshold, the actual pulse onset defined as the first indication of an energy deposition occurs some tens of μs before the trigger fires. The pulse rises relatively slow compared to a liquid scintillator pulse and fulfills the trigger condition after $\sim 50 - 500\,\mu s$. The onset is of particular importance since it gives the timing information for the triple coincidence. The technique to determine the onset is described in further detail in section 4.5.2.

- **(4) peak position and amplitude** The peak position is the point where the pulse (and not a possibly larger pileup pulse) reaches its maximum. The amplitude is the difference between the height of the peak position and the distance to the right baseline. The right baseline is chosen since the distance to the left baseline gives a wrong result if a flux quantum loss occurs in the SQUID electronics (see section 4.5.3).

- **(5) properties of the right baseline** The last $\sim 2\,ms$ of samples before the end of the sample length (or a pileup pulse) is designated as the right baseline. Calculated parameters are position and standard deviation.

- **(6) pileup information** If a second pulse occurs while data is still being

[6] As described in section 3.8.1.6, the memory of the Sis3302 FADC can be divided into smaller units, these are called pages. Whenever a trigger occurs, sampling continues for a defined amount of samples (e.g. $\sim$ 25000 samples in figure 4.8 where the trigger occurred approximately at **(3)** to sample the whole pulse) and then a page flip occurs, i.e. new samples are stored in a different part of the memory of the FADC. This allows several events to be stored independently in the memory before data readout is necessary.

recorded from a previous trigger, the position of this pileup event is determined and only the first part of the pulse will be used for subsequent data analysis. The second pulse is always discarded since the information is not sufficient for data analysis.

4.5.2 Determination of the Pulse Onset

For an event to be considered for the quenching factor determination, the threefold coincidence condition described in section 4.2 has to be fulfilled. Two of the coincidence signals - the chopper pulse and the neutron detection - are precise on the ns level by employing constant fraction discriminators and fast detectors with a signal rise time of $\sim 1\,ns$. A pulse from the cryogenic detector module has a rise time of $\sim 100\,\mu s$ and thus limits the precision of a hardware trigger to the time frame of the pulse rise. Since this is not sufficient to test the triple-coincidence, the onset must be determined with higher precision in the offline data analysis. To do this with the highest possible precision, the very slow cryogenic pulses are sampled with a sampling rate of $\sim 10\,MHz$.

Different techniques to determine the onset have been tested. Generally it can be said, that all methods involving fitting the baseline and the rising edge of the pulse to determine the position of the onset have proven to be very imprecise. This is partly because small and random distortions in the baseline can not be modeled in the fit and partly because a fit limits the information included in ~ 100 independent samples in the region of the onset to a few parameters only.

Figure 4.9 shows a zoom into the section of a pulse around the onset. Every algorithm aiming to determine the position of the onset will be limited by the small fluctuations visible in the baseline, sometimes obstructing the onset position.

The power of the onset determination can be tested directly by checking the resolution of the coincidence peak for example caused by hadronic showers (as discussed in section 6.1.1). The algorithm determining the onset currently employed and giving the best result is based on the following steps:

1. The region between the end of the baseline and the peak position is searched for the point with the highest slope, since this point must belong to the rising edge.

2. The pulse is then scanned to determine the point in the rising edge where the ADC value drops below n times the standard deviation of the baseline. n is usually ~ 4, but sometimes fine tuning is required to evade the artifacts caused by a flux quantum loss (as seen, for example, in figure 4.10 and discussed in detail in the next section). This point is called $x_{4\sigma}$.

3. The pulse is then smoothed by averaging over few samples (typically 5 - 10). The slope $m_{4\sigma}$ of the smoothed pulse at $x_{4\sigma}$ is determined.

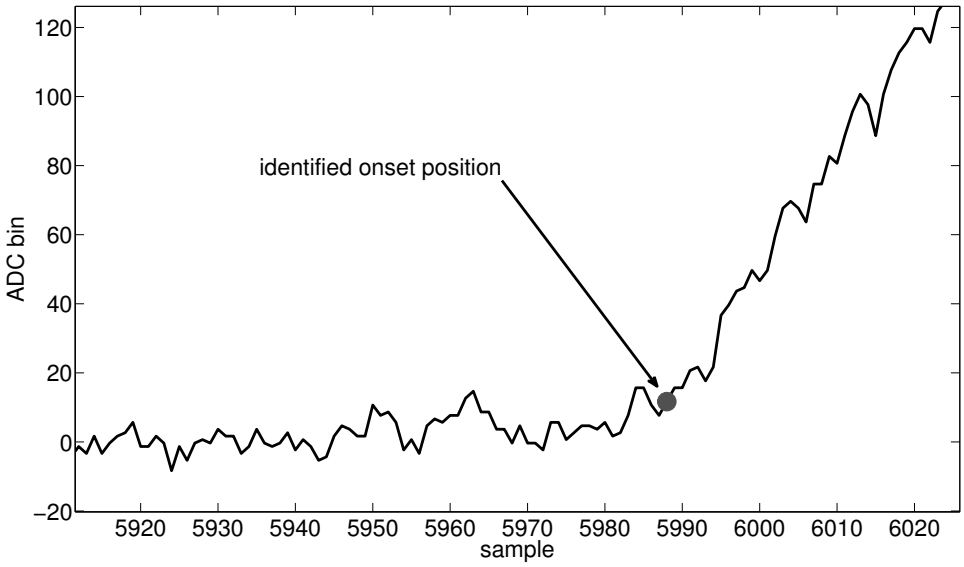

Figure 4.9: A phonon pulse of the cryogenic detector module zoomed in at the onset position. The steps outlined in section 4.5.2 were performed to determine the marked onset position.

4. The point in the pulse is searched where the slope drops below a fraction (typically a third) of $m_{4\sigma}$.

5. The baseline is redetermined for the data points directly prior to the position found in step 4. This is to account for low frequency oscillations sometimes observed that can shift the position of the baseline by few ADC bins, which has a significant impact on the determined onset position.

6. The onset is the point where the pulse is for the last time below 1σ of the baseline deviation before reaching the position calculated in step 4.

This algorithm allows for fine tuning at several steps. Changing experimental conditions[7] may require small optimizations in the parameters for the onset determination. The pulse shown in figure 4.9 has its onset determined by using the steps described previously. Generally it must be said, that the described algorithm and the used parameters have been optimized for the phonon channel. Determining the onset of the scintillation light also works but is less precise. This decision is motivated by the fact that most of the energy of an interaction is visible in the phonon channel. This is especially true for nuclear recoils where the light output is heavily quenched and close to zero.

[7]It has been observed, that the different (electronic, mechanical) noise conditions between two beam times are sufficient to make small changes to the parameters of the onset determination algorithm necessary. Other experimental conditions whose changes might make an optimization of the onset determination necessary include the use of different detectors, stabilization at a different point in the transition curve or even the use of different SQUID parameters.

4.5.3 Flux Quantum Loss Compensation

The transition edge sensor (TES) evaporated or glued on each detector are read out by a SQUID. As has been discussed in section 2.1.1, the magnetic flux through the SQUID is compensated by a feedback coil, whose produced magnetic flux is determined by the SQUID electronics that constantly picks up the voltage over the Josephson Junctions. The response of the SQUID voltage is periodic with the magnetic flux through the SQUID. If the change of the magnetic flux is so rapid that it exceeds the so-called *slew rate*, the SQUID electronics may not be able to compensate the produced external flux. In this case, the flux through the SQUID is not compensated until the external flux change becomes sufficiently slow. Until this happens, the flux Φ through the SQUID may have exceeded the periodicity n times, causing n *flux quantum losses*. This happens when a high energy deposition occurs, leading to a very steep rise in the resistance of the TES. The TES returns to its initial point much more slowly (since the rise time of the pulse is much faster than the relaxation time, the relaxation time is mainly given by the strength of the coupling of the TES to the heat bath). This means that no flux quantum loss occurs when the pulse drops back to the baseline. The SQUID is now operated at a different working point, since the total flux through it has changed by one or more flux quantums. This results in a different baseline before and after the pulse[8]. This phenomenon and the deformation caused by the flux quantum loss is depicted in figure 4.10:

The left panel of the figure shows the complete pulse. The left and right

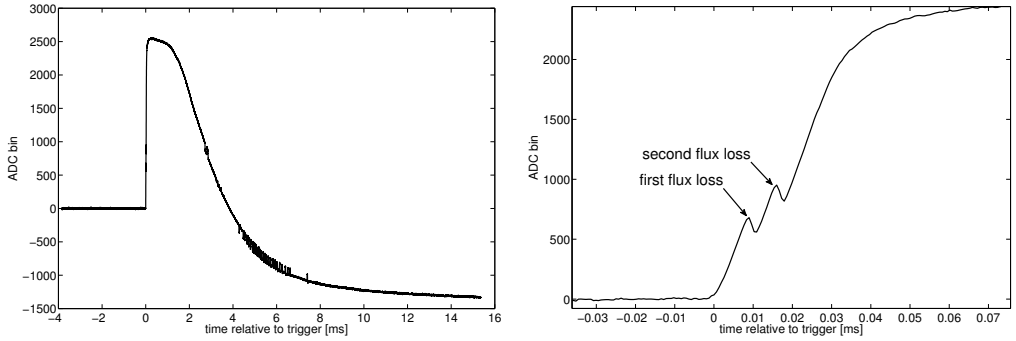

Figure 4.10: Event with a signal rising so fast that the flux compensation of the SQUID electronic fails. The left panel shows the complete pulse, the right is zoomed in on the rising edge. The inverted slope in the rising edge is a signature of a flux quantum loss, two flux quantum losses are detected for this pulse. Since the flux compensation is operative when the pulse returns to the baseline (since the decay time is much larger than the rise time), the left and right baselines differ.

baseline are different. Zooming in on the rising edge (as is done on the right panel) shows a sine-like signature superimposed on the rising edge. These two

[8] When the baseline drops below $-10\,V$ the SQUID is automatically reset and the new DC offset is $0\,V$.

dips indicate two flux quantum losses.

To deduce the energy of such a pulse, a pulse reconstruction algorithm has been written. It checks the difference between the left and right baseline of a pulse. The right baseline being lower than the left is a clear indication of a flux quantum loss event. In such a case the rising edge of the pulse is scanned for the deformations caused by the flux quantum loss. It inverts the slope of the rising edge for some μs. By scanning for the number of slope inversions, the number of lost flux quantums is derived.

The size of each flux quantum loss can be determined by evaluating all the working points of the SQUID. Figure 4.11 shows a histogram of the positions

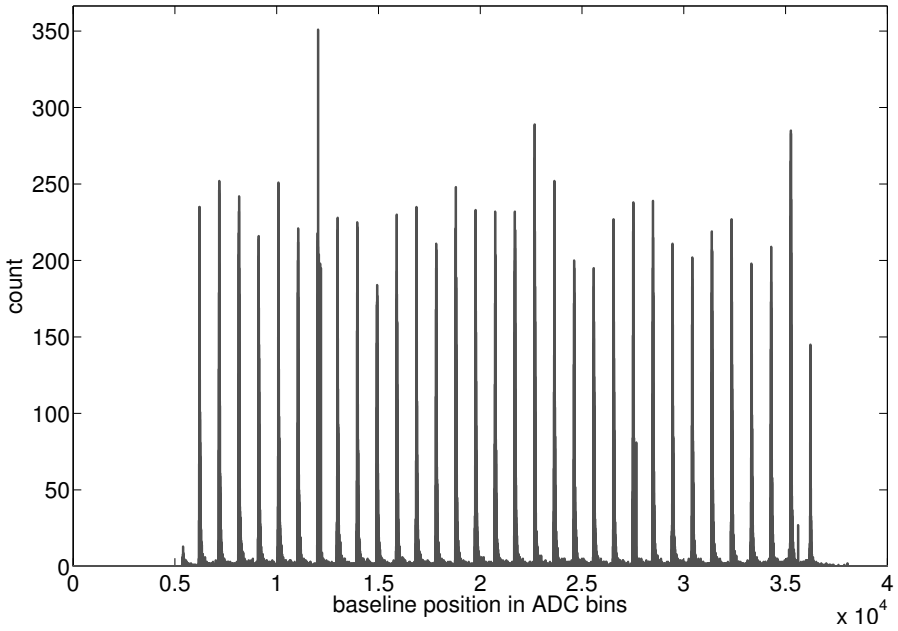

Figure 4.11: The working points of the SQUID found in the ADC data is shown in a histogram. The distance between two neighboring working points equals the size of one flux quantum Φ. The size of a flux quantum is needed for pulse reconstruction in case of a flux quantum loss, see the text for details.

of the baseline of all pulses found in a measurement. The distance in ADC bins is constant between each working point and demonstrates the periodicity of the response of the SQUID to an external magnetic flux. This periodicity equals the size of one flux quantum loss. An algorithm automatically scans all positions and derives the size Φ of a flux quantum.

The DC offset caused by a loss of flux can be corrected by reconstructing the rising edge at the positions where the deformations caused by one or more flux quantum losses were detected. Since the position of the flux quantum loss is known, $n\Phi$ can be added over the region where the pulse is distorted, where n is the number of lost fluxes and Φ the size of one flux quantum. The full procedure is automated and integrated in the data analysis pipeline.

4.5.4 Stability Cut

The pulse shape and pulse height is dependent on the energy deposition and the working conditions of the detector. To deduce the energy deposition by evaluating the pulse shape and height, a constant working point of the detector is required. External interference (e.g. vibrations, temperature changes in the cryostat, electrical noise) can partly be compensated by stabilizing the detector at a preset temperature and operating the detector in electrothermal feedback mode (see section 3.4.3.2). But even with all precautions taken the possibility of a shift in the operating point can never be excluded.

For certain procedures like calibrating the detector module and the construction of a standard event (see section 4.5.8 and 4.5.5.1, respectively) one wants to exclude all data taken in all but one working point. For this, a shift in the working point has to be identified. A clear indication is a systematic change in the standard deviation of the baseline. The left side of figure 4.12 shows the

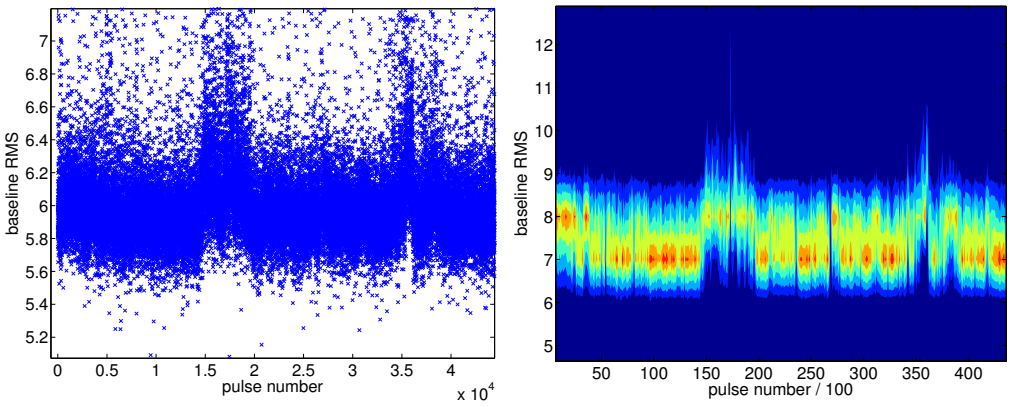

Figure 4.12: Baseline standard deviation of the phonon channel given over a timespan of approximately 1.5h (about 45000 cryodetector pulses). For the right plot the data has been binned and is presented in a contour plot. A systematic change in the baseline is a clear indication for a shift in the working point of the cryodetector while single outliers are a result of heavy pileup or other distortions.

standard deviation of the baseline for a set of subsequent cryodetector pulses over a timespan of ∼90 minutes. Generally it can be seen that most events lie in a well defined band with few outliers. Also visible is a shift in the position of this band occurring at random times. These are a clear indication of a shift in the working point. A cut on baseline stability should exclude events of these two types:

1. Events located outside the region defined by the bulk of events
2. Events located in a region where temporarily the detector is operated in a different working point.

All cryogenic data is scanned automatically performing the cuts defined by criteria 1 and 2. The algorithm executes the following steps:

1. The baseline standard deviation is binned in a two dimensional histogram. This gives the density distribution in the RMS vs time[9] plane shown on the right in figure 4.12. The histogram algorithm applies a smoothing effect by smearing the distribution slightly[10]. The smoothing leads to much more reliable results in the following steps since only 100 events are binned according to their baseline RMS.

2. The highest density in each RMS bin of subsequent 100 pulses is determined, i.e. the most probable baseline standard deviation for every set of 100 pulses.

3. The median position and median density of all the bins with the highest density is calculated, i.e. the region where the cryodetector is operated most of the time. Also calculated are the standard deviation of these values.

4. For all pulses the obtained value for the mean standard deviation of a subset of subsequent pulses is compared against the most probable values of density and position from the whole measurement. If this deviates by more than three standard deviations, the subset of pulses is excluded.

5. The events surviving this stability cut are used to calculate the standard deviation σ of all baseline standard deviations. This value is used to discard all events above and below 3σ of the 'good' value found in step 3.

An exemplary result of the automated cut is depicted in figure 4.13. Events excluded are shown in blue (black), events accepted by the cut are shown in red (gray). The bands assumed to belong to stable working conditions under the outlined criteria are well identified by the algorithm.

It must be noted that the baseline standard deviation is not sufficient to detect all shifts in the working point of the detector (or TES). But in most cases, shifts in the working point are detected this way. The only way to identify all different working points is by recording all data while using a calibration source at the same time to monitor the detector response to a gamma of known energy. This is actually done and allows for an additional working-point-drift correction described in section 4.5.7.

4.5.5 Standard Event Fit

The amplitude calculated as described in section 4.5.1 is not proportional to the deposited energy if the energy deposition is sufficient to drive the transition

[9] The x-axis on the plot is in units of pulse number, the histogram also bins 100 pulses. But since the rate is nearly constant the pulse number is strongly related to an elapsed time.

[10] 40% of an event are placed in its corresponding bin in the two-dimensional histogram. 10% are placed in the bins below, on top, left, and right of the event. 5% are placed in the four cornering bins.

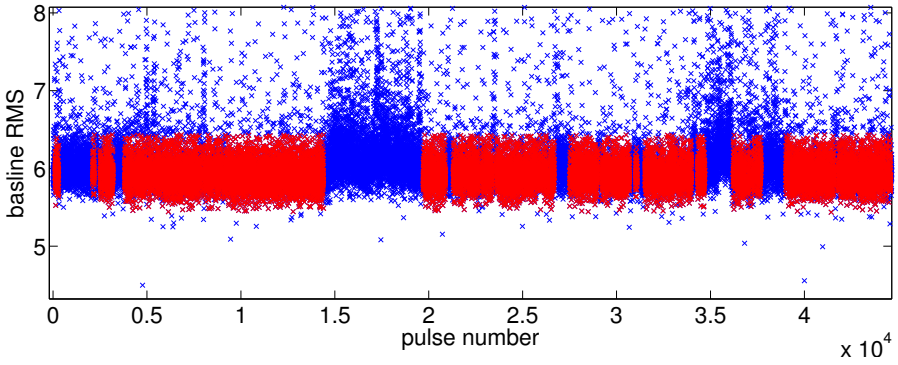

Figure 4.13: The automated stability cut based on the standard deviation of the baseline discards all events with a baseline RMS located outside the band visible in the figure. Good events are found in this band, distorted events or events suffering from heavy pileup usually have a higher baseline RMS. Also all events are automatically discarded that are located in a time period where the detector is running in a different working point, indicated by a systematic change in the baseline RMS. Accepted events are shown in red (gray), excluded events in blue (black).

edge sensor in the region of non-linearity[11]. Plotting the amplitude in the light detector versus the amplitude in the phonon detector yields the result shown in figure 4.14. The two bands (the lower being the nuclear recoil band, the upper the electron recoil band) curve upwards at an amplitude higher than $\sim$ 2000 digitizer channels. This is caused by the phonon channel entering the region of non-linearity and even complete saturation while the scintillation light detector is still in its dynamic range. The gap at a pulse height of $\sim$500 is caused by the artifact visible in figure 4.8 at the same amplitude. The artifact is a feature of the transition edge sensor and is not caused by the data acquisition. The position of the artifact is heavily dependent on the detector parameters (detector bias and temperature) and thus is usually different for each measurement. Figure 4.14 and figure 4.8 show the feature at the same pulse height because both figures are based on the same data. Here it occurs at an amplitude of approximately 500 digitizer channels (as visible in the pileup pulse). This means that certain amplitudes are unavailable, since the pulse height 'jumps' up by few bins if the artifact occurs. The effect of non-linearity, saturation and distorted pulse shapes by artifacts can be compensated by a standard event fit, which is described in this section. By using the standard event fit and a calibration, the energy deposition in the detector can be deduced.

[11]The effect of a non-linear pulse height to energy dependence is actually not only dependent on the transition curve but is independently caused due to electrothermal feedback, see section 3.4.3.2.

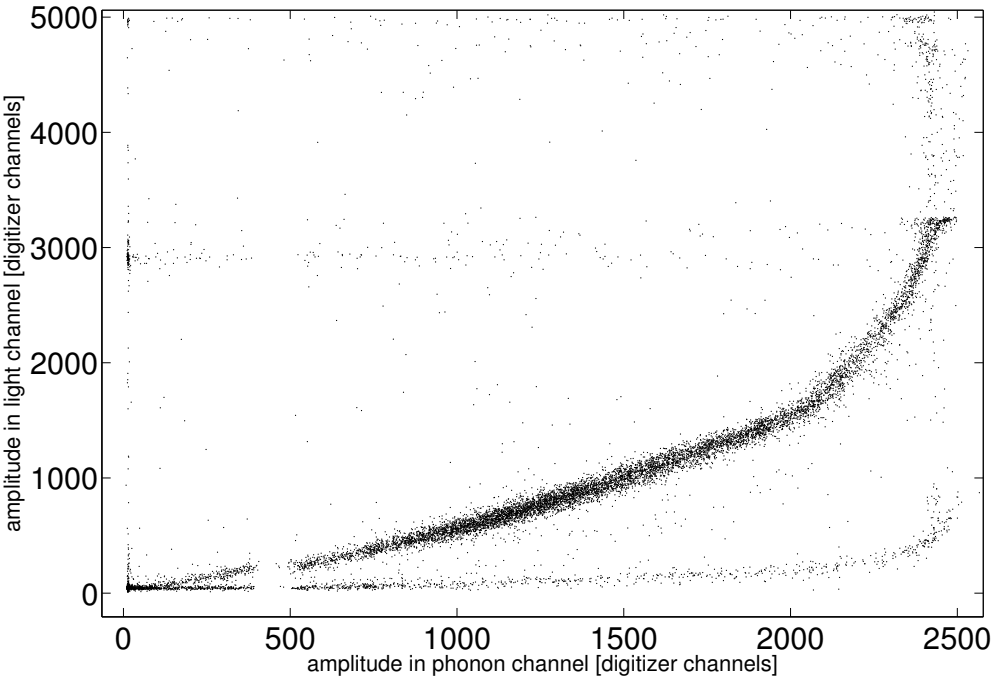

Figure 4.14: This scatterplot shows the energy deposition in both the phonon and light channel for each event. Two bands arise due to the light quenching for nuclear recoil events. The events accumulating at digitizer channel ∼3000 of the light detector are a result of a direct energy deposition by an x-ray coming from the ^{55}Fe-source (see section 3.5.2). The gap in both bands at a pulse height of ∼500 in the phonon channel is due to an artifact in the transition curve of the sensor used for phonon detection. For higher energy deposition the phonon channel is driven to its region of non-linearity and saturation, leading to the curved shape of the bands. The gap and non-linearity can be corrected with a standard event fit.

4.5.5.1 Building a Standard Event

A standard event is a 'perfect' pulse, i.e. it does not suffer from noise or distortion effects caused by non-linearity. Since the noise can be considered random, it cancels out when averaging over a sufficient set of pulses. Linearity can be assumed when the averaging takes place only over sufficiently small pulses.
The data analysis software offers a graphical user interface allowing to group measurements that were taken under similar conditions. This is of importance to ensure sufficient statistics for the averaging process, but also for other subsequent analysis steps like the calibration. Also given is the possibility to select the events used for the standard event summation graphically by defining a region of acceptance in the scatter plot showing the amplitudes for the light and phonon channels, as seen for example in figure 4.14.

Only events not excluded by the following cuts are used for the standard event summation:

- The stability cut described in section 4.5.4.

- The pretrigger information must be complete
- No pileup occurs

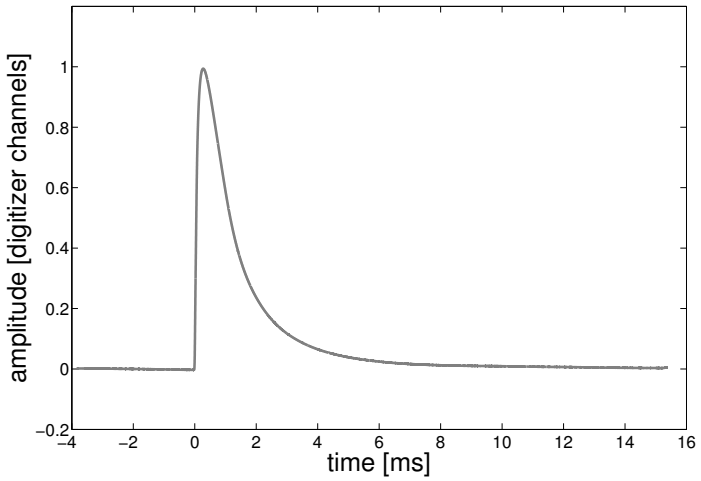

Figure 4.15: The figure shows a so-called standard event for the phonon channel, which is constructed by summing a set of selected pulses. The summation cancels out the noise. The events were taken from an energy region of $\sim 80\,keV$. The pulse height is normalized to 1 digitizer channel.

A standard event based on data recorded for the phonon detector is shown in figure 4.15. Due to the high amount of pulses summed for a standard event (more than 5000 in the case shown) the noise cancels out. Before summation, each pulse is normalized, this results in the standard event having an amplitude of 1.

4.5.5.2 Truncated Standard Event Fit

For the energy reconstruction, a standard event (see the previous section) is scaled until it matches the recorded pulse in a fitting process. The only free parameter for the fit is the onset, since the optimal pulse height giving the best fit (under the criterion of the lowest χ^2) can be obtained analytically. The χ^2 is the sum of all deviations squared between the fitted model and the observed pulse.

To calculate the scaling factor of the standard event bringing it in best agreement with the recorded pulse, the recorded pulse is projected onto the standard event. For this, both the recorded pulse and the standard event with a sample length of N are handled as an N-dimensional vector, with the scalar product between the vectors $\vec{A}$ and $\vec{B}$ defined as:

$$\langle \vec{A} \mid \vec{B} \rangle = \sum_{i=1}^{N} A_i B_i \tag{4.6}$$

Here, A_i/B_i is the i-th component of vector $\vec{A}/\vec{B}$. The amplitude for the standard event giving the lowest χ^2 between the recorded pulse and the scaled standard event is calculated via the projection:

$$amplitude = \frac{\langle standard\ event \mid pulse \rangle}{\langle standard\ event \mid standard\ event \rangle} \tag{4.7}$$

Before the summation each pulse is centered around zero, so that

$$\sum_{i=1}^{N} A_i = 0 \tag{4.8}$$

This last step is important to ensure that the projection of a pulse onto the standard event gives the same amplitude as the same pulse with a constant offset (i.e. a different vertical position of the baseline).

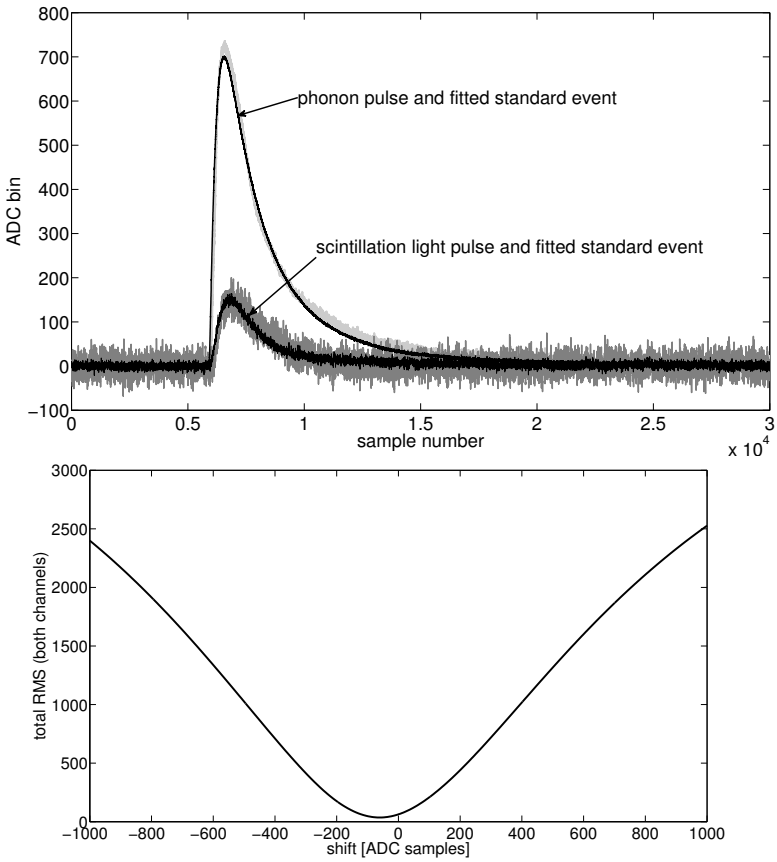

Figure 4.16: Upper figure: Simultaneously recorded phonon and scintillation light pulse and the scaled standard events fitting the data best. Lower figure: The phonon and scintillation light standard events are shifted left and right to correct for the jitter in the trigger. The scaling factors are calculated for each shift. The plot shows the total RMS of both channels for each tested shift, the minimum gives the optimal position found. For both figures, the timebase is $640ns$.

The optimal pulse height is calculated for several different horizontal positions of the standard event. This means a region around the trigger position is scanned, to compensate for jitter in the trigger. The onset position giving the minimum deviation between pulse and scaled standard event is then accepted. This is shown in the lower plot of figure 4.16, where the χ^2 (in the plot referred to as root mean square, RMS) of all tested shift positions is shown. The minimum results in the standard event fitting the data as seen in the upper plot in the same figure. The onset found via this method is not equal to the onset based on the calculations described in section 4.5.2 as it is mostly sensitive to the falling edge of the pulse and not to the initial energy deposition. Approximately, the rising edge gives the time of the particle interaction while the falling edge allows to calculate the energy deposition.

A standard event fit allows to fit pulses as if the transition edge sensor was operated only in the linear region. This is done by fitting only the lower part of the pulse if the pulse exceeds a certain pulse height where the assumption of linearity is no longer valid. Sampled data above this threshold is not taken into account, thus the name 'truncated standard event fit'. This is illustrated

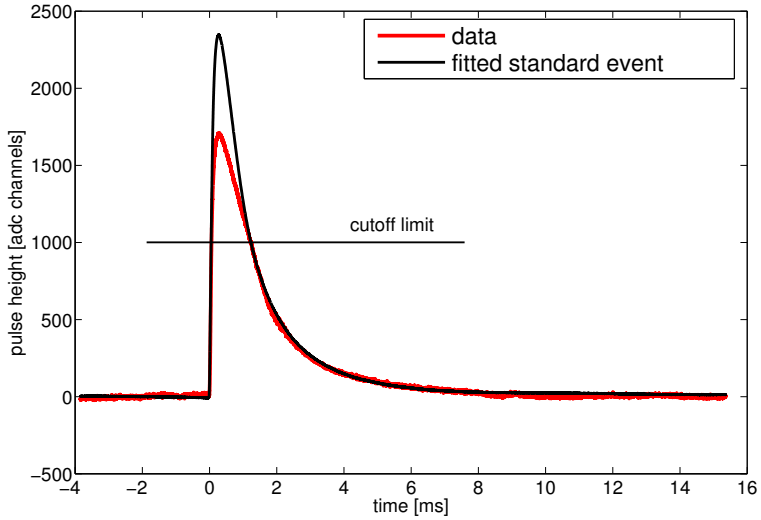

Figure 4.17: For the truncated standard event fit a cutoff is defined above which all samples are discarded. Only the points below the cutoff are accounted for in the fitting procedure. This is done to correct for a change in the pulse shape due to a large energy deposition driving the TES into the non-linear region of the transition curve.

in figure 4.17. The recorded pulse exceeds the cutoff value. The standard event only fits the onset and the tail of the pulse below the cutoff value. It can be seen that the amplitude of the fitted standard event is well above the amplitude of the actual pulse, since the transition edge sensor is driven to the region where it begins to flatten, meaning that the change of resistance is less than expected for the energy deposition.

4.5.5.3 Truncated Standard Event Fit for Pileup Pulses

To maximize statistics and thus make an efficient use of the limited beam time, the beam current is optimzed to reach the maximum rate the cryogenic detector can handle. As a rule of thumb, the beam current is increased until approximately a fourth of all pulses suffer from pileup events as for example shown in figure 4.8. Most of the events suffering from pileup can still be analyzed without loss of information. Similar to the cutoff value defined for the truncated fit, where points above the cutoff are discarded (see figure 4.17), all points after the begin of the pileup and before the begin of the pulse (**1** and **6** in figure 4.8) are also not included in the fitting process.

To test the performance of the fitting procedure for those pulses, a set of 50000 undistorted pulses were grouped according to their pulse height and fitted. The procedure was repeated and with each repetition the pulse was artificially shortened by 1% of its total length to test the reliability of the fitting algorithm for pileup pulses. The resulting fitted amplitude is shown in figure 4.18 for pulses having a height from 20% to 300% of the vertical cutoff value above which all sampled data is excluded in the truncated standard event fit (a typical vertical cutoff is $\sim 100keV$). The vertical cutoff value is of importance here since in the case of a pileup event the data available for the fit procedure is limited by the pileup pulse as well as by the vertical truncation. The trigger occurs at $\sim 20\%$ of the sample length. As long as the pileup occurs no earlier than 40% of the complete pulse length the amplitude is calculated with a precision of 1.5% or better. For pulses larger than 50% of the cutoff value, the amplitude is slightly overestimated in case of a pileup event, for pulses smaller than 50% of the cutoff value, the amplitude is slightly underestimated.

4.5.6 Mandatory Cuts

Some cuts are automatically applied by the data analysis. These are:

- The stability cut described in section 4.5.4.
- If the fitted onset position (as shown in the lower part of figure 4.16) is not found in the window of tested values, the pulse is flagged and discarded.
- If the pileup occurs prior to 45%.

An additional cut of importance is a cut on the quality of the fit for each pulse. The quality is quantified as the reduced χ^2 (in this work also called root mean square, RMS):

$$\chi^2/n_{data} = \frac{1}{n_{data}\sigma} \sum_{i=1}^{n_{data}} (A \times s_i - p_i)^2$$

Here s_i is the standard event (with i the index for each data point), p_i is the recorded pulse and n_{data} the number of fitted data points. A is the scaling factor (or amplitude) of the standard event giving the smallest χ^2, σ is the

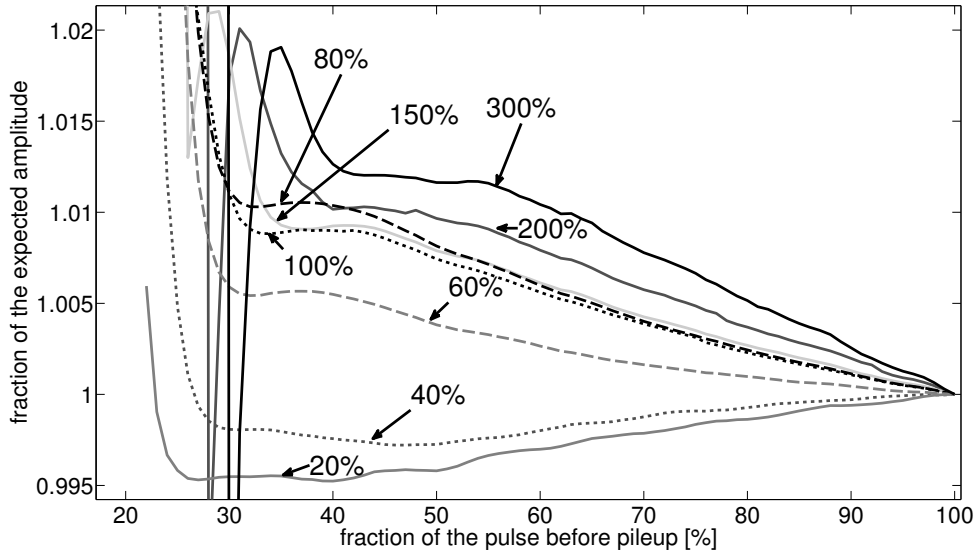

Figure 4.18: A set of complete pulses, i.e. no second trigger occurs in the window defined by the sample length, is fitted with a standard event. The pulses are grouped according to their pulse height, given in percent of the vertical cutoff value used for the truncated fit. The pulse height is indicated for each line directly in the plot, values of 20% up to 300% of the cutoff value were chosen. The obtained result of the fit gives the relative pulse height (for this group) of '1' (on the y-axis) for the complete pulse (i.e. 100% on the x-axis). Now each pulse is shortened and refitted. The fraction of the pulse that was fitted is shown on the x-axis. The obtained pulse height for that group is compared to the pulse height obtained for the full fit (100% on the x-axis). It can be seen that when a pileup pulse does not occur prior to 40% of the sampled length (which is $\sim 20\,ms$) the pulse height is restored with a precision of better than $\sim 1.5\%$

baseline noise of the pulse. The expected value of the RMS for a good event is not constant but dependent on the amplitude. The RMS for a set of pulses dependent on the fitted amplitude is shown in figure 4.19. Generally, the RMS has its lowest values for pulses with low amplitudes while the RMS increases with the energy deposition. The 'dip' in RMS visible at an amplitude of ~ 250 is the amplitude where the standard event was taken from, meaning that it fits these events perfectly. The data analysis software allows to make the RMS cut graphically by selecting only events that lie in the band of the well fitted events shown in figure 4.19. This procedure is done for both the phonon and the scintillation light pulses independently, and a good event must pass the cut for both channels.

4.5.7 Working Point and Neganov-Luke Drift Correction

The working points in both detectors may not be constant over time. Sudden changes in the working point are usually tagged and removed for most subse-

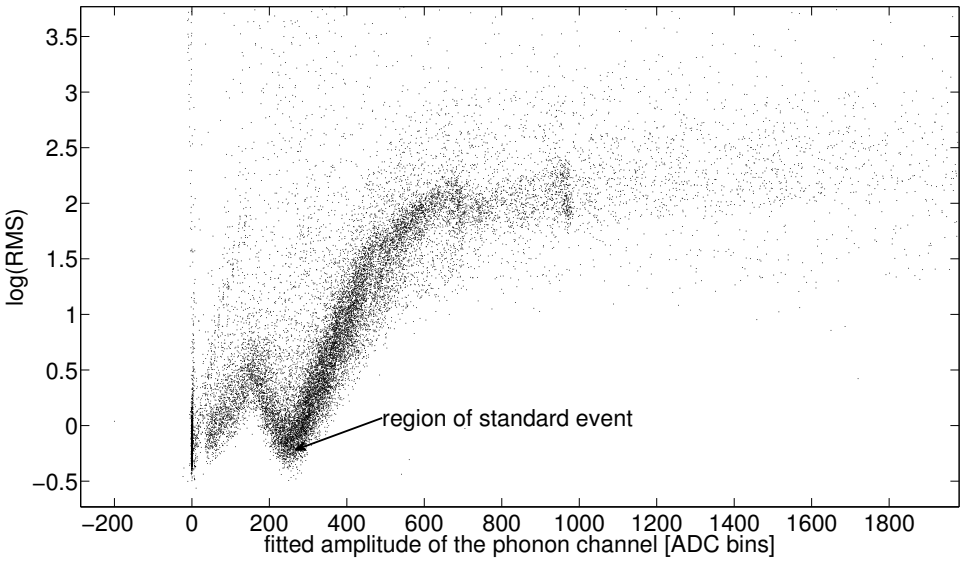

Figure 4.19: The root mean square of the best fit for each pulse versus the amplitude of the pulse. For a fitted amplitude of ~ 250 ADC channels the fit has a minimum. The reason for that is that the standard event has been constructed with events taken from this region, leading to a standard event fitting these pulses perfectly.

quent analysis steps by the stability cut described in section 4.5.4. There are instances where the changes in the working point are much more gradual in nature, the reasons for this may be:

- A slow drift in temperature. Usually these are corrected by the heaters attached to the phonon and scintillation light detectors, but since these correct the temperature of the detector holder which is only weakly coupled to the target crystal, the TES temperature may drift for some time. This happens for example after filling liquid helium or generally after the working point was changed.
- The application of the Neganov-Luke technique to amplify the scintillation light signal (see sections 3.6 and 7.3.5) generally leads to a drift in the detector response. The reason for that is that charges build up at the electrodes, partially compensating the applied external electric field and thus weakening the amplification effect.

Figure 4.20 shows the position of the $356\,keV$ line of the ^{133}Ba gamma source over a time of ~ 6 hours in the phonon channel. The line position is not constant but drifts. In this example, the drift is only of the order of $\sim 5\%$, but especially when using a Neganov-Luke detector the drift can be of the order of 20% or more, significantly weakening the resolution of the detector. Also shown in the figure is a polynomial fit (fourth order) of the time dependence of the observed position of the $356\,keV$ line. Correcting the drift by applying the fitted term linearily to all amplitudes obtained by the truncated standard event

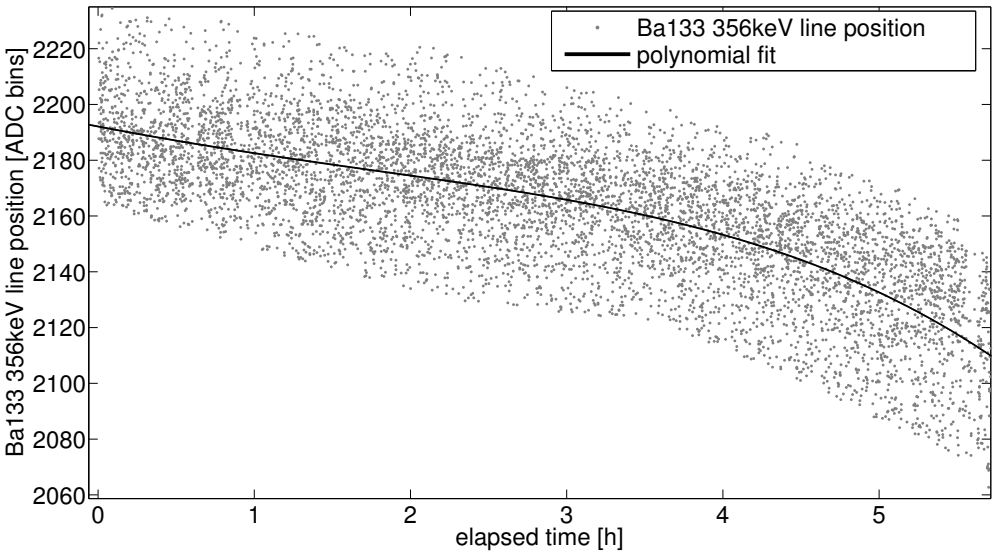

Figure 4.20: The events recorded in the region of the $356\,keV$ line of a ^{133}Ba gamma source shown over time. A drift is visible, leading to a reduced amplitude of $\sim 5\%$ after a time of approximately 6 hours. This drift can be corrected by fitting the position of the line as a function of time. Here a polynomial is used for such a fit.

fit gives the result shown in figure 4.21. In the figure, a histogram of the fitted amplitude of all events before and after the drift correction is shown. The resolution of all lines improves noticeably. The resolution in the cryogenic detector before the drift correction can be worse by orders of magnitude compared to its peak performance, since large drifts can lead to lines completely vanishing. The resolution of the cryogenic detector after applying all cuts and the drift correction is discussed in the next section.

After the drift correction has been performed for the phonon detector, which requires the user to define the region where a line with known energy (for example the $356keV$ line of the ^{133}Ba source) is observed, the procedure is automatically applied to the scintillation light channel. Here no intervention of the user is required, since events with known energy can be selected based on the phonon data, and the observed drift in the light channel is corrected accordingly.

4.5.8 Phonon Detector Calibration

The phonon detector is calibrated by using a set of radioactive sources providing gamma lines of known energy. This has to be done at least once for a single measurement, as described in section 4.5.8.1. After a good working point has been characterized, the known properties of the calibration can be applied to other measurements where only a single decay line is available, as shown in section 4.5.8.2.

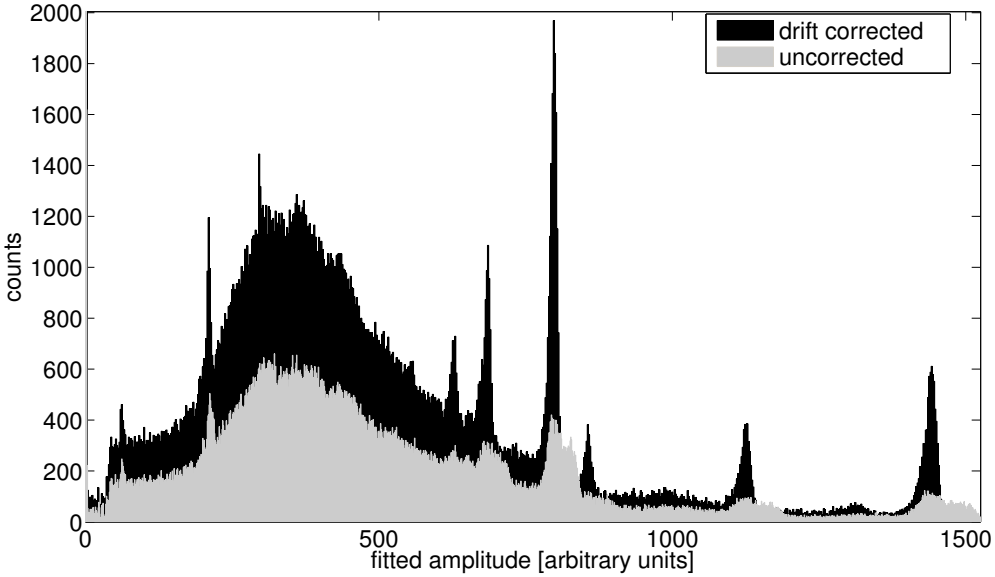

Figure 4.21: A histogram of the events recorded in the phonon channel in the presence of gamma calibration sources (^{57}Co, ^{133}Ba, ^{22}Na, ^{137}Cs, all features are discussed in detail in section 5.2.2). The 356 keV line (which is the strongest line at channel ∼800) exhibits the drift shown in figure 4.20, leading to broadened lines prior to the drift correction (gray area). After applying the drift correction, the resolution of all lines increases. Also they shift their position, which is not of importance since this happens prior to an energy calibration.

4.5.8.1 Single Measurement Calibration

After the standard event fit and the drift correction, the data is ready for calibration. For a single measurement, the calibration is based on a set of radioactive sources providing gammas of known energy in the region of interest. Typically used for calibration are ^{241}Am, ^{57}Co, ^{133}Ba, ^{22}Na and ^{137}Cs. The decay lines in the energy spectrum are selected in a graphical user interface and are then locally fitted by the function F:

$$F = A \times e^{-(x-b)^2/(2\sigma^2)} + m \times x + c \tag{4.9}$$

Here, x is the ADC channel (derived after the truncated standard event fit), A is the amplitude of the line, b its position in fitted ADC channels after drift correction, σ the line width and $m \times x + c$ the local background. The parameters A, b, σ, m and c are the free parameters of the fit, an example is shown in figure 4.22. The fit is applied to all decay lines with sufficient statistics to ensure a meaningful convergence of the fit. This gives a number of points linking the energy E of the decay line to the ADC channel. It is found that this relation is not completely linear. This is expected due to the effect of electro-thermal feedback (see section 3.4.3.2) which reduces the relative amplitude of a pulse with increasing energy deposition. It has been found that the function

$$E(x) = a \times x^k \tag{4.10}$$

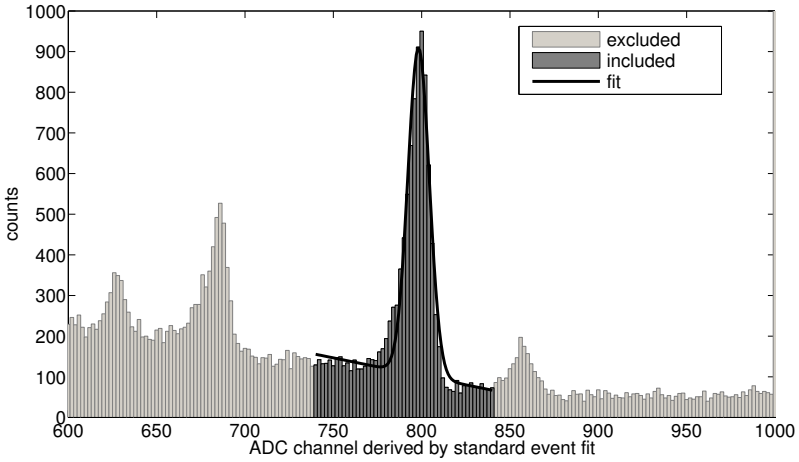

Figure 4.22: The $356keV$ line of a ^{133}Ba source fitted by equation 4.9. The fitting algorithm only considers the dark area, the light area is not included in the fit. The result of the fit with function $F = A \times e^{-(x-b)^2/(2\sigma^2)} + m \times x + c$ and the 95% confidence bounds are $A = 805.2(760.9, 849.4)$, $b = 798.3(797.9, 798.7)$, $\sigma = 6.053(5.646, 6.46)$, $m = -0.8843(-1.28, -0.4883)$ and $c = 809.8(501, 1119)$. Important for the calibration is only the position b of the peak. The intesified flank to lower energies is caused by compton scattering and is discussed in section 5.2.2.

connects the fitted ADC channel x with the energy deposition $E(x)$. Here, the parameter a essentially links the ADC channel to an energy and k accounts for the electro-thermal feedback. Usually, the values of k best fitting the data are found between 1 and 1.3, where a value of $k = 1$ means that the electro-thermal feedback has no influence. Figure 4.23 shows equation 4.10 applied to all lines of a calibration measurement. For the exemplary data set shown in figure 4.23 the parameter k converges at 1.051 ± 0.008, giving the calibration curve shown in the figure. For details on the used sources and the different spectral features see section 5.2.2.

4.5.8.2 Applying a Known Calibration

If the working point is kept reasonably stable, the small drifts still observed (and within a measurement corrected as described in section 4.5.7) change the parameter a in equation 4.10 while k remains constant. Since the slow cryogenic detector module does only permit trigger rates between below $\sim 15\,Hz$, during a beam time the rates caused by calibration sources is kept to a minimum. For this purpose, only the ^{133}Ba source is mounted in the vicinity of the experiment at a distance to still allow the $356keV$ line to be fitted with sufficient statistics to perform the drift correction and calculate the parameter a. The parameter k is determined in a separate calibration measurement as described in section 4.5.8. This ensures maximum efficiency during the actual beam time.

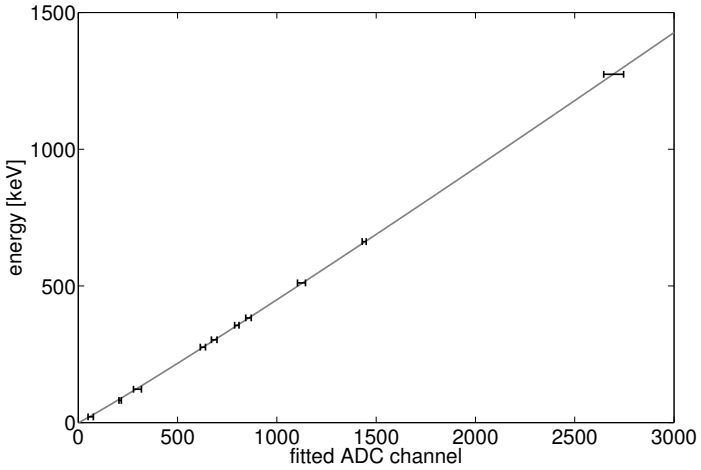

Figure 4.23: The (black) error bars are the 95% confidence bars of the fitted peak position b multiplied by 10 to ensure visibility. The (gray) line is equation 4.10 fitted to the data: $a = 0.317 \pm 0.020$ and $k = 1.051 \pm 0.008$.

4.5.9 Linearization and Calibration of the Light Detector

In recent beam times, the response of the scintillation light detector was observed to be highly non-linear, as seen in figure 4.24. To correct for this behavior, the phonon channel can be used for the calibration: The measurement is binned depending on the energy deposition in the phonon channel. The corresponding amplitudes in the scintillation light channel for the gamma band are fitted by a Gaussian for each bin. The position of the fitted Gaussian is shown as the gray circles in figure 4.24. They in turn are fitted by a spline, whose inverse function is used to linearize and calibrate the light channel. This has the consequence, that the quenching factor of electron recoils is $QF_{ER} \equiv 1$ by definition in all regions where this technique has been applied. As can be seen in the figure, the lowest phonon energy for which the fit was performed is $60keV$, below this energy linearity was assumed for the light channel. The binning and the threshold energy for this process is selected by the user, the rest of the procedure is automated.

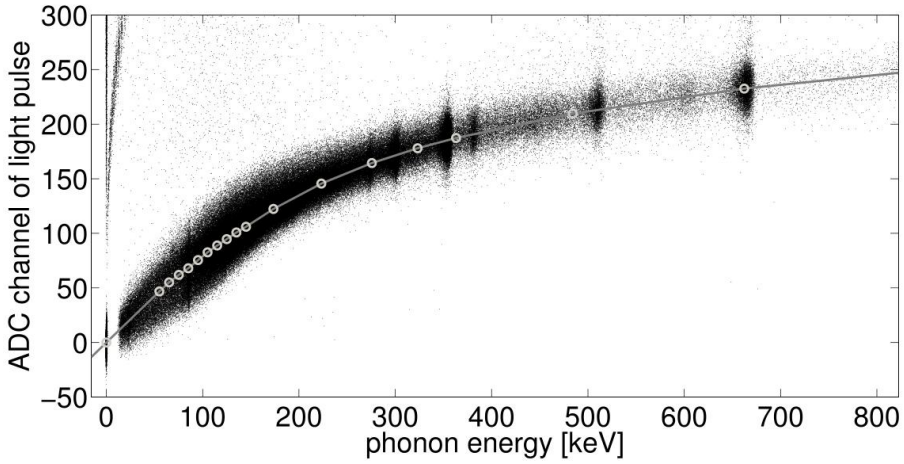

Figure 4.24: Measurement performed after the calibration of the phonon channel, for which the energy deposition is shown on the x-axis. The scintillation light channel (shown on the y-axis) is not calibrated, but since a quenching factor of 1 for electron recoils is a reasonable assumption, it can be seen that the response of the light channel is highly non-linear above an energy of $150keV$. This non-linearity is corrected for by fitting the position of the gamma band for different phonon energies (shown as the gray circles) and fitting these with a spline (gray line). The inverse function of this spline is used to linearize the light channel, leading to a quenching factor of electron recoils of $QF_{ER} \equiv 1$ by definition if this technique is applied.

Chapter 5

Beam Time Analysis I: Low-Temperature Detector Analysis

The beam time analysis is divided into two chapters: This chapter focuses on the data analysis steps required for the calibration and discusses the observed characteristics of the cryogenic detector module. Chapter 6 will evaluate the triple coincidences in detail. To demonstrate the performance of the setup and the data analysis tools, the best beam time to date has been chosen for an in-depth analysis. An overview of this beam time is given in section 5.1. The calibration procedure is detailed in section 5.2 and the data is discussed in section 5.3.

5.1 October 2010 Beam Time: Overview

In October 2010 seven days of beam time were dedicated to the neutron scattering facility for quenching factor measurements. Despite some problems that eventually lead to the failure of the low-temperature detector, excellent data was taken during this beam time. For this measurement, the light-weight detector holder presented in section 3.5.3 was utilized.

For the interpretation of the data, two calibration measurements with gamma sources were scheduled, one before and one after the beam time. To ensure the validity of the energy calibration over the whole run, a ^{133}Ba source was present at all times. Stable working conditions for the light detector were obtained at the end of the first day. The first 30 hours of the beam time were mainly used to establish the required conditions in the accelerator lab, i.e., conditioning the ^{11}B source, guiding the beam to the experiment and optimizing the buncher and chopper parameters to obtain a pulse timing satisfactory for a time of flight measurement. After that, data taking began.

The measurement campaign continued under good conditions until day five, when a failure in the phonon channel of the cryogenic detector module no longer allowed further data taking. The cause of the detector failure is still not resolved, but two probable reasons were identified:

1. Under a microscope, the aluminum connecting the TES evaporated on the $CaWO_4$ crystal shows partial separation from the crystal. This may be caused by the numerous cooldown cycles of the detector from room temperature to mK temperatures and vice versa.
2. Another possible explanation is a very small leakage of helium into the internal vacuum chamber of the cryostat, where it would form a superfluid film that might partially cover the transition edge sensor and thus drastically change the heat capacity of the TES. However, since recent tests performed at room temperature were not revealing any leakage, this scenario becomes unlikely.

Since the phonon detector was no longer operable, no energy calibration could be performed after the beam time. The calibration data taken beforehand was obtained with the working point drifting and not in its final state, making the application of the calibration to the actual beam time data impossible.

Even though this poses some difficulties to the interpretation of the data, the data taken during the few days is of a high quality never reached before in terms of ^{11}B-beam stability and background caused by undesired scattering of neutrons. Also the resolution and the discrimination threshold of the detector are far better than what was achieved in previous attempts.

5.2 Performing the Calibration

The procedure to obtain an energy calibration for the beam time is outlined in section 5.2.1. It has to be applied independently to the calibration data recorded beforehand (discussed in section 5.2.2) and the data obtained in the presence of the neutron beam (section 5.2.3).

5.2.1 General Calibration Procedure

The general calibration procedure for the October 2010 beam time consists of the following steps:

- performing the stability cut
- identification of all working points in the cryogenic detector module
- treating all identified working points independently:
  - summation of a standard event
  - standard event fit

  - drift correction
  - calibration of the phonon channel
  - linearization of the light channel
- combination of all working points

To perform these steps, the data analysis tools presented in chapter 4 are used. With the exception of the identification and combination of the different working points, the analysis steps have been discussed in detail in the aforementioned chapter. Consequently, the following sections will only discuss the particularities of this beam time.

Since no means of an independent calibration for the light channel are available[1] for the October 2010 beam time, the light channel is linearized based on the calibration of the phonon channel above $60keV$ following the procedure outlined in section 4.5.9. This means that the quenching factor of electron recoils (ER) is $QF_{ER} \equiv 1$ by definition for energy depositions above $60keV$. Below $60keV$, linearity between the fitted pulse amplitude and the deposited energy in the light detector is assumed[2]. Thus the quenching factor for electron recoils can deviate from 1 below an energy of $60keV$. Within the resolution of the light detector, no deviation has been observed, though. The linearization technique for the scintillation light detector has been applied to all data sets independently, including the calibration data discussed in the next section.

[1] An independent calibration of the scintillation light detector can, for example, be achieved by using an x-ray source (e.g. ^{55}Fe which emits at energies of $\sim 7keV$), which was done in previous beam times. The application of the calibration established via the observed x-rays on scintillation light pulses, however, proved difficult, since the pulse shape for x-rays is different from the pulse shape of scintillation light pulses. The reason for that is that scintillation light produced in the $CaWO_4$ crystal is emitted over a longer time and homogeneously while an x-ray deposits all its energy at the same time at a single location. For this reason and to reduce the mass of the support structure, the idea of using an x-ray source for calibration was abandoned for all later beam times. During the October 2010 beam time, a LED installed at mK temperatures was present at all times. Short voltage pulses ($\sim \mu s$) were applied and the light produced by the LED was guided via an optical fiber to the light detector. Again, the pulse shape proved to be too different from actual scintillation light pulses. The use of a LED as an independent calibration method is still under investigation and may prove to be a valuable tool at future beam times [114].

[2] Above $60keV$, the calibration of the light channel is based on the calibration of the phonon channel. Below $60keV$, the energy deposition in the light channel is calculated linearly out of the fitted amplitude. Generally, it is preferable to have the calibration of the scintillation light detector independent of the phonon detector up to higher energies. This was not possible for the detector employed during the beam time, the correlation between the pulse height and the energy deposition proved to be highly non-linear above $\sim 60keV$. With the excellent resolution and calibration of the CRESST detectors, a deviation of the quenching factor for electron recoils from 1 to larger values has been observed [94] below $30keV$. This effect is small and not visible with the scintillation light detector used during this beam time. An empirical explanation of this effect is given by Birks [126].

5.2.2 Calibration Data

As described in section 5.1, the only calibration data available from this experimental run was obtained in conditions not applicable to the actual beam time data. A drift in the working point of the detector due to temperature changes decreases the resolution of the detector. The upper part in figure 5.1 shows the calibration data after fitting it with standard events for the scintillation light detector and the phonon detector, but prior to calibration and drift correction. The $356keV$ line of the ^{133}Ba-source visible at a fitted phonon amplitude of $\sim$750-800 channels, for example, shows a drift of only a few percent in the phonon channel but a large drift (from channel 50 to 250) in the light channel. However, following the points outlined in section 5.2, after drift correction and calibration (shown in the lower part of figure 5.1), the data is still very useful for the interpretation of the experiment. Nuclear recoils are expected at a very low light output. Only very few are visible in the scatterplot as expected in the absence of a neutron source. These few nuclear recoils are probably caused by hadronic showers and secondaries of muons. Events with higher scintillation light output than expected for electron recoils can be attributed to an additional energy deposition in the light detector not caused by scintillation light. This can happen when a particle interaction deposits only part of its energy in the target crystal and then scatters a second time in the light detector, depositing a small amount of energy there.

Table 5.1 lists the energies of the gammas emitted by the calibration sources used for this measurement. Figure 5.2 shows the spectrum in the phonon chan-

Isotope	Energy $[keV]$	branching ratio [%]
^{133}Ba	81.0	34.1
	276.4	7.2
	302.9	18.3
	356.0	62.1
	383.9	8.9
^{22}Na	511.0	180.8
	1274.5	99.9
^{137}Cs	661.6	85.1

Table 5.1: The radioactive isotopes used for the gamma calibration shown in figures 5.1 and 5.2. Decay lines with branching ratios too low to be visible in the data are not listed. (source: [127])

nel, where all spectral features from table 5.1 can be identified. The additional line at an energy of $21keV$ is caused by an escape of the tungsten K_α x-ray of $59.3keV$ after excitation by an $81keV$ gamma of the ^{133}Ba source. As can be seen, the lines are not perfectly Gaussian but exhibit an asymmetry to lower energies. Simulations [128] show that this is caused by gammas that are previously Compton scattered in the surrounding material, losing some energy before

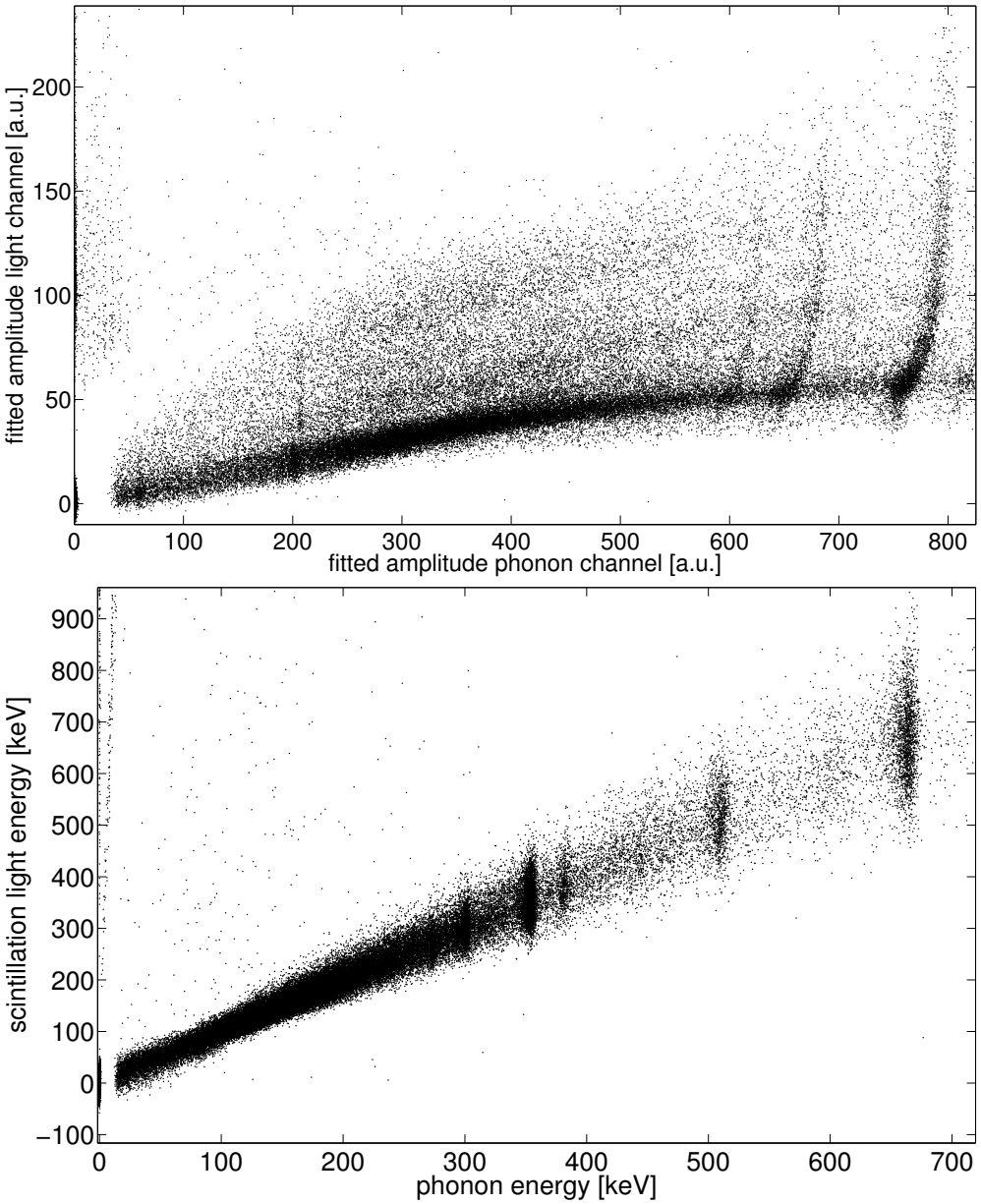

Figure 5.1: Calibration data of the October 2010 beam time. The upper part of the figure shows the fitted amplitude in the light channel vs the phonon channel prior to calibration and drift correction. The drift in the gamma lines, for example the $356keV$ line visible at a phonon amplitude between channels 750-800, is very prominent especially in the light channel, where the line position differs between channels 50 and 250. The lower plot shows the same data after calibration and drift correction. The rather broad gamma band shows that the resolution of the light detector could not be fully restored. The gap to zero energy deposition visible in the lower panel is a consequence of the trigger threshold of this particular measurement.

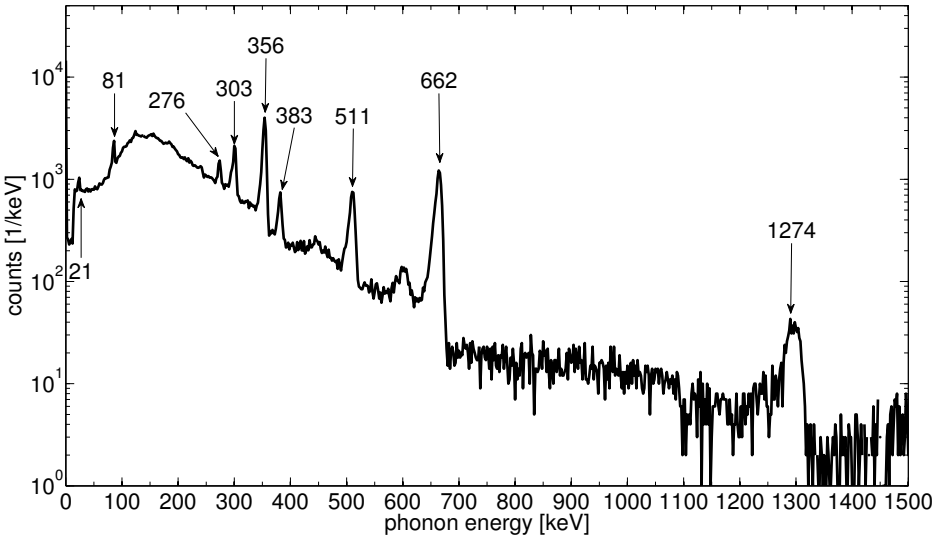

Figure 5.2: The spectrum in the phonon channel obtained by using the radioactive sources ^{133}Ba, ^{22}Na and ^{137}Cs (table 5.1). Fitting the $81keV$ and the $356keV$ lines with a Gaussian gives a resolution of $\sigma_{81keV} = 0.97keV$ (FWHM $= 2.28keV$) and $\sigma_{356keV} = 2.8keV$ (FWHM $= 6.58keV$), respectively. The line with the lowest energy of $21keV$ is caused by the escape of the $59.3keV$ K_α x-ray of tungsten with respect to the $81keV$ line of the ^{133}Ba source. The underlying broad spectral distribution is caused by muons that produce secondary gammas in the surrounding material which then deposit energy in the cryogenic detector [86]. Direct hits by muons deposit several MeV in the target crystal and typically exceed the dynamic range of the detector.

depositing the rest of their energy in the cryogenic detector module. Ignoring this feature and fitting the $81keV$ and $356keV$ lines with a Gaussian gives a line width of $\sigma_{81keV} = 0.97keV$ (FWHM $= 2.28keV$) and $\sigma_{356keV} = 2.8keV$ (FWHM $= 6.58keV$), respectively. A comparison with section 3.4.1 shows that the resolution is decreased by a factor of ~ 2 compared to other measurements. This can be attributed the large temperature drift as well as the detector not running in its final working point.

5.2.3 Calibration of the Beam Time Data

The cryogenic detector module employed at the neutron scattering facility is temperature-stabilized by a resistive heater connected to the detector holder, the temperature of which is also read out continuously to determine the heater current. Still, the system suffers from shifts of the working point, which can be caused by electromagnetic noise. To monitor these shifts (and test the calibration), a radioactive ^{133}Ba source is present at all times during the beam time. The count rate caused by this source is kept low (compared to a calibration measurement) by increasing the distance between the source and the setup. With the position of one gamma line known (generally the most promi-

nent $356keV$ line), the drift of the working point can be corrected and thus a calibration of the phonon channel can be obtained for all relevant energies.

As has been described above, reliable calibration data is not available for the October 2010 beam time, since the calibration discussed in section 5.2.2 is not applicable to all other data taken. The only means of calibration are thus the lines given by the ^{133}Ba source[3] and the $511keV$ line, which is produced by ^{11}C which does a β^+ decay. ^{11}C is a product of the nuclear reaction employed for the neutron production, $^{1}\mathrm{H}(^{11}\mathrm{B}, n)^{11}\mathrm{C}$(see section 3.2.2).

5.2.3.1 Overview: Combination of Different Working Points

The four days of usable beam time data from October 2010 have been saved in a set of 54 folders. A new folder is started either whenever conditions are no longer assumed to be constant or when the time elapsed exceeds ∼2-3 hours (to reduce the size of one analysis chunk). Of these 54 folders, 45 were included in the analysis, discarding the ones where either the neutron beam or the cryogenic detector module was significantly below standard[4]. Within these 45 remaining folders, 18 discrete (small) jumps in the working point in either the phonon or the light detector were detected. These 18 sets of data were treated independently in the following way:

1. The stability cut described in section 4.5.4 was applied.

2. A standard event was built for each of the 18 data sets, as described in section 4.5.5.1. The cutoff value was at $\sim 70keV$ for the light channel and roughly twice that amount for the phonon channel.

3. The standard events were fitted to the data.

4. After performing all cuts described in section 4.5.6, each data set was calibrated using the $276.4keV$, $302.9keV$, $356.0keV$ and $383.9keV$ lines of the ^{133}Ba source (due to the lower count rate caused by the source, the $81keV$ line is only visible in the data sets with the highest statistics) and the $511keV$ line caused by e^+-annihilation.

As will be seen in the next section, the lack of lines available to calibrate above $600keV$ and below $200keV$ leads to a calibration being only accurate within this energy region.

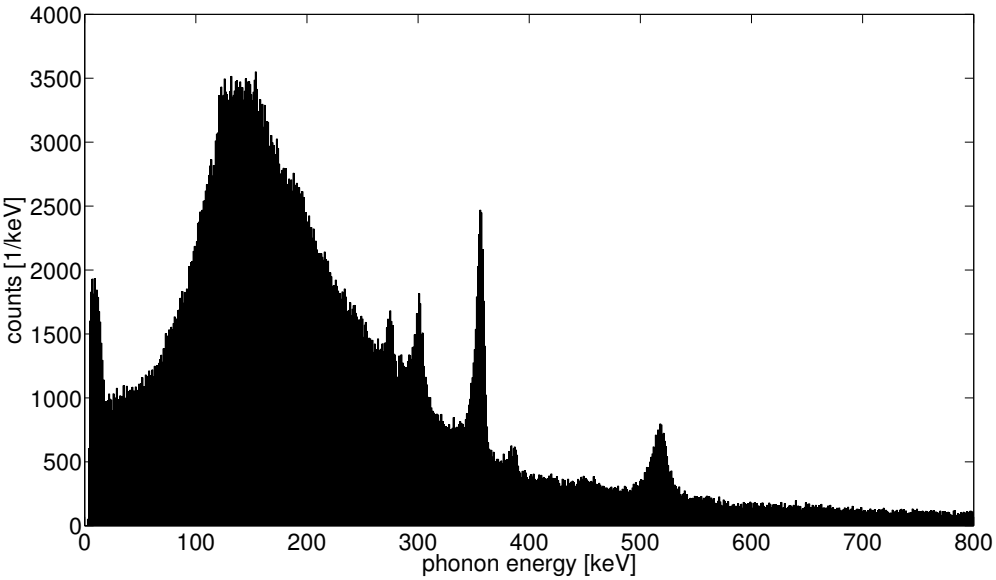

Figure 5.3: Combined calibrated electron recoil spectrum for the phonon channel of all 18 working points that have been identified. The visible peaks are the four ^{133}Ba lines of highest energy and the $511keV$ caused by the β^+ decay of ^{11}C produced in the nuclear reaction. The beam time data is calibrated based on these lines. See the main text for further details.

5.2.3.2 Comparability of the 18 Data Sets

Figure 5.3 shows a spectrum of all electronic recoils in the phonon channel after the combination of all identified discrete working points. The visible features are the lines above $200keV$ from the ^{133}Ba source and the $511keV$ line which originates from the annihilation of a positron coming from ^{11}C. The σ width of the $356keV$ line is $\sigma_{356keV} = 3.5 \pm 0.2keV$. It is broadened after the combination of the working points, for individual measurements with sufficient statistics it is observed at $\sigma_{356keV} \approx 2keV$. No line feature is visible at an energy of $81keV$, where the low-energetic line of the ^{133}Ba-source should appear with the combined statistics of the full beam time:
For the calibration data discussed in section 5.2.2 the observed ratio between the intensities of the lines at $356keV$ and $81keV$ was 7.5 to 1 with a total of ~ 1800 pulses observed at $81keV$ after the subtraction of the background[5] being approximately ~ 4000 pulses. In comparison, the $356keV$ line contains ~ 15000 pulses for the combined beam time data (again after background subtraction),

[3]This does not include the $81keV$ line since the count rate is not sufficient for this line to show up clearly in the calibration spectrum.

[4]The quality of the neutron beam suffers when the strength of of the ^{11}B-source decreases and the stabilization of the beam is no longer given. The data from the low-temperature detector module can drift heavily after refilling liquid helium, which is why data taken directly after the refilling procedure is often discarded.

[5]Each calibration peak is fitted with a function F for the background and the peak, $F = A \times e^{-(\frac{x-b}{c})^2} + mx + c$, with mx representing the local spectral rise or fall in energy, c a constant offset and $mx + c$ the total background at energy x.

leading to an expected $15000/7.5 = 2000$ pulses originating from the $81keV$ line. The background events observed at this energy (assuming a line width of $2keV$ at $81keV$) equals to a total of ~ 6100 events. Thus, the $81keV$ line should be visible in the combined data of all working points. However, figure 5.3 shows no feature at the energy of $81keV$. This is an indication that the calibration is not reliable at this energy, the $81keV$ peak is smeared out after the combination of all 18 working points. The lack of a calibration line at this energy for each individual working point can lead to a statistical and systematic deviation at this energy that can be different for each of the 18 data sets. This will be discussed further in the next section, where the observed inelastic recoils will allow to identify the presence and direction of a systematic deviation.

In total, ~ 3 million pulses are included in the beam time data. After applying all cuts discussed in section 4.5.6, ~ 2 million cryogenic pulses remain. These pulses were recorded during slightly less than 4 days of beam time, equaling a rate of $\sim 6Hz$ of good events including time periods where all data was discarded.

5.3 Cryodetector Data Discussion

In section 5.3.1 the general properties of the observed events are discussed. These can be used to verify the validity of the calibration and to derive possible corrections to it, as is shown in section 5.3.2. The spectral distribution and composition of the nuclear recoil band as well as the resolution of the scintillation light detector in the relevant energy region is discussed in section 5.3.3.

5.3.1 Observed Features and General Properties

The calibration of the October 2010 beam time is based on the observed lines of the ^{133}Ba source and the annihilation peak at $511keV$. After the linearization of the light channel (see section 4.5.9), the data for both channels is presented in figure 5.4. Here the energy deposition of the recorded events in the light channel is plotted versus the energy deposition in the phonon channel. For the plot, only a random (but evenly distributed) sample of 100000 pulses were selected from the recorded 3 million cryogenic pulses to avoid an overcrowded plot. The following classes of events can be identified as denoted in the figure:

- **Electron Recoils (ER)** These are the events that are caused by electron recoils, induced by betas and gammas. The calibration as shown in figure 5.3 is based on events observed in this band.
- **Nuclear Recoils (NR)** Nuclear recoils have a lower light output compared to electron recoils and are located in this band. Nuclear recoils are induced by the neutron beam. The properties of the nuclear recoil band are discussed in detail in section 5.3.3.

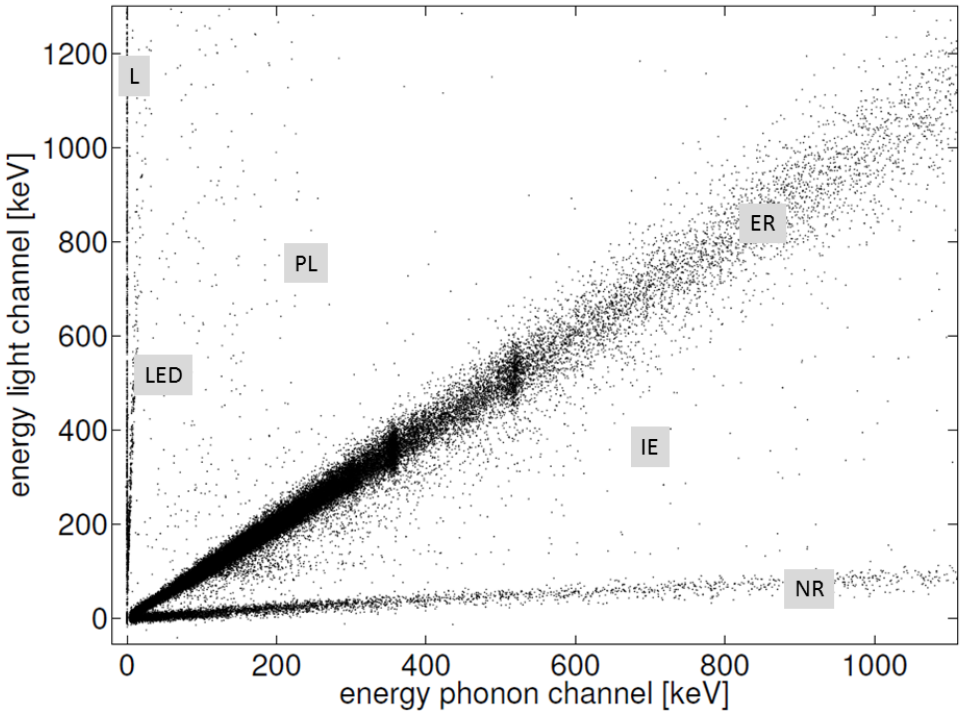

Figure 5.4: The data in the light and phonon channel recorded during the October 2010 beam time. The two most promiment bands originate from electron recoils (ER), induced by gammas and betas, and nuclear recoils (NR), induced by the neutron beam. The other observed types of events are inelastic events (IE) on tungsten, phonon and light detector hits (PL), direct light detector hits (L) and LED pulses (LED). All observed event types are discussed in detail in the text.

- **Inelastic Events (IE)** Events that lie in the region between the nuclear and the electron recoil band are caused by neutron induced inelastic processes[6]: a neutron scatter leaves a nucleus[7] in an excited state. The gamma emitted in the deexcitation process also deposits energy in the detector crystal, which is (since the cryogenic detector is very slow compared to the life times of the excited nucleus) seen in coincidence with the nuclear recoil. In this definition, 'inelastic event' thus means a process that is a combination of a nuclear and an electron recoil event. This definition is not correct in the sense that this defines the region where all inelastic recoils are observed. The nuclear recoil band for example also contains inelastic events where the deexcitation gamma escapes without sufficient energy deposition to lift the observed recoil above the nuclear recoil band (see e.g. simulation in [96]).
- **Phonon and Light Detector Hits (PL)** Before or after an energy deposition in the cryogenic detector module, a particle can also deposit

[6] In CRESST Dark Matter runs, these events might also be caused by α particles.

[7] The excited levels of oxygen and calcium are above $3MeV$. In $CaWO_4$, only tungsten has excited levels at low energies, with the lowest level at $\sim 50keV$.

energy directly in the scintillation light detector by scattering in the silicon substrate. The additional energy deposition in the light channel lifts these events above the electron recoil band.

- **Direct Light Detector Hits (L)** Particles can also scatter only in the light detector. These events show no energy deposition in the phonon channel.
- **LED pulses (LED)** As has been discussed in section 3.6, a LED was included in the setup. Though it turned out these pulses can not be used to establish an independent calibration of the light channel, they are still visible in figure 5.4. They not only show an energy deposition in the light channel, but also induce a small pulse in the transition edge sensor of the phonon channel, since the TES itself absorbs part of the light.

A total of $\sim$ 3 million cryogenic pulses were recorded in the beam time in the presence of the neutron beam. Two million remain after all cuts, of which the representative random selection of 100000 pulses shown in figure 5.4 were extracted. A larger (representative) subset[8] of these two million pulses, containing $\sim$ 950000 events below an energy deposition of $2.5MeV$, are distributed over the discussed classes of events as is listed in table 5.2. The threshold energy of $2.5MeV$ was chosen since the maximal energy transfer of $10.6MeV$ neutrons on oxygen is $2.3MeV$. The observed 1σ discrimination threshold, which is the

	ratio	total
electron recoils (ER)	85.0%	$\sim 805 \times 10^3$
nuclear recoils (NR)	9.0%	$\sim 86 \times 10^3$
inelastic scatters (IE)	2.1%	$\sim 200 \times 10^3$
light and phonon hits (PL)	0.9%	$\sim 9 \times 10^3$
LED pulses (LED)	0.8%	$\sim 8 \times 10^3$
light only (L)	2.0%	$\sim 19 \times 10^3$
sum	100 %	$\sim 950 \times 10^3$

Table 5.2: The distribution of observed events below an energy deposition of $2.5MeV$ over the processes defined in the text and denoted in figure 5.4.

energy at which electron recoils can still be distinguished from nuclear recoils on a 1σ level, is $7.7keV$ after the combination of all working points in which the low-temperature detector was operated. Prior to the combination, for some of the individual working points a discrimination threshold lower than $7keV$ was observed. This emphasizes the good quality of the detector even in the difficult environment in terms of electromagnetic and mechanical noise found at the accelerator laboratory.

[8]The subset of $\sim$950000 events are the events that are initially considered by the triple coincidence search algorithm, which is roughly every second event. It must be noted that this number is much larger than the actual number of coincidences. The large search window that leads to the initial inclusion of these events is motivated by the high uncertainty in the chopper timing. Later stages of the analysis process allow to narrow down the coincidence condition, after the correct coincidence timings were defined.

5.3.2 Uncertainties in the Calibration and Possible Corrections

The calibration of the beam time data is solely based on the $276.4keV$, $302.9keV$, $356.0keV$ and $383.9keV$ lines of the ^{133}Ba source and the annihilation[9] peak at $511keV$. Thus the calibration can be considered reliable in this energy region. To make a statement about the calibration below $200keV$ and above $600keV$, the combined data of the phonon and the light channel is used.

The Calibration below 200keV The tungsten nucleus has inelastic excitation levels at energies from $\sim 100keV$ to $\sim 120keV$ depending on the tungsten isotope [10]. Inelastic recoils can transfer some energy to the nucleus in addition to the energy required for the inelastic excitation. Since the lifetime of the inelastic levels is of the order of a few ns, the decay of the excited state can be considered to be in coincidence with the energy deposition of the incident neutron, since the time resolution of the cryogenic detector module is $\gg ns$. At $100keV$, the produced gamma with the energy of the excited level is usually absorbed by the target crystal, leading to a coincident nuclear and electron recoil. A zoom-in into the region of $100keV$ recoils is shown in figure 5.5 where the region with the observed inelastic tungsten recoils has been marked.

The inelastic tungsten recoils not only show up at the expected energy of $100keV$ to $120keV$, but also at lower and higher energies. The inelastic recoil band appears to be broadened by $\pm 10keV$. No systematic deviation in the calibration is observed after the combination of all 18 individually calibrated data sets. For each individual data set the expected resolution at $100keV$ is comparable ($\sim 1\%$) to the calibration measurement discussed in section 5.2.2 with an addition of a systematic shift to either lower or higher energies. The symmetric distribution to lower and higher energies of the observed inelastic recoils demonstrates that this systematic deviation cancels out, leading only to a line broadening that is estimated to be $\sim 10\%$. For the combined data, the uncertainty in the calibration can thus be treated as completely statistical. For the following discussion the *additional*[11] error at $100keV$ is 10%, decreasing linearily to lower energies (until it reaches $0keV$) and decreasing linearily to higher energies until the additional uncertainty is 0% at $200keV$, where the calibration is considered to be valid.

[9] Here, the $511keV$ line is not caused by positrons from a ^{22}Na-source but by ^{11}C decay. ^{11}C is produced in the nuclear reaction employed for the neutron production, $^{1}\mathrm{H}(^{11}\mathrm{B}, n)^{11}\mathrm{C}$.

[10] The W-isotopes, their natural abundance and excitation levels around $100keV$, from [129]:
^{180}W, 0.12%, 103.5 keV;
^{182}W, 26.5%, 100.1 keV;
^{183}W, 14.3%, 99.1 keV;
^{184}W, 14.3%, 111.2 keV;
^{186}W, 28.4%, 122.6 keV.
Excited levels are also at lower and higher energies, but the accumulation at $100 - 120keV$ leads to a visible band.

[11] The error is added to the general resolution of the detector, given by the width of the observed lines.

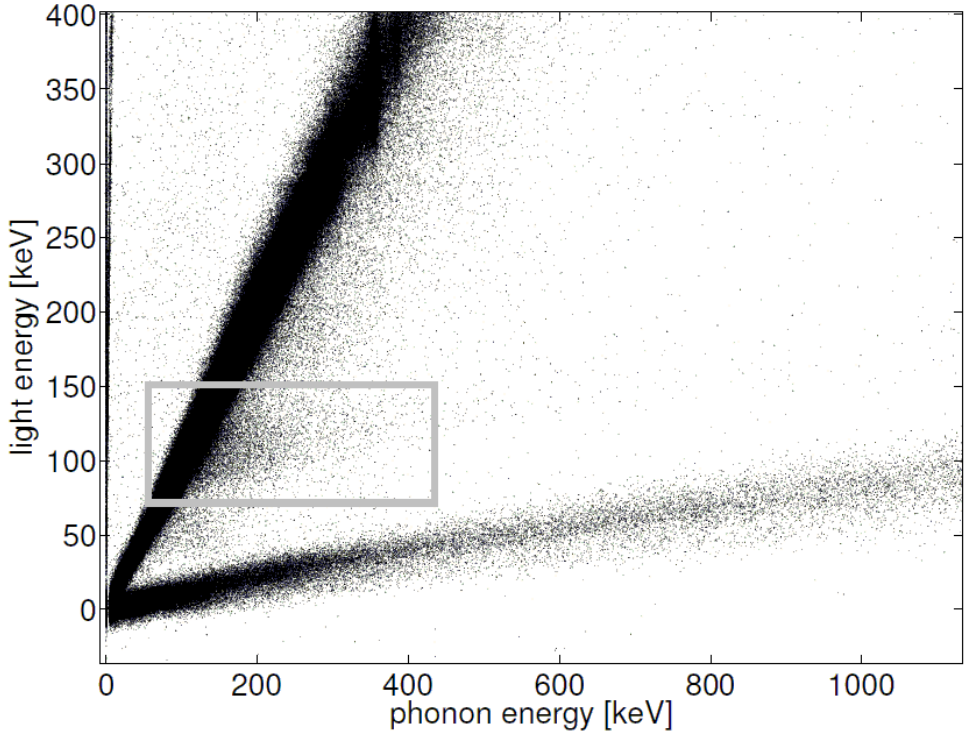

Figure 5.5: A zoom-in with higher statistics of figure 5.4 to the region where the inelastic tungsten recoils are expected (marked with a gray box). In this definition, an inelastic tungsten recoil is the combination of a nuclear recoil leaving the nucleus temporarily in an excited state, and the deexcitation gamma is absorbed in the target crystal. This process is visible as a superposition of a nuclear and an electron recoil, producing an event in between the two well defined bands. The excitation levels producing the marked band are at an energy of $\sim 100keV$ to $\sim 120keV$.

The Calibration Above 600keV The highest available gamma line for the calibration used is at $511keV$. Figure 5.6 shows the nuclear recoil band up to energies of $2.5MeV$. It can be seen that the slope of the nuclear recoil band is not constant. There are three possible reasons for this effect:

1. The calibration in the light channel is not correct. For higher light output the energy deposition is underestimated.

2. The calibration in the phonon channel is not correct. For an energy deposition above $\sim 600keV$ the deposited energy is overestimated.

3. The nuclear quenching factor is not constant but drops at higher energies.

The first possibility can be excluded since the light output for high energetic nuclear recoils is still low due to the scintillation light quenching. The deposited energy in the light detector is equal to an electron recoil of $50keV$ to $200keV$, where the calibration is reliable within the uncertainties discussed above. With no calibration data available above $600keV$, the possibility of a non-constant quenching factor can not be excluded. The observed alpha decays

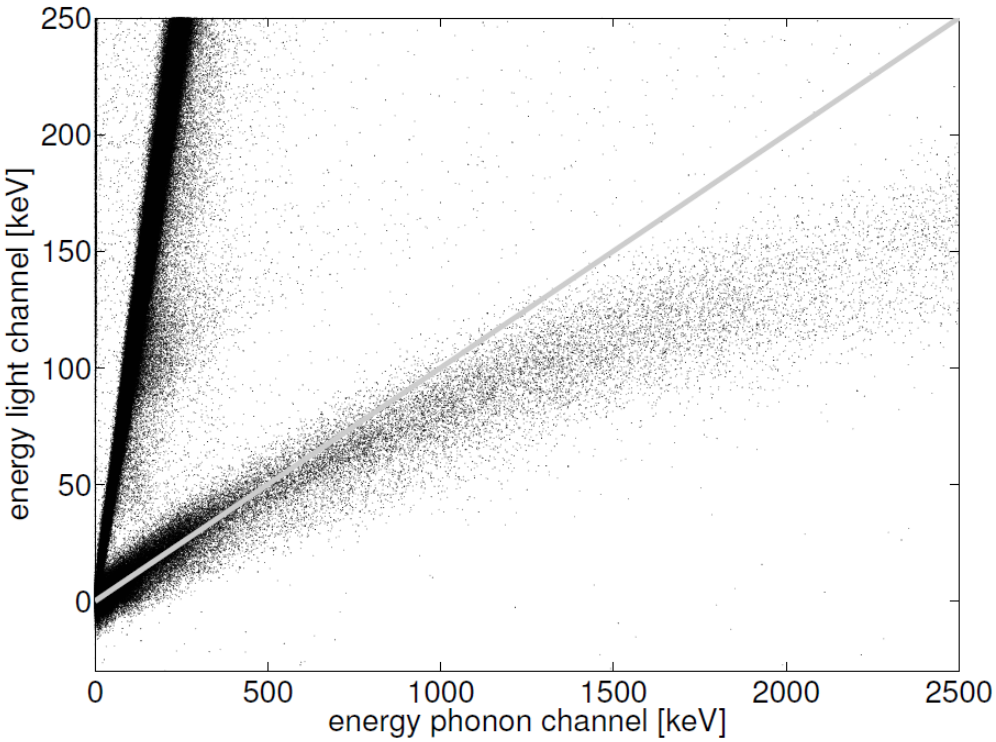

Figure 5.6: The nuclear recoil band for phonon energies up to $2.5MeV$ and the corresponding energy deposition in electron equivalent energy in the scintillation light channel. The gray line indicates the slope of the nuclear recoil band if the oxygen quenching factor is assumed to be 10, which is consistent with the slope observed for events up to $500keV$, where the calibration is considered to be reliable. If the nuclear quenching is constant up to energies of $2.5MeV$ and the calibration is correct, the nuclear recoil band is expected to follow the fitted line. The cause for the observed deviation is discussed in the text.

in the CRESST experiment shown in figure 2.7 and discussed in section 2.2.2.1 at energies of up to $5MeV$ suggest constant quenching factors, though. For the following discussion, a constant quenching factor is assumed accordingly, and the changing slope in the nuclear recoil band is attributed to a systematical deviation in the calibration of the phonon channel at high energies. If assuming a constant quenching factor (illustrated by the gray line in figure 5.6), the energy in the phonon channel is overestimated by $\sim 15\%$ at nuclear recoil energies of $1MeV$. For the quenching factor analysis in the last section of this chapter, the deviation in the calibration is assumed to be 30% towards lower energies for each keV above an energy of $600keV$. With higher energies, the error increases further, but this energy region is of no relevance for the analysis.

The Calibration between 200keV and 600keV Since gamma lines are available in this energy region, the calibration can be assumed to be valid here and the error is estimated to be equal to the 1σ-line width of the $356keV$ line, which is $\sigma_{356keV} = 3.5keV$.

5.3.3 Composition of the Nuclear Recoil Band and Resolution of the Scintillation Light Detector

For the quenching factor measurement, the resolution of the scintillation light detector in the region of interest is of crucial importance. The region of interest, which is $\sim 80{-}110keV$, is defined by the nuclear recoil energy of tungsten recoils induced by $\sim 8{-}11MeV$ neutrons scattered at an angle of 80°. Since the nuclear recoil band is composed of three overlapping distributions (from Ca, W and O), the resolution can not be extracted directly. The resolution of a single band can be obtained by a multi-component fit to the light yield, though. The light yield LY is defined as the observed energy E_L in the scintillation light channel divided by the observed energy in the phonon channel E_{Ph}: $LY \equiv E_L/E_{Ph}$ (see section 2.2.1). The LY for nuclear recoil events depositing $80 - 110keV$ in the phonon channel is shown in figure 5.7.

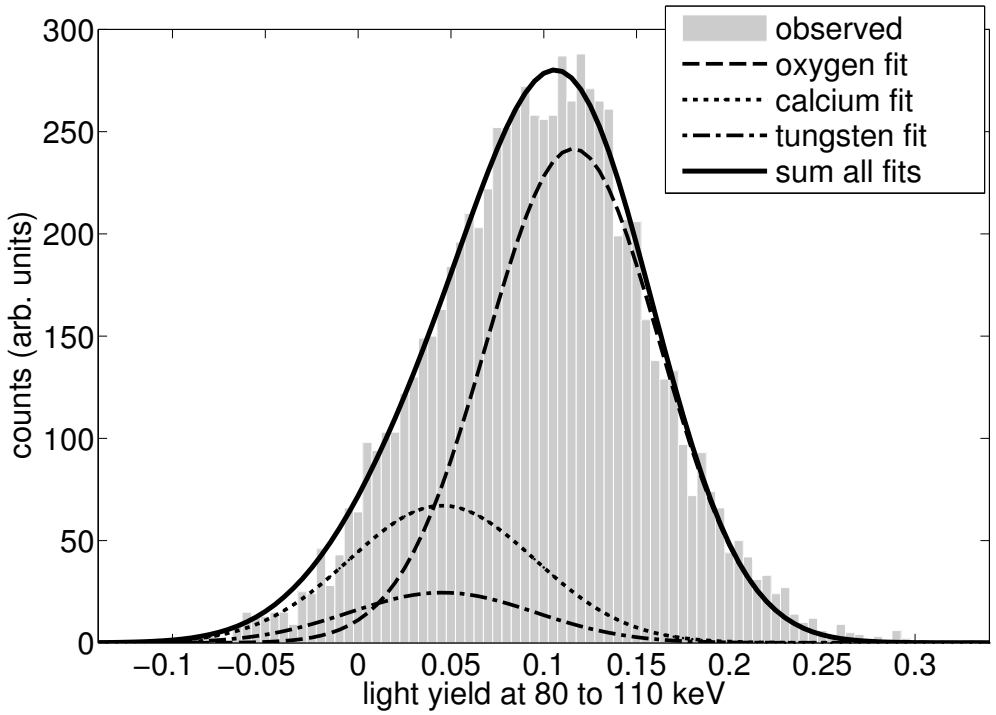

Figure 5.7: The histogrammed light yield as defined in the text for nuclear recoil events between $80keV$ and $110keV$ and the fits of the individual contributions from oxygen, calcium and tungsten. See the main text for details.

The correct description of the nuclear recoil band is a sum of three Gaussians:

$$F = A_O e^{-\frac{\left(x-\frac{1}{QF_O}\right)^2}{2\sigma_O^2}} + A_{Ca} e^{-\frac{\left(x-\frac{1}{QF_{Ca}}\right)^2}{2\sigma_{Ca}^2}} + A_W e^{-\frac{\left(x-\frac{1}{QF_W}\right)^2}{2\sigma_W^2}}. \qquad (5.1)$$

Here, $A_{O,Ca,W}$ are the contributions from each isotope, $QF_{O,Ca,W}$ their respective quenching factors and $\sigma_{O,Ca,W}$ the widths of all three Gaussians. Since the

resolution of the light detector is not sufficient to ensure a meaningful convergence of the fit, the simplification is made that all three Gaussians share the same width σ (which is assumed to be the resolution of the light detector). The function F fitted to the distribution is thus:

$$F = A_O e^{-\frac{\left(x-\frac{1}{QF_O}\right)^2}{2\sigma^2}} + A_{Ca} e^{-\frac{\left(x-\frac{1}{QF_{Ca}}\right)^2}{2\sigma^2}} + A_W e^{-\frac{\left(x-\frac{1}{QF_W}\right)^2}{2\sigma^2}}. \tag{5.2}$$

Strictly speaking, the three nuclear recoil bands do not have the same σ-width, since the contribution to the total resolution from photon statistics is different for each type of recoiling nucleus. But since the observed scintillation light output for all three nuclei is $\leq 15keV_{ee}$, the major contribution to the resolution is the intrinsic noise of the detector and not the photon statistics [114]. Additionally, the parameter space for the amplitudes and the quenching factors is confined to positive values[12]. The results of the fit and the 95% confidence

parameter	fit result	95% confidence bounds
A_O	241.6	(161.7, 321.4)
A_{Ca}	67.1	(-3.8e+07, 3.8e+07)
A_W	24.5	(-3.8e+07, 3.8e+07)
QF_O	8.6	(7.5, 9.7)
QF_{Ca}	22.1	(-2.0e+04, 2.0e+04)
QF_W	22.0	(-5.8e+04, 5.8e+04)
σ	0.047	(0.042, 0.051)

Table 5.3: The fit values for all free parameters in equation 5.2 after fitting the observed light yield for nuclear recoil events in the energy range from $80keV$ to $110keV$ as seen in figure 5.7. The contributions from calcium and tungsten can not be fixed, the two Gaussians for these contributions are highly correlated. The parameter of importance is the resolution σ, which can be extracted reliably.

bounds are shown in table 5.3: Oxygen recoils are well fitted, since they provide the highest contribution to the data. The contribution of calcium and tungsten is very small though and is only visible in the increased intensity to lower light yields compared to a single Gaussian. With the limited resolution of the light detector, it is not possible to fit two Gaussians to the left shoulder of the observed data. A total of two Gaussians is sufficient to describe the data, hence the large errors for the contributions of calcium and tungsten. Within the confidence bounds of the fit, the quenching factor of oxygen can be considered valid and is in agreement with the values observed in the CRESST experiment (see section 2.2.2.1). This fit was employed to extract the resolution of the light detector, which was produced reliably: It is found to be $\sigma = 0.047 \pm 0.05$. In appendix D this procedure is repeated for a two component fit, which is technically not the correct description of the nuclear recoil band but ensures the convergence of the fit without the need of imposing additional boundaries on

[12]Confining the parameter space for variables to physically reasonable values was found to be necessary to ensure the convergence of the fit at physical values. In the case at hand, one of the Gaussians is fitted with a highly negative amplitude.

the free parameters. Here, the resolution is found to be $\sigma' = 0.0466(16)$ when assuming the same width for both components. If the two components are fitted with an individual width for each Gaussian, the result is $\sigma_O = 0.050(2)$ for the major contribution of oxygen recoils and $\sigma_{Ca,W} = 0.034(5)$ for the small contribution of calcium and tungsten recoils. For all further discussion, the width $\sigma = 0.047 \pm 0.05$ from the three component fit is used.

If the resolution of the scintillation-light detector were sufficient, it would be possible to disentangle the components of the nuclear recoil band with such a fit and thus obtain the quenching factors. This approach was studied at higher recoil energies [130, 131], where the nuclear recoil bands are better separated. Ultimately, the same problems were encountered, though. This necessitated the time of flight measurement developed in the scope of the present work, allowing to identify the different contributions to the recoil band independently of the resolution of the scintillation light detector.

The observed σ-width translates directly into an observed resolution of the scintillation light detector at an energy deposition of $10keV$ electron equivalent of $\sigma_{L,10keV} = 4.7 \pm 0.5keV$[13]. Each individual Gaussian as well as the sum of all three is also shown in figure 5.7.

The spectral distribution of nuclear recoil events is shown in the upper part of figure 5.8. The small bump visible at a recoil energy (phonon energy) of $\sim 220keV$ is caused by a resonance at $\sim 1MeV$ in the cross section for elastic neutron scattering off oxygen [130,132]. With sufficient statistics, it can provide an independent means for the calibration of the nuclear recoil band [133]. The distribution of events in the nuclear recoil band will prove to be important when the discussion focuses on accidental coincidences in the next chapter, since these form the largest part of the background for the quenching factor analysis. The spectral distribution of accidental coincidences will follow the observed nuclear recoil spectrum. The fraction of nuclear recoils below a certain energy gives directly the probability of an accidental coincidence occurring above this threshold, (see lower part of figure 5.8). The figure is included here since it is derived from the observed nuclear recoil spectrum, it will be further discussed in section 6.2 of chapter 6.

[13] $10keV$ electron equivalent: For a quenching factor of 10, a nuclear recoil off oxygen at $100keV$ causes the energy deposition of $10keV$ in the scintillation light channel. A σ-width of 0.047 in the light yield at $100keV$ translates into a σ width in the light channel of $0.047 * 100keV$.

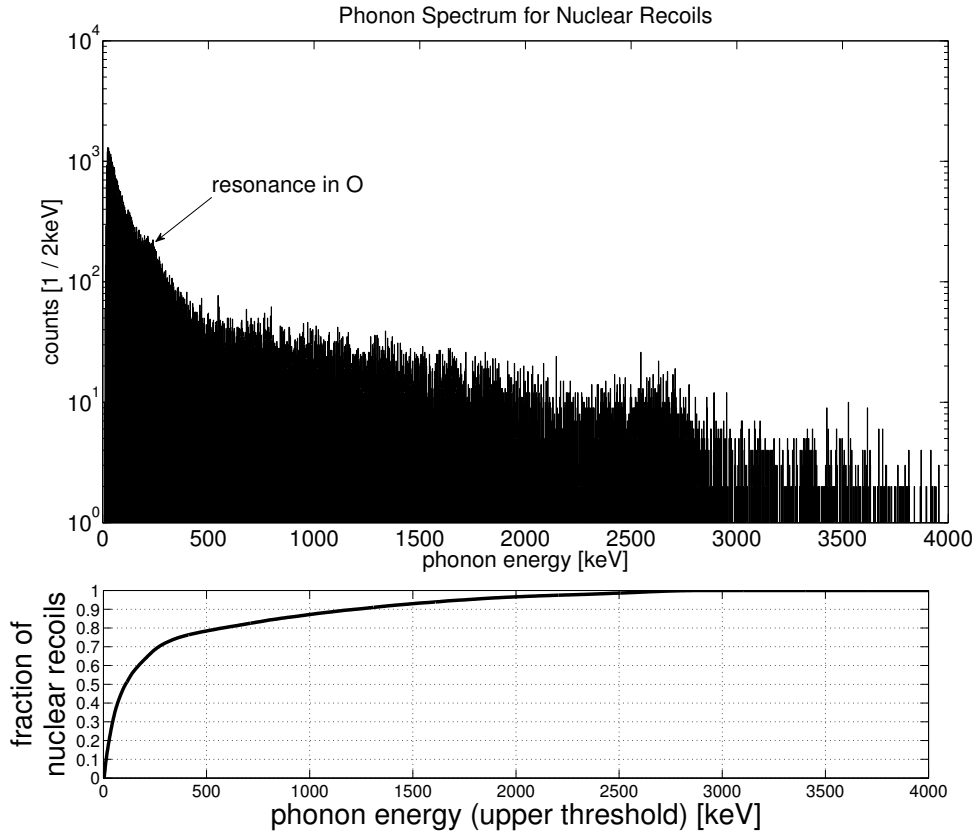

Figure 5.8: Upper panel: Calibrated nuclear recoil spectrum. Lower panel: Fraction of observed nuclear recoils below the energy threshold shown on the x-axis. The discussion in chapter 6 will refer to the lower figure. It is included here to illustrate its direct connection to the observed nuclear recoil spectrum.

Chapter 6

Beam Time Analysis II: Triple-Coincidences

In this chapter we describe the results obtained after applying the data analysis tools presented in chapter 4 to extract the events that were measured in triple coincidence. In combination with the results from chapter 5 this allows us to select the events suited for the quenching factor analysis.

In section 6.1, the general timing properties of the triple coincident events are evaluated and a suitable data set is selected. Section 6.2 focuses on the events suitable for the quenching factor analysis and presents a detailed analysis of the observed events and their underlying mechanisms. A summary of the results is given in section 6.3.

6.1 Triple-Coincidence Timing and the Signal Region

The threefold coincidence is between these three signals:

- Neutron production in the hydrogen cell, signal is given by the chopper. Timing precision: $\sim ns$.
- Neutron detection in the liquid scintillator array. Timing precision: $\sim ns$.
- Neutron induced event in the low temperature detector. Timing precision: $\sim 10\mu s$

The identification of events measured in triple coincidence is critically based on the algorithm determining the timing of the energy deposition in the cryogenic detector module. The timing properties can be tested by using hadronic showers that deposit energy in the cryogenic detector module in coincidence with an energy deposition in several of the neutron detectors. This is described in section 6.1.1. In section 6.1.2, all triple coincidences observed in the October

2010 beam time are identified and discussed, also the properties of events observed in threefold coincidence to be included for the quenching factor analysis are defined. The analysis will show that the bulk of neutron induced events are electron recoils, which are caused by gammas that were produced in inelastic neutron scattering. This is discussed in detail in section 6.1.3.

6.1.1 Testing the Triple-Coincidence Timing with Hadronic Showers

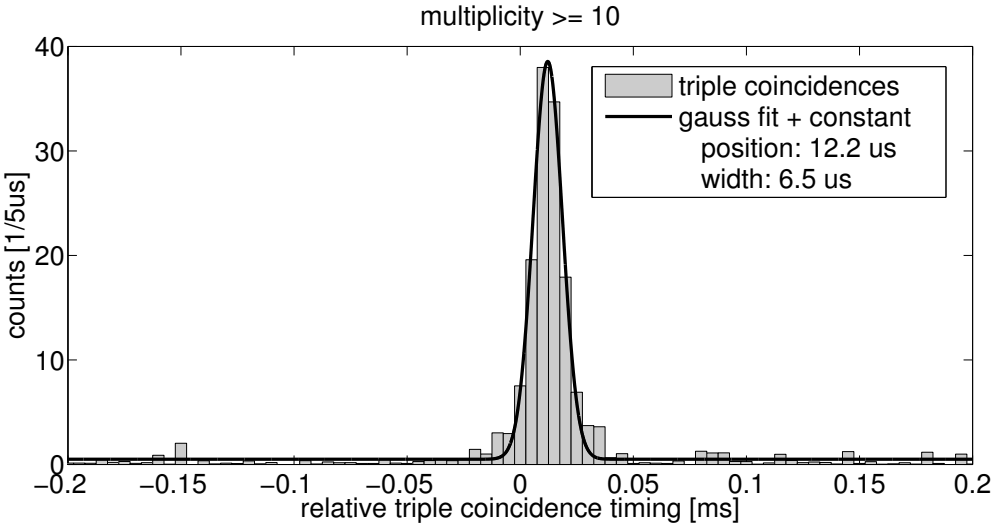

Figure 6.1: Hadronic shower events where more than 10 neutron detectors trigger at the same time (i.e. multiplicity ≥ 10). The time between an energy deposition in the low-temperature detector and the hits in the liquid scintillator array is shown. The position of the peak depends on the determination of the onset (see section 4.5.2). See the text for further details.

The experimental setup is located in hall 2 of the MLL and is thus exposed to hadronic and electromagnetic showers. These showers can be used to test the coincidence search, since hadronic showers will trigger several neutron detectors and possibly the cryogenic detector module. The difference to the real threefold coincidence is that it is not correlated to the neutron beam (i.e. the chopper signal). Since the timing between the chopper and the neutron production has a varying[1] offset of up to $3\mu s$, initially the window for the coincidence search has been kept wide open ($\pm 3\mu s$) to include all correct events and has only been narrowed down after the gamma peaks were correlated to the chopper pulse (see section 4.4.2). Due to the large coincidence window, also the hadronic shower events will show up. They are excluded later, due to their timing and

[1]Since it is possible to accept only one of 2^n chopped beam packages, changing n by one will change the timing by several μs, see section 3.2.1.2. The timing of the logical signal related to the chopper can shift in the same way.

high multiplicity, i.e. the number of triggered neutron detectors, they can be identified easily.

The data is searched for 10 or more neutron detectors triggering within a time window of $\sim 20ns$. The time difference between these 10 (or more) hits to the nearest hit (in time) in the cryodetector is shown in a histogram in figure 6.1. The timing information of a cryopulse is the onset, as extracted via the procedure discussed in section 4.5.2. When fitting a Gaussian plus a constant ($F = Ae^{-\frac{(x-b)^2}{2\sigma^2}} + c$, also shown in figure 6.1) to the coincidence peak, the parameters obtained are $b = 12.2 \pm 0.1\mu s$ and $\sigma = 6.5 \pm 0.1\mu s$. Two aspects are important here:

1. The timing resolution of the low-temperature detector is given by the width σ of the observed distribution. It is found to be $\sigma = 6.5 \pm 0.1\mu s$ for the events caused by hadronic showers. The timing resolution exceeds by several orders of magnitude the time of flight of a neutron, which is typically $\sim 50ns$ at the neutron scattering facility.

2. The position b of the coincidence peak is found to be $b = 12.2 \pm 0.1\mu s$. This means, that the energy deposition occurred on average $\sim 12.2\mu s$ before the determined onset position.

The causality of the triple coincidence, which is first the neutron production, then the scattering in the central detector and then the detection in the neutron detector array, *can thus not be reproduced in this order*. Instead, the energy deposition in the low-temperature detector will be detected after the neutron has been observed in the neutron detector array.

The spectral distribution of the energy deposition in the cryogenic detector for these events follows the distribution observed for all background gammas as seen in figure 5.3. Their mean energy deposition is $\sim 200keV$. As will be seen in section 6.1.2, the σ width decreases for the neutron-induced triple coincidences since the energy deposition in the target crystal is higher for these events and the time of the energy deposition can be extracted with higher accuracy.

6.1.2 Definition of a Suitable Data Set for the Quenching Factor Analysis

After the calculation of the incident neutron energy for all triple coincidence candidates as discussed in section 4.4.3, the neutrons within an energy range of $2-15MeV$ are selected. Additionally, only events are accepted where not more than one neutron detector triggers in this time windows to avoid ambiguity and to completely remove the shower events discussed in section 6.1.1.

Similarly to the hadronic shower events discussed in section 6.1.1, the time difference between the energy deposition in the cryogenic detector module and the detection of the produced neutron is shown in figure 6.2 for events fulfilling the following conditions:

- The event in the neutron detector array must be identified as a nuclear recoil (i.e. must be a neutron and not a gamma).
- The energy of the neutron must be between 2 and $15MeV$ (calculated via the ToF as described in section 4.4.3).
- Not more than one neutron detector must have triggered (i.e. the multiplicity of the event is 1).
- Individual cuts for the three different histograms in figure 6.2:
  - The histogram with high intensity (gray) shows all events in the cryogenic detector module and thus includes all possible triple coincidence candidates, i.e. electron recoils, nuclear recoils, inelastics and the other event types as defined in section 5.3.1.
  - The data shown in black contains only events that were identified as nuclear recoils in the cryogenic detector module.
  - The data shown in white only includes events identified as nuclear recoils in the cryogenic detector module that are caused by neutrons with an incident energy of more than $7MeV$.

As discussed in section 6.1.1, due to the timing resolution of the cryodetector it is not possible to resolve the neutron production, the scattering process and the detection in the order they occurred. The correct signal region is defined by the observed position of the neutron induced coincidence peak. It can be quantified by fitting the coincidence peak with a Gaussian plus a constant:

$$F = Ae^{-\frac{(x-b)^2}{2\sigma^2}} + c. \tag{6.1}$$

Applying this fit to all observed coincidence candidates (i.e. the gray area in figure 6.2), gives for the free parameters and their 95% confidence bounds an amplitude of $A = (139 \pm 14)/5\mu s = (27.9 \pm 2.8)/\mu s$, a peak position of $b = (11.0 \pm 0.1)\ \mu s$, a width of $\sigma = (5.5 \pm 0.1)\ \mu s$, and a constant of $c = (60.4 \pm 2.1)/5\mu s = (12.0 \pm 0.4)/\mu s$. Accepting only events within two standard deviations around the peak position, the ratio[2] of real coincidences (derived from the amplitude A) to accidental coincidences (derived from the constant c) is 1.38. The nature of the observed events in the (gray) triple coincidence peak, which (possibly against intuition[3]) consist mostly of electron recoils, are discussed in detail in section 6.1.3.

[2] calculated as $(N_{[b-2\sigma,b+2\sigma]} - 4\sigma c)/(4\sigma c)$, with $N_{[-\epsilon,+\epsilon]}$ being the number of events between the times $\pm\epsilon$, here chosen 2σ around the peak position. $4\sigma c$ is the number of observed accidental coincidences in the same region.

[3] Since the events in the triple coincidence peak are linked to the detection of a neutron in the neutron detector array detected with the correct time of flight after the interaction of the ^{11}B beam in the hydrogen cell, the neutron induced interaction might be expected to be a nuclear recoil. However, as is seen in figure 6.2 and further discussed in section 6.1.3.1 most events are due to electron recoils.

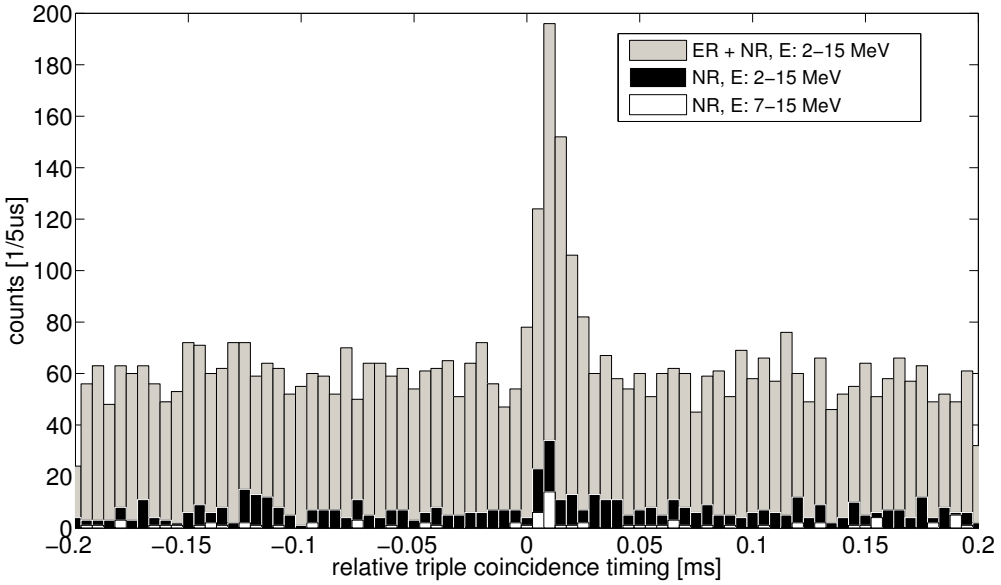

Figure 6.2: Triple coincidence timing spectra. On the x-axis the time difference between an energy deposition in the neutron detector array and an energy deposition in the cryogenic detector module is shown. A positive time means that the energy deposition in the cryodetector was identified after the neutron detection in the liquid scintillator array. For true triple coincidences, the correct sequence of events is at first the neutron production, then the scattering in the cryogenic detector and then the detection of the neutron in the neutron detector array. Due to the timing resolution of the cryodetector being $\sim 10\mu s$, this can not be resolved in this sequence (see the main text). The highest (gray) histogram includes all triple coincidences that were observed in the October 2010 beam time. Most of these events show up as electron recoils (ER) in the cryogenic detector module: the black histogram is the same data as in the gray histogram after removing all electron recoils and only accepting nuclear recoils (NR) in the cryodetector (in every case, a neutron has been observed in the neutron detector array!). For the data shown in black, a high number of unrelated accidental coincidences remains (as seen in the constant offset). The number of accidental coincidences is much lower when only high energetic neutrons (identified by their time of flight) are included in the analysis, as is seen in the white histogram (where only incident neutron energies above $7MeV$ are accepted). See the text for further discussion.

The ratio of real to accidental coincidences becomes considerably higher if not all events are included in the coincidence search but only events that are detected as nuclear recoils in the cryogenic detector module. Triple coincidence data after the nuclear recoil cut is also included in figure 6.2: the two data sets in black and white include only events that are clearly identified as nuclear recoils (as defined in section 5.3.1) in the cryogenic detector module, once for incident neutron energies of $2 - 15MeV$ (black) and once only for incident neutron energies above $7MeV$ (white). To obtain the best ratio between real and accidental coincidences, analysis thresholds between incident neutron energies from 2 to 10 MeV have been tested and fitted by equation 6.1 in $1MeV$ steps. The obtained values for the free parameters of the fit and their 95% confidence bounds are shown in table 6.1. As can be seen, the σ width of the

$E_{n,thresh}$ MeV	A $1/\mu s$	b μs	σ μs	c $1/\mu s$	Signal (S)	bg. (B)	S/B
2	6.9(1.8)	8.7(9)	3.0(9)	1.64(27)	49.4	19.6	2.5
3	6.8(1.5)	8.6(6)	2.4(6)	1.12(16)	39.2	10.8	3.6
4	6.3(1.3)	9.0(5)	2.1(5)	0.72(14)	32.0	6.0	5.3
5	4.8(1.2)	8.5(5)	1.9(6)	0.44(16)	22.6	3.4	6.6
6	3.7(0.9)	8.4(6)	2.4(6)	0.29(16)	21.2	2.8	7.6
7	3.5(0.7)	8.5(6)	2.3(6)	0.19(12)	19.2	1.8	10.7
8	2.3(0.6)	8.8(8)	2.6(8)	0.14(10)	14.6	1.4	10.4
9	2.2(0.7)	8.3(7)	2.4(8)	0.11(08)	13	1.0	13.0
10	1.9(0.9)	7.2(8)	2.6(6)	0.08(06)	12	1.0	12.0

Table 6.1: Results for the triple coincidence peak of data taking into account only nuclear recoils in the cryogenic detector module and incident neutron energies above $E_{n,thresh}$. The table shows the fit results for the amplitude A, position b, width σ and constant c of equation 6.1. The column denoted as signal (S) are the number of observed events in an interval of $\pm 2\sigma$ around the peak position b with the background $4\sigma c$ subtracted. Estimated Background (B) is the calculated number of accidental coincidences derived from the constant c and the acceptance window, thus $B = 4\sigma c$. The ratio of observed real coincidences to accidentals is shown in the last column, S/B. The numbers in parentheses are the 95% confidence level error margins of the fits.

triple coincidence peak for each fitted nuclear recoil data set is smaller compared to (a) the fit values obtained for the hadronic showers (see section 6.1.1, $\sigma_{hadronic} = 6.5(1)\mu s$) and (b) the complete triple-coincidence data set (i.e. electron and nuclear recoils, where the obtained value was $\sigma_{ER+NR} = 5.5(1)\mu s$). This can be understood when comparing the energy deposition. It is higher for triple coincidences producing nuclear recoil events compared to shower events or triple coincidences producing electron recoils:

- The mean energy deposition for shower events is $\sim 200keV$.
- The mean energy deposition is $\sim 590keV$ for *all* neutron induced triple coincidences.

- The mean energy deposition is $\sim 630keV$ for triple coincidences observed with a nuclear recoil in the low-temperature detector.

The higher energy deposition allows to identify the onset with a higher accuracy. This is also reflected in the systematically lower values of the fitted peak position b: $b = (12.2 \pm 0.1)\mu s$ for shower events, $b = (11.0 \pm 0.1)\mu s$ for neutron induced coincidences, $b \leq 9.0\mu s$ for triple coincidences producing nuclear recoils.

The values of the fit allow to confine the actual signal region for the triple coincidence analysis. We define it to be $\pm 2\sigma$ around the peak position b. The number of observed real triple coincidences is given by the total number of events in that time window ($N_{[b-2\sigma,b+2\sigma]}$) decreased by the number of observed accidental coincidences which is derived from the constant $N_{accidental} = 4\sigma c$. The column denoted as signal (S) contains these values after subtraction of the estimated background ($B = 4\sigma c$) shown in the next to last column. The sum of these columns thus give the total number of events in the defined time windows, $N_{[b-2\sigma,b+2\sigma]}$, and the last column shows the signal to background ratio based on these results.

The obtained values for S/B show that incident neutron energies above $7MeV$ are well suited for the triple coincidence analysis while for lower incident neutron energies the background becomes higher. Above $7MeV$, $\sim$19 real and $\sim$2 accidental coincidences are expected. These numbers are based on all data available for the October 2010 beam time, which equals $\sim$3.5 days of total beam time.

6.1.3 Discussion of Neutron-Induced Electron Recoils and Low-Energetic Neutrons

For the triple coincidence search, the data analysis chain only includes events in the liquid scintillator array that were (a) detected after the correct time of flight and (b) identified as a neutron (based on the pulse shape analysis). The corresponding events found in the low-temperature detector are thus neutron induced. The majority of these events show up as electron recoils. This is explained in section 6.1.3.1.

As can be seen in table 6.1, below an incident neutron energy of $7MeV$ the number of accidental coincidences rises steeply at low energies. This behaviour is discussed in section 6.1.3.2.

6.1.3.1 Neutron-Induced Electron Recoils

For the data shown in figure 6.2 the analysis included only events that were detected as neutrons in the neutron detector array with the correct time of flight. Thus, the events in the peak are considered to be neutron induced. The properties of the observed triple coincidence distribution is shown for two data sets in table 6.2. TC denotes the data set including all triple coincidences, i.e.

the gray histogram in figure 6.2, while $TC7$ includes only events that have been linked to incident neutron energies above $7MeV$. As previously, the listed values correspond to the free parameters in equation 6.1, which has been fitted to both distributions. The next to last column, headed $N_{[b-2\sigma,b+2\sigma]}$ gives the number

	A $1/\mu s$	b μs	σ μs	c $1/\mu s$	$N_{[b-2\sigma,b+2\sigma]}$	$4\sigma c$
TC	27.9(2.8)	11.0(1)	5.5(1)	12.0(4)	609	264.0
TC7	4.6(8)	8.8(6)	3.1(6)	1.3(1)	62	16.1

Table 6.2: The properties of the triple coincidence peaks once induced by all neutrons (TC) and once by neutrons with incident energies above $7MeV$ ($TC7$). The values, obtained by fitting, correspond to the free parameters in equation 6.1. TC and TC7 include all types of observed events, which is different to table 6.1, where only nuclear recoils were included.

of events within $\pm 2\sigma$ around the position b of the triple coincidence peak. The last column shows the expected number of accidental coincidences in this time window, which is $4\sigma c$. The triple coincidence peak contains all observed event types defined in section 5.3.1 (while table 6.1 shown on page 128 included only nuclear recoils). Following the event-type definition of section 5.3.1, the nature of the events in the data sets TC and $TC7$ are classified as listed in table 6.3. For reference, the table also includes the nature of uncorrelated events, i.e. events not measured in triple coincidence, as they were listed in table 5.2. The observed accidental coincidences, which are $\sim$264 for TC and $\sim$16 for $TC7$ as listed in table 6.2, are expected to follow the distribution of these uncorrelated events. Consequently, they can be subtracted according to their relative frequency (as given by the % values in the second column of table 6.3) from the observed data, thus the real composition of the observed triple coincidences is obtained. The numbers after subtraction are shown in the last two columns, TC^* and $TC7^*$, respectively. After the subtraction of all accidental coincidences it becomes apparent, that only 19.3% of all neutron induced events show up as nuclear recoils. For higher incident neutron energies, more neutron induced nuclear recoils are observed, e.g. 47% for energies above $7MeV$.

Since the observed electron recoil events must be neutron induced, the processes have to be inelastic. Two classes of inelastic recoils can occur:

- **Inelastic Processes in the Surrounding Material** The mass of the detector is low compared to the total surrounding mass of the cryostat, the radiation shield, the internal vacuum chamber and helium bath. Neutrons scattering in these materials (mainly copper, iron and aluminum) can produce gammas in inelastic processes that can be detected in the neutron detector while the scattered neutron is detected in the neutron detector array.
- **Inelastic Processes in the Detector Material** Inelastic processes can

	uncorrelated	TC	TC7	TC*	TC7*
NR	9.0%	14.6%(92)	37.1%(23)	19.3%(68)	47%(22)
IE	2.1%	3.3%(21)	0.0%(0)	-	-
ER	85.0%	80.2%(504)	62.9%(39)	79.8%(280)	53%(25)
PL	0.9%	0.7%(4)	0.0%(0)	0.6%(2)	-
L	2.0%	0.7%(4)	0.0%(0)	-	-
LED	0.8%	0.5%(3)	0.0%(0)	0.3%(1)	-

Table 6.3: Distribution of events in the cryogenic detector module for different data sets. *Uncorrelated* means that the events did not fulfill the triple coincidence condition. They are included here for reference and their relative distribution is given in %. They are taken from table 5.2 and were derived in the respective chapter. As previously defined, the data set *TC* includes all neutron induced triple coincidences for all incident neutron energies and and *TC7* only triple coincidences for incident neutron energies above $7MeV$. As listed in table 6.2, *TC* and *TC7* include a total of 609 events and 62, respectively. The classification of the event type follows the definition in section 5.3.1 of the previous chapter: *ER* (pure electron recoil), *NR* (pure nuclear recoil), *IE* (inelastic, between the electron and nuclear recoil band), *PL* (event in the target crystal in coincidence with an additional energy deposition in the light detector), *L* (direct light detector hit) and *LED* (LED pulse). The numbers in parentheses are the observed numbers of the corresponding events.
The number of expected accidental coincidences is ∼264 events for the *TC*, and ∼16 for the *TC7* data (see last column of table 6.2). Since these accidental coincidences are uncorrelated, they are assumed to follow the general distribution of events as listed in the first column. Subtracting 264 and 16 events distributed among the event classes as given in column *uncorrelated* from the values listed in columns *TC* and *TC*7 gives the numbers shown in the last two columns, *TC** and *TC7**, respectively. The numbers in parentheses here are the numbers of events after the subtraction and give the composition of the observed triple coincidences.

occur directly in the $CaWO_4$ crystal. In such a process, part of the energy transfer can be considered elastic, i.e. it induces a nuclear recoil. The other part of the energy leads to an excited nucleus, and the gamma produced in the deexcitation process can induce an electron recoil. If the 'elastic' part of the energy transfer to the nucleus is very low while the energy deposition by the gamma is high, the process will appear completely electron-recoil like.

The upper panel in figure 6.3 shows the neutron energies as derived from the time of flight between the hydrogen cell and the neutron detector array for *uncorrelated* (i.e. not linked to a triple coincidence) neutrons. The middle panel in figure 6.3 only shows energies of neutrons that were detected in triple coincidence. It can be seen that the neutron energies are considerably lower in this case. Each neutron that was detected in the neutron detector array requires at least one scattering process since the detector arrays are shielded from the direct neutron beam; this is also true for the *uncorrelated* neutrons. For most materials, the energy loss in the scattering process is very low since the possi-

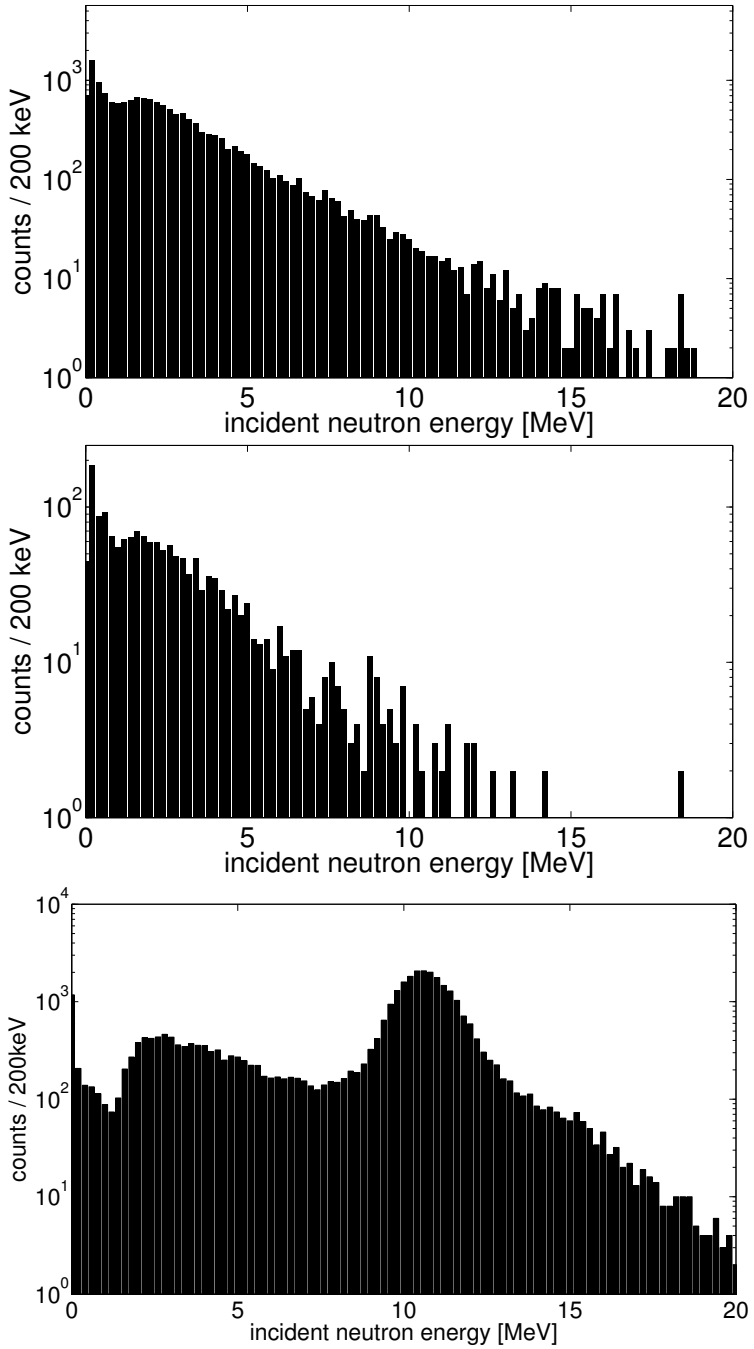

Figure 6.3: Neutron energies seen in the neutron detectors as derived from the neutrons' time of flight between production and detection.
Upper panel: Scattered uncorrelated neutrons (i.e. not detected with an energy deposition in the cryogenic detector) detected in the side detector array.
Middle panel: Scattered correlated neutrons (i.e. measured in triple coincidence) detected in the side detector array.
Lower panel: Neutron energies as measured on the optical axis of the beam, i.e. the unscattered spectrum.

ble targets (aluminum, iron, copper) are much heavier than the neutron. An exception is the liquid helium in the dewar, but simulations [96] and measurements [130] showed that due to the low density and the slim dewar scattering off helium can be neglected. The observed high energy loss of several MeV of neutrons that are linked to an energy deposition in the cryogenic detector (and this high energy loss of several MeV is not detected in the cryogenic detector but only a fraction of it) can thus only be due to an energy loss in inelastic processes. The excited nuclei can cascade to their ground state, producing one or several gammas in the process which can deposit their energy in the cryogenic detector, showing up as an electron recoil linked to a neutron scattering process.

6.1.3.2 Incident Neutron Energies below 7 MeV

As was discussed in section 6.1.2, incident neutron energies below $7MeV$ are not well suited for the triple coincidence analysis due to the high number of observed accidental coincidences. This can be understood when comparing the general spectral energy distribution of scattered neutrons, as seen in the upper and middle panel in figure 6.3, with the energy distribution observed for the unscattered neutrons, as shown in the lower panel of figure 6.3:
The bulk of the neutrons are produced at $10.6MeV$ as is expected from the nuclear reaction $^{1}\mathrm{H}(^{11}\mathrm{B}, n)^{11}\mathrm{C}$ as described in section 3.2.2. This peak is the most apparent feature in the energy spectrum for unscattered neutrons, as seen in the measurement. The spectral distribution of the scattered neutrons on the other hand is just showing an exponential decay to higher energies and apart from that is completely featureless. This is unexpected for neutrons scattering a single time in the central detector or the direct vicinity. Due to the measurement technique, neutrons appear at lower energies if their flight path does not follow the path indicated in figure 4.6 but is prolonged by scattering off materials in the vicinity of the experimental setup, even if not much energy is lost in these scattering processes. This is also visible in the energy threshold: for neutrons measured on the optical axis of the beam (lowest panel), the energy deposition in the neutron detector is not sufficient for pulse shape discrimination for neutrons with energies below $2MeV$, thus the reduction of intensity in the spectrum. For the scattered neutrons, this is not visible. Consequently, for neutrons with a long time of flight, their kinetic energy is drastically underestimated. Effectively this means that only neutrons detected at a short time of flight, which are linked to the highest neutron energies and the shortest path to the detector array, give a sensible result. Long time of flights (or apparently low incident neutron energies) on the other hand are contaminated by neutrons detected in the detector array after an undefined path, thus neither a scattering angle nor a neutron energy are defined for these events. With this an mind, the analysis threshold of $7MeV$ is justified.

6.2 Evaluation of the Events Used for the Quenching Factor Measurement

As discussed in the previous section, nuclear recoils in the low-temperature detector induced by neutrons with an incident energy above $7MeV$ are good candidates for quenching factor analysis. The following section 6.2.1 describes the expected distribution of the observed events depending on the type of scattering process, section 6.2.2 focuses on all measurement uncertainties in the setup that have to be considered for the accepted events and the last section 6.2.3 discusses the observed 21 events.

6.2.1 Expected Triple-Coincidence Distribution Based on Measured Cross Sections and Simulations

For the triple coincidence analysis, only events that lie in the nuclear recoil band of the cryogenic detector module have been selected. The observed events can be attributed to one of the following mechanisms:

- elastic scatters
- inelastic scatters
- multiple scatters
- accidental coincidences

Each mechanism and its likelihood will be discussed in the following paragraphs.

Elastic Scatters As listed in table 6.1, for incident neutron energies above $7MeV$, $\sim$ 19.2 nuclear recoils induced by neutrons scattered by an angle of 80° are observed. The relative angular dependent cross section for neutrons scattering elastically off $CaWO_4$ with an incident neutron energy of $\sim 11MeV$ is shown in figure 6.4 as published in the ENDF data [132]. The cross section of oxygen has been multiplied by 4 to account for the stoichiometric composition in $CaWO_4$. The position of the neutron detectors is at 80° where the cross section for tungsten recoils has a maximum. Due to the finite size of the detector they cover a scattering angle from 78° to 82°. For this solid angle, 64% of all elastic scatters are expected to be off oxygen, 33% off tungsten and 3% off calcium.

In an elastic scattering process, the energy transfer to each nucleus is fixed for each scattering angle and only dependent on the incident neutron energy, E_n. For nuclear recoils detected under a scattering angle of 80°, the energy transfer to each nucleus is as follows:

- 9.7% of E_n for oxygen recoils ($\sim 1.03MeV$ for $E_n = 10.6MeV$)
- 4.2% of E_n for calcium recoils ($\sim 445keV$ for $E_n = 10.6MeV$)

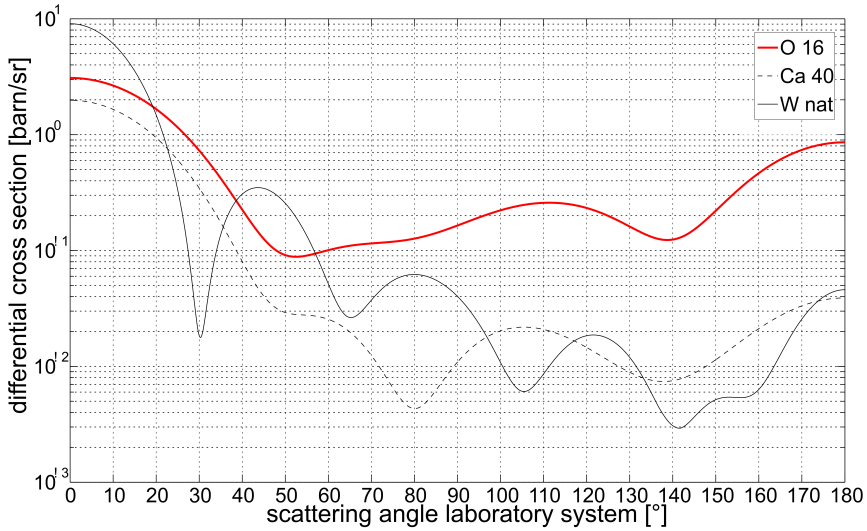

Figure 6.4: Angular dependent relative cross sections for neutrons scattering elastically off the constituents of a $CaWO_4$ crystal for incident neutron energies of $\sim 11MeV$.

- 1.0% of E_n for tungsten recoils ($\sim 106keV$ for $E_n = 10.6MeV$)

Inelastic Scatters Inelastic scatters off a nucleus leave the nucleus after the scattering process in an excited state. Since the deexcitation happens on a timescale that is much smaller than the timing resolution of the cryogenic detector, the gamma produced in the deexcitation process can be considered to be coincident with the scattering process. If the gamma deposits sufficient energy in the $CaWO_4$ crystal, the event will no longer be recognized as a nuclear recoil and will thus be discarded for the quenching factor analysis. Especially for inelastic recoils of higher energies the produced gamma has a high chance of escaping the detector without further energy deposition. In this case the induced inelastic nuclear recoil is similar to an elastic recoil induced by a neutron with its incident energy reduced by the energy required for the excitation of the nucleus[4]. The energy reduction of the incident neutron is underestimated in the calculation of the incident neutron energy described in section 4.4.3 since the total time of flight is shorter because the neutron carries an energy higher on the path s_1 in figure 4.6 than is derived by E_{loss} and the total time of flight. This is especially relevant for inelastic excitations with an energy of several MeV since this leads to a significantly reduced time of flight for s_1 and thus a (slightly) reduced total time of flight. For example, a $11MeV$ neutron requires $\sim 9ns$ for $s_1 = 0.4m$. An inelastic interaction with oxygen and a subsequent deflection by 80° requires $\sim 6.5MeV$, with $6MeV$ not visible in the detector (since the

[4]A precise calculation including momentum conservation actually lowers the energy of the incident neutrons further, but since the nucleus is heavier by at least a factor of 16 compared to the neutron this effect can be neglected in first order.

deexcitation gamma escapes) and 0.5 MeV transferred onto the oxygen nucleus visible as a nuclear recoil. The neutron is left with a kinetic energy of $4.5MeV$, thus for $s_2 = 1.5m$ it requires $\sim 53ns$. Consequently it is detected with a measured total time of flight of $53ns + 9ns = 62ns$ and an energy deposition in the central detector of $500keV$. However, if the incident neutron energy is now calculated according to section 4.4.3, the result is $\sim 5.7MeV$ while the actual incident energy (after subtraction of the energy required for the inelastic process) is $11 - 6 = 5MeV$. For the observed long ToFs of these processes, this difference of $0.7MeV$ is significant.

In the case of oxygen, where the inelastic levels are at very high energies ($\geq 5.7MeV$) and the effect just described is consequently large, the total cross section for inelastic processes is ~ 2.5 times lower than for elastic processes for incident neutron energies of $\sim 11MeV$(see [132]). The number of inelastic oxygen recoils can thus not be discarded, but with the lowest excitation level of oxygen being at $\sim 5.7MeV$, they show up at measured incident neutron energies below $\sim 6MeV$ (equaling a real incident energy of $11MeV$), and are thus not included in the signal region of $7 - 11MeV$ neutrons.

For tungsten, where the inelastic levels start at much lower energies ($50keV$) and the relative cross section is lower, the effect can be completely neglected.

Multiple Scatters Estimations [86] and simulations [96] show that for the geometry of the employed cryogenic detector (cylindrical, $20mm$ x $5mm$) $\sim 7\%$ of multiple scatters are expected. A multiple scattering event of a neutron detected at a specific angle will have deposited more energy in the cryogenic detector module than is expected from a single-scattered neutron (for the respective target nucleus) that is detected at the same scattering angle.

Accidental Coincidences Accidental coincidences are not correlated to the incident neutron they have been accidentally matched to. Thus the energy distribution of these events will follow the general spectral distribution of nuclear recoils as shown in figure 5.8. The lower part of this figure shows the fraction of nuclear recoil events below a certain threshold energy. For example, above an energy of $700keV$, where all elastic scattering events off oxygen are expected, not more than 20% of all accidental coincidences are expected. Since most accidental coincidences are expected at low energies, they are mainly a background source for the tungsten recoils, which are expected at nuclear recoil energies of $\sim 100keV$ for incident neutron energies of $\sim 10MeV$.

6.2.2 Error Estimation

As has been discussed in section 5.3.2, the error in the calibration below 200 keV deposited energy in the phonon channel can be treated statistically. The error in the calibration above 600 keV is dominated by systematic effects; the phonon energy is overestimated by $\sim 15\%$ at nuclear recoil energies of 1 MeV.

The major part of the error is due to the uncertainty in the determination of the neutron energy, which is based on the following parameters:

- Time of flight: The 1σ-timing resolution of the neutron detectors is estimated to be $1.1\,ns$ (as discussed in section 3.3.3). The observed 1σ-width of the gamma peak caused by the interaction of the ^{11}B-beam with the hydrogen cell is $1.49ns$ as observed in section 3.2.3. The latter value is used for the uncertainty of the time of flight measurement. The time of flight for $11\,MeV$ neutrons is $\sim 41.8\,ns$ for a distance of $190\,cm$ (which is the total path length the neutrons travel between production and detection). An error of $\pm 1.49\,ns$ translates to an error of $\sim \pm 0.85\,MeV$ for $11\,MeV$ neutrons (relative error: $\sim$7%). With lower neutron energies (and thus a longer time of flight) the relative error is reduced: For a time of flight of $80ns$ (belonging to neutrons with an energy of $3.0MeV$), the same error translates to an uncertainty of $\pm 0.1MeV$ of the kinetic energy of the neutron (relative error: $\sim$3%).

- Distance: The distance between the hydrogen cell and the cryogenic detector, s_1, as well as the distance between the cryogenic detector and each neutron detector, s_2, has been measured precisely. Still, the finite space of the target crystal ($2\,cm$) and the hydrogen cell ($4\,cm$) introduces a 1σ error of $\pm 1.4\,cm$ (adding the errors quadratically) for s_1. Due to the depth of the liquid scintillator cell of $10\,cm$ and the crystal size ($2\,cm$) an error of $\pm 3.3\,cm$ is assumed for s_2. An error of $\pm 3.6cm$ for $s_1 + s_2 = 190cm$ translates to an error of $\sim 0.41\,MeV$ for neutron energies of $11MeV$.

- Scattering angle: The neutron detectors have been placed at a scattering angle of 80°. The distance to the cryogenic detector is $\sim 155cm$ and the side of the liquid scintillator cell facing the detector has a width of $5\,cm$. This translates to an uncertainty in the scattering angle of $\pm 2°$. This changes the energy transfer to the nucleus, which, if treated as an additional error in the incident neutron energy, amounts to an error of $0.5\,MeV$ for incident neutron energies of $11\,MeV$.

For $11MeV$ neutrons, the total 1σ-error adds up to

$$\sigma_{11MeV} = \sqrt{0.85^2 + 0.41^2 + 0.5^2} MeV \approx 1.07 MeV.$$

The error is calculated for all incident neutron energies based on the discussed uncertainties. The observed nuclear recoil energy for a fixed scattering angle is a fraction of the incident neutron energy (see section 6.2.1). The discussed error for the incident neutron energy translates accordingly to an error of the recoil energy: For a scattering angle of θ =80° and an error of $1.07MeV$ estimated for an incident neutron energy of $11MeV$, the error amounts to $\sim \pm 102keV$ for oxygen recoils, $\sim \pm 45keV$ for calcium and $\sim \pm 11keV$ for tungsten recoils.

6.2.3 Observed Events for the Evaluation of the Quenching Factor

Table 6.1 (see section 6.1) lists the properties of the observed triple coincidence peaks and the underlying accidental coincidences for the following cuts:

- Multiplicity is 1, i.e. only one neutron detector has triggered.
- The neutron detector that has triggered has detected a neutron.
- A nuclear recoil has been detected in the cryogenic detector module.

For incident neutron energies above $7MeV$, the triple coincidence peak is at a position of $\sim 8.5\mu s$ with a σ width of $2.3\mu s$. Accepting events within 2σ around the peak position, i.e. from $3.9\mu s$ to $13.1\mu s$, 21 events are within these bounds. Two of these are expected to be accidental coincidences. Figure 6.5 shows the energy deposition in the phonon channel for all observed 21 events plotted against the calculated incident neutron energy. The error bars are the errors of the calibration that have been discussed in section 5.3.2. The dotted black lines show the expected recoil energies for oxygen (energy transfer is 9.7% of incident neutron energy), calcium (4.2% energy transfer) and tungsten (lowest dotted line, 0.1% energy transfer). The solid and dashed gray lines around each of the dotted black lines indicate the 1σ and 3σ errors of the expected energy transfer based on the error of the measured incident neutron energy, as discussed in section 6.2.2.

The 21 observed events are either elastic single or multiple scatters, inelastic processes or accidental coincidences. A detailed discussion of the observed events can always be challenged since only a statistically low number can be attributed to each mechanism. With this in mind, a discussion follows of all observed events and their most probable cause. In the following paragraphs, E_I is the incident neutron energy and E_{NR} the observed energy of the nuclear recoil in the cryogenic detector.

Elastic Oxygen Recoils 9 events are observed at high incident neutron energies from $E_I \approx 9MeV$ to $E_I \approx 12MeV$ and an energy deposition of $E_{NR} \approx 1200\,keV$ in the cryogenic detector module, which, when taking into account the overestimation of the energy deposition in the phonon channel, lie in the acceptance region of 1σ for elastic oxygen recoils. One additional event $E_I = 11.2MeV$ and $E_{NR} = 1500keV$ is too high in energy by few keV to be included in the 1σ acceptance region (when including the error bar).
At $E_I = 7.2MeV$ and $E_{NR} = 700keV$ is an additional event that can clearly be attributed to elastic scattering off oxygen.

If taking the 3σ acceptance region into account, an additional 2 recoils at $E_I = 7.6MeV$ and $E_I = 9MeV$ can be attributed to elastic oxygen scattering. Generally, inelastic oxygen scatters (with the gamma produced in the

deexcitation process escaping the detector module without further energy deposition) are also expected below the oxygen acceptance band, but with the lowest excited level of oxygen at $\sim 6MeV$, these events are expected at measured incident energies of $6MeV$ (see the discussion in section 6.2.1). For reference, the deviation of the two recoils at $E_I = 7.6MeV$ and $E_I = 9MeV$ observed below the 1σ acceptance region would require an inelastic excitation of $4.2\,MeV$ and $2.6\,MeV$ for an incident energy of $11\,MeV$ when neglecting all measurement uncertainties. Consequently, both these events can most likely also be attributed to elastic oxygen scattering.

Another scenario for these two events is a multiple scatter, once scattering off oxygen and once off a heavier nucleus, see the discussion below. In total, 11 elastic scattering events off oxygen have been observed, with two additional events which, within the limited statistics, can only be attributed to oxygen within the 3σ region.

Elastic Tungsten Recoils As has been discussed in section 6.2.1, 64% of all elastic neutron scatters at an incident energy of $\sim 11\,MeV$ are expected to be off oxygen and 33% off tungsten. With 11 oxygen recoil events clearly identified, 5 ± 2 are expected for tungsten. Three events, at $E_I = 7.7MeV$, $E_I = 8.4MeV$ and $E_I = 9.8MeV$ can be identified that fit the expected recoil energies for tungsten very well.

Elastic Calcium Recoils 3% of all elastic scatters are expected to be off calcium. With the number of observed elastic oxygen and tungsten recoils being (at least) a total of 14, the likelyhood for one or more elastic calcium recoil to occur is ∼35%. One observed event with an incident neutron energy of $E_I = 11.2\,MeV$ and $E_{NR} = 500keV$ fits the characteristica of a calcium recoil very well.

Multiple Scatters Three events have been observed at an energy in the phonon channel well above what is expected for elastic oxygen recoils. Two of these are at $E_I \approx 7.5MeV$ with $E_{NR} > 1200keV$ and one at $E_I = 9.6MeV$ with $E_{NR} = 1650keV$. As can be seen in the lower panel of figure 5.8 in section 5.3.3, the likelihood for the three events to be accidental coincidences observed at a recoil energy of $\sim 1.2\,MeV$ to $\sim 1.6\,MeV$ is less than 10^{-3}. But they do fit the expected energy of multiple scatters very well if both scatters were off oxygen. As has been discussed in section 6.2.1, 7% of all nuclear recoils are expected to be multi-site scatters, which equals 1.4 ± 1.2 events for a total of 20 observed events.

The two events discussed previously at $E_I = 7.6MeV$, $E_{NR} = 600keV$ and $E_I = 9MeV$, $E_{NR} = 700keV$ that can not with certainty be attributed to oxygen might also be multiple scatters with one partner being a heavy nucleus (either calcium or tungsten) and the second partner oxygen, lifting the recoil to higher energies.

Unidentified Events The event at $E_I = 7.3MeV$ and $E_{NR} = 25keV$ can not be attributed to any mechanism caused by a triple coincidence. Accidental coincidences are expected mainly at low energies, making it probable that the observed recoil is not linked to any detected scattered neutron.

6.3 Beam Time Summary

In section 6.2.1 all possible contributions to events measured in triple coincidence were discussed. Based on the cross sections and simulations, relative event rates were predicted. Table 6.4 summarizes the observed events and lists the corresponding predictions. The elastic and inelastic scattering processes are given relative to elastic scattering off oxygen which is defined to be 100%. The

	expected relative to *elastic O*	observed
elastic O	100%	11-13 (100%)
elastic Ca	5%	1 (9%)
elastic W	50%	3 (27%)
inelastic O	0%	0 (0%)
multiple	7% total	3-5 (14% - 23% total)
unidentified	10% total	1 (5% total)

Table 6.4: Based on cross sections, simulations and kinematics, the expected relative occurrence of the different mechanisms for observed triple coincidences can be formulated. For the elastic and inelastic scattering processes, they are given relative to oxygen. Multiple scattering events and accidental coincidences (here called *unidentified events*) are given relative to all events. The column headed *observed* shows the total number of observed events for this mechanism and their relative occurrence relative to elastic oxygen recoils or to all events (total).

two events that were observed at an incident neutron energy of $E_I = 7.6MeV$ and $E_I = 9.6MeV$ can either be attributed to elastic oxygen scattering or to multiple scattering events of which one scattering partner was a heavier nucleus. For one event no underlying mechanism was identified. This event has been related to the accidental coincidences of which two are expected among the total of 21 events.

It has been clearly shown in his chapter that the events that are measured in triple coincidence can be extracted with a very advantageous signal to background ratio of 10:1. The identified events can be linked to elastic scattering processes and will allow the direct measurement of the quenching factor after sufficient statistics are obtained. The number of events needed to give a value for the quenching factor depends on the resolution of the light detector and the actual quenching factor. This will be discussed in the next chapter.

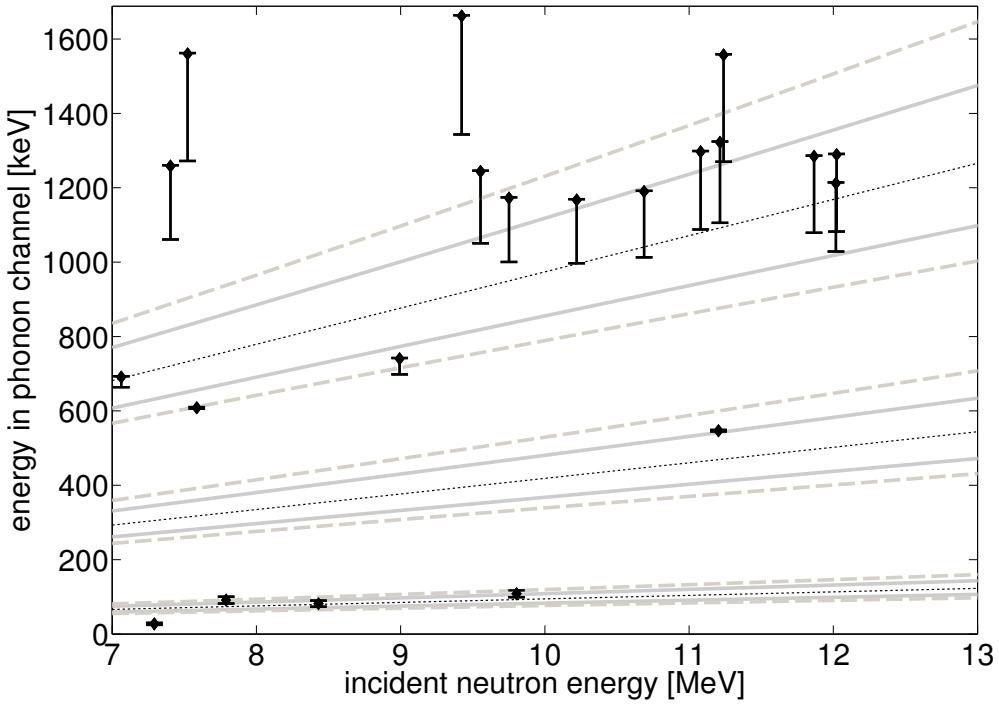

Figure 6.5: The 21 events included in the triple coincidence cut for incident neutron energies above $7MeV$ are shown in this plot. The error bars shown are the estimated errors of the calibration in the phonon channel of the cryogenic detector module, where the energy deposition in the phonon channel is likely to be overestimated by 15% for nuclear recoils of $1MeV$. Within the region where calibration data was available ($200keV$ to $600keV$), the error is given by the σ width of the observed calibration lines, giving an error $\pm 3.5keV$). This is discussed in detail in section 5.3.2. The dotted lines show the calculated (from elastic scattering kinematics) recoil energy for oxygen, calcium, and tungsten, which is 9.7%, 4.2% and 0.1% of the incident neutron energy, respectively. The solid lines give the 1σ acceptance region for each recoil type, the dashed lines show the 3σ acceptance region. The errors included in the calculation of these lines are the finite size of the hydrogen cell, the target crystal and the neutron detectors, leading to an uncertainty in the scattering angle and the path between neutron production and detection. Also included is the uncertainty in the time of flight measurement.

Chapter 7

Ongoing Upgrades and Future Improvements

In chapter 6 the performance of the triple coincidence search was shown. The extracted number of triple coincidences is not sufficient to obtain a result for the quenching factor of tungsten. Section 7.1 discusses the required number of events dependent on the resolution of the scintillation light detector. This accentuates two main directions for improvements: a) increase of the statistical yield per beam time, b) improvement of the resolution of the scintillation light detector. Section 7.2 discusses methods to increase the number of observed triple coincidences. The more promising approach is an increase in resolution of the light detector: Several possibilities to achieve this goal are described in section 7.3. In section 7.4 the ongoing and future efforts are summarized.

7.1 Required Statistics

As was shown in the previous chapter, the experiment allows to clearly identify the events measured in triple coincidence and attribute them to the underlying scattering mechanism. However, higher statistics are required to derive a value for the quenching factor (QF) of tungsten. The number of required events depends on the resolution of the scintillation light detector and the QF: the higher the QF (and subsequently lower the amount of the measured scintillation light) and the worse the resolution of the scintillation light detector, the more events are required.

This is shown in figure 7.1: The number of events required to derive the quenching factor with a precision of 15% is calculated depending on the quenching factor. A resolution of the scintillation light detector as observed in the October 2010 beamtime (i.e. $\sigma_{L,10keV} = (4.7 \pm 0.5keV)$) and a hypothetical detector with a resolution improved by factors of 2 and 3 were assumed. The calculations are based on a generated random distribution of nuclear recoil events in

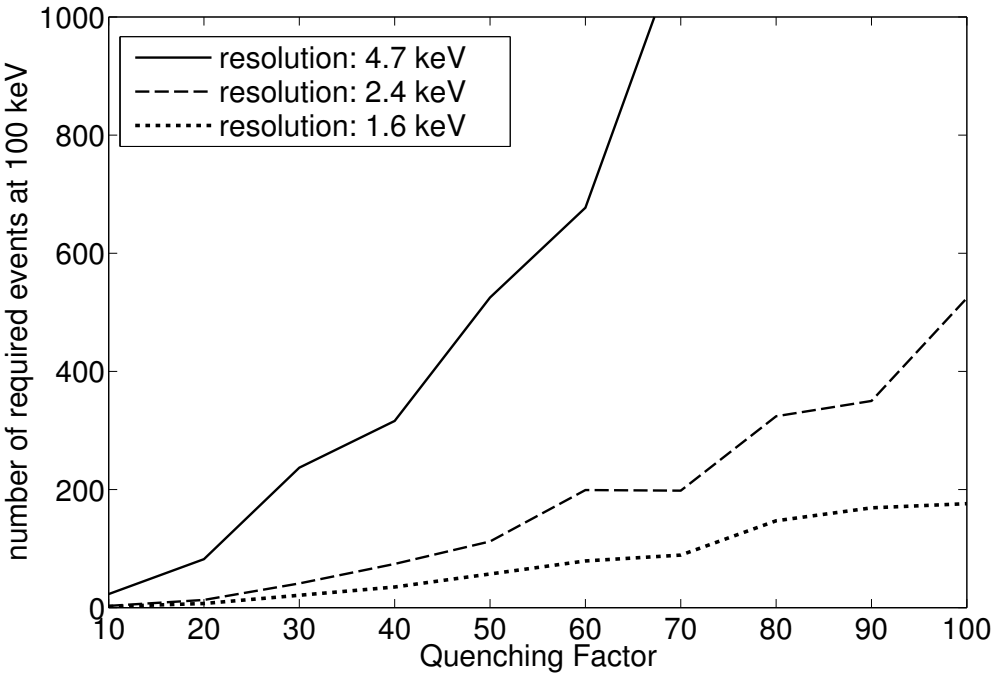

Figure 7.1: Calculated number of events (at a recoil energy of $100keV$) required to determine the quenching factor with a precision of 15%. With the increasing quenching factor, the amount of scintillation light decreases and more observed events are needed. The calculation has been performed for the resolution of the light detector observed during the October 2010 beam time (i.e. $4.7keV$ at $10keV$ electron equivalent) and was repeated for a theoretical resolution improved in comparison by a factor of two and three. The number of required events decreases drastically if the resolution of the light detector is improved.

the signal region with a σ-width of the detector resolution. It is subsequently fitted with a Gaussian and the QF is extracted. This is done for different numbers of events and repeated 500 times. The required number of events is the number where the standard deviation of the 500 extracted QFs equals 15% of the total QF. With the QF increasing (and the light output becoming more and more compatible with zero) more events are required.

In the current setup and with an assumed quenching factor of tungsten $QF_W = 30$, a total of ~ 240 events are required, for $QF_W = 40$ the number of events rises to ~ 310. With an improved resolution of $2.4keV$, which is regularly achieved in the CRESST experiment at Gran Sasso[1], the number of required events is ~ 40 for a quenching factor of $QF_W = 30$ and ~ 75 for $QF_W = 40$. This clearly shows the need for increased statistics (see section 7.2) and an increased resolution (section 7.3) in the scintillation light channel.

[1]CRESST achieves a resolution of $\sigma_{L,10keV,CRESST} \leq 1keV$. For some detectors it is below $500eV$ [134].

7.2 Increasing the Number of Observed Triple-Coincidences per Beam Time

The statistics can be improved by generally optimizing the beam time procedure as discussed in section 7.2.1 or by increasing the solid angle covered by neutron detectors, see section 7.2.2.

7.2.1 Beam Time Optimization

For the October 2010 beam time the expected number of tungsten recoils based on the observed oxygen recoils was ~ 6 (observed were 3). The usable data was recorded in ~ 3.5 days. Optimizations of the beam and especially of the cryogenic detector module were necessary. In total, the amount of saved data equals $\sim$2.6 days of actual 'live' data, which corresponds to an efficiency of the experiment of $\sim$70%.

The cause for the required interruptions is understood. Most of them can be eliminated if the stability of the low temperature detector is maintained without continuous fine tuning by the experimenter. With the exception of few experimental runs (of which the October 2010 beam time is a prime example), this is the usual case. The downtime can be reduced to the phases where cryogenic liquids (i.e. helium and nitrogen) have to be filled.

For a beam time limited to interruptions caused by the refilling cycles ($\sim 5h$ every four days) and an additional two hours scheduled every day for optimization purposes, the downtime can be limited to 10%. In such a case, the expected number of observed triple coincidences for elastic tungsten recoils, when leaving all other parameters unchanged, is $\sim$15 for a full week of beam time at an efficiency of 90%. To determine the quenching factor with a 1σ precision of 15% of the total value, this still requires $\sim$ 20 beam times for a QF_W in the range between 30 and 40. In comparison: For oxygen (which has a quenching factor of $QF_O \approx 10$) less than one beam time is required, even at nuclear recoil energies of $100keV$.

7.2.2 Increasing the Number of Neutron Detectors

Currently, the data acquisition includes 40 ADC channels, eight provided by each of the five Sis3320 flash ADCs (see section 3.8.1.5). 30 channels are currently used by the neutron detectors introduced in section 3.3.2. An additional six neutron detectors were supplied to us from the Eberhard-Karls-Universität Tübingen [135]. These have already been installed and tested, they cover a solid angle equal to the total of all other 30 neutron detectors (since each individual detector covers a larger area). In fact they were present during the October 2010 beam time, but were not shielded from direct neutrons since the construction of a suitable neutron shield could not be scheduled before the beam time began. During the data analysis it became obvious that these detectors

greatly increased the number of accidental coincidences, consequently all events in these detector were discarded.

Additionally, since the data acquisition was designed with expandability in mind, the number of ADC channels can be increased easily by adding additional VME modules. With the number of observed coincidences being proportional to the solid angle covered by the neutron detectors, the amount of required beam time can be directly reduced.

7.3 Improving the Resolution of the Light Detector

As is seen in figure 7.1, the resolution of the scintillation light detector is critical for the quenching factor analysis. Improving the resolution by a factor of two (i.e. from $4.7keV$ to $2.4keV$) reduces the number of required (for a quenching factor of $\sim$40) tungsten recoil events to ~ 60 observed triple coincidences, which can be obtained in ~ 4 beam times if leaving the current setup unaltered in all other aspects. Generally, the resolution of the scintillation light detector critically depends on five parameters:

1. **Total Energy Deposition:** While this can be considered trivial, the relative resolution of the light detector increases with the total energy deposition.

2. **Calibration:** As has been shown in section 5.3.2, uncertainties in the calibration of the detector module will ultimately lead to a reduced resolution.

3. **Working Point:** After the combination of all working points as described in section 5.2.3.1 the observed 1σ discrimination threshold between electron and nuclear recoils of the detector is $7.7keV$, while it was better than $7keV$ for some of the individual measurements. Thus the observed peak performance of the detector is 20% better than the average performance over the whole beam time. It is desirable that the optimal working point is maintained over the whole beam time.

4. **Amount of Detected and Produced Scintillation Light:** The amount of detected scintillation light is dependent on the number of produced photons in the crystal and the collection efficiency of the light detector.

5. **Intrinsic Resolution of the Light Detector:** If points 2 and 3 are optimized, the detector runs at its peak performance. This peak performance can be further improved, for example by using the Neganov-Luke technique.

The following subsections will address each of the five points in detail.

7.3.1 Higher Total Energy Deposition

For a scattering angle of $\theta = 80°$ and an incident neutron energy of $\sim 11MeV$, the nuclear recoil energy is $\sim 110keV$ for elastic scattering off a tungsten nucleus. For a quenching factor of $QF_W = 30$ this corresponds to a scintillation light output of $\sim 3.7keV$ electron equivalent, for $QF_W = 40$ to $\sim 2.8keV$. The energy deposition can be either increased by measuring at a higher scattering angle or by increasing the incident neutron energy.

The employed nuclear reaction $^{1}\mathrm{H}(^{11}\mathrm{B}, n)^{11}\mathrm{C}$ as described in section 3.2.2 results in neutron energies of $\sim 10.6MeV$ for incident ^{11}B ions with a kinetic energy of $E_{^{11}\mathrm{B}} = 61.5MeV$. Other nuclear reactions (presented in [136]) allow the production of neutrons with higher energies. For example, the nuclear reaction $^{1}\mathrm{H}(^{15}\mathrm{N}, n)^{15}\mathrm{O}$ produces neutrons with a kinetic energy of $\sim 20MeV$ by employing a ^{15}N beam at $\sim 130MeV$. While this energy is accessible at the MLL, the produced ^{15}N-beam intensity is low because of the inability of nitrogen to form negative ions, necessitating the formation of NO^- to allow acceleration. Also, the increased energy reduces the time of flight, which leads to a higher relative error of the ToF measurement and an increased uncertainty in the neutron energy.

7.3.2 Calibration and Working Point Stability

The quality of the calibration and the working point stability are linked, since the knowledge of the working point allows the accurate application of a calibration. Currently, the working point is monitored by using a ^{133}Ba source. The distance between the source and the cryogenic detector was sufficiently close for the $276.4keV$, $302.9keV$, $356.0keV$ and $383.9keV$ lines to be visible in a data set of ~ 50000 recorded pulses, which is the smallest subset of recorded data in one working point during the October 2010 beam time. As has been discussed in section 5.3.2, this posed a problem for the calibration below $200keV$. Usually, this is prevented by employing a calibration obtained with radioactive sources producing lines at all energies. Due to the failure of the low-temperature detector in the October 2010 beam time, such data was not available. As a safeguard, additional radioactive sources can be employed during the actual beam time, for example ^{57}Co which produces a line at $122.1keV$ or ^{241}Am ($59.1keV$).

An alternative method is the use of heat pulses directly injected into the transition edge sensor of each detector, as done in the CRESST experiment at Gran Sasso. This allows to automatically correct the working point, since the pulses are injected with a known pulse height and, based on the response of the detector, the working point can be immediately adjusted. If a system equivalent to the design employed at Gran Sasso is applicable to the neutron scattering facility is currently under investigation in the scope of a diploma thesis [137].

For the light detector, test pulses can also be injected by using a LED. This system was tested in the October 2010 beam time, but the pulse shape of a

short (∼500 ns) light pulse produced by the LED proved to be too different from the scintillation light pulses of a crystal. Consequently, the pulses could not be related to an energy deposition. Still, the LED pulses can be used for the drift correction and to test the working point stability if no radioactive source is present. The use of the LED for calibration purposes is still under investigation.

7.3.3 Detected Scintillation Light: Different Crystal Geometry and Increased Absorption

A diploma thesis was dedicated to evaluate the dependency of the scintillation light output of a target crystal based on the geometry of the absorbing material and the position of the particle interaction [138]. Since $CaWO_4$ has a high refractive index of $n_{CaWO_4} = 1.95$, the angle for total reflection is small ($\theta_c \approx 31°$) and light can easily be trapped on an 'infinite' path without the chance of escaping the crystal. This trapped light will be self-absorbed and the detectable scintillation light is reduced. If this effect is dependent on the position of the particle interaction, it will not only lead to a reduced light output, but also to an additional line broadening that may be asymmetric. It has been shown [138] that both effects occur for the cylindrical shape currently used in all CRESST-like detectors. Based on simulations, a gain of a factor of 2.5 in resolution has been estimated for a cubic shape or a truncated square pyramid compared to a cylindrical crystal.

Of equal importance for the amount of detected photons is the absorption efficiency of the material forming the substrate of the scintillation light detector: it has been shown [139] that black silicon absorbs 15% more light than the normal silicon absorbers currently employed. Black silicon is produced by etching nano holes that are much smaller than the photon wavelength into the silicon waver. The resulting structure forms a medium with a continuously changing refractive index which reduces the reflectivity of the absorber and consequently increases absorption.

7.3.4 Produced Scintillation Light: Composite Detector Design

To evaporate the transition edge sensor (TES) onto the target crystal, it needs to be heated to ∼300°C to ∼400°C (depending on the material of the thin film) for the thin film to properly connect with the crystal. Since this is done in the absence of any atmosphere, oxygen diffuses out of the crystal, leading to an oxygen deficiency. It has been shown (see [140]) that this causes a reduced scintillation light output. This can be prevented by using the composite detector design (see [83, 114, 141, 142]): here the transition edge sensor is evaporated on a separate substrate and then glued to the absorber crystal. If the interface between the absorber material and the substrate is sufficiently thin, the phonon propagation through the glue is nearly unhindered. This eliminates the need to heat the crystal and the full scintillation light output is maintained.

7.3.5 Intrinsic Resolution: Neganov-Luke-Light Amplification

The signal produced by an energy deposition in the light detector which is detected by the transition edge sensor can be amplified by employing Neganov-Luke-light amplification. This technique is briefly introduced in section 7.3.5.1. Section 7.3.5.2 shows the results recorded with a single light detector and section 7.3.5.3 shows the preliminary results obtained for a detector module operated at the neutron scattering facility in the scope of a beam time.

7.3.5.1 Neganov-Luke Technique

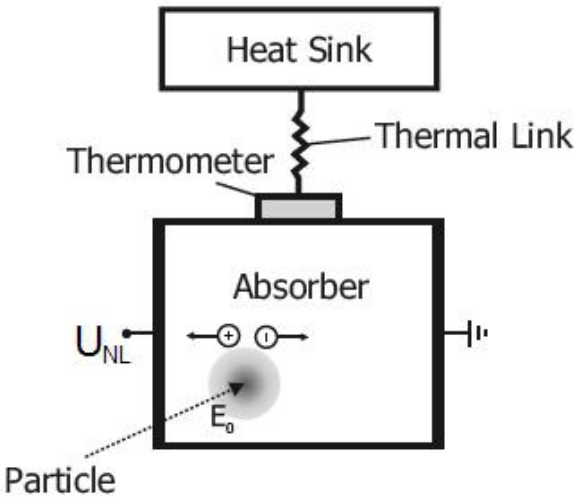

Figure 7.2: The working principle of a Neganov-Luke-amplified scintillation light detector: photons produce electron-hole pairs in the semiconductor that is employed as absorbing material (silicon in the case of the detector used at the neutron scattering facility). These electron hole-pairs are drifted by the Neganov-Luke voltage U_{NL}. Since the charge carriers scatter off the crystal lattice, they produce additional phonons which are also detected by the transition edge sensor (thermometer).

The working principle of a scintillation light detector (as outlined in section 2.1) is based on the detection of phonons which were produced in the material (silicon) by the absorption of photons. In a semi-conductor, the absorption of photons leads to the generation of electron-hole pairs. In light detectors following the standard design of a CRESST light detector, these pairs recombine. By applying a voltage across the substrate, the recombination is prevented and the charge carriers are drifted through the substrate. The drifting charges produce additional phonons when they scatter off the crystal lattice. This is called the Neganov-Luke effect, and it has been extensively studied at our institute in Garching [114]. The realization of this technique is shown schematically in

figure 7.2. The charge drift is achieved by an electrical field, which is produced by the Neganov-Luke voltage U_{NL}. To apply the voltage, electrodes are evaporated directly on the silicon substrate. The achieved performance of such a light detector is discussed in the next section.

7.3.5.2 Achieved Amplification under Optimal Conditions

By using a LED, light pulses with a defined light output can be produced that allow the characterization of a Neganov-Luke light detector. Figure 7.3 shows a light pulse once without (left) and once with (right) a Neganov-Luke voltage applied. The light pulse is produced by a LED and it is ensured that

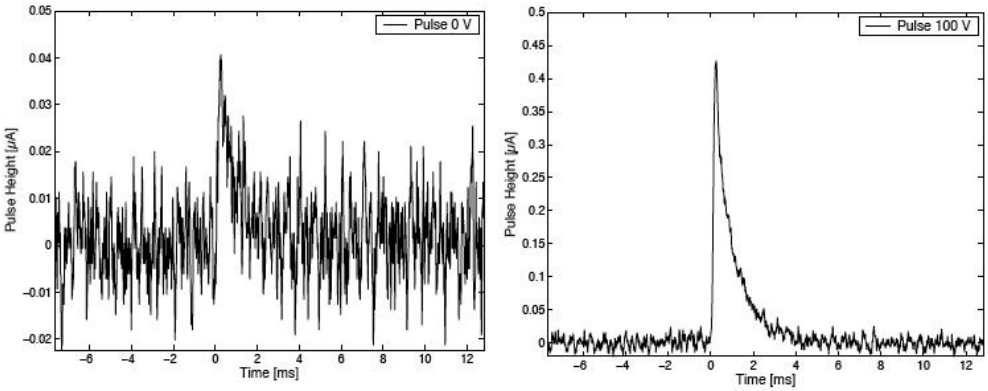

Figure 7.3: The left figure shows a light pulse (produced by a LED) as observed in a detector with no Neganov-Luke voltage applied. All working points of the detector were scanned and the working point with the best signal to noise ratio was chosen for the measurement. The right figure shows a LED light pulse of the same energy deposition (which is ensured by using the LED as a light source) with a Neganov-Luke voltage of $U_{NL} = 100V$ applied. The gain in signal to noise is a factor of ∼10. Figures from [114].

the energy deposition in the light detector is the same for both cases. For both measurements, the detector is operated at its peak performance, i.e. the working point has been optimized to ensure the highest achievable signal to noise ratio [114]. With the Neganov-Luke voltage applied, the observed gain in signal to noise ratio is ∼10.

The amplification and gain in signal to noise ratio is dependent of the applied voltage. This dependency is shown in figure 7.4. As can be seen, for applied voltages above $U_{NL} \approx 150V$, the signal to noise ratio saturates. This is caused by additional noise that occurs at higher voltages. For this particular light detector, the highest observed gain in signal to noise is observed at an applied voltage of $100V$.

At least partially, the electrical charge carriers are not dissipated via the electrodes. Instead, they accumulate at the electrodes and build up an addi-

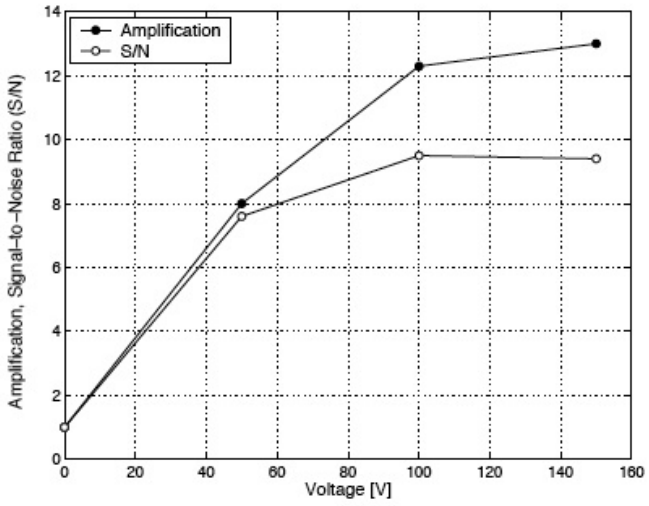

Figure 7.4: The achieved amplification depending on the applied Neganov-Luke voltage U_{NL} is shown for voltages from $U_{NL} = 0V$ to $U_{NL} = 150V$. Also shown is the gain in signal to noise ratio. Since additional noise is observed at voltages above $U_{NL} \approx 150V$, the signal to noise ratio decreases for higher electric fields. Figure from [114].

tional electrical field, which weakens the applied electrical field produced by the Neganov-Luke voltage U_{NL}. This effect is shown in figure 7.5: over time, the observed pulse height decreases. This decrease is dependent on the pulse rate in the detector. This behavior is expected, since a higher count rate causes more space charges to build up. The full amplification in the light detector can be restored by flashing the light detector for $\sim 10s$ with long ($\sim 1ms$) LED pulses of high intensity with the external Neganov-Luke voltage being disabled[2]. As has been discussed in section 4.5.7, the data analysis suite developed for the scattering experiment in the scope of the present work has a drift correction already built-in the standard analysis pipeline. This program was developed specifically with Neganov-Luke amplification in mind and allows the user to correct the observed time dependent change in amplification. This restores the correlation between the observed pulse height and the deposited energy.

7.3.5.3 Preliminary Neganov-Luke Setup at the Neutron Scattering Facility

The results discussed in the previous section have been achieved by using a single light detector which is not coupled to a scintillating crystal but illuminated by a LED. In the scope of the May 2010 beam time, a CRESST-like detector module was equipped with a Neganov-Luke light detector. Here, a phonon pulse and the associated Neganov-Luke-amplified scintillation light pulse were

[2]The external voltage has to be disabled to prevent the flow of high currents that ultimately will warm up the detector module.

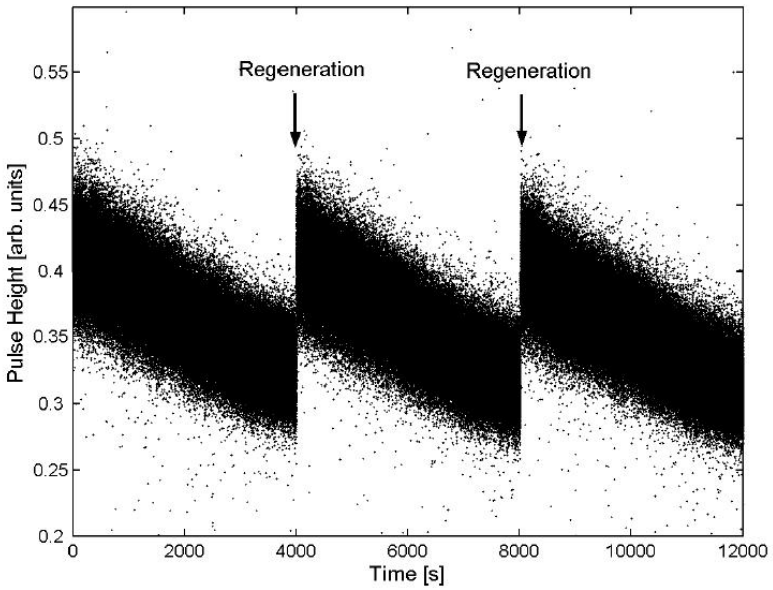

Figure 7.5: The observed pulse height in the light detector over time. The light is produced by a LED, which emits light pulses of a constant intensity. It can be seen that the observed pulse height decreases over time. This is caused by space charges that build up at the electrodes of the light detector, which weaken the applied electric field and consequently reduce the Neganov-Luke amplification. The space charges can be eliminated by regenerating the substrate, which is done by disabling the external field and flashing the light detector with the LED for $\sim 10s$. The full amplification is restored after the regeneration cycle. Figure from [114].

measured in coincidence. The ideal performance as described in section 7.3.5.2 could not be reproduced for two reasons:

1. The Neganov-Luke light detector used for this measurement was not the same as the one with which the results discussed in section 7.3.5.2 were obtained since it was not available. Instead, due to time constraints, a detector with a higher energy threshold and lower resolution was used.

2. The noise conditions at the scattering facility were found to be worse than at the laboratory where the tests were made. Additional external fields seemed to interfere with the Neganov-Luke light detector and hindered the application of high electrical fields.

Figure 7.6 shows the observed energy deposition in the scintillation light detector plotted vs. the energy deposition in the phonon channel for this detector in the presence of the neutron beam, in the upper figure with no voltage applied and in the lower figure with a Neganov-Luke voltage of $U_{NL} = 50V$. The two bands originating from electron and nuclear recoils are clearly visible. The observed discrimination threshold is improved by a factor of ~ 3 if a Neganov-Luke voltage is applied. Due to the mentioned problems, the detector performs

worse than the detector used during the October 2010 beam time (which was discussed in section 5.3.1, the detector employed in this beam time was operated without Neganov-Luke amplification), but the measurement still demonstrates the enormous potential of a Neganov-Luke amplified light detector.

7.4 Concluding Remarks on Future Upgrades and Measurements

While statistics can be improved by longer measurement times and by adding additional neutron detectors, the key for a successful quenching factor measurement lies in further increasing the resolution of the scintillation light detector: As discussed in section 7.1, the required number of nuclear recoils to measure the quenching factor of tungsten with sufficient precision is reduced by a factor of six if the resolution of the light detector is improved by a factor of two. This resolution has already been achieved by CRESST detectors at the Gran Sasso laboratory. With the combination of the different upgrades outlined in section 7.3, especially an optimized crystal geometry and the application of the Neganov-Luke technique, we expect to significantly increase the detector resolution in the near future.

The data acquisition and the data analysis pipeline developed in the scope of the present work already include Neganov-Luke read out and analysis capability. This was tested in the May 2010 beam time, where, for the first time, a complete CRESST-like detector module was operated with the Neganov-Luke amplification technique at the neutron scattering facility.

For the long term future, the characterization of new target materials is foreseen. This will be achieved by utilizing the composite detector design (see section 7.3.4), which allows to exchange the target crystal and read out the energy deposition with a glued TES.

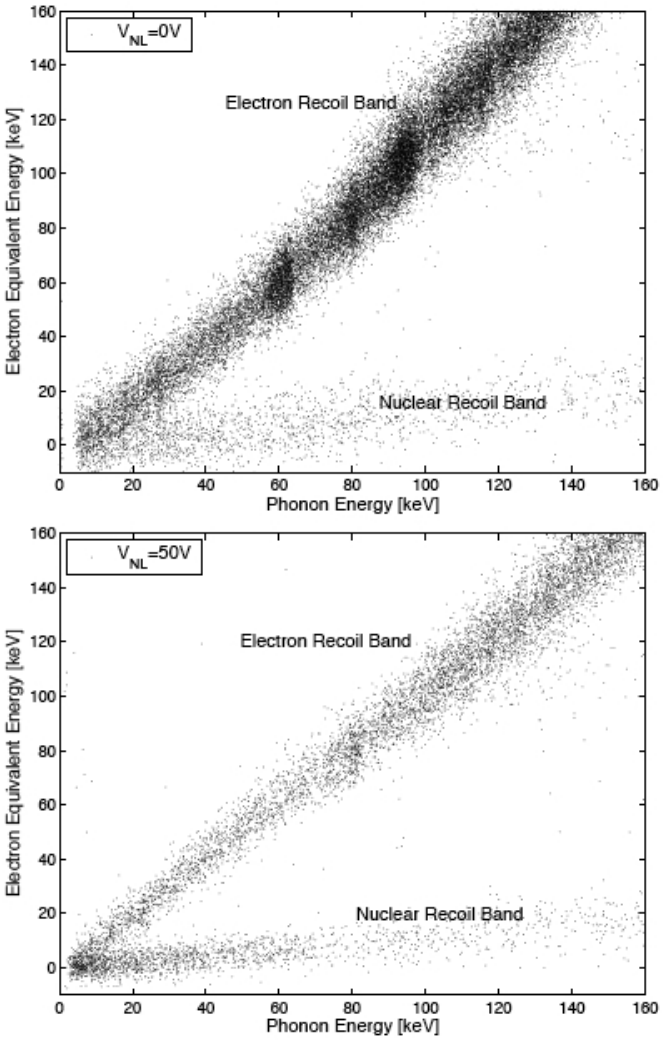

Figure 7.6: The energy deposition in the scintillation light channel plotted vs. the energy deposition in the phonon channel in the presence of a neutron beam. The upper figure shows the obtained result with no Neganov-Luke voltage, while for the other measurement shown a voltage of $U_{NL} = 50V$ has been applied. The observed discrimination threshold for $U_{NL} = 0V$ is $\sim 30keV$, for $U_{NL} = 50V$ it is $\sim 10keV$. The absolute performance of the detector is worse than that achieved in the October 2010 beam time (for comparison see section 5.3.1) and is also worse than the performance of the Neganov-Luke detector discussed in section 7.3.5.2. Figures from [114].

Chapter 8

Conclusions

To date, every positive claim for the direct detection of WIMPs (Weakly Interacting Massive Particles) is disputed by the zero-result of other direct-search experiments, in particular CDMS (Cold Dark Matter Search) and XENON, and will most probably remain disputed until an observed signal is consistent among different target materials, i.e. the expected rate dependency of coherent nuclear scattering being $\sim A^2$ is observed. Due to the low expected event rate of less than 10 events per kg and year, background suppression in particular of electron recoils caused by γ and β radiation is crucial. To achieve this, most direct-search experiments favor an approach where two quantities of a particle interaction are measured simultaneously, for example heat and light as in CRESST (Cryogenic Rare Event Search with Superconducting Thermometers), heat and ionization as in CDMS and EDELWEISS (Expérience pour DEtecter Les Wimps En Site Souterrain) or ionization and light as in XENON. The relative distribution of the deposited energy over the measured channels depends on the type of interaction, allowing to discriminate between electron and nuclear recoils. The latter are expected to be induced at few keV by WIMPs. The definition of the signal region for a target material is crucial, and currently suffers from the lack of a precise understanding of ionization and scintillation processes at these very low energies. Consequently, the WIMP-signal region is defined empirically with the help of the measured nuclear quenching factors, which characterize the observed response of a detector to a nuclear recoil. In CRESST they quantify the reduced scintillation light output of nuclear recoils compared to electron recoils of the same energy, for other experiments the definition is accordingly.

Motivated by the CRESST and the future EURECA (European Underground Rare Event Calorimeter Array) WIMP search programs, an experiment for the measurement of the light-quenching factors of present and future target materials at low temperatures has been set up at the MLL (Maier-Leibnitz-Laboratorium) in Garching: Nuclear recoils can be induced by accelerator-produced neutrons of known energy in the bulk of the detector material at $\sim 10mK$. To disentangle multi-component nuclear recoil bands, for example

of $CaWO_4$, the scattered neutrons' time of flight and the scattering angle are measured. This allows a precise determination of the low-temperature detector response to electronic and nuclear recoils, and to characterize the signal region for WIMPs with unprecedented accuracy.

In the scope of the present work, a ^{3}He/^{4}He dilution refrigerator was set up and equipped with SQUIDs (Superconducting Quantum Interference Devices) and the wiring required for the low-temperature detector operation and readout. The system was tested in several cooldown procedures and allows the operation of a CRESST-like detector module consisting of a phonon and a scintillation light detector. Despite the challenging environment in terms of shielding and electromagnetic noise conditions found at the accelerator laboratory, a remarkably good discrimination threshold between electron and nuclear recoils of $\sim 7.7keV$ (1σ) was reached. The 1σ-resolution of the nuclear recoil band at $100keV$ total energy deposition was found to be $4.7keV$.
The combination of a slow ($\sim \mu s$ to $\sim ms$) low-temperature detector with fast ($\sim ns$) neutron detectors for a coincidence measurement exceeds the capabilities of commercially available hardware solutions: The conditions to perform a coincidence measurement between detectors the time constants of which differ by up to six orders of magnitude have to be provided. In the present work, the problem was solved by expanding the dynamic range of commercially available electronic modules and by developing a powerful event reconstruction algorithm. To achieve this, the data acquisition (DAQ) was upgraded to VME standard which was found to provide a sustainable (and compatible) basis also for future developments. The VME modules were selected according to our requirements. To allow the monitoring of all relevant parameters during a beam time, a customized DAQ software was developed, which gives direct feedback on all relevant experimental parameters (e.g. pulsed neutron source properties, pulse-shape discrimination of the neutron detectors, operational state of the low-temperature detector). The DAQ software streams all data to disk, the actual event reconstruction is then performed offline.
For the data analysis, an extensive software suite has been written. It includes all required tools, beginning from low-level data access, data preprocessing and the automatic recognition and correction of readout errors, as well as high-level functions required for fitting the pulses from the low-temperature detector and to perform pulse-height drift compensation and calibration. The algorithms were optimized and tested successfully in several beam times.
The performance of the experiment and the data analysis tools were demonstrated by means of an in-depth analysis of a successful beam time that took place in October 2010. Here, 20 coincident events with a signal to background ratio of 10 : 1 were extracted out of 3 million low-temperature events and the underlying scattering mechanisms were identified.
The statistical yield paired with the resolution of the currently employed scintillation light detector is not sufficient to give results for all quenching factors in $CaWO_4$. To increase the statistical yield, additional neutron detectors have now been installed, roughly doubling the total solid angle sensitive to neutron scattering. To improve the resolution of the light detector, the experiment was

upgraded with the capability to operate a detector with Neganov-Luke light amplification. This effect describes the generation of additional phonons by drifting photon-induced electron-hole pairs in the semiconducting substrate of the light-detector by an applied electric field. First preliminary tests have already been performed in the scope of the present work and such new light detectors are planned to be used in future beam times.
The modular and versatile design of the DAQ and data analysis also allowed the determination of the proton quenching factor of the liquid scintillator employed in the Double Chooz experiment. For the investigation of new liquid scintillators, e.g. for LENA (Low Energy Neutrino Astronomy), further beam times are planned.

It was shown that the low-temperature neutron scattering facility allows the characterization of detectors employed in Dark Matter search experiments. In this world-wide unique setup, the nuclear quenching factors can be measured directly in the bulk of the target crystal at mK temperatures and will allow an accurate determination of the signal region for a positive WIMP signal. The setup is of high importance for the current phase of the CRESST Dark Matter search experiment, its future upgrades in which also the use of new target materials is foreseen and for the planned ton-scale multi-material-target experiment EURECA.

Appendices

Appendix A

EJ-301 Data Sheet

EJ-301 LIQUID SCINTILLATOR

This scintillator exhibits excellent pulse shape discrimination (PSD) properties, particularly for fast neutron counting and spectrometry in the presence of gamma radiation. It is identical to the widely reported NE-213 and, therefore, exhibits all of the properties of that scintillator.

EJ-301 can be supplied ready for immediate use encapsulated at the factory in sealed aluminum or glass cells of a variety of types made to the customer's required dimensions. It is also supplied in bottles or drums sealed under inert gas. However, after being transferred to a cell or tank it should be deoxygenated again by sparging with pure nitrogen or argon for a duration proportional to the cell size immediately before sealing in order to achieve excellent PSD performance.

PROPERTIES

Light Output (% Anthracene)	78%
No. of Blue Photons per 1 MeV of Electron Energy	12,000
Wavelength of Maximum Emission	425 nm
Specific Gravity	0.874
Atomic Ratio, H:C	1.212
No. of C Atoms per cm^3	3.98×10^{22}
No. of H Atoms per cm^3	4.82×10^{22}
No. of Electrons per cm^3	2.27×10^{23}
Flash Point (T.O.C.)	26°C (79°F)
Boiling Point at one atmosphere	141°C (285°F)
Refractive Index, n_D	1.505
Decay Time (short component)	3.2 ns
Bulk Light Attenuation Length	2.5-3 meters
Mean Decay Times of First 3 Components (ref. 1)	3.16, 32.3 & 270 ns
No. of Photoelectrons per kev energy loss using an RCA-8575 PMT (ref. 1)	1.7
Alpha/Beta Ratio, "fast" (ref. 2)	0.073
Alpha/Beta Ratio, "slow" (ref. 2)	0.098

EJ-301 EMISSION SPECTRUM

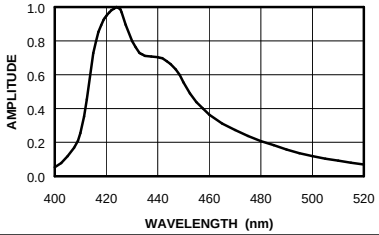

ELJEN TECHNOLOGY
1300 W Broadway
Sweetwater TX 79556 USA

Tel: (325) 235-4276 or (888) 800-8771
Fax: (325) 235-0701
Website: www.eljentechnology.com

EJ-301, pg. 2

Pulse Shape Discrimination

PSD figure of merit, M, is defined as the separation between the neutron and gamma peaks divided by the sum of the FWHM of the neutron and gamma peaks at 1 MeV electron energy. Measurements of 3.5 [ref. 3, Fig. 1] and 3.9 [ref. 4, Fig. 6] have been reported. PSD figure of merit, D, defined as the separation between the neutron and gamma peaks divided by the variance in the PSD signals at 1 MeV electron energy is 11.3 [ref. 3, Fig. 1].

For values of M and D at other energies and for electron rejection ratios, see Figs. 3a, 3b & 4 of ref. 3 and Fig. 6 of ref. 4.

Response to Protons:

$E = 0.83P - 2.82\,(1 - \exp(-0.25P^{0.93}))$ where P is the proton energy in MeV and E is the electron energy in MeV that gives the same light output in the range 1-300 MeV. [ref. 5] A more precise study in the energy range 5-17 MeV developed the following relationship [ref.6].
$E_e(\text{MeV}) = -1.092 + 0.5517E_p + 0.00461E_p^2$

Neutron and Gamma Spectrometry

The absolute differential efficiency and neutron spectra for a nominally 5 cm dia. x 5 cm cell for energies between 0.2 and 22 MeV are presented in reference 7. Gamma spectra analysis at energies above 3 MeV taken with three different sized scintillators is presented in ref.8. Methods of analyzing neutron and gamma spectra are compared in ref. 9.

References

1. F.T. Kuchnir & F.J. Lynch, “Time-Dependence of Scintillators and the Effect on P.S.D.”, IEEE Trans. Nucl. Sci., **NS-15**, No. 3, (1968) 107-113
2. J.B. Czirr, “The α/β Ratio of Several Organic Scintillators”, Nucl.Instr. & Meth. **25** (1963) 106-108
3. R.A. Winyard and G..W. McBeth, “Pulse Shape Discrimination in Inorganic and Organic Scintillators”, Nucl. Instr. & Meth. **98** (1972) 525-533
4. J.M. Adams and G.White, “A Versatile Shape Discriminator for Charged Particle Separation and its Application to Fast Neutron Time-of Flight Spectroscopy”, (<100 keV – 20 MeV), Nucl. Instr. & Meth. **156** (1978) 459-476
5. R.A. Cecil et al, “Improved Predictions of Neutron Detection Efficiency for Hydrocarbon Scintillators from 1 MeV to about 300 MeV”, Nucl. Instr. & Meth. **161** (1979) 439-447
6. A.Aksoy et al, “Response-function Measurement of an NE-213 Scintillator Using the 2H(d,n)3He Reaction”, Nucl. Instr. & Meth. In Phys. Res. (1994) 486-491
7. V.V. Verbinski et al, “Calibration of an Organic Scintillator for Neutron Spectrometry”, Nucl. Instr. & Meth. **65** (1968) 8-25
8. L.Buermann et al, “Response of NE-213 Liquid Scintillation Detectors to High-energy Photons (Eg>3 MeV)”, Nucl. Instr. & Meth.in Phys. Res. **A332** (1993) 483-492
9. R. Koohi-Fayegh et al, “Neural Network Unfolding of Photon and Neutron Spectra Using an NE-213 Scintillation Detector”, Nucl. Instr. & Meth. In Phys. Res. **A329** (1993) 269-276

ELJEN TECHNOLOGY
1300 W Broadway
Sweetwater TX 79556 USA

Tel: (325) 235-4276 or (888) 800-8771
Fax: (325) 235-0701
Website: www.eljentechnology.com

Appendix B

Expanding the Dynamic Range of the v1190 TDC

The v1190 64 channel TDC has a dynamic range of $96\,\mu s$. This limitation is imposed on the TDC by the 19 bit size foreseen for every timestamp at a resolution of the least significant bit of 200ps. To count the number of rollovers (one occurring every 96 us), at least one hit in every 96 us window has to be ensured. A pulser housed in the VME controller (see section 3.8.1.2) connected to one of the TDC channels is used for that. The readout buffer of the TDC contains the timestamp and the channel number for each hit. Each of the 64 TDC channels is polled subsequently for registered hits, a registered hit is then stored in the output buffer. This can lead to the v1190 on board logic to place hits occurring in different channels when not further apart than 20 ns in the wrong order, meaning a later hit can be stored earlier in the output buffer than possible previous hits. When reconstructing the amount of rollovers that occurred until a specific hit, this has to be taken into account.

This is done by setting the period of the pulser to less than half of the rollover time, so at least two pulses are recorded before each rollover. The channel connected to the pulser is called the keep-alive channel. The last hit in the keep-alive channel is called t_0, the hit before that is called t_{-1}. If the condition

$$t_0 < t_{-1}$$

is true, the rollover counter c_{ro} is increased by one. It is saved with every event and allows to reconstruct the absolute time. Taking hit misplacement into account, the cases shown in figure B.1 can occure. Each case has a unique feature. By comparing the time of the hit t_{hit} with the last two recorded hits in the keep-alive t_0 and t_{-1}, the conditions of each case are:

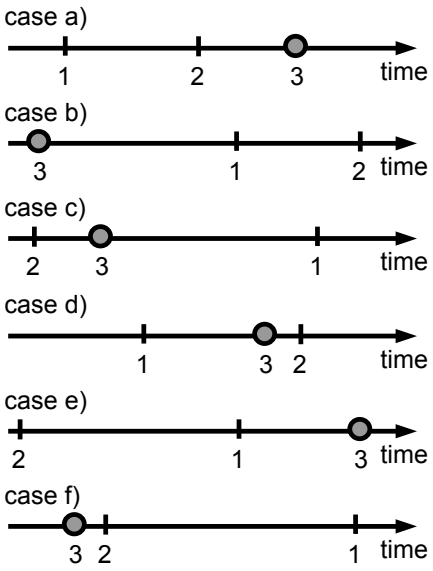

Figure B.1: All possible cases of relative hit placement in the TDC. The timeline spans the whole dynamic range of the TDC, after the dynamic range is exceeded the time is again recorded from 0. The circle denotes a hit in any channel but the keep-alive, while the lines mark the last two hits in the keep-alive channel (coming from a pulser). The numbers indicate the order in which they have been read out. Each hit is compared to the last two times of the keep-alive channel. Cases a) to c) show the three possibilities where no hits are misplaced, cases d) to f) have hit misplacement occur for the last pulser hit and 'real' hit. See the text for details.

case a) No hit misplaced

$$\begin{aligned} t_{hit} &\geq t_0 \\ t_{hit} &> t_{-1} \\ t_0 &> t_{-1} \end{aligned}$$

The current rollover counter c_{ro} applies to t_{hit}.

case b) No hit misplaced

$$\begin{aligned} t_{hit} &< t_0 \\ t_{hit} &< t_{-1} \\ t_0 &> t_{-1} \end{aligned}$$

The rollover counter c_{ro} is too low by 1 for the current hit t_{hit}.

case c) No hit misplaced

$$\begin{aligned} t_{hit} &\geq t_0 \\ t_{hit} &< t_{-1} \\ t_0 &< t_{-1} \end{aligned}$$

The current rollover counter c_{ro} applies to t_{hit}.

case d) Last hit misplaced

$$\begin{aligned} t_{hit} &< t_0 \\ t_{hit} &> t_{-1} \\ t_0 &> t_{-1} \end{aligned}$$

The current rollover counter c_{ro} applies to t_{hit}.

case e) Last hit misplaced

$$\begin{aligned} t_{hit} &> t_0 \\ t_{hit} &> t_{-1} \\ t_0 &< t_{-1} \end{aligned}$$

The rollover counter c_{ro} is too high by 1 for the current hit t_{hit}.

case f) Last hit misplaced

$$\begin{aligned} t_{hit} &< t_0 \\ t_{hit} &< t_{-1} \\ t_0 &< t_{-1} \end{aligned}$$

The current rollover counter c_{ro} applies to t_{hit}.

Appendix C

Data Analysis Details

C.1 Details on Data Organization

C.1.1 Folder Structure

The data recorded in a beam time campaign is organized in a folder structure. The data contents of one folder were recorded over a time period during which the experimental conditions are assumed to remain unchanged. This means no intentional interference or changes are induced by the experimenters, but it does not exclude unwanted changes, for example a shift in the working point of the low-temperature detector (see section 4.5.4) or a change in the ion source of the accelerator, especially chopper and buncher settings (see section 3.2.1.2).

By convention, the name of the folder holds the date, the consecutive folder number for that day and the radioactive sources used. The format looks like the following:

- YYYY-MM-DD_#_sources

For example the directory name '2009-08-29_3_beamBa133Na22' would indicate that its contents were recorded on the 29th of August in the year 2009 with the (neutron) beam and Ba133 and Na22 as additional calibration sources and that it is the third directory of that day.

To limit the amount of data one folder holds, writing in a new folder is started every few hours by the experimentalist, or whenever the experimental conditions are changed.

C.1.2 Measurements

Within the data acquisition and data analysis, the term 'measurement' refers to a specific data set within one folder. A folder recorded during a beam time run typically contains several dozen to several hundred measurements. A new

measurement is started automatically if a TDC reset (see section 3.8.2.1 for details) occurs. Otherwise, subsequent data would be unusable due to ambiguity of all timestamps. The current measurement number is included in every file name belonging to the data set. The first measurement number used is 0.

C.1.3 Files and File Types

The DAQ software writes the data of all types of VME modules to individual files. For each file type, a maximum file size is specified. When one file reaches its size limit, writing to new files for all file types of the corresponding module is started. The file number for this data type is increased by one. With each new measurement the file number is initialized to 0. All files of all modules in a folder share the same base name, chosen by the user. The file type, measurement number and file number is appended. By convention, the base name (in the DAQ and analysis software and the following description referred to as 'filenameBase') holds the used sources and sometimes the date, and is thus of a similar format as the folder name is.

In the following description, #m stands for the measurement number and #f stands for the file number. For further details, including the format of the written files, a detailed manual is in preparation.

C.1.3.1 v1190 TDC files

The v1190 TDC writes three types of files for each measurement.

- *filenameBase*_tdc_#m_#f.dat
  This file contains the tdc hits in the order given by the module. Channel number and tdc time is saved.

- *filenameBase*_tdc_times_#m_#f.dat
  The TDC times file contains all trigger times in real time, that is time and date of the current day. This information is derived from the clock settings of the DAQ system, also known as the system time.

- *filenameBase*_measurementProperties_#m.dat
  For each measurement a properties file is written that contains all necessary settings of the TDC module, for example the used resolution. This information is necessary to interpret the binary data contents of the TDC file.

C.1.3.2 Sis3302 ADC files

The Sis3302 writes three types of files for each measurement.

- *filenameBase*_Sis3302_#m_#f.dat
  The Sis3302 raw data file contains the complete pulses of all recorded cryodetector channels.
- *filenameBase*_Sis3302_prop_#m_#f.dat
  The Sis3302 pulse properties file holds all additional information for each recorded event in the Sis3302 raw data file. This includes timestamps and saved channels. This file is necessary to interpret the data in the raw data file.
- *filenameBase*_Sis3302_vitals_#m.dat
  This file contains all vital informations that remains constant for this measurement. Pretrigger settings and chosen resolution are saved here. One file is written for every measurement.

C.1.3.3 Sis3320 ADC files

The Sis3320 writes two files for each measurement.

- *filenameBase*_Sis3320_#m_#f.dat
  All PMT pulses and integration gate results are saved in the Sis3320 file.
- *filenameBase*_Sis3320_vitals_#m.dat
  The gate lengths and positions (see section 3.8.1.5 and 4.4.1) are saved in this file.

C.2 Low Level Data Access

The DAQ software (see section 3.8.2) reads out the VME modules and saves the relevant information to disk. In a first step, this data has to be made readable to Matlab and the user. The data is saved in a binary format.

C.2.1 Sis3302 Data Access

The Sis3302 saves the cryodetector pulses. Data access is realized with the following functions:

- *readSis3302*
  This function reads the *properties* and *vitals* file. It contains all timestamps and saved detectors that are archived in the raw data file. Also the exact positions of each pulse in the raw data file are returned.
- *getPulseSis3302*
  One pulse of rawdata is read out. The result contains all saved channels for a single event. Readout is limited to one pulse at a time to minimize memory usage.

C.2.2 Sis3320 Data Access

Several routines to access the Sis3320 data have been written. They are all similar in architecture but are needed for different steps in the analysis.

- *readSis3320FileChannel*
  This routine reads a single file of Sis3320 data. Also it converts the file to a different format for faster data access in all future calls to this function. The result only contains the ADC data of one single channel.
- *readSis3320Measurement*
  This function returns all hits in a measurement for a given channel. It makes several calls to *readSis3320FileChannel*. Also, it saves an additional converted file for faster data access in the future.
- *readAllSis3320MeasurementsForDetector*
  Similar to the previous function, but it reads all measurements of a folder.
- *loadSis3320Vitals*
  This routine reads the vitals file to retrieve the integration gate information. It is needed for the pulse shape integration.

C.2.3 v1190 TDC Data Access

Three routines are used to access the TDC data.

- *readTdc64File*
  This routine provides basic access to the TDC raw data without any preprocessing.
- *getTimesChannel*
  This function uses *readTdc64File* to get all hits of a specific TDC channel. It loops over all measurements and thus contains the hits of the complete folder.
- *getTimesChannelList*
  This function can be used to greatly speed up the process of *getTimesChannel* since it does the channel sorting for all channels in one single step.

C.3 Module Clock Synchronization

The clocks of the different ADCs and TDCs run at different speed relative to each other. For triple coincidence identification, the clocks have to be synchronized.

C.3.1 About Clock Deviation

Real clocks are not ideal. That means that their frequency typically deviates from the expected frequency by few percent. As we will see below, this deviation can be described as a term constant over time in the order of few percent and a time dependent term in the order of 10^{-5} or smaller. The constant term describes the general mean deviation of the sampling clock from their desired frequency, i.e. the 200 MHz clock of the Sis3320 ADC typically runs at $200(\pm 5)$MHz. This deviation is different for each module and clock but can be considered a constant property. It can be determined relative to another clock by checking the different times after a synchronized start.

The time dependent term is much smaller but still causes a deviation of several $\sim 100ns$ over a short time ($\sim 1s$). It may be caused for example by differing temperatures of the quartz. It can not be determined prior to matching all ADC times to the TDC time. The algorithm to match the different times must be robust enough to match the times despite of this deviation.

C.3.2 Clock Synchronization Technique

Each detector supplies its signal to one of the ADCs and the TDC. See the wiring scheme (see figure 3.23) for further details. For the photomultiplier tubes (PMTs) this is done by splitting the anode signal and feeding it to the Sis3320 ADC as well as to the constant fraction discriminator (CFD), which forwards a logical signal of ECL standard to the TDC. For the Sis3302, this is realized by supplying the logical signal that is emitted whenever the trigger condition of the ADC is met to the TDC. This way, each trigger gets a timestamp by the TDC and by one of the ADCs, if the signal is above threshold in both modules. The goal is to map each ADC hit to one of the TDC hits.

An additional difficulty is that one module might not recognize a hit (because it is near to the threshold, for example) while the other module does. The data analysis software then undertakes the following steps automatically in the following order for each ADC channel:

1. **Rescaling of the ADC data.** The time difference between the first and the last timestamp for this ADC channel is calculated. The same is done for this channel in the TDC. This gives a good estimate about how different the clocks run on average. The ADC timestamps are then rescaled so that the elapsed times show up as equal. This rescaling is typically of the order of one to three percent

2. **Removal of subsequent hits.** The TDC has a different dead time than the ADC. The ADC's deadtime is much larger since it records several data points for each event while the TDC only stores the timestamp. Subsequent triggers within some hundred ns are thus removed from the TDC data to have the same amount of deadtime in both modules. This

ensures that no hit in the ADC data is matched to a TDC datum that could not have been seen by the ADC.

3. **Fingerprint matching.** This step makes use of the fact that the clock deviation is negligible compared to the elapsed time between two subsequent triggers. The algorithm selects ten subsequent data points of ADC data for every 100 data points. The time pattern on which these ten hits occurred are considered unique since the time difference between two hits is purely statistical in nature. Because of this uniqueness it is referred to as a *fingerprint*.

   Afterwards the TDC data is scanned for the hit pattern that has the highest similarity to the one in the ADC data. Figure C.1 shows TDC data scanned for such a pattern, the y-axis shows the RMS between a fingerprint in the ADC compared to the TDC. The position of the minimum indicates at which pulse number TDC and ADC sampled the same data.

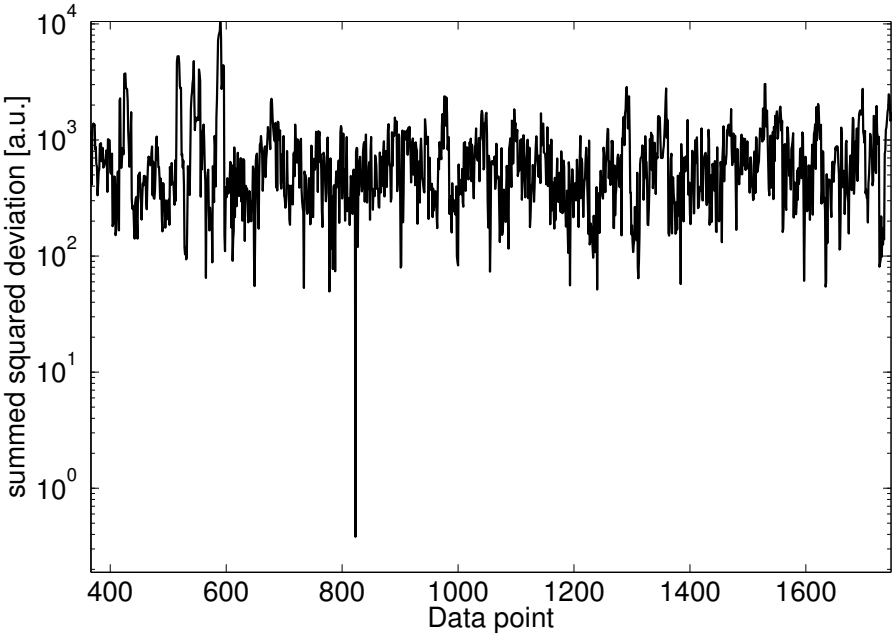

Figure C.1: The process of fingerprint matching for a fingerprint of 10 points length. On the x-axis the pulse number of the TDC hits is shown, the y-axis shows the deviation (RMS) of the ADC data for this print on a logarithmic scale. See the text for details.

4. **Checking the matched points for consistency.** The previous point is repeated for every 100 data points of ADC data. This results in several approximately equally spaced ADC data points matched to their corresponding TDC data. This means that the points should be in ascending order and the ADC time should approximately match the TDC time. These assumptions allow to remove outliers. Outliers are mainly caused

by missing hits in one of the modules, that means a hit was registered near the threshold and was only recognized by one module. Figure C.2

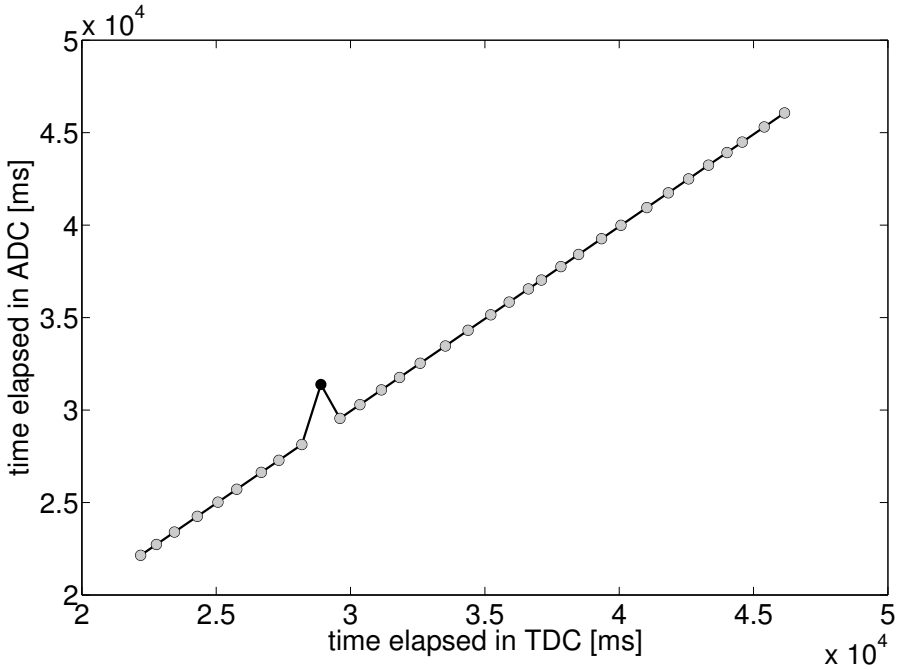

Figure C.2: The assumed ADC time of approximately equidistant data points is shown versus the TDC time. The assumed time is based on the ADC hit pattern matching a TDC pattern with minimal deviation. The data points marked with a gray circle have been accepted as correct, the outlier (marked in black) is recognized and removed. See the text for details.

shows where the ADC data has been matched to their assumed TDC hits. The outlier is recognized, only the points marked with gray circles fulfill the consistency checks (monotony, matching a linear fit). At this point, only few events of ADC data are matched to the TDC, but these allow to match all other points in between.

5. **Matching all points.** The matched hits remaining after all consistency checks function as 'anchors' to match all data in between. All remaining ADC timestamps are matched to their corresponding TDC timestamps by assuming a linear correlation between the matched times. Figure C.3 shows the deviation of the ADC and TDC timestamps after correction of the linear term. It can be seen that sometimes the ADC clock and at other times the TDC clock runs faster. The deviation is of the order of few hundreds of *ns*.

The steps described above are fully automated and highly reliable. The used functions are called

- *mapTimestampsSis3320*

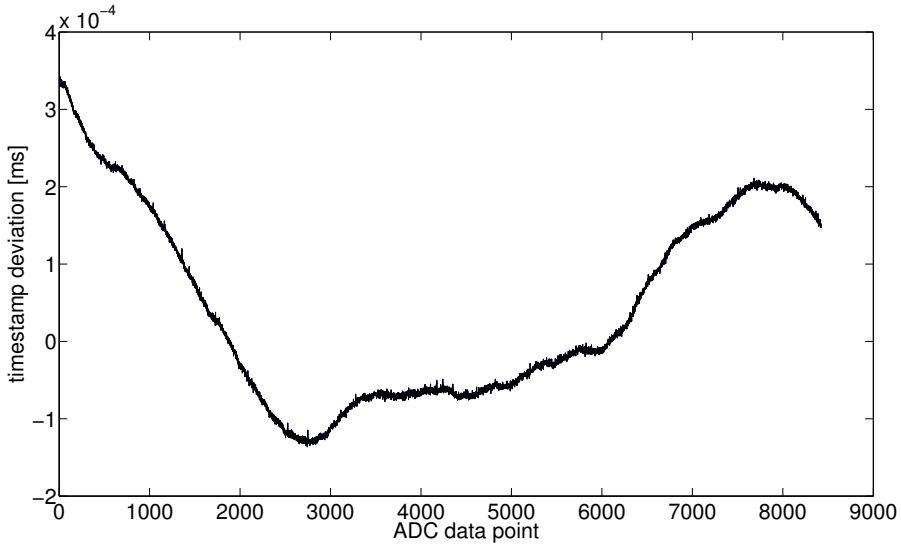

Figure C.3: Timestamp deviation after first-order correction. The deviation is about $3 * 10^{-4} ms$ with sometimes one module clock and sometimes the other running faster.

- *mapTimestampsSis3302*
- *fingerprintMatching*
- *removeSubsequntHits*

Appendix D

Nuclear Recoil Band Composition

To derive the resolution of the light detector for nuclear recoils in the signal region for the quenching factor analysis (i.e. $80-110keV$), a three-component fit was applied to the nuclear recoil band in section 5.3.3. To assure convergence of the fit, the free parameters had to be confined to physical values and the width for all three Gaussians was assumed to be the same. Limited by the resolution of the light detector, the three components could not be fitted reliably. Even though a three-component fit is the correct description, the fitting procedure is here repeated with two Gaussians and all parameters free, meaning that one Gaussian is fitted to the oxygen distribution and one to the contributions by calcium and tungsten, since the latter can not be resolved individually. The fit is first applied with the two Gaussians not sharing the same width σ. The equation is:

$$F = A_O e^{-\frac{\left(x-\frac{1}{QF_O}\right)^2}{2\sigma_O^2}} + A_{Ca,W} e^{-\frac{\left(x-\frac{1}{QF_{Ca,W}}\right)^2}{2\sigma_{Ca,W}^2}}. \tag{D.1}$$

The individual components and the data is shown in figure D.1. The fitted values and their 95% confidence bounds are shown in table D.1.

parameter	fit result	95% confidence bounds
A_O	275.1	(269.9, 280.3)
$A_{Ca,W}$	49.0	(36.9, 63.1)
QF_O	9.35	(9.11, 9.59)
$QF_{Ca,W}$	48.8	(29.9, 67.8)
σ_O	0.050	(0.048, 0.052)
$\sigma_{Ca,W}$	0.034	(0.029, 0.039)

Table D.1: Obtained values for the two-component fit to the nuclear recoil band.

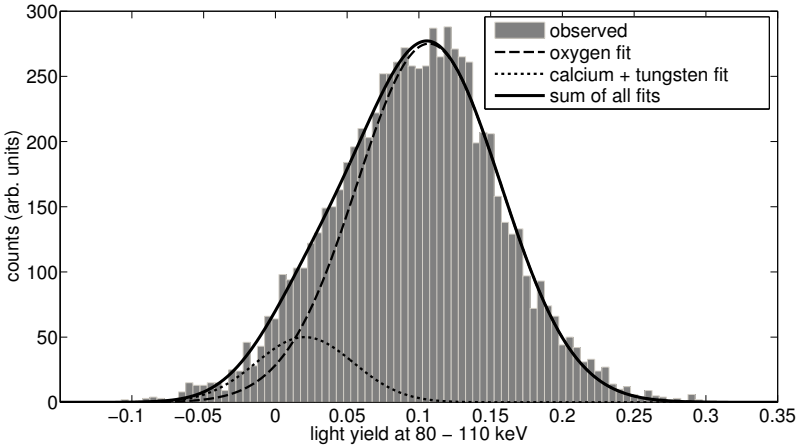

Figure D.1: The light yield of nuclear recoils observed at recoil energies between $80keV$ and $110keV$ fitted with the sum of two Gaussians (equation D.1). The individual Gaussians are shown as well, the fit values are listed in table D.1. See the text for details.

The fit is repeated with the assumption that both Gaussians share the same width as in section 5.3.3, i.e. $\sigma_O = \sigma_{Ca,W} = \sigma$. The obtained values for this case are listed in table D.2. The fit and the individual components are shown

parameter	fit result	95% confidence bounds
A_O	241.6	(232.8, 250.3)
$A_{Ca,W}$	91.6	(76.3, 106.9)
QF_O	8.64	(8.43, 8.84)
$QF_{Ca,W}$	22.1	(19.8, 24.3)
σ	0.0466	(0.0451, 0.0482)

Table D.2: Obtained values for the two-component fit to the nuclear recoil band with both Gaussians sharing the same width.

in figure D.2.

The parameter of importance is the resolution of the light detector. It was $\sigma = 0.047(5)$ when derived from the three component fit in section 5.3.3. The two component fit with two Gaussians with individual width gives $\sigma_O = 0.050(2)$ and $\sigma_{Ca,W} = 0.034(5)$. The width of the Gaussian attributed to oxygen is found to be the same within the errors. This is expected since the observed distribution is dominated by oxygen recoils and this contribution can be fitted most reliably. When fitted with the same width for both Gaussians, the extracted resolution is $\sigma = 0.0466(16)$.

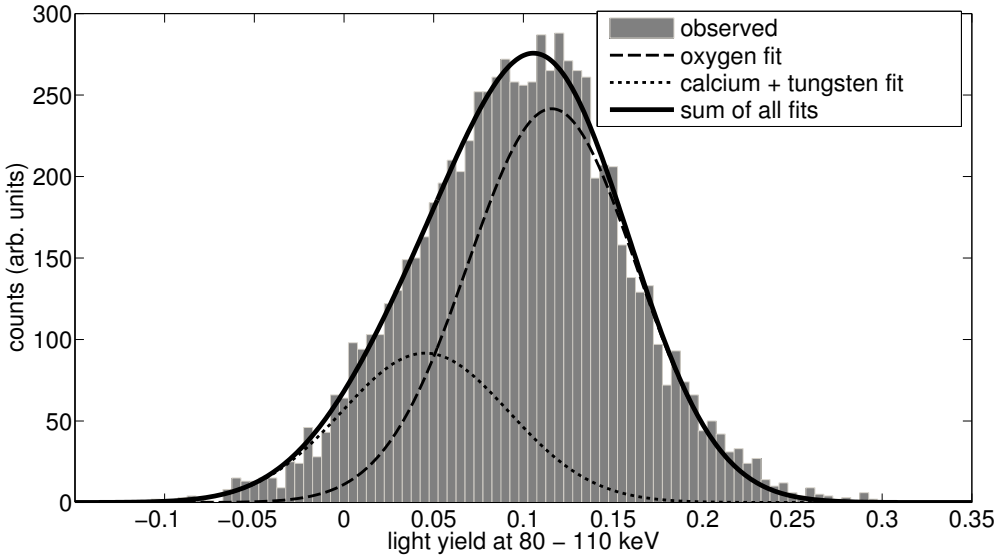

Figure D.2: The light yield of nuclear recoils observed at recoil energies between $80keV$ and $110keV$ fitted with the sum of two Gaussians. Compared to the fit shown in figure D.1 both Gaussians share the same width σ. The fit results are shown in table D.2.

Bibliography

[1] F. Zwicky, Helvetica Physica Acta **6**, 110 (1933).

[2] F. Zwicky, Astrophysical Journal **86**, 217 (1937).

[3] D. Walsh, R. F. Carswell, and R. J. Weymann, Nature **279**, 381 (1979).

[4] X. Wu, T. Chiueh, L. Fang, and Y. Xue, Monthly Notices of the Royal Astronomical Society **301**, 861 (1998), arXiv:astro-ph/9808179.

[5] A. Refregier, Annual Review of Astronomy and Astrophysics **41**, 645 (2003), arXiv:astro-ph/0307212.

[6] A. N. Taylor, S. Dye, T. J. Broadhurst, N. Benitez, and E. van Kampen, Astrophysical Journal **501**, 539 (1998), arXiv:astro-ph/9801158.

[7] V. C. Rubin and W. K. Ford, Jr., Astrophysical Journal **159**, 379 (1970).

[8] V. C. Rubin, W. K. J. Ford, and N. Thonnard, Astrophysical Journal **238**, 471 (1980).

[9] K. G. Begeman, A. H. Broeils, and R. H. Sanders, Royal Astronomical Society, Monthly Notices **249**, 523 (1991).

[10] A. A. Penzias and R. W. Wilson, Astrophysical Journal **142**, 419 (1965).

[11] G. Gamow, Nature **162**, 680 (1948).

[12] G. Gamow, Physical Review **74**, 505 (1948).

[13] G. F. Smoot *et al.*, Astrophysical Journal Letters **396**, L1 (1992).

[14] R. K. Sachs and A. M. Wolfe, Astrophysical Journal **147**, 73 (1967).

[15] I. A. Strukov, A. A. Brukhanov, D. P. Skulachev, and M. V. Sazhin, Physics Letters B **315**, 198 (1993).

[16] N. Jarosik *et al.*, The Astrophysical Journal Supplement **192**, 14 (2011).

[17] NASA, WMAP Science Team, Nasa picture archive, `http://map.gsfc.nasa.gov/media/080997/index.html`.

[18] N. Sánchez and Y. Parijskij, *The early universe and the cosmic microwave background: theory and observations*, NATO science series: Mathematics, physics, and chemistry Vol. 130 (Springer, 2003).

[19] J. R. Primack and G. R. Blumenthal, What is the dark matter? - Implications for galaxy formation and particle physics, in *NATO ASIC Proc. 117: Formation and Evolution of Galaxies and Large Structures in the Universe*, edited by J. Audouze & J. Tran Thanh Van, pp. 163–183, 1984.

[20] V. Springel *et al.*, Nature **435**, 629 (2005), arXiv:astro-ph/0504097.

[21] D. Clowe *et al.*, Astrophysical Journal **648**, L109 (2006), arXiv:astro-ph/0608407.

[22] G. Bertone, D. Hooper, and J. Silk, Physics Reports **405**, 279 (2005), arXiv:hep-ph/0404175.

[23] R. D. Peccei and H. R. Quinn, Physical Review D **16**, 1791 (1977).

[24] R. D. Peccei and H. R. Quinn, Physical Review Letters **38**, 1440 (1977).

[25] R. L. Davis, Physics Letters B **180**, 225 (1986).

[26] G. G. Raffelt, Axions in astrophysics and cosmology, in *Dark Matter in Cosmology, Clocks and Tests of Fundamental Laws*, edited by B. Guiderdoni, G. Greene, D. Hinds, & J. Tran Thanh Van, pp. 159–+, 1995, arXiv:hep-ph/9502358.

[27] H. Primakoff, Physical Review **81**, 899 (1951).

[28] C. E. Aalseth *et al.*, Nuclear Physics B Proceedings Supplements **110**, 85 (2002).

[29] S. Andriamonje *et al.*, Journal of Cosmology and Astroparticle Physics **4**, 10 (2007), arXiv:hep-ex/0702006.

[30] E. Arik *et al.*, Journal of Cosmology and Astroparticle Physics **2**, 8 (2009).

[31] L. D. Duffy *et al.*, Physical Review D **74**, 012006 (2006), arXiv:astro-ph/0603108.

[32] K. J. Mack and P. J. Steinhardt, ArXiv e-prints (2009), 0911.0418.

[33] K. J. Mack, ArXiv e-prints (2009), 0911.0421.

[34] B. Pontecorvo, Soviet Journal of Experimental and Theoretical Physics **6**, 429 (1958).

[35] R. Davis, D. S. Harmer, and K. C. Hoffman, Physical Review Letters **20**, 1205 (1968).

[36] Q. R. Ahmad *et al.*, Physical Review Letters **87**, 071301 (2001), arXiv:nucl-ex/0106015.

[37] A. Goobar, S. Hannestad, E. Mörtsell, and H. Tu, Journal of Cosmology and Astroparticle Physics **6**, 19 (2006), arXiv:astro-ph/0602155.

[38] J. R. Bond, G. Efstathiou, and J. Silk, Physical Review Letters **45**, 1980 (1980).

[39] C. S. Wu, E. Ambler, R. W. Hayward, D. D. Hoppes, and R. P. Hudson, Physical Review **105**, 1413 (1957).

[40] S. Dodelson and L. M. Widrow, Physical Review Letters **72**, 17 (1994).

[41] M. Milgrom, Astrophysical Journal **270**, 365 (1983).

[42] J. D. Bekenstein, Physical Review D **70**, 083509 (2004).

[43] R. Reyes *et al.*, Nature **464**, 256 (2010).

[44] G. Bertone, Nature **468**, 389 (2010).

[45] L. Bergström, Reports on Progress in Physics **63**, 793 (2000), arXiv:hep-ph/0002126.

[46] V. Bertin, E. Nezri, and J. Orloff, European Physical Journal C **26**, 111 (2002), arXiv:hep-ph/0204135.

[47] F. Aharonian *et al.*, Physical Review Letters **97**, 221102 (2006), arXiv:astro-ph/0610509.

[48] S. D. Hunter *et al.*, Astrophysical Journal **481**, 205 (1997).

[49] C. Sander, ArXiv e-prints (2007), 0710.4439.

[50] P. Ullio, L. Bergström, J. Edsjö, and C. Lacey, Physical Review D **66**, 123502 (2002).

[51] A. Ibarra and D. Tran, Journal of Cosmology and Astroparticle Physics **7**, 2 (2008).

[52] G. Bertone and D. Merritt, Modern Physics Letters A **20**, 1021 (2005), arXiv:astro-ph/0504422.

[53] R. Catena and P. Ullio, Journal of Cosmology and Astroparticle Physics **8**, 4 (2010).

[54] J. D. Lewin and P. F. Smith, Astroparticle Physics **6**, 87 (1996).

[55] J. F. Navarro, C. S. Frenk, and S. D. M. White, Astrophysical Journal **462**, 563 (1996), arXiv:astro-ph/9508025.

[56] L. Bergström, P. Ullio, and J. H. Buckley, Astroparticle Physics **9**, 137 (1998), arXiv:astro-ph/9712318.

[57] R. H. Helm, Physical Review **104**, 1466 (1956).

[58] A. Gütlein *et al.*, ArXiv e-prints (2010), 1009.3815.

[59] A. K. Drukier, K. Freese, and D. N. Spergel, Physical Review D **33**, 3495 (1986).

[60] DAMA Website, `http://people.roma2.infn.it/~dama/web/nai_dmp.html`.

[61] R. Bernabei *et al.*, Nuclear Instruments and Methods in Physics Research A **592**, 297 (2008).

[62] R. Bernabei *et al.*, European Physical Journal C , 167 (2008).

[63] J. March-Russell, C. McCabe, and M. McCullough, Journal of High Energy Physics **5**, 71 (2009).

[64] D. Smith and N. Weiner, Physical Review D **64**, 043502 (2001), arXiv:hep-ph/0101138.

[65] G. Angloher *et al.*, Identification of Dark Matter 2010 (IDM2010) Proceedings, to be published .

[66] E. M. Drobyshevski, Modern Physics Letters A **23**, 3077 (2008).

[67] C. E. Aalseth *et al.*, ArXiv e-prints (2010), 1002.4703.

[68] A. L. Fitzpatrick, D. Hooper, and K. M. Zurek, Physical Review D **81**, 115005 (2010).

[69] J. P. Ralston, ArXiv e-prints (2010), 1006.5255.

[70] XENON100 Collaboration *et al.*, ArXiv e-prints (2011), 1103.0303.

[71] XENON100 Collaboration *et al.*, ArXiv e-prints (2011), 1104.2549.

[72] J. I. Collar and D. N. McKinsey, ArXiv e-prints (2010), 1005.0838.

[73] Warp Collaboration, Acciarri, R. *et al.*, Astroparticle Physics **28**, 495 (2008), arXiv:astro-ph/0701286.

[74] M. Laffranchi, A. Rubbia, and the ArDM collaboration, Journal of Physics Conference Series **65**, 012014 (2007), arXiv:hep-ph/0702080.

[75] J. A. Nikkel, W. H. Lippincott, and D. N. McKinsey, International Journal of Modern Physics A **20**, 3113 (2005).

[76] T. Shutt *et al.*, Physical Review Letters **69**, 3531 (1992).

[77] Z. Ahmed *et al.*, Physical Review Letters **102**, 011301 (2009).

[78] The CDMS Collaboration and Z. Ahmed, ArXiv e-prints (2009), 0912.3592.

[79] The CDMS II Collaboration, Science **327**, 1619 (2010).

[80] EDELWEISS Collaboration *et al.*, Physics Letters B **687**, 294 (2010).

[81] G. Angloher *et al.*, Astroparticle Physics **18**, 43 (2002).

[82] G. Angloher *et al.*, Astroparticle Physics **31**, 270 (2009).

[83] S. Roth *et al.*, Optical Materials **31**, 1415 (2009).

[84] S. Henry *et al.*, Journal of Instrumentation **2**, 11003 (2007).

[85] V. B. Mikhailik *et al.*, Physical Review B **69**, 205110 (2004).

[86] W. Westphal, *Development and Characterization of Cryogenic Detectors for the CRESST Experiment*, Technische Universität München, 2008.

[87] R. F. Lang *et al.*, Astroparticle Physics **32**, 318 (2010).

[88] W. Westphal *et al.*, Nuclear Instruments and Methods in Physics Research A **559**, 372 (2006).

[89] P. C. F. di Stefano *et al.*, Journal of Applied Physics **94**, 6887 (2003), arXiv:physics/0307042.

[90] R. F. Lang and W. Seidel, New Journal of Physics **11**, 105017 (2009).

[91] C. Cozzini *et al.*, Physical Review C **70**, 064606 (2004), arXiv:nucl-ex/0408006.

[92] Q. Kronseder, *Quenching Factor Measurement of CaWO4*, Diploma thesis, Ludwigs-Maximilians-Universität, 2010.

[93] S. Pfister, Private Communication, 2011.

[94] S. Pfister, *Suche nach Dunkler Materie mit dem CRESST-II-Experiment*, PhD thesis, Technische Universität München, 2010.

[95] P. Huff, *Messung der Lichtausbeute von Rückstosskernen in CaWO4*, Diploma thesis, Technische Universität München, 2006.

[96] S. Scholl, *Non-Cosmogenic Neutron Background Simulation*, Phd thesis, in preparation, Universität Tübingen.

[97] H. R. Wulandari, *Study On Neutron-Induced Background in the Dark Matter Experiment CRESST*, PhD thesis, Technische Universität München, 2003.

[98] T. Jagemann *et al.*, Astroparticle Physics **26**, 269 (2006).

[99] T. Jagemann, *Measurement of the Scintillation Light Quenching for Nuclear Recoils induced by Neutron Scattering in Detectors for Dark Matter Particles*, PhD thesis, Technische Universität München, 2004.

[100] M. Drosg, Nuclear Instruments and Methods in Physics Research A **254**, 466 (1987).

[101] R. Strauss, *Quenching Factor Measurements of CaWO4 at mK Temperatures by Neutron Scattering for the Dark Matter Experiments CRESST and EURECA*, Diploma thesis, Technische Universität München, 2010.

[102] T. M. Undagoitia, *Measurement of light emission in organic liquid scintillators and studies towards the search for proton decay in the future large-scale detector LENA*, PhD thesis, Technische Universität München, 2008.

[103] G. Knoll, *Radiation detection and measurement* (Wiley, 2000).

[104] Eljen Technology, `http://www.eljentechnology.com/`.

[105] F. T. Kuchnir and F. J. Lynch, IEEE Transactions on Nuclear Science **15**, 107 (1968).

[106] E. Simon *et al.*, Nuclear Instruments and Methods in Physics Research A **507**, 643 (2003), arXiv:astro-ph/0212491.

[107] Picowatt, `http://www.picowatt.fi/`.

[108] F. Pobell, *Matter and methods at low temperatures*, third ed. (Springer, Berlin, 2007).

[109] Oxford Instruments, `http://www.oxinst.com/`.

[110] supracon AG Jena, `http://www.supracon.com/`.

[111] Magnicon, `http://www.magnicon.com/`.

[112] R. Strauss, PhD Thesis, In Preparation, Technische Universität München.

[113] P. M. Berglund, H. K. Collan, G. J. Ehnholm, R. G. Gylling, and O. V. Lounasmaa, Journal of Low Temperature Physics **6**, 357 (1972).

[114] C. Isaila, *Development of Cryogenic Light Detectors with Neganov-Luke Amplification for the Dark Matter Experiments CRESST and EURECA*, PhD thesis, Technische Universität München, 2010.

[115] Rohde und Schwarz, `http://www.rohde-schwarz.de/`.

[116] Caen, `http://www.caentechnologies.com/`.

[117] Struck Innovative Systeme GmbH, `http://www.struck.de/`.

[118] J. Christiansen, HPTDC, Version 2.2, High Performance Time to Digital Converter for HPTDC version 1.3, 2004, `www.star.bnl.gov/public/tof/electronics/hptdc_manual_ver2.2.pdf`.

[119] N. Instruments, Labview, `http://www.ni.com/labview/`.

[120] Q. C. Nokia, Qt, `http://qt.nokia.com/`.

[121] Mathworks, Matlab, `http://www.mathworks.com/products/matlab/`.

[122] M. Goodman Thierry Lasserre, ArXiv High Energy Physics - Experiment e-prints (2006), arXiv:hep-ex/0606025.

[123] J. Meyer, *Realization and Characterization of the Muon Veto Scintillator and the Buffer Liquid of the Double Chooz Experiment*, Diploma thesis, Technische Universität München, 2010.

[124] M. Wurm *et al.*, ArXiv e-prints (2011), 1104.5620.

[125] J. Scherzinger, Diploma Thesis, In Preparation, Technische Universität München, 2012.

[126] J. B. Birks, *The theory and practice of scintillation counting / by J.B. Birks* (Pergamon Press, Oxford [England], 1964).

[127] R. B. Firestone, C. M. Baglin, and S. Chu*Table of isotopes* No. v. 1-2 (Wiley, 1999).

[128] H. Kraus, Contribution to CRESST Collaboration Meeting, private communication, 2008.

[129] National Nuclear Data Center (NNDC) at BNL, Evaluated Nuclear Structure File (ENSDF), Database version of March 28, 2011.

[130] C. Coppi, *Quenching-Factor Measurements for Cryogenic Dark Matter Detectors*, Phd thesis, Technische Universität München, 2009.

[131] J. Lanfranchi *et al.*, Optical Materials **31**, 1405 (2009).

[132] M. Chadwick *et al.*, Nuclear Data Sheets **107**, 2931 (2006).

[133] C. Coppi *et al.*, In preparation, to be published.

[134] F. Proebst, Private Communication, 2011.

[135] G. Deuter, PhD thesis, in preparation, Technische Universität Tübingen.

[136] M. Drosg, Monoenergetic neutron production by two-body reactions in the energy range from 0.0001 to 500 MeV. An overview, in *IAEA TC Meeting on Accelerator-Based Neutron Sources*, KFKI, Debrecen, Hungary, 1999.

[137] S. Wawoczny, Diploma Thesis, In Preparation, Technische Universität München.

[138] M. v. Sivers, *Optimizing Detectors for Dark Matter*, Diploma Thesis, Technische Universität München, 2010.

[139] S. Koynov, M. S. Brandt, and M. Stutzmann, Applied Physics Letters **88**, 203107 (2006).

[140] P. Huff, *Optimierung szintillierender Tieftemperaturkalorimeter für den direkten Nachweis von Teilchen der Dunklen Materie*, Diploma thesis, Bayerische Julius-Maximilians-Universität Würzburg, Max-Planck- Institut für Physik München, 2007.

[141] J. Lanfranchi, T. Lachenmaier, W. Potzel, and F. von Feilitzsch, Nuclear Instruments and Methods in Physics Research A **520**, 135 (2004).

[142] J.-C. Lanfranchi, *Development of a new composite cryogenic detection concept for a radiochemical solar neutrino experiment*, PhD thesis, Technische Universität München, 2005.

Danksagung

Mein tief empfundener Dank gilt allen, die in den letzten Jahren zum Gelingen dieser Arbeit beigetragen haben: meinen Kollegen und Betreuern, meinen Freunden und meiner Familie.

Besonderer Dank gebührt Prof. Dr. Franz von Feilitzsch, meinem Doktorvater, der mich immer ermutigt hat und in vielen langen Gesprächen wertvolle Ratschläge zur Physik und darüber hinaus gegeben hat.
Ich bedanke mich auch bei Prof. Dr. Lothar Oberauer und Prof. Dr. Schönert für die Hilfestellung und ihr Interesse an dem Neutronenstreuexperiment.

Dr. Walter Potzel und Dr. Jean-Côme Lanfranchi danke ich für die langjährige Betreuung meiner Tätigkeit. Sie gaben mir jederzeit wertvolle Hilfe und waren in ausdauernden Diskussionen immer für mich da, besonders auch in den schwierigen Monaten vor der Abgabe dieser Arbeit.

Ein ganz besonderer Dank gilt Raimund Strauss. Ohne seine mutigen Verbesserungen sowie seinen (tatsächlich auch im Sinne des Wortes) unermüdlichen Einsatz hätte das Experiment heute nicht seinen hohen Standard erreicht.

Auch bedanke ich mich bei Dr. Chiara Coppi und Dr. Christian Isaila, die tolle Kollegen waren und viel zu dem Experiment beigetragen haben. Ich bedanke mich bei Wolfgang Westphal für seine Unterstützung und Hilfestellung. Ich bedaure es, ihm diesen Dank nicht mehr persönlich aussprechen zu können. Für weitere Unterstützung, viele Stunden im Beschleunigerlabor sowie zahlreichen Diskussionen über CRESST bedanke ich mich bei Dr. Sebastian Pfister und Sabine Roth.

Vielen Dank auch an Walter Carli und die Operateure am Beschleuniger, die durch ihr Fachwissen viel zum Gelingen des Experiments beigetragen haben. Auch hätte der Betrieb unseres Experiments während der Strahlzeiten nicht aufrecht erhalten werden können ohne die Unterstützung aus Tübingen. Vielen Dank dafür an Klemens Rottler, Stephan Scholl, Igor Usherov, Christoph Sailer, Gerhard Deuter, Marcel Kimmerle, Sebastian Diebold und Marc Pfeifer.

Mein ganz besonderer Dank gilt Herrman Hagn, der mit seinem Wissen und seinem Einsatz zu jeder Zeit für uns da war. Seine Unterstützung bei elektronischen Problemen war unverzichtbar. Vielen Dank auch an unser Werkstattpersonal Harald Hess, Erich Seitz und Thomas Richter für die hervorragende Arbeit. Ich bedanke mich für viele nette Gespräche und eine Menge Hilfe bei administrativen und sonstigen Problemen bei Beatrice van Bellen, Alexandra Füldner, Sonja Kraus und Maria Bremberger.

Des Weiteren danke ich allen hier nicht namentlich erwähnten Kollegen und Helfern für die angenehme Atmosphäre, für ihren Rat und ihre Unterstützung, auch während der zahlreichen Nachtschichten. Mein Dank gilt auch der gesamten CRESST Kollaboration.

Besonderer Dank gilt meinen Eltern, Großeltern und Gerd für ihre fortlaufende Unterstützung.